UNIVERSITÀ
DEGLI STUDI
DI PADOVA

SEDE AMMINISTRATIVA: UNIVERSITÀ DEGLI STUDI DI PADOVA

DIPARTIMENTO DI SCIENZE CHIMICHE

CORSO DI DOTTORATO DI RICERCA IN SCIENZA ED INGEGNERIA DEI MATERIALI

CICLO XXIX

Synthesis of Graphene supported on Cu(111) and investigation by Electrochemical Scanning Tunneling Microscopy

Coordinatore: Ch.mo Prof. Gaetano Granozzi

Supervisore: Dr. Christian Durante

Co-supervisore: Prof. Stefano Agnoli

Dottorando: Dmytro Chirkov

Abstract

The aim of this thesis is twofold: to investigate graphene (Gr) as a protective layer for metal substrates and to use Gr as a support for the growth of metal (both noble Pd, and non-noble Co) NPs, which were also studied as catalysts for the hydrogen evolution reaction (HER).

The thesis begins with an introduction in Chapter 1. Chapter 2 provides an overview on the most relevant structural and chemical properties of the investigated materials, and about the synthesis techniques that were exploited to prepare the investigated systems. Moreover, it presents the essential theoretical background and practical details regarding the different techniques and experimental methods that were used in this work.

Chapter 3 is dedicated to the description of synthesis of high quality Gr layers on both polycrystalline and single crystal copper substrates by low pressure Chemical Vapour Deposition (LPCVD) in a cold-wall reactor. With respect to other methods reported in the literature, this method is highly scalable, reproducible and applicable to several different substrates and allows the preparation of films of excellent quality.

Chapter 4 presents the main results about the morphological properties of Gr films prepared by catalytic CVD on clean copper, using ethylene (C_2H_4) gas as the precursor at a total pressure 0.5 ÷ 1 mbar. This chapter reports also a systematic study of the electrochemistry of Gr by EC-STM in different electrolyte solutions (HCl, $HClO_4$, H_2SO_4, KOH) at room temperature. The electrochemical properties of clean copper electrodes in the same experimental conditions were used as a benchmark to understand the effect of Gr. The combination of ex-situ methods with in-situ electrochemical STM allowed obtaining a rather complete information about the studied materials. Samples were thoroughly investigated using a multitechnique approach exploiting the use of Raman spectroscopy, Scanning Electron Microscopy (SEM) and X-ray Photoelectron Spectroscopy (XPS) immediately after the synthesis and after the exposure to the electrochemical environment.

The fabrication and characterization of metal NPs is discussed in Chapter 5. The electrodeposition of Pd from $PdSO_4$ in H_2SO_4 solution onto a Gr/copper substrate was

carried out in a three-electrode cell equipped with the STM system. Alternatively, the metal NPs were deposited by Physical Vapour Deposition (PVD), since this technique allowed a better control of NP size and coverage. In this case both Pd and Co NPs were investigated as prototypical examples of a noble and a non-noble metal. Finally, the reactivity of the NPs toward HER was investigated combining the electrochemical characterization with the results from EC-STM.

Contents

Abstract 4

Contents 6

Acronyms 9

1. Introduction 11

2. Theoretical and experimental background 14

2.1. Introduction 14

2.2. Graphene 14

2.3. Copper substrate 16

2.4. Graphene on copper 21

2.5. Graphene preparation methods 22

2.6. Mechanism of graphene growth 24

2.7. Ex situ graphene characterization techniques 24

2.7.1. Raman spectroscopy 24

2.7.2. Scanning Electron Microscopy 26

2.7.3. X-Ray Photoelectron Spectroscopy 26

2.7.4. Low-energy Electron Diffraction 27

2.8. In situ graphene characterization techniques 27

2.8.1. Electrochemical fundamentals 27

2.8.2. The electrode/electrolyte interface 31

2.8.3. Cyclic Voltammetry 33

2.8.4. The electrochemical cell 35

2.8.5. Corrosion behavior 37

2.8.6. Experimental 38
2.8.7. Electrochemical Scanning Tunneling Microscopy 39
2.8.8. Theoretical principle of tunneling effect 40
2.8.9. EC-STM Set-Up and working principle 43
2.8.10. EC-STM electronics 51
2.8.11. Tunneling tips 53
2.8.12. Bipotentiostat 54
2.8.13. Scanner calibration 55
2.9. Metal NPs 56
2.10. Preparation and characterization of metal NPs 57
2.10.1. Physical Vapour Deposition 57
2.10.2. Electrochemical deposition 58
3. Preparation of graphene on copper 60
3.1. Introduction 60
3.2. Results 62
3.3. Conclusions 74
4. Investigation on graphene films 75
4.1. Introduction 75
4.2. Ex situ electrochemical measurements of Gr on Cu 75
4.3. STM investigation of G on Cu in air 88
4.4. STM investigation of graphene on copper in water 94
4.5. EC-STM measurements 95
4.5.1. $HClO_4$ electrolyte solution 97
4.5.2. HCl electrolyte solution 107
4.5.3. H_2SO_4 electrolyte solution 118

4.5.4. KOH electrolyte solution 123
4.6. Conclusions 128
5. Investigation of metal NPs deposited on Gr films 129
5.1. Introduction 129
5.2. Palladium 129
5.3. Cobalt 140
5.4. Conclusions 150
6. Summary 151
Bibliography 153
Appendix A. Papers and conferences 170
Papers 170
Conferences 170

Acronyms

ARXPS	Angle-Resolved X-Rays Photoelectron Spectroscopy
BE	Binding Energy
CE	Counter Electrode
CV	Cyclic Voltammetry
DR	Double-Resonance
EDL	Electrical Double Layer
EDX	Energy Dispersive X-ray
EC-STM	Electrochemical Scanning Tunneling Microscope
FCC	Face-Centered Cubic
FFT	Fast Fourier Transformation
FWHM	Full Width Half Maximum
GO	Graphene Oxide
Gr	Graphene
HER	Hydrogen Evolution Reaction
HOPG	Highly Ordered Pyrolytic Graphite
HOR	Hydrogen Oxidation Reaction
IHP	Inner Helmholtz Plane
LEED	Low-Energy Electron Diffraction
LPCVD	Low Pressure Chemical Vapour Deposition
NP	Nanoparticle
OHP	Outer Helmholtz Plane
ORR	Oxygen Reduction Reaction
PID	Proportional Integral Derivative

PSRE	Pseudo Silver/Silver Chloride Reference Electrode
PVD	Physical Vapour Deposition
RE	Reference Electrode
RHE	Reference Hydrogen Electrode
SCE	Saturated Calomel Electrode
SEM	Scanning Electron Microscopy
STM	Scanning Tunneling Microscopy
TM	Transition Metal
UHV	Ultra-High Vacuum
UPD	Underpotential Deposition
WE	Working Electrode
XPS	X-Ray Photoelectron Spectroscopy

1. Introduction

The fast decrease of fossil fuels (carbon, oil and natural gas) reserves due to the rapid increase of the global demand of energy, together with the harmful effects on the environment and on human health caused by the effects of the intensive exploitation of such sources, are pushing toward the development of new technological solutions for energy production. Different technologies based on renewable sources (sun, wind, water, etc.) have been intensively developed during the last two decades. One of them is the fuel cells technology, which is based on the conversion of the chemical energy present in the chemical bonds of different fuels such as hydrogen or alcohols, into electric energy by means of catalytically active materials. The only byproduct produced by these reactions is water, which than can be used again as a source of H_2 and O_2 gases, through an electrolysis process [1]. The possibility to obtain H_2 from water with high efficiency and low costs opens the way for a circular economy based on hydrogen as unique energy vector. Therefore, catalytic materials to be used for the hydrogen evolution reaction (HER), are currently deeply investigated. The catalysts showing the higher catalytic activity in this reaction are constituted by platinum nanoparticles (NPs) deposited onto an amorphous carbon substrate [1]. Platinum is one of the most expensive and scarcest metals on earth, hence, the reduction of the Pt amount in the catalysts or its replacement with less expensive metals is a fundamental objective for cost reduction, which is mandatory requirement for a global implementation of the hydrogen economy. The first potential candidate for platinum metal catalyst substitution is palladium, because it has similar properties, higher resistance to CO poisoning and lower cost in comparison with Pt, although only limitedly. Another possible metal that can be used as catalyst for HER is cobalt, which on the contrary is much less expensive and more abundant. More recently, it has been demonstrated that carbon-transition metals (Fe, Co, Ni) systems could be a new class of efficient electrocatalysts for HER [2,3]. However, the present performances are still not comparable to platinum and great improvements of the catalytic efficiency and durability are necessary. Both these properties are dependent on the dimension and structure of metal NPs, and on their interaction with the carbon-based support. In the last years, in order to tackle these issues

and to acquire a fundamental knowledge, graphene-based model systems have been the object of several investigations. Graphene (Gr), a one-atom-thick two-dimensional layer of sp^2 hybridized carbon atoms arranged into a planar honeycomb network, has recently emerged as an ideal candidate for supporting metal NPs, because of its extraordinary properties such as high electric and thermal conductivity, strong mechanical properties, huge surface area and excellent chemical stability. Moreover, its ability to form long range superstructures called Moiré patterns as a consequence of the electronic and physical interaction with a slightly mismatched or rotated substrate lattice can be effectively exploited for controlling at the nanoscale the morphological features of metal NPs.

Actually, the combination of electronic and morphological modulation of the Moiré allows a precise control of the nucleation and growth of metal NPs with nanoscale precision and it can be used as a tool for controlling the dimension and arrangement of metal NPs [4,5]. By controlling the size of metal clusters, it is then possible to tune the catalyst reactivity and selectivity. This opens the way to the rational design of new materials, and to the development of effective model systems for heterogeneous catalysis investigations. In fact, Gr-based systems have proven to be very good models systems to study heterogeneous processes (reactions at the gas–solid or liquid–solid interface) at the nanoscale.

The investigation at the atomic scale of the solid/liquid interface is of great interest in modern electrochemistry. Catalytically active NPs deposited on well-defined surfaces have attracted a great deal of attention in recent decades since they represent excellent model systems for studying very fundamental processes occurring in electrochemical reactions. In order to correlate the electrochemical behavior of supported metal NPs with their structural properties, a detailed characterization at the nanoscale under *in situ* electrochemical conditions is required. In this context, ElectroChemical Scanning Tunneling Microscope (EC-STM) is the perfect tool for the characterization of surface structures and interfacial electrochemical processes since it may be operated even during electrocatalytic reactions and has the potential to achieve atomic scale resolution.

An advantage of *in situ* EC-STM is that the same area can be imaged over time, and even as the potential is changed, without removing the electrode from the electrochemical environment. Thus, one can study the progressive morphological changes on a surface

during etching, corrosion or deposition, and gain a detailed understanding of structural changes at the atomic level.

Two highly versatile techniques for the preparation of nanostructured metal films are electrochemical metal deposition and PVD. These two methods are extremely interesting in the context of the study of electrochemical model systems, since PVD allows obtaining highly precise metal clusters with tailored properties that can be precise investigated by surface science techniques, whereas electrochemical deposition is the most natural technique for preparing NPs directly in an electrochemical environment and therefore can be *in situ* investigated by electrochemical techniques and *in primis* by EC-STM.

Deposition of metal NPs on Gr and their EC-STM studies are still lacking.

2. Theoretical and experimental background

2.1. Introduction

The first part of the PhD project was dedicated to the construction and optimization of the experimental setup used for the preparation of graphene (Gr) films on copper substrates by cold-wall Low Pressure Chemical Vapor Deposition (LPCVD) technique. For clarifying the role of growth temperature, pressure of the gas precursor and time of growth, several experiments were carried out. These parameters were changed in each experiment in order to find the optimal recipe for obtaining high quality Gr.

The deposited films were then characterized by different characterization techniques that can be classified in two groups*: in situ* and *ex situ* techniques. In *ex situ* techniques, the sample is removed from the reaction ambient, possibly exposed to an uncontrolled ambient (i.e. atmosphere) and then subjected to the analysis. In contrast, *in situ* methods are performed maintaining the sample in highly controlled dynamic conditions that are required for carrying out a specific function. For example, in case of electrochemical reactions this consist in the investigation of the sample when it is immersed in electrolyte and is maintained at a specific potential. The main goal of Gr characterization is to determine the quality of grown films in terms of amount of defects and quantification of the number of layers in a given sample. As matter of fact, the properties of Gr are strongly dependent on the thickness and defectivity.

This chapter briefly discusses Gr preparation and introduces the most important characterization techniques used in this work.

2.2. Graphene

Graphene (Gr) is a one-atom-thick two-dimensional layer of sp^2-bonded carbon atoms with a planar honeycomb crystal structure. It is the most basic building block of all carbon allotropes such as fullerenes, carbon nanotubes and graphite [6]. The first calculations of the Gr band structure, done by Wallace in 1947 [7], show that the unit cell of single-layer Gr

(highlighted in grey on Figure 1a) consists of two nonequivalent carbon atoms, A and B, separated by 1.42 Å, with a lattice constant of 2.46 Å, which reports also the corresponding reciprocal space lattice. Each atom has s, p_x and p_y orbitals and is bonded to three neighbor atoms in the lattice, forming an sp^2 atomic network. The p_z orbitals overlap between neighboring atoms resulting in empty π* and filled π states. The empty π* band and the filled π band, which respectively form the valence and the conduction bands in Gr, have a linear dependence of the energy vs the momentum k at the K points of the Brillouin zone. Such bands therefore in the reciprocal space form an upward and downward cone (the so-called Dirac cone) that share the apex. In pure self-standing graphene Gr, the single point where the two π bands cross each other coincides with the Fermi level and is called Dirac point. As a consequence of these electronic features of the bands, the electrons in Gr behave as massless Dirac fermions.

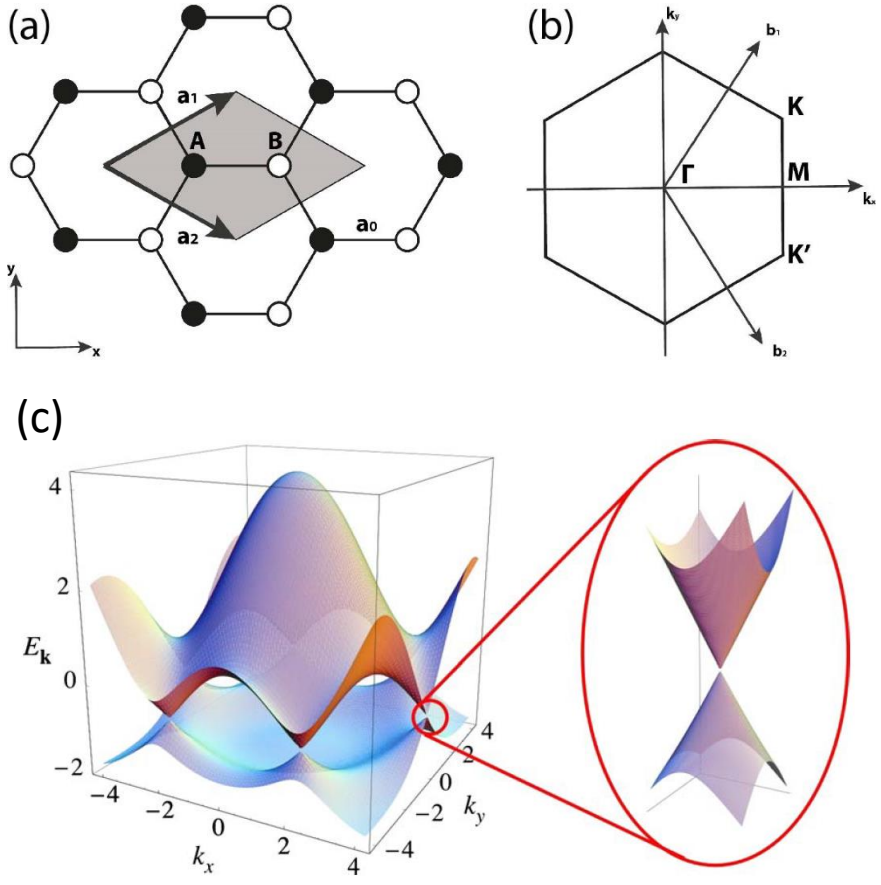

Figure 1. Crystal structure of Gr with the unit cell: (a) 2D hexagonal lattice of Gr in real space; (b) reciprocal lattice; (c) Electronic dispersion in the honeycomb lattice with energy spectrum and zoom in of the energy bands close to one of the Dirac points [8].

Gr was first isolated in the form of small flakes in 2004 [9]. Before, it was presumed that two-dimensional materials were thermodynamically unstable and Gr could not exist as an isolated single sheet. The term *graphene* is a combination of the word *graphite* and the suffix *–ene* that is used for polycyclic aromatic hydrocarbons, e.g. naphthalene, coronene, anthracene [10]. It has attracted great interest because of its outstanding electrical [8], optical [11], chemical [12], mechanical [13,14] and thermal [15] properties such as an intrinsic mobility limit of 2×10^5 cm^2/Vs [16], ballistic transport up to micron distances at room temperature [17], half-integer quantum Hall effect, absorption of only 2.3% of visible light [11] and high thermal conductivity of about 5×10^3 W/mK [15]. These exciting properties of Gr can open the way for a great number of potential applications in many different fields, such as flexible transparent electronics [18,19], energy storage [20], integrated circuits [21], field effect transistors [22,23], super capacitors [24], composite materials [25] and sensor technology [26]. It is thought that it may eventually replace many of the currently used materials of nowadays technology.

2.3. Copper substrate

Copper is a chemical element with the symbol Cu (from Latin: cuprum, *aes cyprium* "metal of Cyprus") and an atomic number of 29. It has electron configuration $[Ar]3d^{10}4s^1$. It is an important transition metal that has different attractive properties such as ductility, high electrical and thermal conductivity.

The samples used in this work were a polycrystalline copper foil (0.127 mm, 99.9%, Alfa Aesar® GmbH, Germany), polycrystalline copper disks (99.9%, Sigma-Aldrich), polycrystalline disks from copper gaskets for UHV systems (oxygen free copper, Tectra GmbH, Germany), and two single crystals with copper surfaces Cu(100) and Cu(111) (MaTeck GmbH, Germany). The single crystals have a disc shape of 8 mm diameter (thus exhibiting a geometric area of 0.5 cm^2) and 2 mm thickness.

Polycrystalline Cu (pCu) were used for determination of the Gr CVD parameters, which allowed to obtain high-quality Gr, and for investigation of the Gr stability on the surface in air and different electrolytes, and for studying the Gr protective properties for Cu dissolution reaction in acidic and alkaline solutions.

For a detailed investigation of the morphology and surface structure of the Gr/Cu samples at the nanoscale level, it is quite useful to use substrates with a well-known structure. Single crystals are optimal candidates since thy are characterized by a high level of order, low amount of defects and precise number and known type of surface structures. Crystalline copper has a face-centered cubic (fcc) unit cell with the nearest neighbor distance (NND) of Cu-Cu equal to a_{Cu} = 2.56 Å. The two most stable surfaces are the low-index (100) and (111) planes, which are shown in (Figure 2). These two surfaces have a square surface unit cell and a trigonal one for the (100) and (111) orientation, respectively. Consequently, one-fold (on top of one atom), two-fold (bridging two atoms) or four-fold coordination (in the hollow between four atoms) sites can be identified on the (100) surface. The coordination is equal to the number of surface atoms directly bound to an adsorbate at these sites. Correspondingly, the (111) surface has one-fold, two-fold and two types of three-fold sites, i.e. fcc- and hexagonal closed packed (hcp)-sites [27].

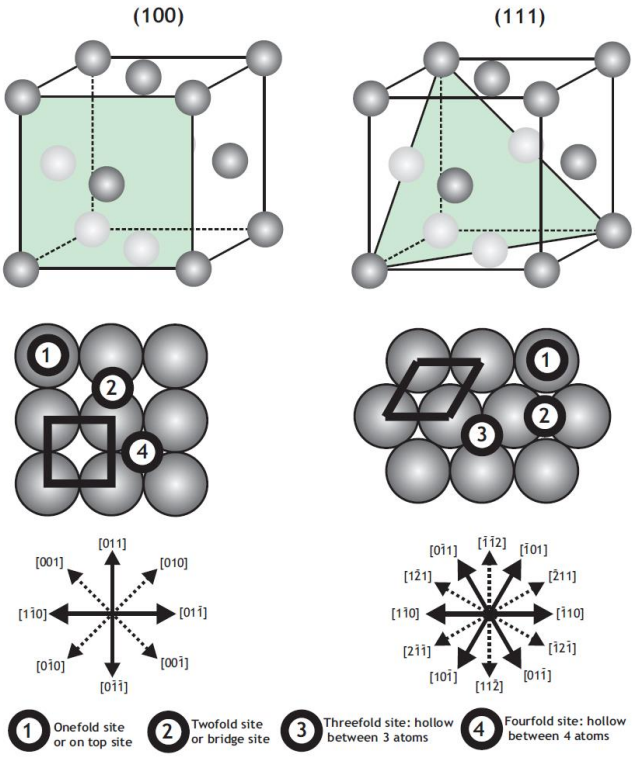

Figure 2. (100) and (111) planes of a face-centered cubic (fcc) metal.

According to Wood et. al. intrinsic crystallographic structure of the Cu substrate influences the Gr growth even more. For example, at low pressure and temperature the

fastest growth rate is on (111) surface [28]. On the other hand, Han et. al. reported that the extrinsic morphological features of copper surface such as roughness, grain boundary, defects, and impurity particles play a crucial role for forming nucleation seeds of monolayer and multilayer Gr [29].

The copper surface is always covered by native oxide films when exposed to the air. Copper(I) oxide is the corrosion product with the highest formation rate during the early stages of corrosion of copper in air at room temperatures [30]. As opposed to noble metals, which can be easily prepared by flame annealing, copper should be electropolished in order to remove the oxide film from the surface. Polycrystalline copper samples before CVD growth were polished firstly mechanically with sand paper and then with a 0.1 μm deagglomerated alumina suspension and finally electrochemically etched in 50% orthophosphoric acid (H_3PO_4, 84.8% VWR) solution at a voltage 2 ÷ 2.4 V, which was applied between the Cu anode and a platinum foil (about 2 cm^2) for about 30-60 sec at room temperature. Electropolishing in orthophosphoric acid was a good choice to achieve a sufficient degree of surface cleaning and low roughness. After this procedure, the substrates were rinsed with Milli-Q water, isopropanol and dried with argon gas. Copper foils and Cu(111) samples were only electropolished before Gr growth.

According to the Pourbaix diagram in aqueous solutions [31], Cu is relatively stable at slightly cathodic potentials in the whole pH range. At more positive potentials, copper dissolves to Cu^{2+} at pH < 7, but at pH > 12 it forms soluble hydroxide complexes (Figure 3), whereas it forms crystalline Cu_2O and CuO at neutral to weakly alkaline pH. The oxide formation, thickness and stability are dependent on pH, applied potential and polarization time. The composition of the oxide layers formed at higher pH has been studied qualitatively and quantitatively by different electrochemical and surface analytical methods [32–44], including EC–STM [45–49].

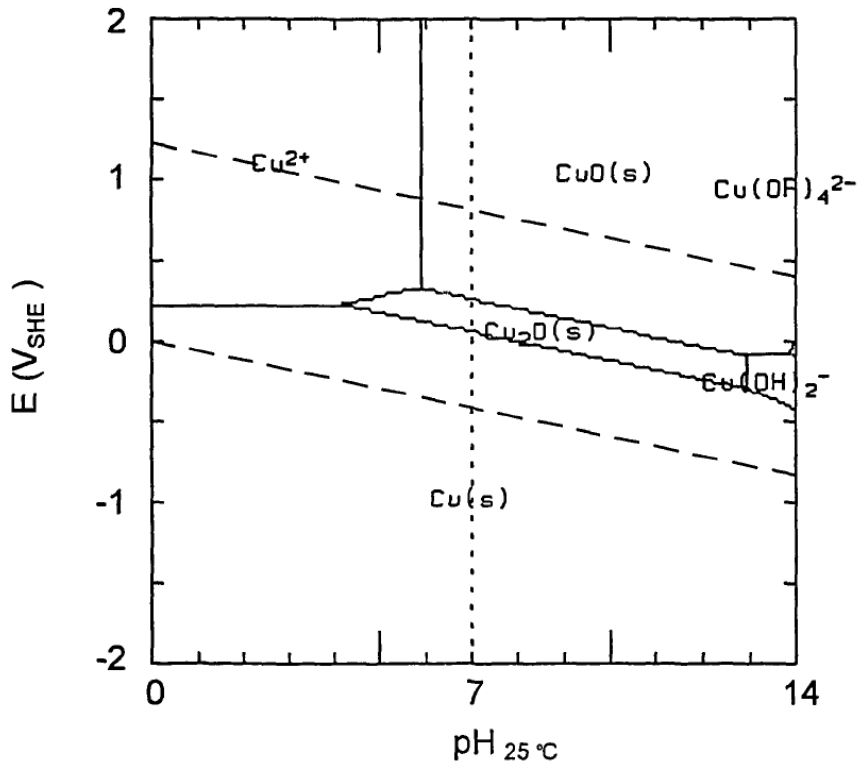

Figure 3. Pourbaix diagram for copper at 25 °C [31].

Copper is stable with no tendency to corrode in water and in non-oxidizing acids, such as CH_3COOH, H_2SO_4, HCl, $HClO_4$ and H_3PO_4, as long as the concentration of oxidation agent, for example, dissolved oxygen (air), is low. In oxidizing acids and in aerated solutions of ions that form copper complexes (e.g., CN^-, NH_4^+), corrosion can be severe. The rate of corrosion increases as a function of dissolved oxygen concentration and temperature and because the solubility of oxygen decreases with temperature it may show a maximum as temperature is increased [50]. The lowest observed corrosion rate is in distilled water. In seawater the corrosion rate of copper is about 25 ÷ 50 µm/yr [51]. The corrosion rates of copper in a dilute (up to 1%) non-oxidizing acids (H_2SO_4, HCl and $HClO_4$) in the absence of air is usually less than 4 µm/yr. In the solutions, which contain as much air as is absorbed in quiet contact with the atmosphere, the corrosion rates generally range from 20 to 250 µm/yr. The rate is higher (0.2 ÷ 1.25 mm/yr) in air-saturated solutions of non-oxidizing acids [52]. In solutions, corrosion resistance depends on the presence of a surface oxide film through which oxygen must diffuse in order for corrosion to continue.

In acid solution, the corrosion products of copper are soluble. Hydrogen ion reduction will drive the dissolution reaction at a very low rate, even at low pH [53]. Dissolved oxygen may be reduced on copper and this strongly accelerates the corrosion rate. The reduction of oxygen occurs simultaneously with the reduction of protons, and it can accelerate the copper dissolution. Due to limited solubility in water, the transport of oxygen to the copper surface limits the maximum rate of oxygen reduction that occurs with concentration polarization.

In acidic aqueous environments at ambient temperatures copper dissolves anodically forming the divalent ion Cu^{2+}.

$$Cu \rightarrow Cu^{2+} + 2e^{-} \qquad (1)$$

In aerated neutral or alkaline solutions (pH > 7) the corrosion product is predominantly cuprous oxide Cu_2O, responsible for protection of Cu from further corrosion, which is formed by the electrochemical process:

$$4Cu + 2H_2O \rightarrow 2Cu_2O + 4H^{+} + 4e^{-} \qquad (2)$$

Cathodic reaction can be written as:

$$O_2 + 2H_2O + 4e^{-} \rightarrow 4OH^{-} \qquad (3)$$

When two conductive materials, electrically connected, are immersed in a conductive solution, an electrochemical potential between these two electrodes appears. It causes the corrosion of the more electronegative electrode of the couple (anode). The other, more electropositive electrode, plays the role of the cathode and it is partly or completely protected from the corrosion. Copper metals are almost always cathodic to other common structural metals, such as steel and aluminum. Copper metals usually corrode preferentially when coupled with high-nickel alloys, titanium, or graphite.

2.4. Graphene on copper

The interaction between Gr and Cu is relatively weak with a low binding energy (BE) of 33 meV per carbon atom [54] comparable to the inter-planar coupling strength of graphite (25 meV per carbon atom) [55].

Graphene monolayer is impermeable to gas molecules [56]. In first several studies it was observed that Gr is a promising anticorrosion material with the best performance under harsh corrosive conditions over a short time scale. Chen et al. report that Gr shows an excellent protection performance and inhibits the oxidation of the underlying Cu, at least for brief periods, when subjected to high temperature annealing [57]. Browson et al. reported the existence of a slow electron transfer of Gr towards some electrochemical reactions, used for kinetics study, and due to its larger inert basal plane than reactive edge plane, passivation of the underlying supporting material [58]. In this case, the electrochemical dissolution of the copper should be suppressed by the presence on the surface of inert Gr layer, when the reaction sites are blocked.

However, recently Zhou et al. and Schriver et al. reported that the corrosion of Cu covered by Gr is stronger in air when the exposure time is extended to several months. The increase of the corrosion kinetics was explained considering the formation of galvanic cells as a result of the contact between the Gr and copper phases in contact within electrolytic solutions, which promotes the Cu electrochemical corrosion process [59,60]. Gr as a more noble electrode plays the role of the cathode and copper dissolves as the anode. The ratio between anodic and cathodic areas is an important factor that affects galvanic corrosion. In our case, when the cathodic area of Gr is large and the anodic area (as the defects in Gr layer or uncovered parts of copper) is small, the corrosion rate of the small anodic area may be high, instead of situation when the anodic and cathodic areas are equal in size. At relatively low area of copper open regions the galvanic cell through which copper corrosion takes place is composed of a small anode and a large cathode, i.e. the current density at the anode is much higher than that of the cathode. Only a completely suppressed ion conduction through microscopic channels in Gr coating can prevent the formation of a galvanic cell. It was shown that nanometer-sized structural defects in the Gr are responsible for the limited passivation. An increase in Gr defects enables long-term oxidation.

It is known that the mismatched Gr/Cu interface allows electrolyte intercalation between the two materials [61]. This leads to corrosive changes on top of the copper despite the protection. However, the quantitative characterization of this process faces significant difficulties. since polycrystals are non-uniform and can differ for many aspects such as average copper grain size, which might impact the corrosion rate. For these reasons, the efficiency of Gr protection for polycrystalline copper requires further investigations.

2.5. Graphene preparation methods

The scientists from University of Manchester K. Novoselov and A. Geim in 2004 developed a method to isolate Gr [9]. They used a simple scotch tape to peel off layers of Gr from HOPG. Gr with a perfect crystal structure prepared by mechanical exfoliation shows extraordinary properties, but this method is not a scalable process for producing large-area Gr sheets. The size of Gr is usually limited to micrometers and the productivity of this method is very low. The thickness and the size distribution of Gr in this way are rather random, and cannot be controlled at a large scale.

Another technique to obtain large scale Gr is the thermal decomposition of silicon carbide (SiC). When SiC is heated in vacuum or in an inert atmosphere, only the silicon atoms leave the surface due to the difference in the vapor pressures of silicon and carbon, and the remaining carbon atoms spontaneously form an epitaxial Gr film on the surface [62]. However, this method has some important disadvantages, such as noticeable densities of defects and domains with variable thickness [63]. In addition, the transfer of Gr to another substrate is complicate [64] and the process is relatively expensive.

An alternative route to prepare Gr at low cost is based on the reduction of graphene oxides (GO) [65]. The basic method of GO preparation was developed by Hummers et al. [66]. The GO, which is chemically oxidized from graphite crystal and dispersed in aqueous solution due to the interaction between water and oxygen-containing functional groups introduced in its basal plane, can be easily deposited on substrate in monolayer or few-layer form. The GO can be then reduced into Gr, but this process is never complete and many structural defects and different functional groups (tertiary alcohols, epoxides, carboxyls, carbonyl) still remain, which profoundly alter Gr native properties.

One of the most promising techniques for the growth of Gr is thermal Chemical Vapour Deposition (CVD) on transition metal (TM) substrates [19,67–69]. This is one of the most competitive methods for the growth of *single* layers of Gr on a large scale. This method provides numerous unique advantages such as industrial scalability, relatively low temperature processing, easy transfer onto other substrates. It shows great potential for its large-scale production at low cost and its integration in industrial applications. Thermal CVD is a chemical process by which a substrate kept at high temperature is exposed to chemically active precursors and the desired product is deposited onto the substrate after a thermally promoted chemical reaction. The method mainly involves the adsorption, decomposition and recombination of carbon-containing gas on the catalytic metal surface at high temperatures either at low or atmospheric pressure, which eventually results in the formation of a thickness controlled Gr film.

The thermal CVD process of Gr growth on TM surfaces occurs at high-temperature and different growth mechanisms can be involved according to the carbon solubility in the metal. For the growth on TM with high carbon solubility such as Nickel, the Gr layer forms during sample cooling through a surface segregation process and involves the formation of intermediate carbide phases and complex surface intermediates. In this case, the formation of single layer is possible, but requires a very careful control of the growth kinetics and is strongly depended on the history of the materials (i.e. pre-existing carbon contamination, previous thermal treatment etc.). The growth of Gr on TM with very low carbon solubility such as Cu is relatively simpler, since the synthesis is limited to the surface of the catalyst and mainly involves the catalytic decomposition of the precursor, which leads to the formation of carbon species that diffuse on the surface and nucleate forming Gr islands [69].

For our investigations Cu was chosen as a substrate because it is an excellent substrate material for the monolayer Gr growth due to its low carbon solubility at elevated temperatures [70] and high catalytic activity for the reaction of decomposition of hydrocarbons and C-C bond formation [69]. The CVD growth process of Gr on Cu is self-limiting on the surface: due to the negligible solubility of C in Cu, once a monolayer of Gr fully covers the surface, no metal catalyst is left to decompose the precursor, impeding therefore any further growth [67].

In our studies ethylene (C_2H_4, 3.5, Messer) was used as carbon precursor due to its higher reactivity in comparison to methane used in "classical" hot-wall CVD [67]. Compared to CH_4, which is a commonly used carbon source for Gr growth, C_2H_4 has a lower decomposition temperature.

2.6. Mechanism of graphene growth

Several groups have studied the growth mechanism of Gr on Cu from hydrocarbon precursor, proposing different models [69,71–76]. Gr growth on Cu follows classical nucleation theory in a similar to other thin film growth [77,78]. Kim et. al. showed that Gr growth is a result of the supersaturated fraction of carbon-ad-atom species crystallization. Nucleation density of Gr depends on the mobility of the carbon adatom species and their desorption rate. According to their study the growth-limiting step is the attachment of C_{ads} species to the graphene edges [71].

The nucleation of Gr is favorable on the step edges because such irregularities on the atomic scale contain dangling bonds that present lower energy barrier for attachment to the adatoms that govern Gr growth [79].

High temperature is required for the growth of the highly perfect Gr [67]. At lower growth temperature the mobility of adatoms that leads to thin film growth is low, which means that before they can attach to existing growing sites, they can interact with other surface atoms and start a new nucleus. This determines the formation of highly polycrystalline Gr films with a limited size of the single crystalline domains and consequently a large number of domain boundaries. [80,81].

2.7. *Ex situ* graphene characterization techniques

2.7.1. Raman spectroscopy

The main technique for Gr characterization is *Raman spectroscopy*. This is a fast, nondestructive and highly sensitive method with high spatial resolution, which allows to obtain the essential information about structural and electronic properties of Gr, providing a

detailed physicochemical fingerprint of Gr. The main reason why Raman spectroscopy is used for Gr characterization is the speed of analysis. Typical measurement times is about a few minutes. Raman spectroscopy (named after C. V. Raman) is a spectroscopic technique used to study vibrational, rotational, and other low-frequency modes in a material [82].

It relies on inelastic scattering, or Raman scattering, of monochromatic light, usually from a laser in the visible, near infrared, or near ultraviolet range. The laser light interacts with molecular vibrations, phonons or other excitations in the system, resulting in the energy of the laser photons being shifted up or down. The shift in energy gives information about the vibrational modes in the material.

Every band in the Raman spectrum corresponds directly to a specific vibrational frequency of a bond within the molecule or phonon in crystalline materials. The vibrational frequency and hence the position of the Raman band is very sensitive to type of vibration and weight of the atoms at either end of the bond.

In case of crystalline materials, in a first-order Raman process, light is absorbed with the energy and momentum of the incident photon, and the scattered light is typically downshifted by the energy of a phonon, with momentum that is the sum of the momenta of the incident light and that of the excited phonon. Considering the typical wavelength of the radiation used, the wave vectors **q** of the phonons that can be probed by Raman spectroscopy are very small compared to the size of the Brillouin Zone (BZ).

In a second-order Raman process, the requirement of $\mathbf{q}\approx 0$ is relaxed, and a pair of $\mathbf{q}\neq 0$ phonons with wave vectors **q** and -**q** are relevant. The second- (and higher-) order Raman processes generally give a broad background signal in the Raman spectra. Such higher-order processes can have large intensities, comparable to the first-order process when two of the three intermediate states in the two-phonon scattering (or one-phonon and one-elastic scattering) process are real electronic states [83]. Then, the double-resonance (DR) effect results in spectral features as intense as the first-order resonance Raman process. Such processes are well known and are called *DR Raman processes*. Because of the DR effect, sp^2 carbons show a strong first-order G-band feature as well as strong second-order DR 2D-band [83,84].

In our experiments, Raman spectroscopy measurements were acquired at room temperature with a Thermo Scientific Fisher spectrometer with a laser wavelength of 532 nm for all spectra. A 50x LWD (Long Working Distance) microscope objective focused a 5 mW laser beam to a probe pinhole spot about 50 µm in diameter, that corresponded to 1.1 µm spot size. Each point scan was an average of minimum 3 spectra taken at random locations cross the sample and individual spectrum was an average of 10 exposures each of 10 seconds. Raman spectra were acquired on Gr/Cu without any transfer step.

2.7.2. Scanning Electron Microscopy

Scanning Electron Microscopy (SEM) was used to observe the morphology, spatial distribution, homogeneity and coverage of Gr films. The electron microscopy images were recorded using a Supra 35VP Gemini scanning electron microscope (Zeiss, Germany). Using SEM, the boundaries of various types of surface defects can be easily observed on the sample surface. For the SEM measurements, the samples were fixed with a conductive carbon tape on a 25 mm aluminum sample holder. The images were acquired by the "In-Lense" mode at an accelerating voltage of 5 kV and a working distance of 3-5 mm. Elemental analyses were performed by Thermo Scientific Flash 2000 analyzer.

2.7.3. X-Ray Photoelectron Spectroscopy

The chemical composition and chemical changes induced by the electrochemical measurements were analyzed by X-Ray Photoelectron Spectroscopy (XPS), a technique developed by Nobel Prize winner Prof. Siegbahn. By this spectroscopic technique is possible to determine the chemical composition of surfaces up to 1 nm depth. XPS since it is able to provide quantitative elemental analysis, but also to determine the chemical nature and oxidation state of the detected elements is the most widely used analysis tool in surface characterization. Atoms throughout the periodic table, except helium and hydrogen can be detected by XPS. The sensitivity for the lighter elements is from 1 to 10 % whereas for the heavier elements it can be on the order of 0.1 atomic percent.

For acquiring photoemission spectra, it was used an EA 125 Omicron electron analyzer equipped with five channeltrons, working at a base pressure of 10^{-10} mbar. The XPS data

were collected at room temperature with the Al Kα line (hv = 1486.6 eV) of a non-monochromatized dual-anode DAR450 X-ray source using an energy step of 0.1 eV, 0.5 s collection time, and 20 eV pass energy. (Survey 0.5 eV steps, 0.25 s collection time, and 50 eV pass energy). Curve fitting of C 1s and O 1s lines was performed with Gaussian-Lorentzian-Product function and Shirley background using KolXPD software.

2.7.4. Low-energy Electron Diffraction

Low-energy Electron Diffraction (LEED) is the widely-used method to have structural information of the crystalline surfaces and thin layers. The low-energy electrons with kinetic energy of 10 ÷ 500 eV have a mean free path of 0.4 ÷ 2.0 nm [85], which gives the possibility to get information about the topmost layers of the surfaces. LEED patterns were taken with the incident electron beam energy between 40 and 100 eV. All LEED patterns were recorded at room temperature.

2.8. *In situ* graphene characterization techniques

In this thesis, *in situ* Gr characterization was performed by two main experimental methods: 1) electrochemical cyclic voltammetry, and 2) the electrochemical scanning tunneling microscopy.

2.8.1. Electrochemical fundamentals

This part of the chapter provides a brief description of the fundamentals of electrochemical processes. The electrochemical concepts, the experimental methods as well as the technical terms employed in this work are introduced. The traditional models of the electrode/electrolyte interface structure, thermodynamics and electrode kinetics will be explained. Furthermore, the cyclic voltammetry technique as one of the most important methods to characterize the solid/liquid interface, used in this work, will be presented, describing its theoretical principles, instrumentation and applications.

Electrochemistry covers all phenomena in which a chemical change is the result of electric forces and, vice versa, where an electric force is generated by chemical processes

[86]. It includes the properties and behavior of electrolytic conductors in liquid or solid form. Several of these phenomena occur at interfaces between electronic and electrolytic conductors where the passage of electric charge is connected with an electrochemical reaction, a so-called *Red-Ox reaction*:

$$Ox + ne^- = Red \qquad (4)$$

where *Ox* is the oxidized species, *Red* is the reduced species, and *n* is the number of electrons exchanged between *Ox* and *Red*.

An electrochemical reaction is a heterogeneous chemical process involving the charge transfer to or from an electrode, generally a metal, carbon or a semiconductor [87]. The charge transfer may be a cathodic process in which an otherwise stable species is reduced by the transfer of electrons from an electrode. Examples of such reactions, which are important in electrochemical technology, include:

$$2H_2O + 2e^- = H_2 + 2OH^- \qquad (5)$$

$$M^{n+} + ne^- = M \qquad (6)$$

Conversely, the charge transfer may be an anodic process where an otherwise stable species is oxidized by the removal of electrons to the electrode and relevant examples would be:

$$2H_2O = O_2 + 4H^+ + 4e^- \qquad (7)$$

$$M = M^{n+} + ne^- \qquad (8)$$

The number of reactant molecules involved in an electrode reaction is related stoichiometrically to the number of charges (electrons) flowing in the circuit. This is the basic argument of the laws formulated by Michael Faraday in 1832–1833 [88].

Faraday's law correlates the total charge *Q*, C, passed through a cell to the amount of product, *N*, mol:

$$Q = nFN \qquad (9)$$

where *F* is Faraday's constant, *F* = 96485,3 [C/mol], and *n* is the number of electrons transferred per mole of product. Faraday's law can be used in many applications, such as

electrogravimetry (to find the amount of substance deposited at an electrode) and coulometry (to find the total amount of electricity required for complete electrolysis of a compound); it can also be used for finding the number of electrons implicated in an electrolytic process.

Conduction of electric current in conductors can be electronic or ionic, depending on the type of charge involved. Substances exist where conduction is mixed (i.e., where both ions and electrons are moving). *Electronic conduction* is found in all metals and also in certain other substances: carbon materials (graphite, carbon black), some oxides and other inorganic compounds (e.g., tungsten carbide), and a number of organic substances. *Ionic conductors* (conductors of the second kind) are also known as *electrolytes*. This term is used not only in the sense of an ionic conductor (e.g., in expressions such as "solid electrolytes", but also in a second sense, in speaking of substances that ordinarily are not conducting but produce ionic conduction after being dissolved in water or in another solvent (e.g., in terms such as "electrolyte solution" and "weak electrolyte" [88].

The relationship between the concentration of oxidized species C_O, concentration of reduced species C_R, and free energy (ΔG, J/mol) (reaction 1) is given as:

$$\Delta G = \Delta G^0 + \frac{RT}{nF} ln(\frac{C_O}{C_R}) \qquad (10)$$

where R is the universal gas constant (8.3145 J/mol K) and T is the absolute temperature in K, C_O and C_R are the concentrations of the oxidized and reduced forms, respectively, of the electroactive species. The critical aspect of this equation is that the ratio of reduced to oxidized species can be related to the Gibbs free energy change (ΔG), from which we can then derive the potential (E, V):

$$\Delta G = -nFE \qquad (11)$$

Here E is the maximum potential between two electrodes, also known as the open-circuit potential (E_{oc}) or the equilibrium potential, which is present when no current is flowing through the cell, and F is Faraday's constant. If the reactant and product have unit activity, and E is for the reaction in the direction of reduction (left to right in equation (1), then equation (8) can be written as

$$\Delta G^0 = -nFE^0 \quad (12)$$

In this case, the potential E^0 is known as the *standard electrode potential* (i.e. established in the standard conditions: T = 298 K, P = 10^5 Pa, C_O/C_R = 1) and it relates to the *standard Gibbs free energy change* (ΔG^0, J mol^{-1}). It should be noted here that due to the minus sign in equation (9), all spontaneous reactions (i.e., with $\Delta G^0 < 0$) will have a positive standard electrode potential ($E^0 > 0$).

The mathematical expression describing the correlation between potential and concentration for a cell reaction is a central point of electrochemistry and is known as the *Nernst equation* (obtained by combining equations (10)–(12)):

$$E = E^0 + \frac{RT}{nF} ln(\frac{C_O}{C_R}) \quad (13)$$

Application of the potential to an electrode can change the ratio (C_O/C_R) at the electrode surface which, in general, will make C_O and C_R at the electrode surface different from those in the bulk of solution. When this is the case, there is a driving force for transport (diffusion) of analyte to or from the electrode surface in an attempt to equalize the concentrations. This transport of analyte to the electrode surface, coupled with the oxidation or reduction of analyte as it arrives at the surface, determines the value of the current. If electron transfer is fast, then the current is determined only by the rate of mass transfer of analyte to the electrode surface. The difference in concentration between the solution near the electrode surface and that far from it is in turn determined by the value of the applied potential, via the Nernst equation.

At an electrode surface, two fundamental electrochemical processes can occur: faradaic and non-faradaic (also called capacitive). Capacitive processes are caused by the charge of the electrode surface as a result of a potential variation, or by an adsorption process. Capacitive current does not involve any chemical reactions (charge transfer), it only causes accumulation (or removal) of electrical charges on the electrode and in the electrolyte solution near the electrode. There is always some capacitive current flowing when the potential of an electrode is changing. In contrast to faradaic current, capacitive current can also flow at constant potential if the capacitance of the electrode is changing for

some reason, e.g., change of electrode area, adsorption or temperature. Faradaic currents are a result of electrochemical reactions at the electrode surface.

2.8.2. The electrode/electrolyte interface

Electron transfer of electrochemical reaction occurs at the interface between an electronic conductor (metal or semiconductor electrode) and an ionic conductor (an electrolyte which contains ions). Therefore, understanding of the structure and composition of this interface is important for studying the kinetics and mechanism of electrochemical reactions.

Electrode, exposed to an electrolyte solution, may carry an excess charge located at the surface. This charge must be counterbalanced by the ionic excess charge on the solution side of the interface. It forms an array of nonuniformly distributed charged species (ions, dipoles) in the liquid phase called an *electrical double layer* (EDL).

Different models of the interface region near the electrode surface in solution have been proposed (Figure 4). The first model of the EDL was suggested by Helmholtz in 1879. According to his concept, EDL has rigid structure and can be described as a parallel plate capacitor with a metal from one side and ions of the electrolyte from the other side at a distance δ, which is that of the closest approach of an ion's center to the surface. The calculated capacitance was in good agreement with experimental values, but this model didn't take into account dependence of the capacitance on potential and concentration of ions. It neglected the Boltzmann distribution of the ions present in the electrolyte. Gouy (1910) and Chapman (1913), independently, modified the Helmholtz model, where thermal diffusion of the ions in the double layer was taken into account. The combined effects of the electrostatic forces and of the thermal motion in the solution near the electrode surface give rise to a diffuse distribution of the excess ions, and a *diffuse double layer* is formed (Figure 4b). As the result, the potential in this layer decreases exponentially with increasing distance from the surface. Unlike the Helmholtz model, the Gouy–Chapman model provides a qualitatively correct calculations of the capacitance minimum around the potential of zero charge (pzc, the potential at which no excess charge is present on the electrode surface) and of the capacitance changes that occurs with different values of concentration and potential. The Gouy-Chapman model, however, is limited to the description of the double layer at at

high ion concentrations (more than 10^{-2} M). The disagreement can be explained by the fact that in the Gouy–Chapman model, unlike that of Helmholtz, charge carriers assume as the point charges and distribution as a continuum which does not correlate with its discrete nature.

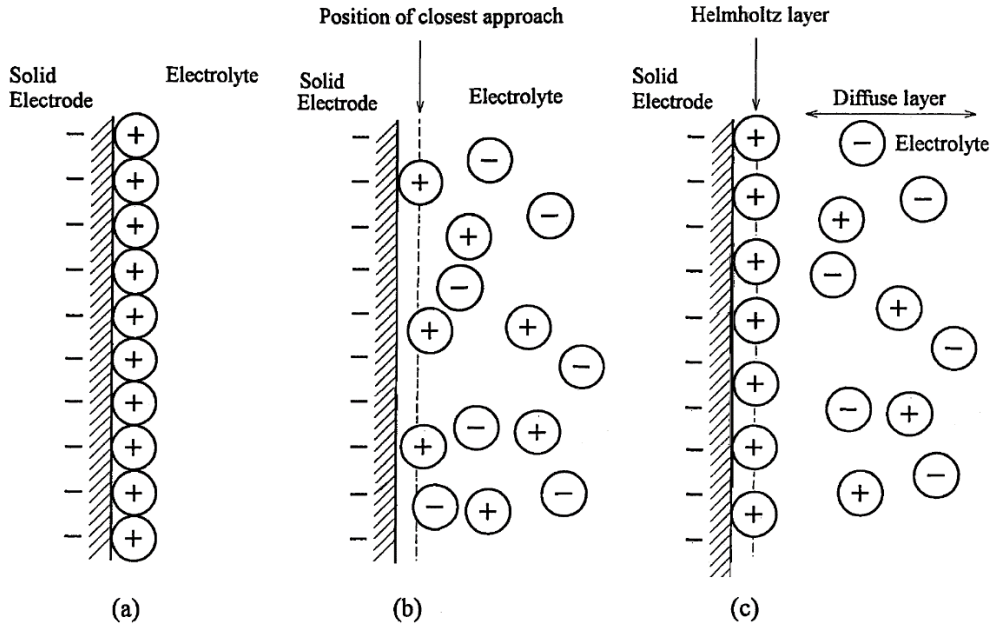

Figure 4. Three models of the electrochemical interface: (a) the Helmholtz fixed (rigid) double layer, 1879; (b) the Gouy-Chapman diffuse double layer 1910-1913; (c) the Stern-Grahame double layer, 1924, being a combination of the Helmholtz and the Gouy-Chapman concepts [89].

The most sufficient model for the description of the EDL (Figure 4c) was proposed by Stern in 1924 and improved by Grahame in 1947 [90]. Stern combined the two models of Helmholtz and Gouy-Chapman into a one, where divided the EDL in two regions: Helmholtz layer and the diffuse double layer. Grahame suggested that instead of two the EDL consists of three parts (Figure 5). First part (counting from the metal surface), is called *inner Helmholtz plane* (IHP). It contains party desolvated specifically adsorbed ions and solvent molecules. In second region, *outer Helmholtz plane* (OHP), where only solvated ions are present. In IHP the strong chemical forces are operate when in OHP ions interact with the electrode surface only electrostatically through the solvated shells. Both Helmholtz layers represent the compact layer, where potential drops linearly. The Helmholtz layer is then followed by the diffuse double layer region, which is disordered due to the thermal motion of the ions. A preliminary calculation of the electrochemical potential in the diffuse double

layer under the simplistic view of the ions as point charges shows an exponential decrease of the potential with the distance x from the electrode surface (Figure 5).

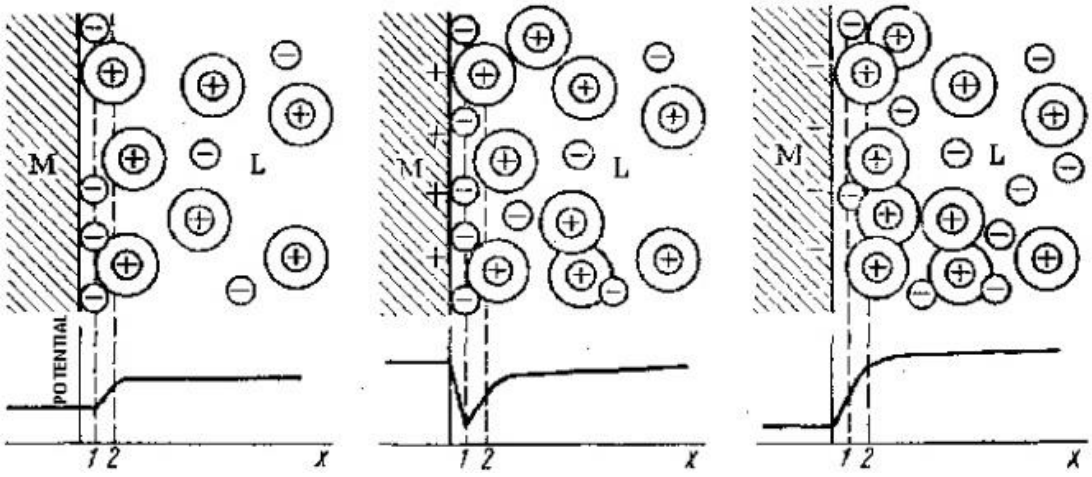

Figure 5. Schematic representation of the solid/liquid interface

The capacitance of the double layer consists of a combination of the capacitance of the compact layers in series with that of the diffuse layer. For two capacitors in series, the total capacitance is given by:

$$\frac{1}{C} = \frac{1}{C_H} + \frac{1}{C_d} \qquad (14)$$

2.8.3. Cyclic Voltammetry

The electrochemical techniques provide a very sensitive method to study surface processes. The cyclic voltammetry (CV) is one of the most commonly used electroanalytical potentiodynamic technique for the study of electroactive species and electrode surfaces. The CV was first reported in 1938 by Matheson and Nicols and described theoretically by Randles [91] and Sevcik [92] ten years later. It is the most sensitive direct method for examination of both the kinetic and thermodynamic aspects of electrochemical surface processes and study of reaction mechanisms.

In CV the most often a three-electrode arrangement is used, consisting working electrode (WE), counter electrode (CE) and reference electrode (RE).

This technique based on changing linearly the potential of the WE at a known sweep rate. At the beginning the working electrode is held at some potential, E_i, where no

electrode reactions occur. During measurement, the potential is swept linearly at a rate v between two limiting potentials E_1 and E_2 (Figure 6). In conventional experiments the sweep rate ranges from a few mV/s up to a few hundred V/s. The same sweep rate is normally chosen for the forward and reverse sweep.

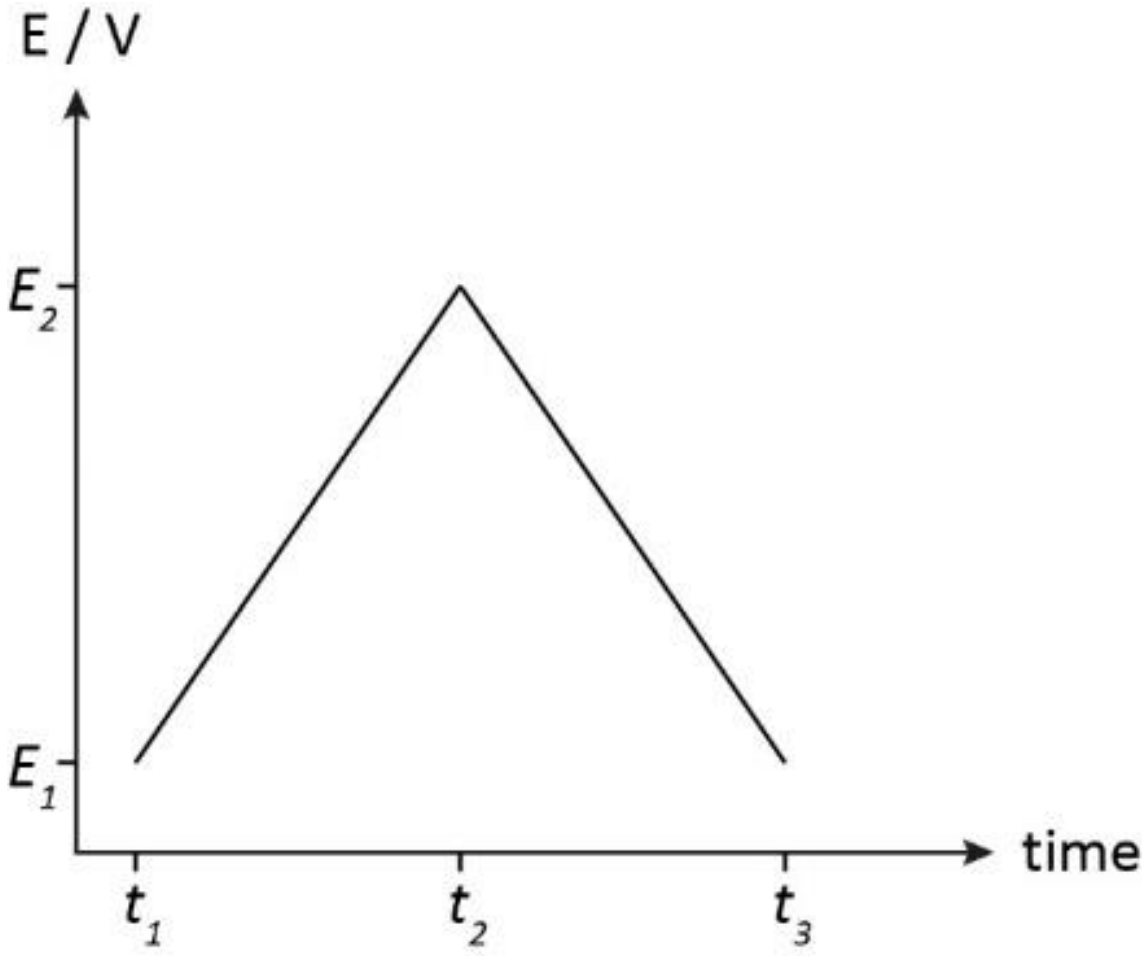

Figure 6. Potential-time profile for cyclic voltammetry.

The corresponding current is recorded as a function of the varying potential. The voltammogram is a display of potential on the x axis and current on the y axis. This current-voltage curve is referred to as the cyclic voltammogram and it gives information about reactions occurring on the WE surface. For the cathodic scan (applied potential is decreasing) the current has a negative sign, for the anodic scan (applied potential is increasing) the current has a positive sign. From the obtained voltammogram one can normally interpret whether the system is reversible, quasi-reversible or irreversible. A cyclic voltammograms for reversible and irreversible systems are shown in (Figure 7).

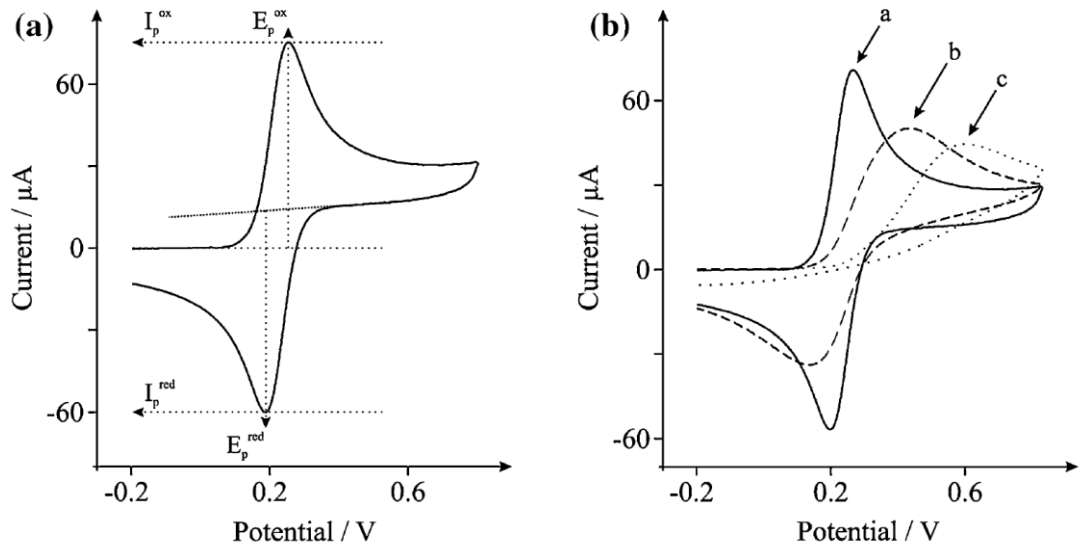

Figure 7. Cyclic voltammograms of the electrochemical reaction: a) reversible; b) irreversible.

The peak current i_p in this voltammogram is given by:

$$i_p = (2.69\times10^5)n^{3/2}AD^{1/2}v^{1/2}C \qquad (15)$$

where i_p is the peak current (in amperes, *A*), *n* is the number of electrons passed per molecule of analyte oxidized or reduced, *A* is the electrode area (in cm^2), *D* is the diffusion coefficient of analyte (in cm^2/s), *v* is the potential sweep rate (in V/s), and *C* is the concentration of analyte in bulk solution (in mol/cm^3).

Hence, depending on what is already known about a given system, it is possible to get information about the diffusion coefficient, the number of electrons per molecule of analyte oxidized or reduced, and/or the redox potential for the analyte, all from a single experiment. Unfortunately, the CV is not the best one to obtain quantitative data about electrochemical nucleation processes.

2.8.4. The electrochemical cell

Three-electrode cells are the most commonly used setup in electrochemical studies, especially when the cell resistance is relatively high (Figure 8). In this configuration, the potential of the WE is monitored relative to the reference potential; however, the current passes between the WE and a separate CE. Since no (or little) current passes to the RE, it

approaches ideal nonpolarizability and is hence a reliable reference for potential control. Experimentally, the RE is placed as close as possible to the WE in order to minimize (uncompensated) solution resistance where control of the voltammetric current scale will also be critical, as mentioned above. The position of the RE should not interfere with the mass transfer of electrolyte species.

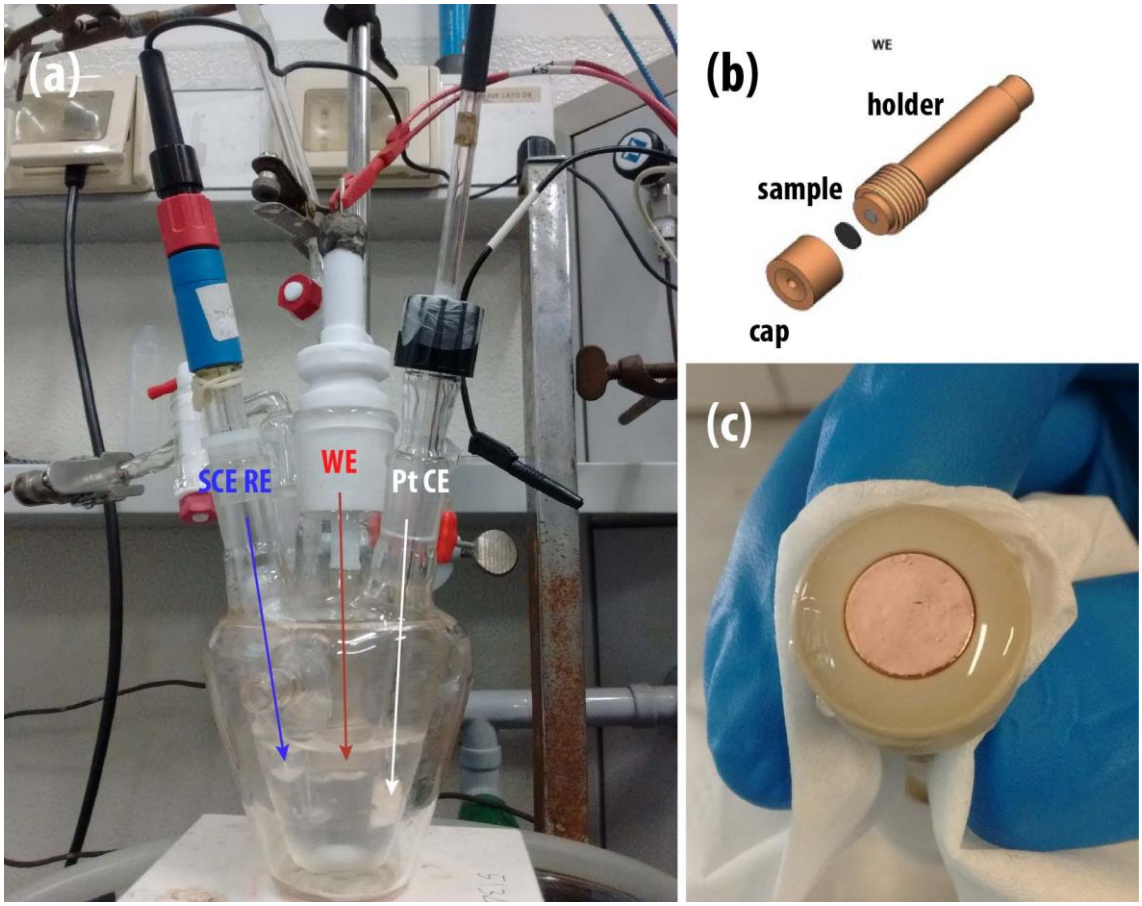

Figure 8. (a) Standard three-electrode cell; (b) sample holder; (c) Gr/Cu(111) in the sample holder.

The purpose of the RE is to provide a stable, reproducible voltage to which the WE of an electrochemical cell is referred. The potential value should not vary with time and should be reproducible from electrode to electrode. Different reference electrodes were used. In the beginning the pseudo-Ag/AgCl (pSRE) or Pt wire, for their easy applicability, were chosen as reference electrodes but due to different electrolytes they were not stable and changes with different conditions. The switch to external reference electrode (RHE or SCE), connected to the STM electrochemical cell by Tygon tube and glass capillary, allowed to have stable reference potential. To separate the reference electrode and the cell, a salt-bridge

containing saturated KNO_3 solution was employed aiming to avoid the contamination from trace amount of the specifically adsorbing agents. When SCE electrode was used, the potential shift was +0.293 V.

The role of the CE is to supply the current required by the WE, without limiting the measured response of the cell. The processes occurring on the CE is not considered; it is usually made of inert materials (noble metals or carbon/graphite) to avoid its dissolution. It should have a large area compared to the WE. A platinum foil c.a. 0.8 cm^2 served as CE in this work.

In many electrochemical studies, an inert atmosphere is needed to prevent the interference of the oxygen reaction at the electrode surface. Typically, ultra-high-purity nitrogen or argon is used. Nitrogen is less expensive, whereas the density of argon is greater than that of air and hence provides a better protection layer over the electrochemical solution. In practice, the solution is bubbled with the inert gas for at least 20 min by inserting the tubing into the solution. Then the tubing is withdrawn from the solution with a separation of a few mm above the solution surface. In so doing, an inert atmosphere is maintained within the reaction compartment. One can increase the efficiency of protection by reducing the exposure of the reaction compartment to the outside atmosphere, for instance, by sealing the opening with parafilm or Teflon tapes (but make sure to have a small leak so that pressure will not be built up inside the reaction chamber). Another concern is the choice of tubing used in the setup. For aqueous solutions, generally most synthetic tubings (Nylon, Teflon, etc.) are acceptable. For organic solutions, care must be taken to make sure that the tubing is inert in the solvent to prevent the interference in electrode reactions.

2.8.5. Corrosion behavior

Corrosion occurs when electrons are released from the metal (oxidation) and gained by the elements (reduction) in solution. When the cathodic and anodic reactions are in equilibrium and the current decreased to zero, the value of the potential in this equilibrium is called corrosion potential (E_{corr}). E_{corr} is measured between the reference and working electrodes and is used for a quantitative description of the corrosion protection of the material. In the

case of less negative E_{corr} values, the materials are considered as better corrosion protected. Corrosion potential (E_{corr}), corrosion current density (i_{corr}) and corrosion rate can be determined from so called Tafel plot [84]. Forward scan was used as a cathodic polarization curve for the Tafel plot, and the backward scan, as an anodic curve, respectively.

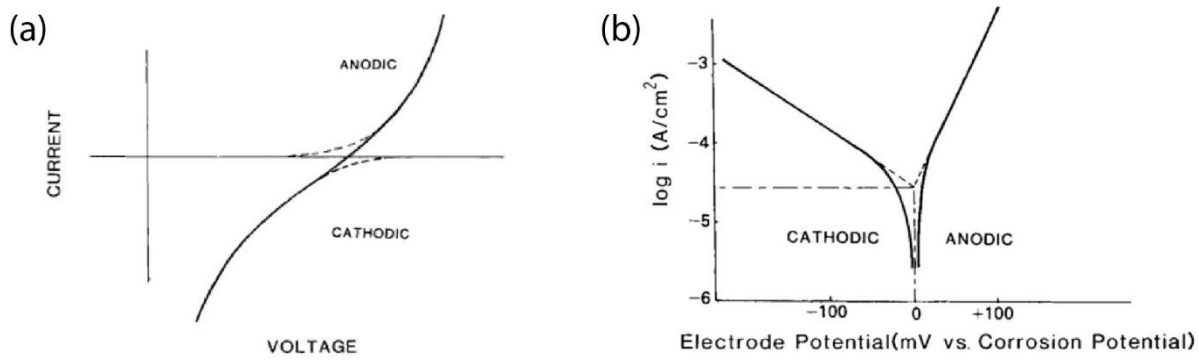

Figure 9. (a) Schematic plot of current density-voltage behavior of superposed corroding couple with Tafel control of each reaction; (b) Current density-overpotential curves for a metal-hydrogen corrosion couple emphasizing the Tafel kinetics for each reaction [93].

The Tafel extrapolation technique for measurement of corrosion kinetic parameters was introduced by Stern and Geary [94]. The technique may be used to determine the anodic and cathodic Tafel slopes as well as the corrosion current density. It has been widely used for the investigation of corrosion kinetics, with the most success in acidic solutions and other systems in which there are soluble reaction products. The corrosion current density (i_{corr}) can be determined by the extrapolation of the Tafel branches to their interaction at the corrosion potential. The extrapolation is shown by the dotted lines in Figure 9b [93].

2.8.6. Experimental

All electrochemical measurements were performed at room temperature using a potentiostat Autolab PGSTAT 101 (Metrohm Autolab, The Netherlands), Biologic SP-300 (BioLogic Science Instruments, France) or bipotentiostat of EC-STM. All solutions were prepared with ultra-pure water (Millipore Milli-Q, 18 MΩ cm) and were degassed prior to electrochemical measurements for at least 20 min by a continuous flow of high purity, oxygen free nitrogen or argon gas through the electrolyte solution leading to the removal of present oxygen. Sulfuric acid (95%, Fluka), perchloric acid (67-72%, Fluka), hydrochloric acid (≥37%, Sigma-Aldrich), and potassium hydroxide (pellets, 86.8%, VWR Chemicals) were used

for electrolytes preparation. All chemicals used were of analytical grade and were used as received, without any further purification.

All chemical reservoirs and units were routinely cleaned before experiments by flushing with piranha solution (H_2SO_4(95%): H_2O_2(30%) - 2:1) and then with several cycles of cleaning in an ultrasonic bath of fresh bi-distillated and in the last cycle Milli-Q water, which led to the removal of all contamination.

One part of electrochemical measurements was conducted using a three-electrode system: working electrodes were CVD Gr film grown directly onto the polycrystalline Cu disks (diameter 8 or 10 mm). They were secured into a PEEK housing unit. (Cu(111) single crystal was mounted in a PEEK holder). A Viton O-ring defining the working surface (diameter 4 mm); a platinum wire counter and a SCE reference completed the circuit.

2.8.7. Electrochemical Scanning Tunneling Microscopy

The home-built EC-STM instrument, developed and described in detail by Wilms et al. [95], was used in all of the experiments included in this thesis. Thus, here I will describe the theoretical principles of the STM, electrochemical techniques and the experimental set-up.

With the invention of the first Scanning Tunneling Microscope (STM) by Gerd Binnig and Heinrich Rohrer at IBM in the early 1980s [96] it became possible to realize the ideas of Richard Feynman about the synthesis of any chemical substances atom by atom in a control way. It has revolutionized the field of surface science since it allows the surface topographic real-space imaging and analysis on an atomic scale. For their brilliant invention, Binnig and Rohrer shared the 1986 Nobel Prize in physics.

The STM allows to study the structure of material surfaces at the atomic scale. It's a valuable tool for the study of thin Gr layers on the metal surfaces [97–99]. It gives important information about the film structure.

The early STM work had originally been focused on the gas/solid interface in vacuum, but it was later realized that it could also be used to obtain images of surfaces in contact with liquids. As a result, it has fast raised the interest of scientists for application of the STM tool in electrochemistry. The first STM working at solid-liquid interfaces has been introduced

by Sonnenfeld and Hansma in 1986 [100]. The so-called ElectroChemical Scanning Tunneling Microscopy (EC-STM) are able to image directly the electrode surface in solution (*in situ*). Different important electrochemical processes, such as corrosion, electrodeposition, adsorption, as well as surface modification and passivation were studied by *in situ* EC-STM [101]. The structural information on the atomic level makes it highly useful instrument.

In electrochemistry, it could be used to study *in situ* of metal electrochemical phase formation, to image an electrode surface before and after electrodeposition and, more generally, to study electrode reactions as a function of the structures on the electrode surface.

2.8.8. Theoretical principle of tunneling effect

Here I describe elementary theory of tunneling effect only briefly on simplified one-dimensional model shown in Figure 10.

The scanning tunneling microscopy is based on the phenomenon of quantum-mechanical tunneling effect between two solids through a classically forbidden energy barrier. When two electrodes (in our case the tunneling tip and the working sample) are brought close enough together that the distance is only a few angstroms, and a voltage between the electrodes is applied, electrons can tunnel from the tip to the surface or vice-versa and it produces a current flow. In this case, electrons tunneling from occupied states below the Fermi level of the donor electrode (sample) into unoccupied states above the Fermi level of the acceptor electrode (tip). This phenomenon can be fully explained by quantum mechanics.

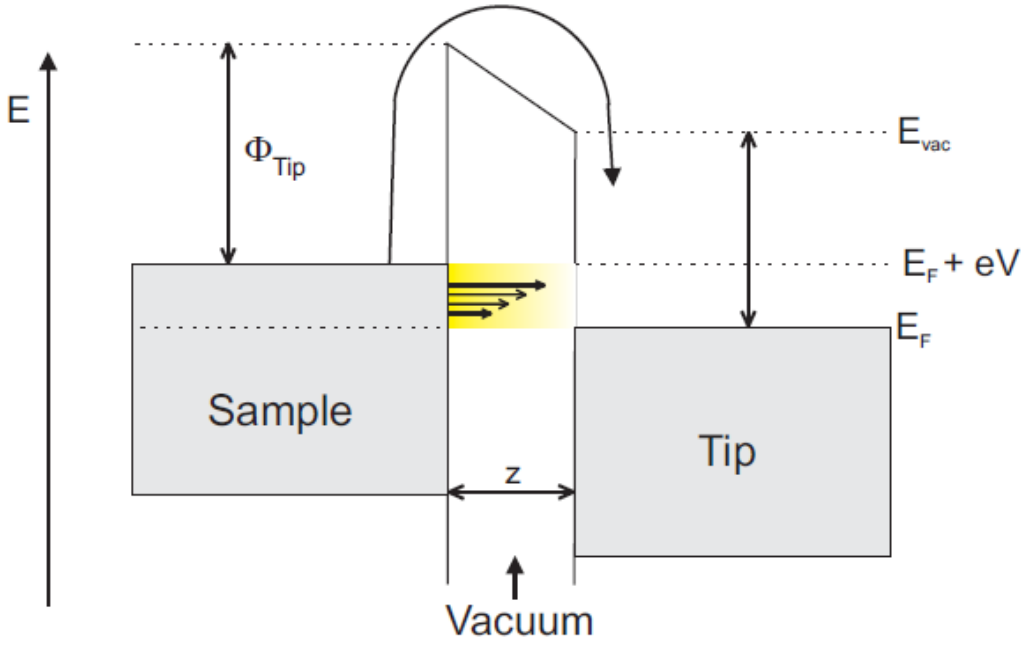

Figure 10. Energy level diagram of a tunneling barrier between tip and sample.

In quantum mechanics, the electron is described by a wave function $\psi(z)$, which satisfies the one-dimensional Schrödinger equation (16):

$$-\frac{\hbar^2}{2m}\frac{d^2}{dz^2}\psi(z) + \Phi(z)\psi(z) = E\psi(z) \qquad (16)$$

at a given position z (m is the mass of the electron, $\hbar$ is the reduced Planck's constant (1.05 × 10^{-34} *J s*), Φ is the barrier height in eV and z is the width of the barrier). Its solution in the classical forbidden region is:

$$\psi(z) = \psi(0)e^{-kz} \qquad (17)$$

where

$$k = \frac{\sqrt{2m(\Phi - E)}}{\hbar} \qquad (18)$$

is a decay constant that describes an electron penetrating through the barrier into the z direction. Electrons can also propagate in the opposite direction (−z direction) indicating that tunneling is bidirectional.

After the invention of STM, Tersoff and Hamann introduced a model [102,103] based on Bardeen's tunneling theory [104]. The tunneling tip in this model is assumed locally

spherical with local radius of curvature R, with the center located at $\vec{r}_0$ and z is the distance from tip to the surface (Figure 11).

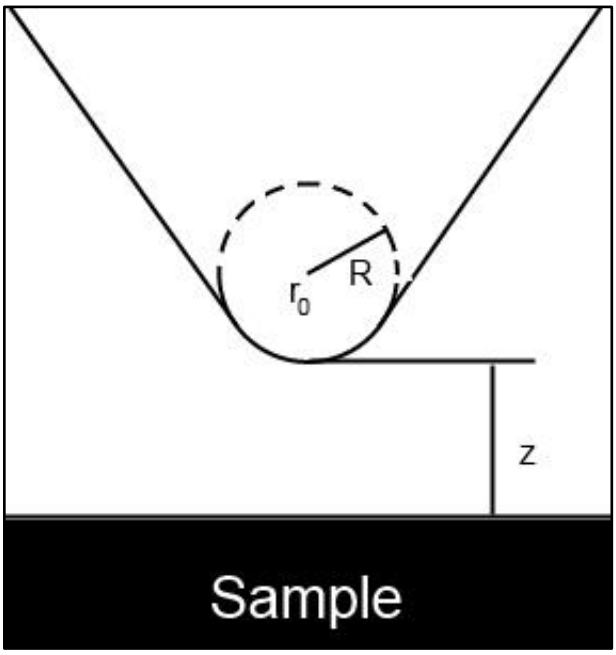

Figure 11. Schematic picture of tunneling junction in Tersoff and Hamann (TH) model.

The TH model represents the tip with potential and wave functions arbitrarily localized, in words, modeled as a geometrical point. According to this model, the tunneling current I_t can be described by first-order perturbation theory as:

$$I_t = \frac{2\pi e}{\hbar}\sum_{\mu,\nu} f(E_\mu)[1 - f(E_\nu + eV)\left|M_{\mu\nu}\right|^2 \delta(E_\mu - E_\nu) \qquad (19)$$

where $f(E)$ is the Fermi distribution function, V is the applied voltage, $M_{\mu\nu}$ is the tunneling matrix element between tip states ψ_μ and the surface states ψ_ν. In case of a vacuum barrier under the condition of a small tunneling distance, a small tunneling voltage and a low temperature:

$$I_t \propto V_b e^{-kz\sqrt{\Phi}}\rho(\vec{r_0}, E_F) \qquad (20)$$

This formula shows that the tunneling current I_t depends linearly on the applied tunneling bias voltage V_b and the local state density ρ of the sample surface at the location of the center of curvature of the tip r_o, but exponentially on the distance z between

tunneling tip and sample. the exponential dependence of the current I_t on the distance z is critical to the high resolution of the scanning tunneling microscope.

2.8.9. EC-STM Set-Up and working principle

The EC-STM combines STM with three-electrode electrochemical cell and bipotentiostat, allowing to perform experiments with the local surface probe technique in an electrochemical environment.

The detailed construction of the entire scanner including tunneling tip and scanner holder is shown in Figure 12.

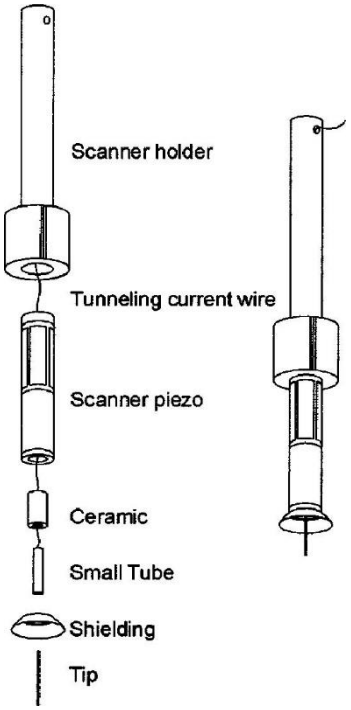

Figure 12. Construction of the scanner [105].

The tunneling tip is hold by small tube connected to the ceramic tube. The ceramic tube is inserted into the piezo scanner and another side of the piezo scanner is inserted then in the scanner holder (aluminum). The tunneling tip with a diameter of 0.25 mm is simply pushed into the precisely fitted small tube, so a quick replacement is possible. The outer side of the piezo scanner tube is metallized by silver coating and five isolated from each other electrodes are etched out. On the upper half of the tube four equal electrodes are located. They are used for the lateral x, y movements. The lower half of the scanner tube is

surrounded by the only one entire electrode. It is an electrode for the vertical z movement of the scanner. The inner surface of the scanner is also metalized with a thin silver layer and this inner electrode is grounded. The tip is connected to the preamplifier by the shielded tunneling current wire and the ceramic tube is used for insulation of the tip from the inner electrode of the piezo scanner. A more detailed description can be found in [95].

The basic scheme of the tunneling unit is shown in Figure 13a. The concept is based on the initially proposed by K. Besocke drift-stable construction [106]. The piezo scanner is fixed in the center of a gliding ring with the three ramps at the top plane. The ramps are responsible for the coarse approach of the tip to the sample surface via a "stick and slip mechanism" [107]. The ring is supported by three piezoelectric legs, made of the same material as the piezo scanner. So, they have the same coefficient of thermal expansion, whereby a compensation of the vertical drift is achieved. For a lateral drift compensation, the rotational symmetry-to-tip construction is provided. The tunneling tip goes through the hole in base plate and after the electrochemical cell is mounted from the bottom of the plate the tip reaches the sample into the electrolyte.

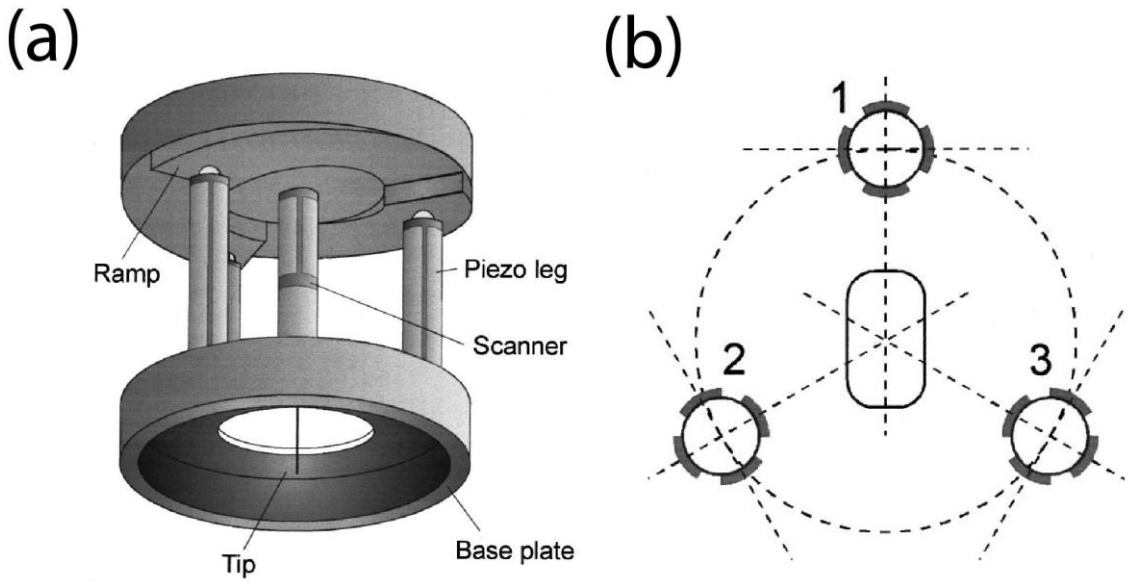

Figure 13. Scheme of the tunneling unit; (b) orientation of electrodes on piezo legs [105].

The bottom parts of the piezo legs are glued to the base plate and the top parts are closed on, each with a stainless steel ball in order to allow sliding on the ramps. The legs have outside four equally sized electrodes, which extend over the entire length. Across these

electrodes, they can be deflected by the corresponding control signals like the scanner in any horizontal directions. The piezolegs are aligned in way that two electrodes are tangent to the circle, which is based around the scanner and the distance between the scanner and legs is a radius (Figure 13b). In this way a rotating movement can be achieved by controlling only the tangentially oriented electrodes, which leads to the coarse approach.

The schematic drawing, together with the photograph, in Figure 14 shows the simple construction of the EC-STM.

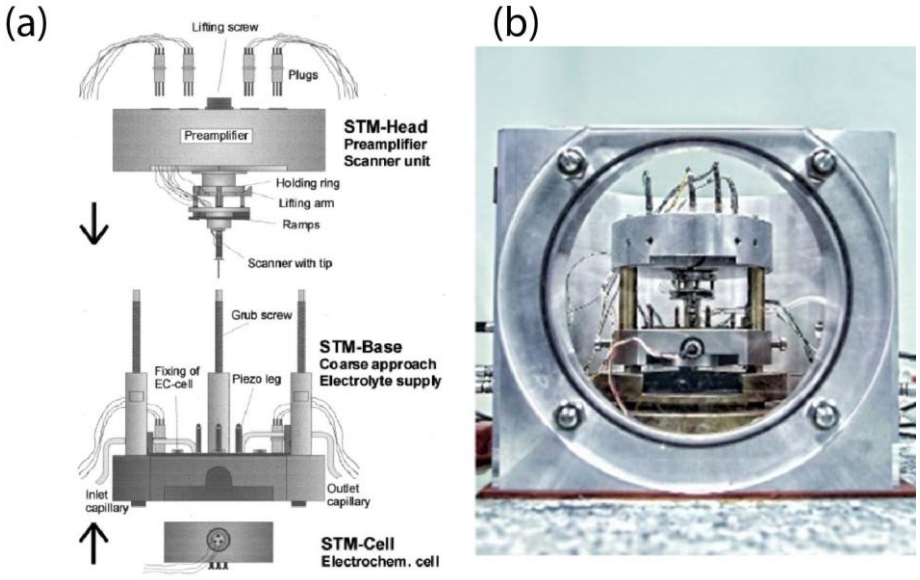

Figure 14. EC-STM setup: (a) disassembled [105]; (b) assembled in aluminum chamber.

The main part of the instrument is the EC-STM chamber containing the STM unit (STM-head, STM-base) as well as the electrochemical (EC) cell. The EC-STM chamber is milled from a solid aluminum block. It can be filled with a protective argon gas for keeping the atmosphere inside of the chamber free from atmospheric oxygen. It also plays role as electromagnetic, thermal and acoustic shield. The chamber is placed on a heavy granite plate which is attached via four steel springs to the room ceiling. It effectively protects the EC-STM from low frequency vibrations (< 1 Hz) transmitted by the building. For damping higher frequencies (> 100 Hz) the STM-base stands on a stack of three brass plates separated by rubber feet. For the electrical connection of the STM scanner and EC cell thin and light electrical wires are used.

The STM-head carries the STM piezo scanner unit and the tunneling current preamplifier. The STM-head is installed on the STM-base and stabilized by grub screws. After the scanner unit is lowered down by the lifting screw, the ramped ring rests freely on the three piezolegs attached at the STM-base. Scanner unit with the tip is now mechanically decoupled from the STM-head and is kept down stable only by gravity. From now the scanner can be controlled by the STM control unit and the computer in order to approach the tip to the sample. After the tunneling tip reaches the tunneling regime, all the fine movements and the recording images can be controlled by the computer system. The potential applied to the sample is under control and adjusted by the bipotentiostat unit.

The EC cell in the EC-STM is fixed into the STM-base from the below (Figure 14a). It is connected to the electrolyte supply system by Tygon tubes (Saint-Gobain, France). The electrolyte in the reservoir is degassed by the argon gas, in order to reduce the amount of dissolved oxygen, and then fed into the EC cell. The pump is connected to the outlet of the EC cell to protect the system from the overload of the electrolyte.

The electrochemical cell is shown in a schematic representation in Figure 15. It is a relatively small, rigid and compact. The inner diameter of the cell is 24 mm. The radial symmetry helps for the drift stability of the entire assembly. The reached electrolyte volume around 2.5 ml is a sufficient to assume stable electrochemical conditions.

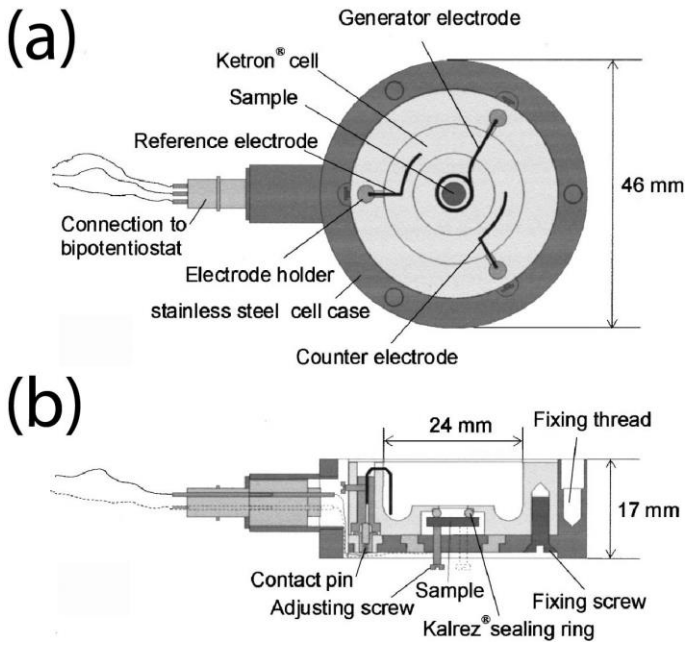

Figure 15. Electrochemical cell: (a) top view; (b) cross section [105].

The actual cell made of a new synthetic material (Ketron®), which is harder than, for instance, Teflon® or Kel-F® and therefore easier to machine. In addition, it has a lower thermal expansion coefficient and an extremely high acid resistance. This inner cell is housed in a stainless steel cell case. The cell is mounted from the bottom of the base plate and fixed by three screws so the tip can reach the surface of the sample into the electrolyte from the hole in the base plate. The electrochemical cell is completely autonomous and can also be used outside of the microscope, for example, for the preparation of the sample or for making cyclic voltammetry.

In the cross section drawing (Figure 15b) the placement of the sample is shown. It is fixed by three adjusting screws. From the top the sample is sealed with the acid-resistant o-ring (Kalrez®). Only the surface of interest is exposed to the electrolyte. The electrical contact of the sample is done via the screws. The sample can be easily installed and removed. During installation, the Ketron® cell is first removed from the steel cell case. After preparation of the sample, it is simply placed in the Ketron-cell and the cell case is fastened with three connecting screws. Now just a re-adjustment of the set screws must be done to produce a uniform pressure on the sample. Removal is carried in reverse order.

The electrode wires (Ø = 0.5 mm) in the cell are screwed into special electrode holder made of brass and thus easily replaceable. The holders themselves are firmly anchored in the Ketron®-cell automatically via resilient gold gilt spring contact pins with the corresponding pins of the connector contacts when inserting the cell into the steel case. The sample is isolated from the cell case and it is grounded.

Reference and counter electrodes are located diametrically opposite in the cell (Figure 15a). This is true even if an external reference electrode is used, the capillary tube then dips at the point where there is now the wire electrode. This arrangement reduces a potential gradient between the reference electrode and the sample when a current flow because the current density between the sample and the counter electrode is concentrated. So we can work without a Luggin capillary, which would be placed directly above the sample and would thus hinder the free movement of the tunneling tip.

Two electronic units are connected to the EC-STM. The first one is a STM controller which is used for the STM unit operation and for controlling the piezo scanner movement

and displaying the STM images on the monitor of the connected computer. The second one is a bipotentiostat for the operation of the EC cell and measuring and recording of the cyclic voltammograms displayed on the other computer system.

The electrochemical cell of the instrument is equipped with the electrodes necessary in order to control the sample potential and flowing electrochemical reactions. A bipotentiostat permits the use of conventional measuring methods such as cyclic voltammetry to receive the current-voltage curves. The three-electrode assembly also allows the simultaneous recording of cyclic voltammograms and tunnel images.

Figure 16 shows the working principle of the STM. When a sharp metal tip is brought into a distance z of only some angstroms to the conducting surface of the sample under study and a bias voltage of some mV to V is applied, electrons can tunnel from the filled tip states into the empty sample states or vice versa, depending on the polarity of the bias voltage. The resulting tunneling current I_t is of the order of a few nA and has a strong (exponential) dependence on the tip-sample separation. This property of the tunneling current plays the crucial role in STM and allows to control the sample-tip separation with high vertical resolution.

When a voltage is applied to a piezo scanner tube, a mechanical deformation occurs, leading to the tip movement due to the inverse piezoelectric effect. The lateral tip position x, y and the tip sample distance z is controlled by STM control unit in the pm-range. By applying the voltage V_x between the one of the upper outer electrodes and inner electrode which works as the reference electrode and is connected to signal ground leads to a lateral displacement of the scanner in direction depending on the sign of the voltage. Applying an equal amount of voltage with opposite sign to opposite electrode doubles the effect of the scanner tube banding in the same direction (x-direction). The same process occurs in y-direction by applying antisymmetric voltage V_y to the electrodes offset by 90°. A voltage V_z applied to the lower electrode leads according to the sign to contraction or elongation of the scanner and thus a movement of the tip in the z-direction. With a single scanner the tip can be moved in all three spatial directions.

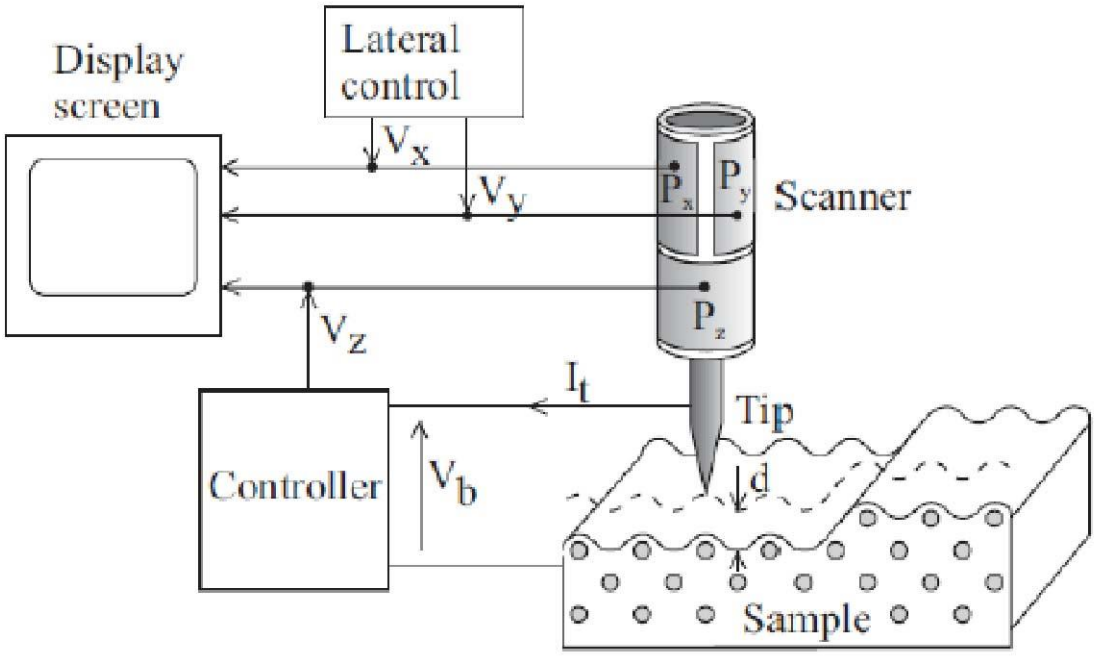

Figure 16. Operation principle of the STM. V_b is bias voltage; I_t is tunneling current; V_x is Lateral control voltage on x direction; V_y is Lateral control voltage on y direction; V_z is vertical control voltage (z direction) [107].

The simplest way to obtain a STM image is to measure directly the variation of the tunneling current as a function of the scanning position while keeping the distance between tip and sample surface constant (constant height mode). Higher scan rates can be applied which is advantageous to eliminate thermal drift effects in high resolution imaging. The scanner is at very high speeds but no longer able to follow the corrugation sufficiently. For this mode the surface of the sample must be very smooth because there is a risk that the tip rams with larger corrugations in the sample, since it cannot escape due to the pre-set height. A vertical drift could shrink the tunneling distance and change the real information about the surface. This constant height mode is used just in specific cases.

Instead of directly recording the atomic variation of the current, however the usual procedure is to keep the tunneling current constant and maintain the distance while scanning across the surface (constant current mode). This is done by changing the distance between the tip and surface using a feedback loop. This enables it to follow even the smallest details of the surface it is scanning. In constant current mode, when mowing the tip laterally over the surface a PID controller controls the tip-sample distance such that the detected tunneling current remains constant. According to formula (20) the tunneling

distance z must be kept constant (provided that the other parameters do not change). In order to get an image, the voltage required at the piezoelectric crystal to adjust the distance z is recorded. The resulting vertical z-signal contains the information about the topography of the surface. In the computer control, this signal is generated to a gray-scale image shown on the monitor display. Bright color indicates higher places, and dark color accordingly deeper places. In this mode, comparatively large and rough sample areas can be imaged without any damage of the tip or the sample surface (”tip crash”). However, the scan rate must be kept quite slow allowing the feedback system to control the z-position of the tunneling tip. Care must be taken when interpreting STM images, since it is actually the electronic density of states at the surface that is been probed rather than physical structure.

The lateral control voltages ensure the line by line scanning of a selected surface area. Three identical piezolegs are fixed in the base plate and the gliding plane with three ramps is found on the top. The coarse approach works by stick and slip mechanism. A sawtooth voltage is applied to the tangentially directed electrodes [108]. During the slow increasing of the voltage legs are bended in a tangential direction and this leads to the movement of the scanner unit. During the fast bend back the legs into theirs vertical starting position it happens without the movement of the ring. At the next step, it is then rotated again one step further. The sawtooth signal thus leads to an almost continuous rotation of the ring. The slope of the ramps thereby effects conversion of the rotational movement to a downward movement of the scanner. Wherein a slope of the ramp of 1/60 results in a step size of, for example, 1 micron to a lowering of the tip to 17 nm per step. The convergence speed can be varied within certain limits by amplitude, frequency, and slope of the sawtooth signal.

The tip is lowered by the rotation of the scanner unit. After the scanner stops the tip ends in the sample center. The simple rotary motion of the tip results always in a place within a very limited area on the surface. The sealing o-ring has an inner diameter of 4 mm. The hole for the sample in the cell having the same diameter, so the free sample surface is 0.12 cm^2. By a differential driving of the piezolegs, it is possible to perform a specific lateral movement of the scanner and thus to reach every place on the free surface.

During the coarse approach a rotational movement is realized. For this reason, the legs are arranged so that two electrodes are aligned tangentially. By driving these electrodes (X^+, X^-) in the tangential direction the desired rotation is obtained.

The STM images were analyzed with WSxM 5.0 image analysis software, published and maintained by Nanotec Electronica S.L. [109]. The software permits to plot line profiles, Fourier transform the images, adjust their contrast and apply filters, i.e. Gaussian. In order to avoid to introduce false information into the picture most of these techniques were not applied. Usually the contrast was slightly adapted and linear backgrounds subtracted. Rarely the image size was reduced in order to increase the size of details and highlight them. Fourier filtering or very slight Gaussian filtering were used to decrease the level of noise in the final image. However, in the analysis of the STM images unfiltered data were used. This avoids the risk of analysis induced distortions.

2.8.10. EC-STM electronics

Only a short overview of the electronics will be given in this part. More detailed description can be found in [95]. Compared to what is presented in the work of Wilms some changes in electronics were done. Figure 17 shows a simplified scheme of the EC-STM control.

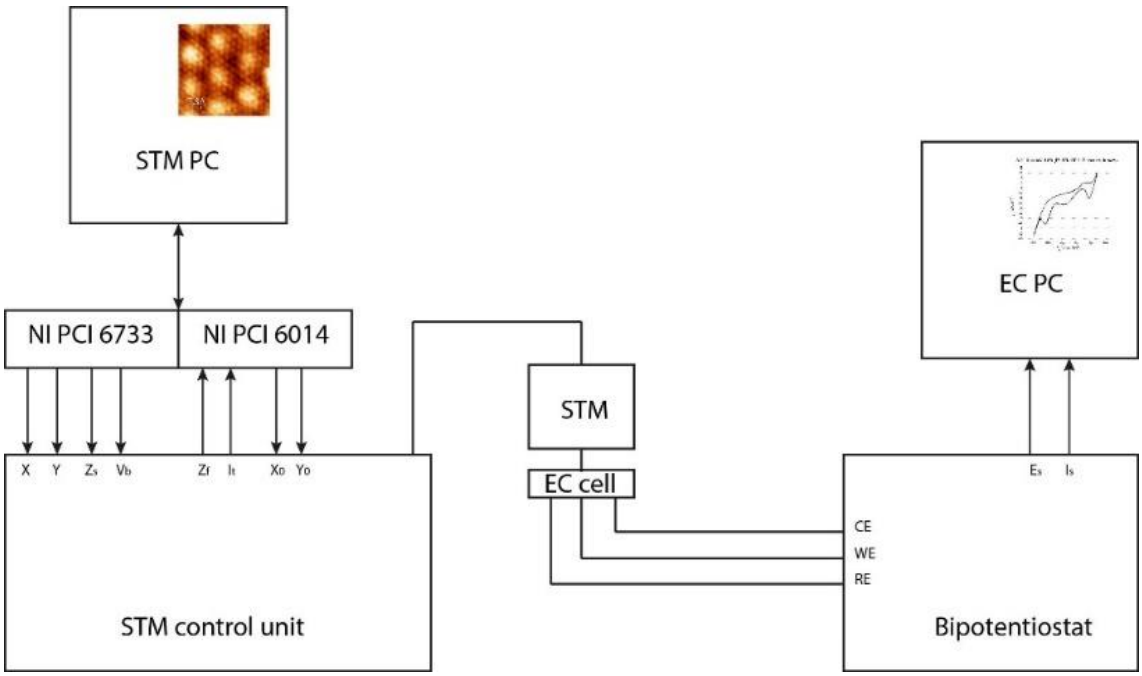

Figure 17. Simplified scheme of the EC-STM control.

The STM control unit is connected to the computer by two multi-function boards. Due to the necessity of using more modern and powerful PC the old electronic boards with ISA type connection were replaced by new one from National Instruments (NI). The chosen boards have similar parameters with old in order to make as less as possible modifications to the software of the STM controller. The NI PCI 6733 board has four independent 16-bit digital to analog (D/A) channels. It controls the X, Y-motion of the scanner, the computer-generated Z-Slow (Z_s) signal and a digitally adjustable bias voltage (V_b). The NI PCI 6014 has a fully isolated 12-bit analog to digital (A/D) channels that read the tunneling current (I_t) and Z-Fast (Z_f). These two signals are used for display and control the tunneling distance. The NI PCI 6014 has besides two 12-bit D/A channels, used for the offsets for the X, Y-movement.

System allows to record a small image (e.g. 1 nm × 1 nm) with atomic resolution and large topographic images with the maximum scanner square area achievable 2 µm × 2 µm.

The lateral x, y-movement of the tip is performed by antisymmetric voltages (V_{x+} , V_{x-}, V_{y+}, V_{y-}) generated in the computer and applied to the respective opposite x, y-electrodes as an output from digital-to-analog converter (DAC). The maximum output voltage of the converter boards is ± 10 V, but the electrodes in order to be driven must go up to ± 100 V to achieve a correspondingly larger extension. In the simplest case, high voltage operational amplifier with the voltage gain for ten times is required.

The converter card provides a 16-bit resolution. In comparison to previously developed EC-STM, the digital controller (old controller) has been replaced by an analog controller (NI boards). For the control of the z-signal a simple proportional integral (PI) control algorithm is used. The advantage is that even if computer break down the tip control continues to operate and thus prevents a crashing the tip into the sample.

The tunneling current with ten-turn potentiometer can be adjusted continuously. This can even be done during the tunneling image acquisition, which will create new opportunities for obtaining better results. Now it's possible not only specify a setting and then see the result. The adjustment can be made during the acquisition and the parameters can be optimized during the imaging.

During a scan the tunneling current I_t and the height signal Z-Fast are recorded. The computer displays only Z-signal, which contains the height information, in a grey-scale

image. It is red by a 12 bit analog-to-digital converter (ADC). Only the Z-fast signal is put onto PC to display the corrugation.

The vertical control Z-signal is divided into two parts, in the Z-Fast and Z-Slow. The maximum expansion of the scanner in the vertical direction is ± 110 nm, atomic corrugations are in the range of less than 1 nm. Therefore, it has sense to specify a signal Z-Slow for the coarse approach of the scanner and Z-Fast for the measurement of corrugation with a higher resolution proportion. In *Constant Current Mode*, a PI controller generates the signal for the vertical displacement (Z-Fast) from the tunneling current signal. Z-Slow is generated by integrating Z-Fast. Both signals are added together and supplied to the z-electrode of the scanner. The time constant of the integrator is dimensioned such that the Z-slow changes only slowly (in relation to the scanning speed). Integration causes the deflection of the Z-Slow scanner controls such that Z-Fast is held in the time average to a value of 0. Z-Slow thus ensuring the coarse approach, which is needed to bring the tip into the tunneling current range, while Z-Fast has to follow only the corrugation. The amplification factor of Z-Fast is set in three stages. In the sensitivity setting, a vertical resolution of 5.5 nm at 12 bit, which are reached 1.3 pm per bit.

The software, developed for the control of almost all functions of the STM by user from through the program commands, was little bit modified in order to make new boards of NI works.

2.8.11. Tunneling tips

The atomically sharp tunneling tip is a crucial element of any STM. All tunneling tips (STM tips) used in this work were made of pure tungsten wire (99.95%, Advent Research Materials Ltd, England). tungsten is commonly used because electrochemical etching techniques can be used to create very sharp tips. The STM tips were electrochemically etched from a 0.25 mm diameter wire. This wire was pierced through a Pt wire loop as the counter electrode, which then was briefly immersed in 2M KOH electrolyte in order to suspend a thin layer of the electrolyte after immersion (Figure 18a). An alternating potential with an amplitude of ±4 V and a frequency of 100 Hz was applied between the tip and the Pt loop electrode. It led to the dissolution of the tungsten in contact with the KOH etching solution. The etching was

continued until the free end of the tungsten wire fell off due to the gravity. The tips then were carefully cleaned in bi-distillated water and dried. After that they were coated by a polyethylene (ethylene-vinyl acetate) based thermal glue (UHU GmbH, Germany). The coating of STM tips is necessary to minimize electrochemical reactions at the STM tip surface during the *in situ* STM experiments. In order to cover the STM tip, it was pushed through a heated hot drop of glue polymer, melted at 150°C. Only a very small tip apex remains uncovered (Figure 18b). After a cool down and hardening time of usually 16 h the STM tips is ready for use.

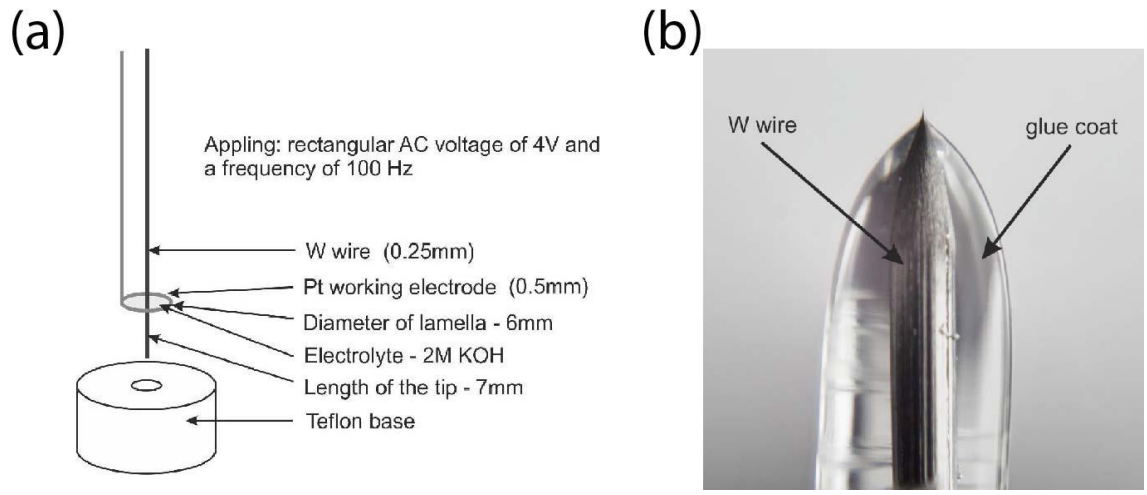

Figure 18. (a) Scheme of the tip etching set-up; (b) Photo of the covered tip [KosmalaThesis]

The tip length is out of the small tube should not be too large for reasons of stability. On the other hand, however, the tip must be able to immerse deep enough into the electrolyte. Appropriate length of the tip is around 7 mm. This value can give a maximum electrolyte level above the sample surface of about 4 mm. Another 3 mm of the tip length serves as a safety margin against a wetting of the small tube and the scanner piezos due to capillary forces.

2.8.12. Bipotentiostat

A bipotentiostat used in EC-STM is not commercial and was developed by group of Bonn University. It works with a real and not virtual grounded working electrode. The current through these electrodes can't therefore be directly measured. Instead, the current is measured through the counter electrode, which corresponds to the current through the

working electrode. The bipotentiostat has the task to control electrodes and to measure their currents independently from the potential of the counter electrode. In special measurement mode it can also control the tip bias potential. The measuring ranges of current extend over six orders of magnitude from 100 mA down to 1 μA with a resolution of less than 10 nA. To cover this wide range two different current/voltage converters is used.

2.8.13. Scanner calibration

The EC-STM needs to be calibrated from time to time, especially after the change of the scanner; for this purpose the STM measurements of Cu(100) single crystal in hydrochloric acid were performed. The obtained STM images (Figure 19) shows the surface morphology and atomic structure of the Cu(100) electrode in the presence of specifically adsorbed chloride anions at potentials within the double layer regime, where electrochemical reactions do not occur (black arrow in Figure 19c). In 10 mM HCl solution, the adlayer lattice is square and commensurate with respect to the substrate lattice. The adlayer can be described by c(2×2) unit cell [110,111]. The steps are 0.25 nm height (insert in Figure 19a) and the nearest neighbor distance is 3.64 ± 0.05 Å, measured by Furie transform (insert in Figure 19b); both values are in a good agreement with literature.

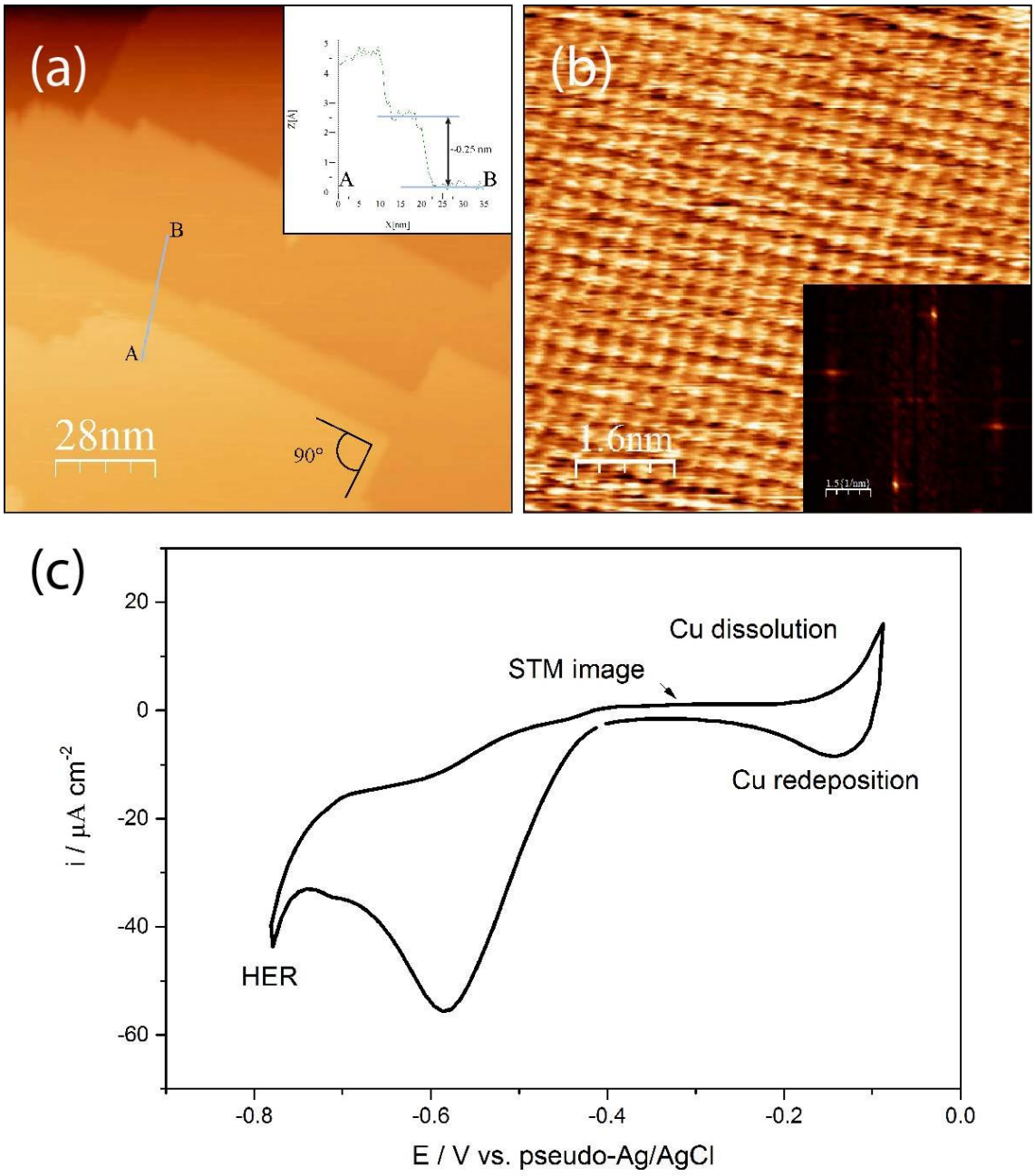

Figure 19. (a) STM image of Cu(100) in 10 mM HCl at -0.31V vs. pSRE (I_t = 1.8 nA, V_b = +209 mV); (insert) the profile line from image (a); (b) an atomically resolved image of the c(2 × 2)-Cl ad-layer; (insert) the power spectra obtained by using Fourier transforms of the image (b); (c) cyclic voltammogram of Cu(100) in 10 mM HCl at scan rate 10 mV/s.

2.9. Metal NPs

Detailed knowledge of the whole range of the parameters of catalytic processes is very important. Characterization of the model catalytic systems at the nanoscale is a fundamental step for better understanding of main parameters such as structure, morphology of reactive

particles and mechanisms of catalytic reactions. Undoubtedly, the most common and important heterogeneous electrocatalysts are supported by carbon based materials metal nanoparticles (NPs). Fabrication of regular arrays of equally sized (monodisperse) highly ordered clusters of metal NPs on a flat substrate is a central goal for nanotechnology. The mismatch between the Cu substrate and the Gr layer, called a Moiré pattern, creates an orderly array of ripples in the Gr with periodicity of several nanometers, which can be used as a support for well-organized metal NPs growth with nearly perfect long range order (narrow size distribution). First reports of study the Gr as support for metal NPs was done by N'Diaye et al. They show that Moiré of Gr on Ir(111) could be used for obtaining identical 82-atom Ir clusters [4]. These systems can be used as model catalysts for basic understanding of electrocatalytic properties. Goodman et al. suggest Gr as a support for metal NPs in studies of catalytic reactions, such as the oxygen reduction reaction (ORR) and the hydrogen evolution/oxidation reaction (HER/HOR), which are important for technical applications, due to its chemical inertness and thermal stability [5].

It was hypothesized that with the EC-STM measurements of the Pd and Co NPs on the Gr/Cu substrate can be understand the mechanism of the HER or structure changes in the catalyst model during electrochemical reaction. The most studied topics in HER are the role of the electrolyte and the electrode material and the behavior of the reaction intermediate. The important parameters influencing the electrocatalytic properties of supported NPs can be particle size, particle dispersion, density of low-coordinated surface atoms, and influence of the substrate material.

2.10. Preparation and characterization of metal NPs

2.10.1. Physical Vapour Deposition

Physical Vapour Deposition (PVD) is a vacuum process used to deposit very thin films on substrates for a wide variety of commercial and scientific purposes. In order to be able to study the metal NPs/Gr/Cu catalytic systems by EC-STM tool, PVD was used in order to deposit NPs. This technique allows to control quite precisely the amount of metal deposited and by acting on the evaporation flux also on the morphology. In the present study, Pd and

Co were evaporated in UHV conditions on Gr/Cu samples, from a Pd or Co rod (diam. 2 mm) with a purity of 99.95%, which were bombarded with electrons. The samples were prepared using the electron beam evaporator (Thermo VG Scientific) under the following conditions: ≤ 10^{-9} mbar, 1 ÷ 1.1 kV voltage and the emission current during this treatment around 10 and 12 mA for Pd and Co, respectively. Each Gr/Cu sample was cleaned before metal deposition by thermal annealing for 1 hour at 300 °C performed by resistive heating (temperature was measured using K-type thermocouple). Here also the deposition at various time was done.

2.10.2. Electrochemical deposition

Electrochemical metal deposition is another important method to synthesize supported nanoparticles with a well-defined amount of foreign metals from solution. The mechanism of this process still requires deep study [112].

Electrochemical deposition of metals is a process of the reduction of metal ions M^{z+} from electrolyte solutions represented by:

$$M^{z+} + ne^- \rightarrow M \qquad (21)$$

Electrons *n* for the electrochemical deposition process could be provided in two different ways: by an external power supply (electrodeposition), and by a reducing agent in the electrolyte (electroless deposition). Deposition reaction occurs at the interface between a liquid solution and a solid metal electrode. During the electrodeposition positively charged metal ions M^{z+} attracted by negatively charged electrode adsorbs on the surface and reduce to the solid metal after a charge transfer. In aqueous solutions metal ions are hydrated by water molecules. The deposition reaction depends on two main processes: the diffusion of electroactive species from the bulk solution to the electrode surface (mass transport step) and the electron transfer at the surface interface (charge transfer or discharge step). For the discharge of metal ions, electrons have to cross the phase boundary between ion conductor (i.e. the electrolyte) and the electron conductor (i.e. the metal electrode). It involves the change in the structure of the ions, such as partial removal of the hydrate shell or geometric deviations from the situation in the bulk solution. The charge transfer reaction corresponds to a thermally activated process for which the activation energy barrier varies with the

applied electrode potential. The exchange of electrons due to an electrochemical process occurring at the electrode surface gives rises to a current, which is a measure of the reaction rate taking place at the electrode. A mathematical relationship between the current density *i* (expressed in A/cm) and the applied overpotential η is given by the Butler-Volmer equation:

$$i = i^{+} + i^{-} = i_o[\exp\left(\frac{(1-\alpha)zF}{RT}\eta\right) - \exp\left(\frac{-\alpha zF}{RT}\eta\right)] \qquad (22)$$

The overall current density *i* is actually the sum of the partial current densities related to the anodic (metal dissolution) and cathodic (metal deposition) partial reactions (i^+ and i^-, respectively). The electrochemical charge transfer coefficient α is a measure of the symmetry of the activation barrier ($0 < \alpha < 1$). i_o corresponds to the exchange current density and is related to reaction kinetics.

Metal deposition on different substrates experimentally take place at potentials which are different from the thermodynamically calculated values for various reasons. It can be shifted to more positive deposition potentials than the Nernst potential (this process known as underpotential deposition, UPD) or to more negative potentials due to limitations in charge transfer or nucleation, or to undesired side reaction such as solvent decomposition. The initial stages of electrochemical metal deposition occur at potential positive of the Nernst (reversible) potential for the corresponding bulk metal deposition (UPD).

Contrary to gas phase deposition in the ultra-high vacuum environment (UHV), the electrodeposition is ruled by the value of the applied overpotential (η) which not only determines the kinetics of the ion transfer reaction but also may affect the deposition process by changing the electrode surface properties (anion co-adsorption, surface reconstruction).

It was reported that Pd grows in a layer-by-layer manner on Cu(111) at the initial stage of growth (less than a few monolayers) [113]. In contrast, electrodeposition of metals on HOPG substrate occurs via a Volmer–Weber mechanism in which three-dimensional clusters are formed [114].

3. Preparation of graphene on copper

3.1. Introduction

The first part of the research work was focused on the growth of high quality Gr films on copper samples. This study was necessary in order to prepare in a reliable way surfaces with controlled morphology and defectivity, to be used for the following electrochemical characterization. The main process parameters that were studied were the temperature and the pressure of the ethylene gas.

The deposition of Gr in all experiments, was performed in a custom-built Cold-Wall Low Pressure Chemical Vapour Deposition (LPCVD) chamber (Figure 20a). Only a small volume of the chamber was heated l to the working temperature by a resistively heated stage in order to bring the sample at the temperature necessary for the Gr growth. A rotary pump allowed to reach a background pressure that before the deposition process was lower than 10^{-2} mbar. This good level of vacuum allowed to reduce possible contaminations in the Gr films. High purity gases were introduced in the chamber through a leak valve and dosed on the sample surface by a capillary ending with the shower-like outlet. The heating stage, made up by a molybdenum sample holder in direct contact with a pyrolytic boron nitride (PBN) resistive heater (Tectra GmbH, Germany) was mounted on a CF 63 flange fixed at the bottom of the chamber (Figure 20b). Electric current in the range between 0.5 and 6.0 A allowed to reach a temperature higher than 1000°C (Figure 20c) in a very short period. Three side and one front flanges were fitted with viewports in order to introduce light and inspect the working zone of the system. The pressure in the chamber was monitored by a full range gauge PKR-251 (Pfeiffer vacuum, Germany). The temperature was measured by a chromel/alumel K-type thermocouple (Figure 20b) attached to the molybdenum platform mounted on PBN resistive heater. This latter was controlled by an external DC power supply. The samples, fixed to a transferable molybdenum sample holder, were inserted in the chamber and placed on the heater using a transfer rod through the frontal fast entry. This system allows the deposition of Gr on different kinds of samples such as foils, polycrystalline disks or single crystals. Overall the reactor was designed to allow a very precise temperature

control over a very large range with very fast heating and cooling ramp since these factors make the CVD process very productive and versatile. The control of temperature is particular crucial for Gr growth, since a very high temperature, rather close to melting point of copper (1083°C [115]) is require for obtaining large domains and defect free structures. Different modifications of the sample holder were carried out in order to obtain stable measurements of the temperature. The final design involved a combination of a molybdenum sample holder with a round hole fitting the sample, lying on a molybdenum plate (2.5 mm thick, 99.95% metal basis, Alfa Aesar GmbH, Germany). The thermocouple was connected to the stage in the Cold-Wall LPCVD chamber, so the position of the sample and the thermocouple were fixed, which allowed to obtain a good reproducibility of the experiments.

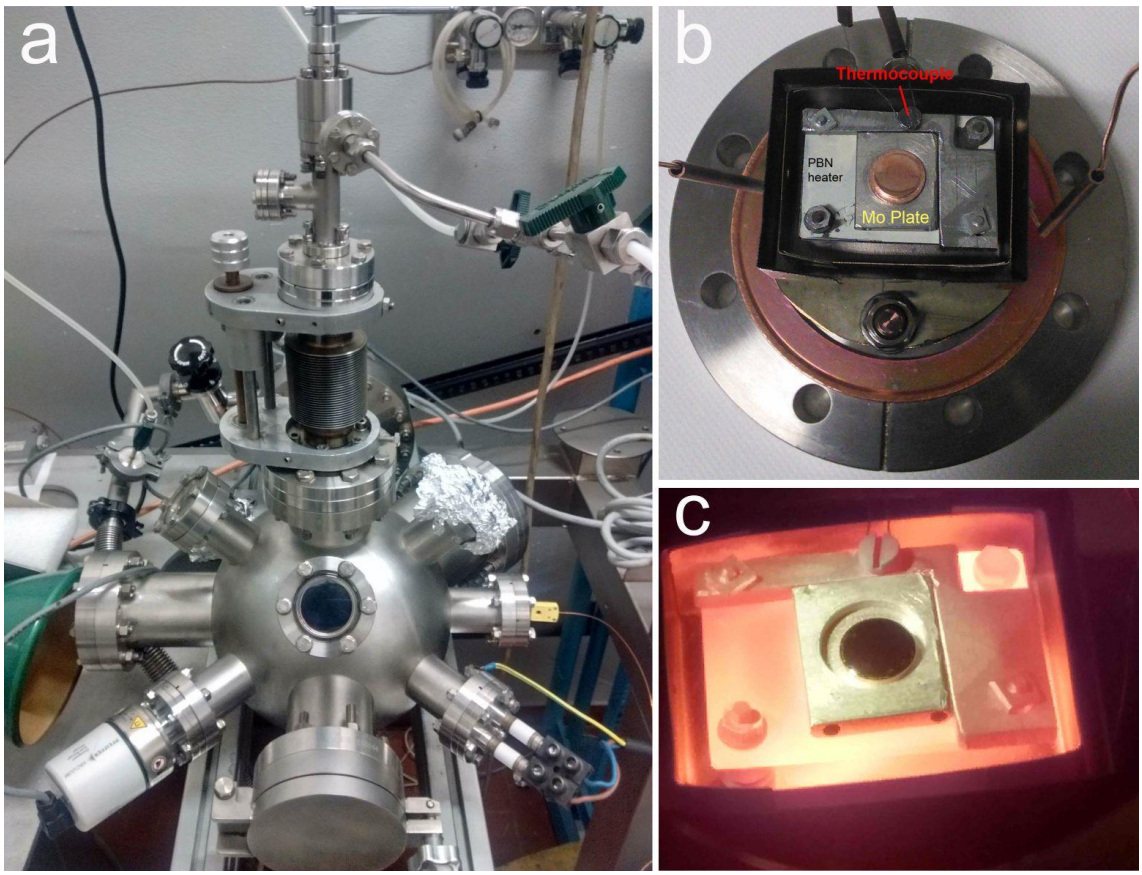

Figure 20. (a) LPCVD chamber; (b) PBN heater stage; (c) Mo sample holder on the PBN heater during the CVD process.

After the construction of the instrumental apparatus and trial and error optimization for reaching a good control of the main experimental parameter, the next step was the

investigation of the role played by the growth parameters of the LPCVD system on the properties of Gr thin films.

3.2. Results

Figure 21 reports the typical temperature and pressure profiles during the optimized CVD process. Prior to each growth, the system was evacuated to a vacuum of 0.01 mbar using the rotary pump. The Cu samples were then heated and annealed under a flow of H_2. This gas was used in order to remove the native copper oxide layer from the surface and other possible contaminants. At relatively high temperature, Cu is easily oxidized in the presence of even low traces of oxygen. It was found that annealing for 15 min at temperature higher 800°C in hydrogen atmosphere is usually sufficient to remove almost all oxides. For polycrystalline Cu thermal annealing was performed at elevated temperature to increase the grain size before the growth step. A substrate with a coarse crystalline texture is required to obtain homogeneous Gr layers since the presence of many grain boundaries triggers the formation of multilayers since represent regions of an increased uptake of carbon. In the second growth step, H_2 was shut off and a C_2H_4 was introduced in the chamber with a total pressure around 1 mbar. After completion of the growth, the ethylene supply was shut off, and the samples were cooled down to room temperature. The process yields high quality and high purity final products potentially at large scale.

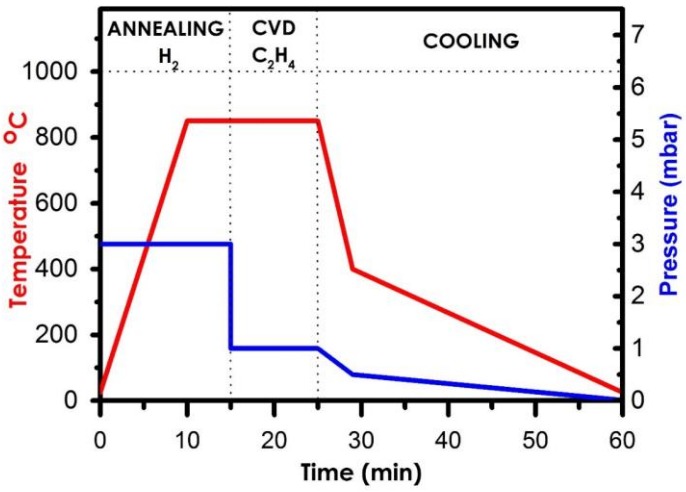

Figure 21. The temperature (red) and pressure (blue) profiles of the CVD process for Gr growth.

Some authors suggested to keep hydrogen flow during the Gr growth to avoid copper oxidation [22,67,116]. When we try using a mixture of hydrogen and ethylene, the side processes of the Gr etching by hydrogen start to compete with the main reaction. As a matter of fact H_2 is known to etch Gr at high temperature through hydrogenation [117].

As it can be seen from Figure 22, Gr islands have hexagonal holes (marked with yellow arrows) as a result of the reaction with hydrogen. To avoid this problem, the hydrogen gas was completely shut off after the annealing for pre-cleaning. Only the ethylene was dosed in the chamber.

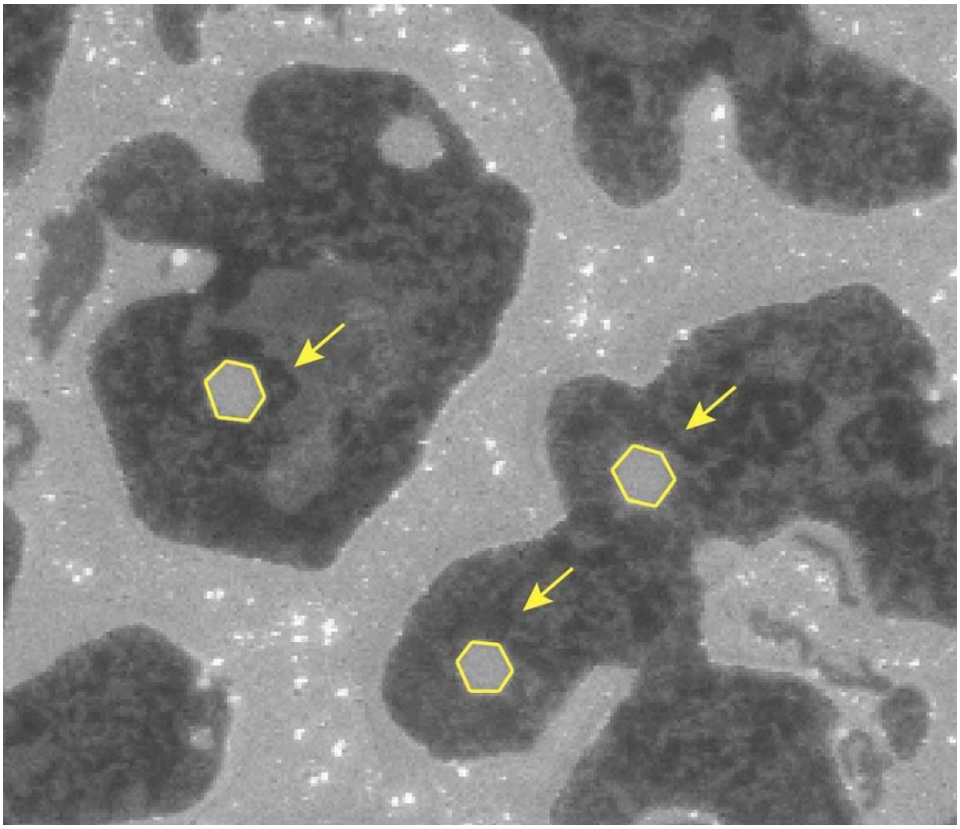

Figure 22. SEM image of Gr/Cu(111). Hydrogen etching (Image size: 6 µm x 5 µm).

It is known that due to the limited coordination of surface atoms, a metal surface can melt at a temperature that is significantly lower than the melting point of the bulk material; moreover the low pressure of the deposition conditions may further enhance this effect [118]. Since the growth temperature is very close to the melting point of Cu, adsorption of carbon atoms and desorption of Cu atoms can dramatically change the surface morphology. Considering the high temperature during the annealing and growth ~900°C, and the low

pressure in the chamber, 0.1 ÷ 1 mbar, the evaporation of the metal is not surprising. On bare areas the fast evaporation of Cu produces large holes, while the regions already covered by Gr maintain their height. These two opposite processes lead to a very rough surface characterized by large pits at the micrometric length scale. Figure 23 shows an optical microscope image of a Cu(111) sample after the growth of Gr at 900°C: it may be clearly seen that after the Gr growth all the surface is characterized by a diffuse pitting due to the copper evaporation.

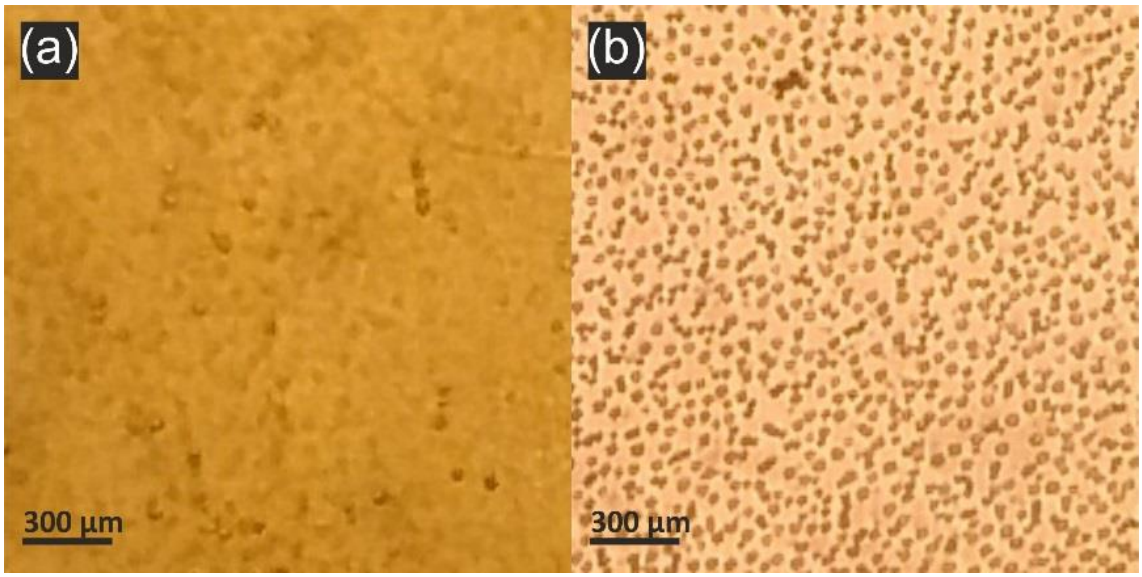

Figure 23. Optical microscopy images of Cu(111) surface before (a) and after (b) deposition of G. (Annealing: 3 mbar of H_2, 900 °C, 5 min; CVD: 1 mbar of C_2H_4, 900 °C, 15 min).

This phenomenon is further enhanced at higher temperature and lower pressure.

When the ethylene pressure is reduced below 0.1 mbar, no Gr deposition is observed at any of the used temperatures. Actually, in order to grow Gr it is necessary to reach a critical surface concentration of carbon atoms above which nucleation is possible. This can be obtained by increasing the ethylene pressure, however this has to be done in extremely controlled conditions otherwise excessive supersaturation could be reached with a massive nucleation, which would lead to the formation of highly polycrystalline Gr layer with many defects. Temperature and pressure are closely intertwined and has to be optimized simultaneously. Actually, it has to be considered that at relatively high temperature the sticking coefficient of C_2H_4 decreases and the desorption of carbon enhanced. Both these phenomena reduce the number of carbon species on the surface, hindering the formation of

stable Gr nuclei. Figure 24 reports the Raman spectra observed after the growth of Gr on Cu(111) at three different temperatures 850, 900 and 950°C. The spectra are displayed with a vertical offset for clarity. As it may be observed there are no signal coming from Gr. At temperature higher than 900°C the evaporation rate of Cu is extremely high and leads to a huge surface roughness (Figure 24d) as evidenced by the change in the morphology observed with the optical microscope. From these data it results evident that a minimum ethylene pressure is necessary to grow Gr and on the other hand the temperature must be carefully controlled in order to guarantee a good surface diffusion, but low enough to prevent pitting by copper sublimation.

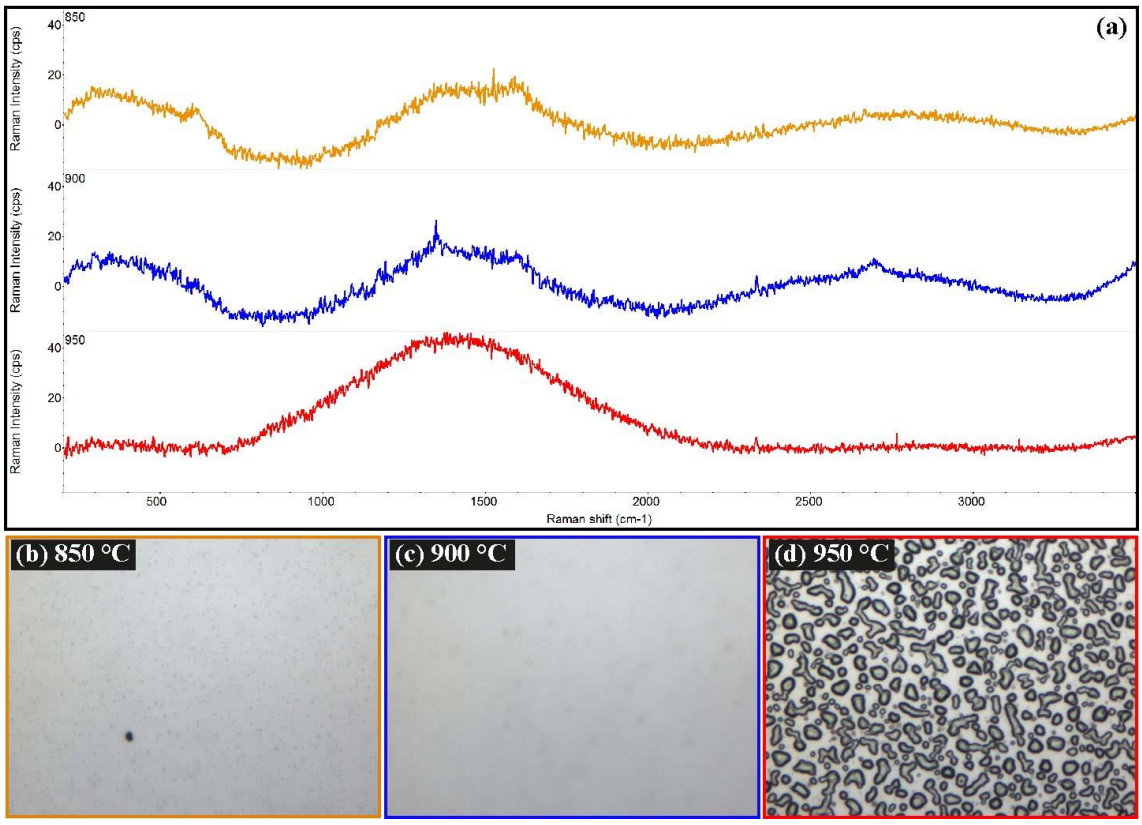

Figure 24. (a) Raman spectra of Gr samples grown at 0.1 mbar, 30 min, and temperature: 850 °C, 900 °C and 950 °C; optical microscopy image (105 x 140 µm) of Cu(111) surface after deposition of Gr: (b) 850 °C; (c) 900 °C; (d) 950 °C.

In order to study the effect of C_2H_4 pressure on Gr growth, different pressure in the range from 0.5 to 1 mbar was used in different experiments. The growth temperature was fixed at 850°C for all experiments in order to avoid Cu evaporation. Table 1 summarizes the conditions for this set of experiments.

Table 1. Graphene grown on Cu(111) at different pressure of C_2H_4 at 850°C.

Sample #	Pressure, mbar	D band, cm^{-1}	G band, cm^{-1}	2D band, cm^{-1}	I_{2D}/ I_G	I_D/ I_G
1	1	1358	1592	2716	0.6	0.2
2	0.7	1361	1591	2719	0.61	0.3
3	0.5	1365	1593	2716	0.67	0.27

Figure 25 shows a typical point scan Raman spectrum of the Gr/Cu(111), corresponding to sample number 1 in Table 1.

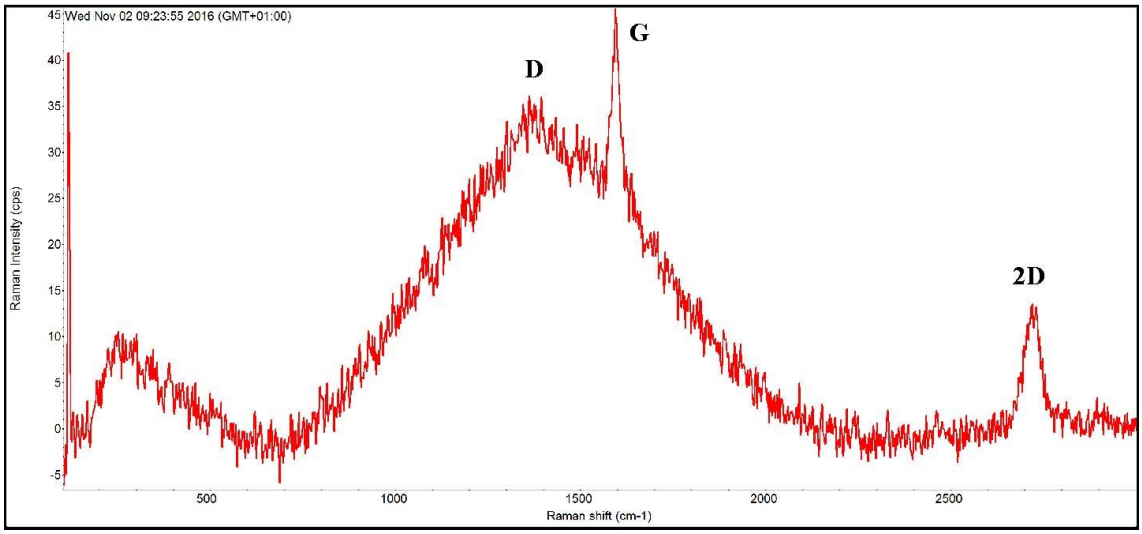

Figure 25. Raman spectrum of Gr/Cu(111) grown at 850 °C, 1 mbar, 18 min.

There is a very large literature dealing with the Raman spectra of carbon materials and in particular of Gr. It is widely accepted that the Raman spectrum of G present three intense peaks: G (around 1595 cm^{-1}), 2D (around 2720 cm^{-1}) and D (around 1360 cm^{-1}). Since Raman spectra were acquired on copper substrate, the peak locations are shifted with respect to the spectra of suspended Gr or Gr/SiO_2/Si [119]. The G band represents the main peak of Gr. This band is due to the in-plane bond stretching motion of pairs of sp^2 carbon atoms. It confirms Gr formation on Cu. The 2D band (also known as G') is a double resonance phonon process of Gr and is a fingerprint of the number of Gr layers by the analysis of the peak

shape and width. It has been previously reported that the 2D band of monolayer Gr can be fitted by a single Lorentzian function with a full width at half-maximum (FWHM) of ca. 30 ÷ 40 cm^{-1}, whereas the band splits into several overlapping Lorentzian peaks in the case of multilayer Gr, which results in a broad and asymmetric peak shape [120]. The 2D band is the second order of the D band. Sometimes it is referred to as an overtone of the D band. It is the result of two phonon lattice vibrational process. The D band, centered around 1360 cm^{-1} is attributed to disorder-induced first-order scattering. It becomes active in presence of lattice disorder. The intensity of the D peak is sensitive to the type of defect [121] and grain boundaries [122].

The I_{2D}/I_G peak ratio is another very important parameter since its value is strongly affected by layer number also when Gr is supported on different substrates [123,124]. In pure single layer Gr supported on Si/SiO_2, the 2D band is typically around 4 times larger than the G band and the D band is absent. With increasing number of layers, the 2D peak becomes broader and loses its characteristic Lorentzian line-shape [120]. Since the G peak is attributed to intralayer effects, it results that its intensity scales with the number of layers.

Raman spectrum of as-grown Gr on Cu shows fluorescence, caused by the substrate [125], but peaks in the Gr Raman spectrum can be clearly identified. This background can be easily subtracted analytically, hence below in this thesis all the Raman spectra will be shown with Cu background subtracted.

Figure 26 shows the Raman spectra of Gr layers obtained according to the conditions in Table 1, at various pressure of ethylene from 0.5 to 1 mbar. The intensity is renormalized to the G band intensity and the spectra are vertically displaced for clarity. As it can be seen from Raman spectra and from Table 1, at higher pressure, the peaks ratio I_D/I_G, which is connected to the number of defects and therefore to the average dimension of the Gr islands, is lower probably due to a better uptake of carbon which allowed the formation of larger Gr grains and a more complete coverage of the copper substrate. The peaks ratio I_{2D}/I_G is around 0.6-0.7 which is lower than for suspended Gr. Normally, the growth of Gr on Cu by low pressure CVD is a self-limiting process over a wide parameter range [67,126]. The lower value of I_{2D}/I_G ratio can be explained by the strong interaction with the Cu substrate. It will be discussed in more detail in the next chapter.

For the preparation of the Gr films on Cu the pressure of 1 mbar was chosen in order to suppress the Cu evaporation and have fast deposition process. A pressure of ethylene 1 mbar for 10 min was enough to cover fully the Cu surface with Gr.

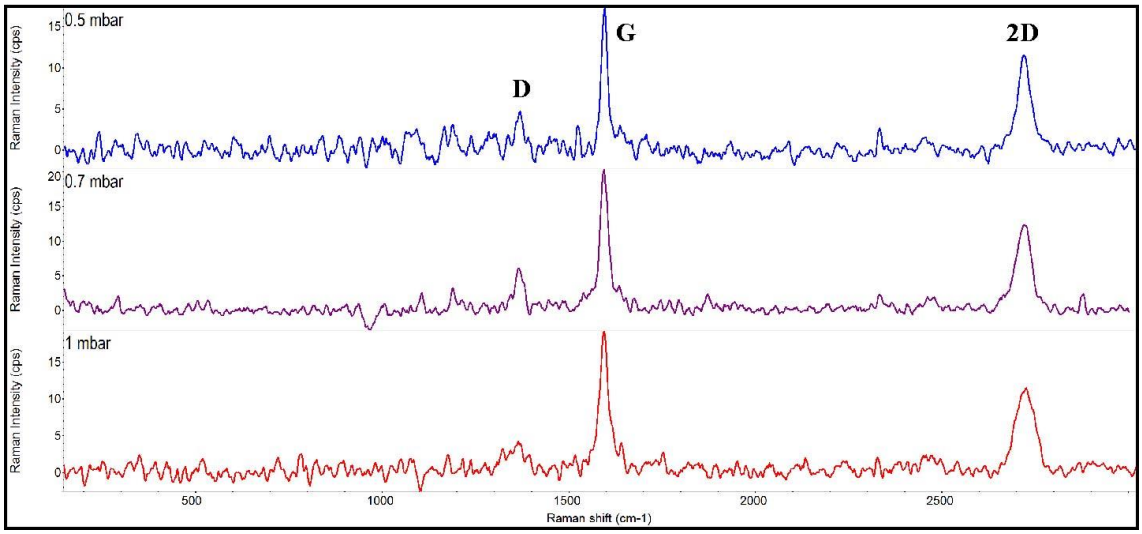

Figure 26. Raman spectra of Gr/Cu(111) samples for various pressure of C_2H_4

At temperatures higher than 800°C the ethylene molecules used as precursors get enough energy to decompose once in contact with the reactive surface Cu atoms and combine in Gr [127]. In order to study the effect of temperature on Gr growth, the temperature was varied between 800 ÷ 950°C range, while a pressure of 1 mbar (enough to suppress strong copper evaporation) and a growth time (time between the start of the ethylene flow and cooling of the sample) around 10 ÷ 20 min (to be sure of complete coverage of the surface of Cu by Gr) were chosen and maintained fixed as suggested by the results of previous experiments. Table 2 summarizes the growth conditions. The Raman spectra corresponding to these growth conditions are shown in Figure 27. By inspecting the value of the I_D/I_G intensity ratio, it may be deduced that the quality of layer decreases for increasing temperature. This temperature dependence is in disagreement with the results from the literature where in general it is reported that a higher temperature (up to 1000°C) is associated with a better quality of Gr layers [19,67]. In our case, the rise in the number of defects with temperature can be understood from the fact that the evaporation of the Cu atoms increases the roughness of the surface and the desorption of C_{ads} creates more local defects in the Gr films. From Table 2, the increase of the I_{2D}/I_G peak ratio with increasing of

the temperature from 0.6 to 0.9 indicates that Gr interact less with the surface when fast evaporation of Cu takes place.

Table 2. Graphene growth parameters with varying temperature and growth time

Sample #	Temperature, °C	Pressure, mbar	Time, min	D-band, cm^{-1}	G-band, cm^{-1}	2D-band, cm^{-1}	I_{2D}/ I_G	I_D/ I_G
1	950	1	10	1363	1599	2717	0.84	0.38
2	900	1	10	1362	1593	2714	0.77	0.29
3	880	1	15	1366	1594	2720	0.73	0.38
4	870	1	5	1364	1589	2709	0.61	0.2
5	850	1	18	1358	1592	2716	0.6	0.2
6	830	1	15	1361	1593	2720	0.6	0.2
7	800	1	1	-	-	-	0	0

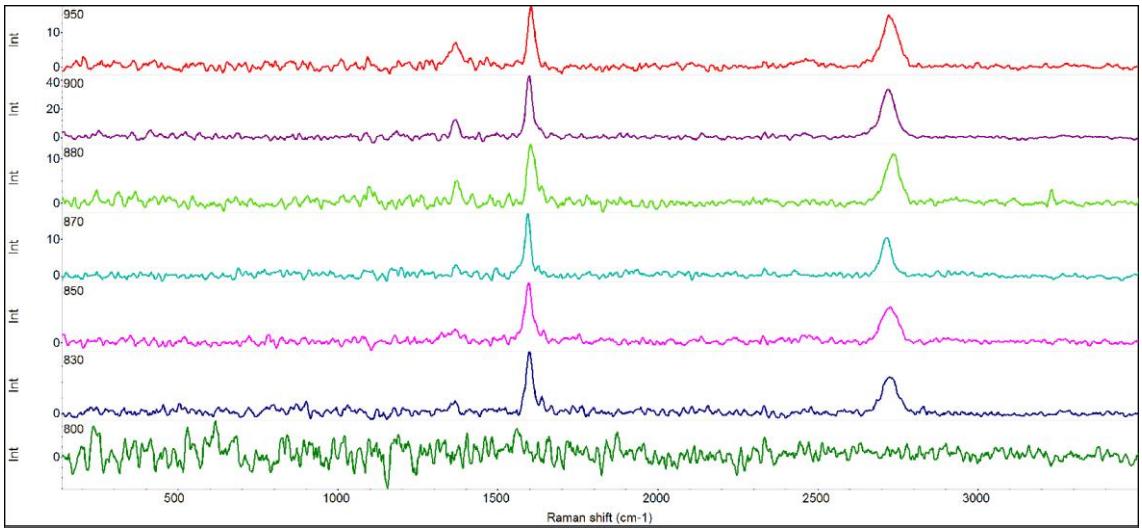

Figure 27. Raman spectra for the as-prepared Gr/Cu (copper background is subtracted) at various growth temperature.

The full progression of the ratios of I_{2D}/I_G and I_D/I_G peak intensities are plotted as a function of the temperature of the growth in Figure 28.

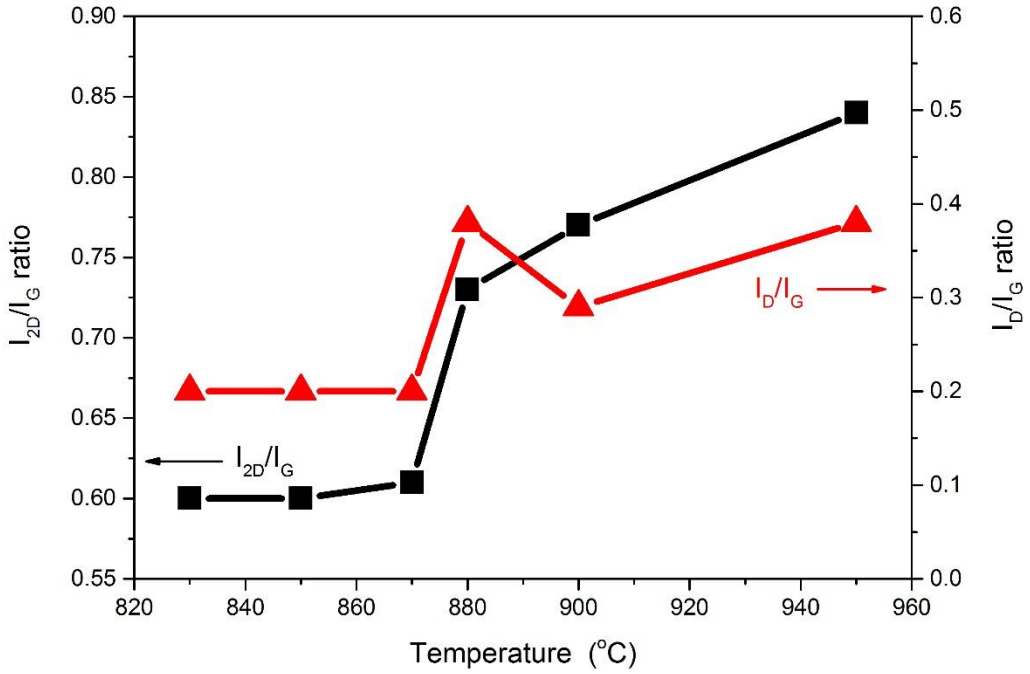

Figure 28. Plot of the dependence of peak intensities ratio I_{2D}/I_G (black ■) and I_D/I_G (red ▲) from the temperature of growth.

The relative intensity ratio of I_D to I_G has been significantly increased at the deposition temperature of higher 850°C for Gr. It results in the formation of more structural defects.

The conclusion of this set of experiments is that a high growth temperatures can rise the number of defects in Gr films as well as increase the surface roughness due to sublimation of the Cu under the low pressure growth [128], which is not good for the next STM measurements that require very flat surfaces with low number of defects and overall for the reproducibility of results. Figure 26 and Figure 27 show that the growth process strongly depends on the temperature of the sample and pressure of ethylene due to the competition between the Gr deposition and copper sublimation. In fact, high 2D band and low D band, attesting the formation of a good Gr layer, are present when working at pressure around 1 mbar and temperature 850°C.

At pressure 1 mbar and temperature 850 ÷ 880°C, the growth time was progressively reduced until a partial coverage of the Cu surface was observed by SEM measurements. A growth time of 5 min was already sufficient for the full coverage of the surface of Cu sample. To see the spatial variation of Gr films across the substrate, SEM images were acquired

(Figure 29). Because the secondary electron yield for copper is significantly higher than that for Gr, the Gr appears dark in these images.

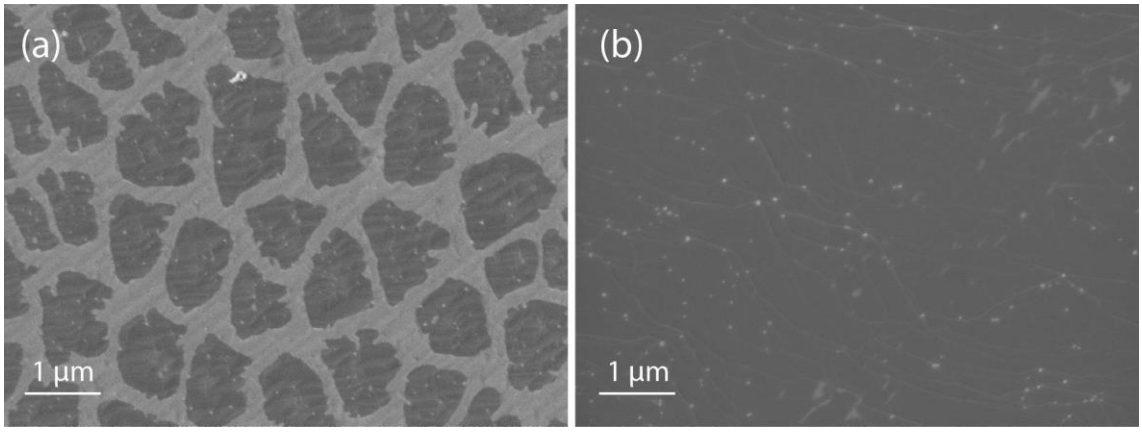

Figure 29. SEM image of: (a) partially covered; (b) fully covered Cu sample by Gr layer.

Figure 29a shows typical SEM image of the partially covered surface of Cu by Gr layer, where the dark irregularly shaped Gr islands and the bright regions of the bare Cu can be seen. Small Gr islands with size around 1.5 µm were found in less than 5 min. The shape of the Gr islands is not well-defined as at very low vacuum growth, when the shape of Gr flakes is four-fold [129], or perfectly hexagonal, at high pressure deposition of Gr [76]. Similar observation was done by Celebi et al. at the study of the initial stages of Gr growth on copper by ethylene decomposition [127]. As the growth time is increased, the Gr domains progressively increase in size until they coalesce into a continuous layer (Figure 29b). On the fully covered samples, a completely homogeneous Gr layer covers the Cu substrate step-edges and shows continuous grain boundaries. The SEM micrographs indicate the presence of bright dots, especially on the Cu step-edges, which are probably related to copper oxide (Cu_xO) particles [130,131].

In order to identify the chemical nature of the layer, XPS measurements were undertaken. The survey spectra taken on the Gr/Cu(111) samples, grown at 850°C and 900°C, indicate the exclusive presence of C, Cu, and O (Figure 30). The C 1s photoemission peak (284.2 eV) is observed in all the analyzed spectra. On the spectra of the samples prepared at 900°C, the O1s peak is centered at 532.9 eV, which corresponds to the C-O groups present on the surface, bound to the morphological defects during the Gr growth

and/or after the transfer in the ambient atmosphere from the preparation chamber to the XPS analysis chamber.

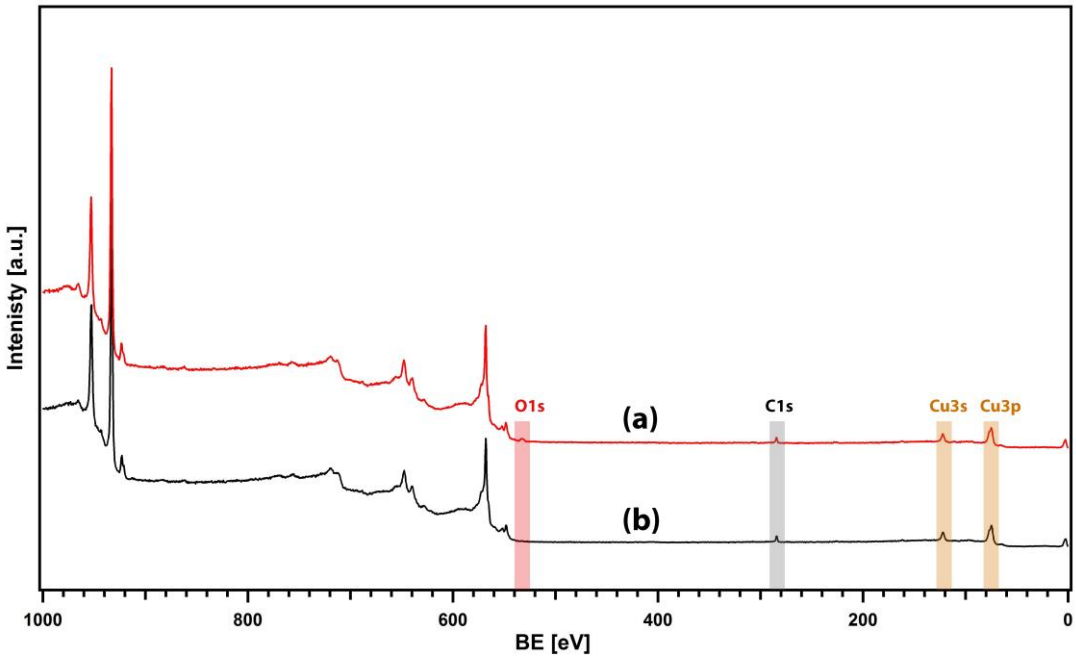

Figure 30. XPS survey scans taken in the 0-1000 eV spectral region for Gr/Cu(111) grown at (a) 900°C and (b) 850°C.

In order to get more precise information about the chemical identity of the presented elements, the C 1s and O 1s energy regions have been recorded with high resolution and the corresponded peaks were fitted with Gaussian-Lorentzian-Product function. The O 1s and C 1s spectra are presented in Figure 31.

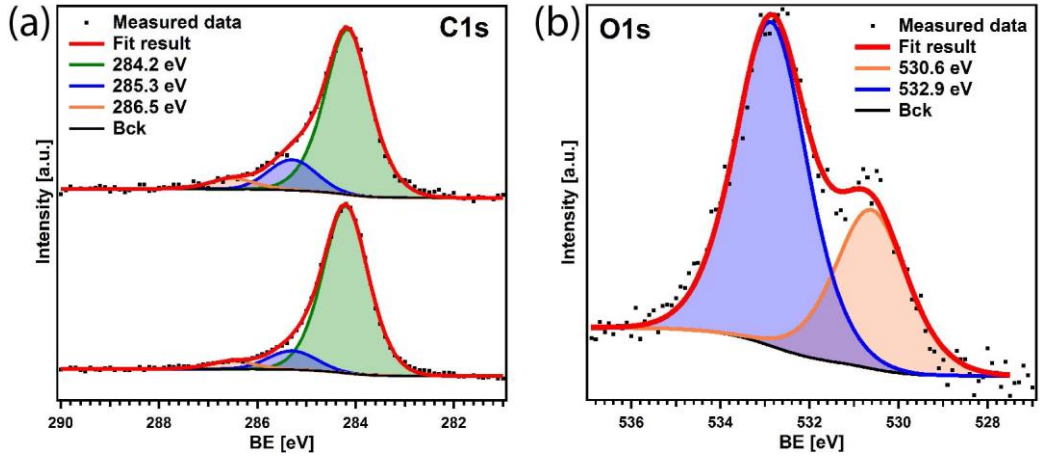

Figure 31. Core level photoemission lines and relative deconvolution into the single chemical components of C 1s (a) and O 1s (b).

The multi-peak analysis of the C 1s signals gives three clearly visible components (Figure 31a). The peak, centered at 284.2 eV can be attributed to sp^2 hybridized C, which is the main constituent of the Gr structure. The peak at 285.3 eV is due to sp^3 carbon, whereas the third peak at 286.5 eV is assigned to C-O bonds as previously reported by Mattevi et. al. [132].

The second most intense peak of the spectrum is O 1s, which indicates presence of the oxygen [133]. While it might originate from the contamination physisorbed from the air, its intensity suggests that it is mostly tied to the presence of copper oxides on the surface of the samples. Two main components have been identified: one at 530.6 eV, which can be attributed to C-O defects and lattice oxygen in Cu_2O, and a second component at 532.9 eV, which is distinctive of OH groups that can be adsorbed on the oxide surface (figure 31b).

Figure 32 shows the results of the LEED pattern (85 eV) observed on a Gr layer supported on Cu(111) surface. As it can be clearly seen in the figure, the patterns consist of six symmetric sharp bright spots that are characteristic of well-ordered (111) surfaces (orange circles) and a ring structure with lower intensity (white circles marks the brighter spots of the circle). The ring could be explained by the existence of different crystalline orientations of the Gr on Cu(111). Gottardi et al. reports similar results when comparing the Gr growth on pure Cu(111) surface with oxidized Cu(111) [134]. The additional hexagonal spots observed around the integer spots (blue circles) indicates the existence of a superstructure such as a Moiré pattern.

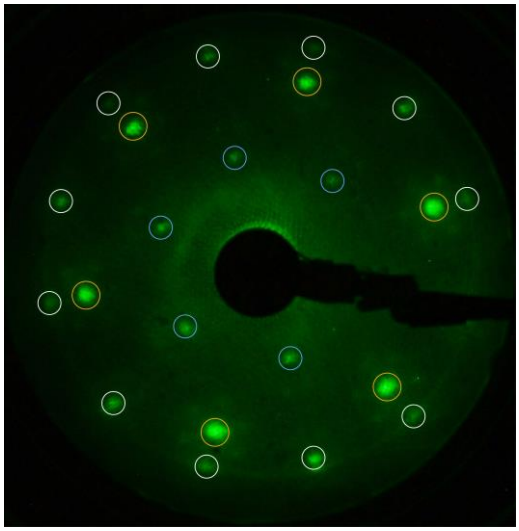

Figure 32. LEED image of the Gr/Cu(111).

3.3. Conclusions

In conclusion, a cold-wall thermal LPCVD chamber for the deposition of Gr on metal surfaces was designed and practically realized. This CVD reactor demonstrated to be very versatile and allowed to obtain high quality Gr layers. Interestingly, due to its excellent control of temperature it is perfectly suited to study the growth kinetics in CVD processes and its use can be possibly expanded to prepare and study 2D materials other than Gr.

The effect of different process parameters such as time of growth, precursor gas composition, pressure and temperature on the deposition of Gr on Cu substrates were systematically investigated.

Raman spectroscopy was used as the main tool to characterize the nature of the obtained Gr films. Additional characterization by SEM, XPS, and LEED substantiated the results.

No Gr was observed at pressures below 0.1 mbar, even after long deposition time. Full surface coverage with a continuous layer of Gr grains was obtained for pressures higher than 0.25 mbar, when the necessary carbon surface supersaturation could be obtained.

The temperature for the deposition of Gr was optimized by considering that the minimum temperature necessary for an effective decomposition of the ethylene precursors is 800°C, whereas an upper limit is imposed by the sublimation of copper atoms at temperature higher than 850 ÷ 900°C.

The body of our experimental data allowed us to identify 850°C, 1 mbar ethylene, and 5 minutes of exposure, as the best conditions for the growth of high quality monolayer Gr films that fully covers the copper substrate. The resulting Gr film was polycrystalline with single domains with a spatial extension of a couple of microns. Both XPS and Raman spectroscopy suggested that the resulting films exhibit a very low amount of structural and chemical defects.

4. Investigation on graphene films

4.1. Introduction

This part of the thesis reports the electrochemical and STM data of Gr films, deposited by LPCVD on Cu. Based on the microscopy and spectroscopy analysis, discussed in the previous section, the Gr layers, objects of the electrochemical investigation, were grown in the experimental conditions that allowed the best quality and reproducibility. Bare Cu samples were used as a background to differentiate between the behavior of substrate from the Gr films. Detailed description of the Cu metal corrosion behavior in acid solutions can be found in Chapter 2.

One of the aims of the present work was to highlight the stability of Gr and the underlying copper support (i.e. corrosion and/or spontaneous dissolution of metal) in several aqueous electrolytes. Electrochemical characterization was carried out to understand the electrochemical properties of Gr films and Cu substrate in different acidic and alkaline electrolyte solutions and the behavior of the Gr layer during the electrochemical reactions. The effects of SO_4^{2-}, Cl^- and ClO_4^{2-} on the initial oxidation stages of Cu covered with Gr layer in acidic solutions are discussed, along with the most investigated naked Cu electrode taken as reference for an appropriate comparison. To our knowledge, there are no detailed studies of the influence of Gr on the protection of anodic oxidation of Cu, and the debate about the Gr protection properties is still opened.

4.2. *Ex situ* electrochemical measurements of Gr on Cu

The Gr defects or grain boundaries can promote unwanted surface reactions of Cu substrate with ions or molecules coming from the electrochemical environment. Only Gr with low density of defects and grain boundaries can sufficiently protect the underlying Cu surface [60,135]. The electrochemical characterization of the as-prepared Gr films on polycrystalline Cu (Gr/pCu) was carried out by cyclic voltammetry (CV). The Gr coatings on Cu were tested

by exposing it to deaerated acidic electrolytes (0.1 M $HClO_4$, 10 mM HCl, and 5 mM H_2SO_4) so that to understand in which conditions the material is stable.

In the adopted investigation procedure, the open-circuit potentials (E_{oc}) for bare and Gr coated Cu were monitored for 5 min until a stable potential was reached, after that CV tests were carried out. E_{oc} is the potential of the working electrode relative to the reference electrode when no net current is observed and/or no potential is being applied to the system, therefore it represents an equilibrium condition. However, if more than one electron transfer reaction takes place at the electrode surface, the open-circuit potential is a mixed potential defined by the kinetics of all simultaneous electrochemical reactions (metal deposition/dissolution and H_2 evolution or O_2 reduction, as typically found in corrosion). In the present case, E_{oc} measurements of similar samples showed slight fluctuations during a typical measurement, indicating the reproducibility and stability of the all investigated systems. Figure 33a-c shows the cyclic voltammograms of Gr on polycrystalline Cu recorded in deaerated 0.1 M $HClO_4$, 10 mM HCl and 5 mM H_2SO_4 electrolytes. These curves were obtained starting the potential sweep from the $E_{oc} \approx 0.2 \div 0.25$ V vs. RHE, in the cathodic direction (forward scan), to a lower limit ($E_{LL} \approx -0.45 \div -0.55$ V vs. RHE) where hydrogen evolution reaction (HER) occurs. Subsequently the potential sweep was inverted for scanning in the anodic direction (backward scan) to an upper value where Cu starts to dissolve ($E_{UL} \approx 0.25 \div 0.40$ V vs. RHE), and then was swept back to the initial starting potential. The results for the bulk polycrystalline copper was also reported since it served as a reference for evidencing possible changes in the electrochemical behavior. This was a crucial point for our experiments, as the corrosion of copper is heavily dependent on the environmental conditions, such as temperature, pressure and composition of atmosphere [136].

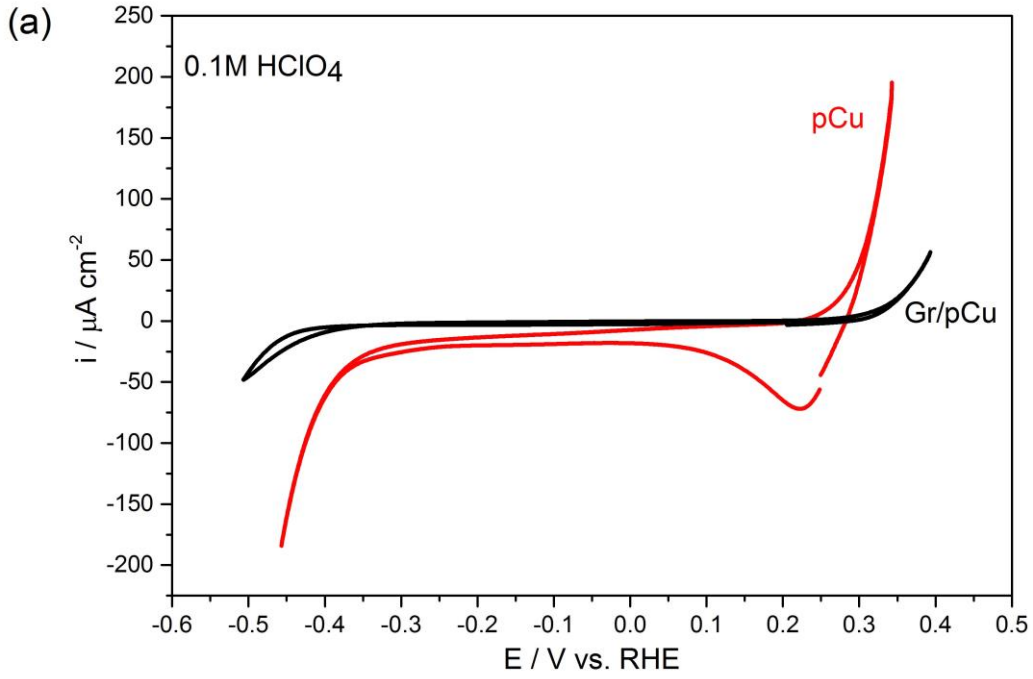

Figure 33a. Cyclic voltammograms of Gr on polycrystalline Cu (Gr/pCu) in 0.1 M $HClO_4$ (scan rate: 10 mV/s).

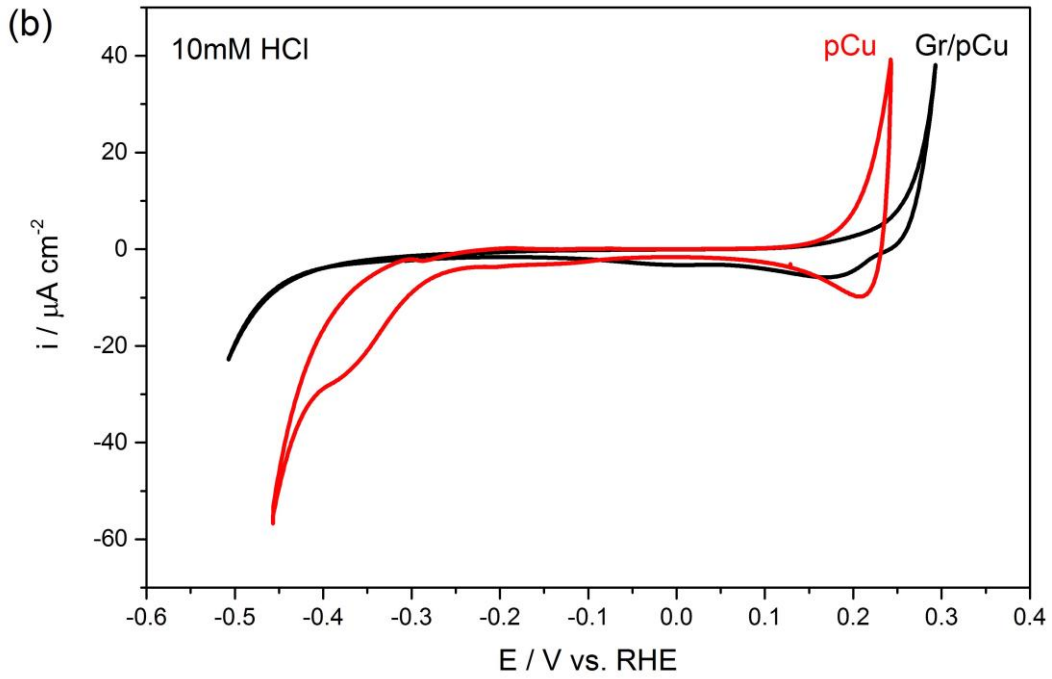

Figure 33b. Cyclic voltammograms of Gr on polycrystalline Cu (Gr/pCu) in 10 mM HCl (scan rate: 10 mV/s).

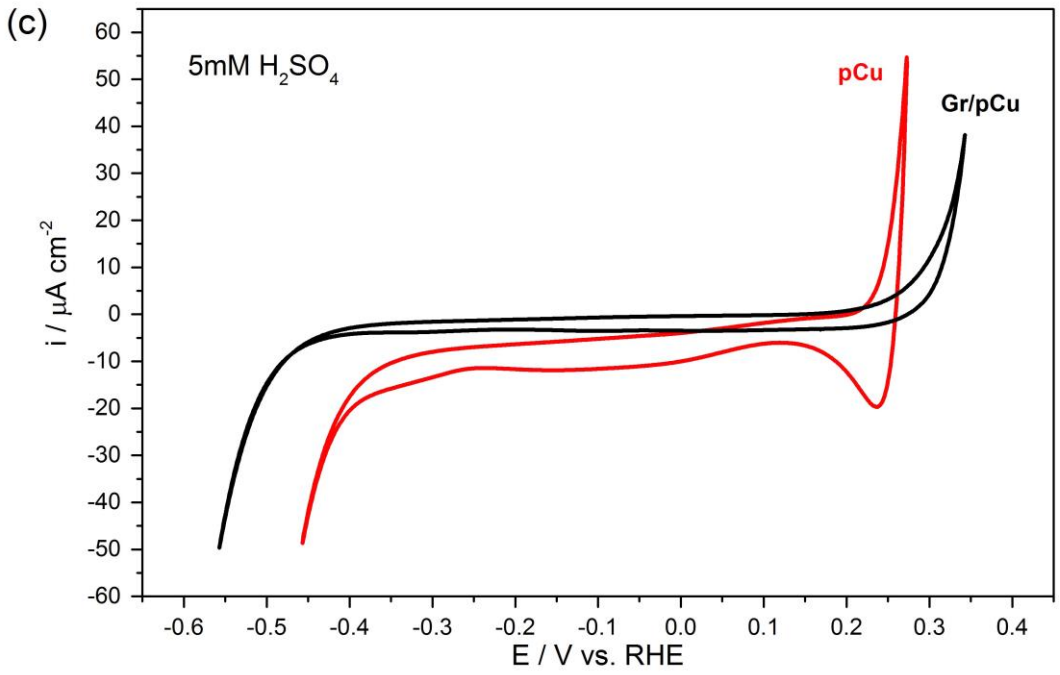

Figure 33c. Cyclic voltammograms of Gr on polycrystalline Cu (Gr/pCu) in 5 mM H_2SO_4 (scan rate: 10 mV/s).

CVs for Gr/pCu show a wider accessible potential window in all electrolytes with respect to the bare pCu electrode (around 0.7 ÷ 0.8 V). The onset potential of HER for Cu in all acids is around -0.35 V due to the similar pH value of the solutions. Gr films produce higher overvoltage for the HER with onset potential (-0.4 ÷ -0.5 V) as well as the dissolution of bulk copper that starts at more positive potentials, when the Gr layer is present. A wide available potential window is typical for Gr and all the carbon electrode materials [137]. A second aspect that must be taken into account is a very small capacitive current (-3.2 ÷ -3.5 µA/cm^2), which is common for graphitized carbon materials especially HOPG with more ordered structure and lower number of defects [138–141].

In all the three cases, it is evident that the Gr layer protects the Cu surface and remains attached to the surface even after the electrochemical experiments. This is confirmed by Raman spectra recorded before and after the electrochemical measurements as reported in Figure 34, where Raman spectra before and after electrochemical experiment evidence the same vibrational fingerprint.

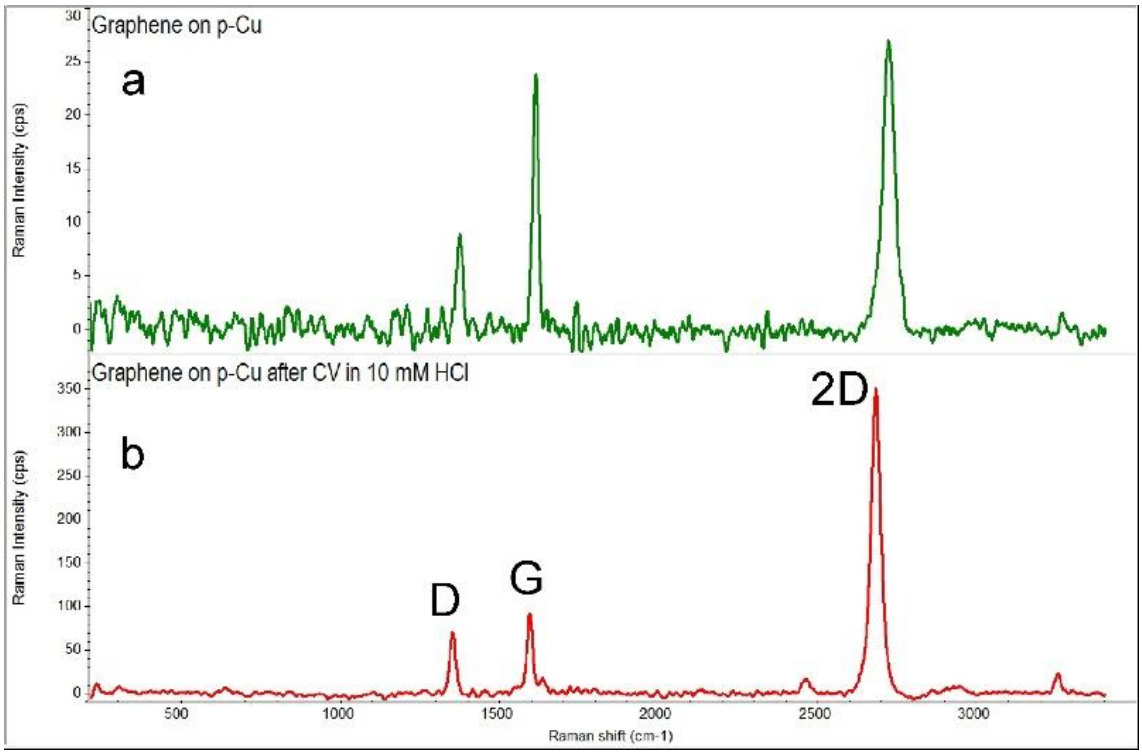

Figure 34. Raman spectra of the Gr/pCu before (a, green line) and after (b, red line) the electrochemical experiments in 10 mM HCl.

Figure 35 shows difference in the CVs of fully and partially covered Cu by Gr layer. Partially covered sample, confirmed by SEM image of Figure 35c, presents large copper areas exposed to the electrolyte. It is clear from the comparison between the CVs, measured on fully and partially covered sample, that the potential window is wider as long as the Gr covers the pCu surface otherwise HER and Cu dissolution are anticipated at more positive and negative potential, respectively (Figure 35a).

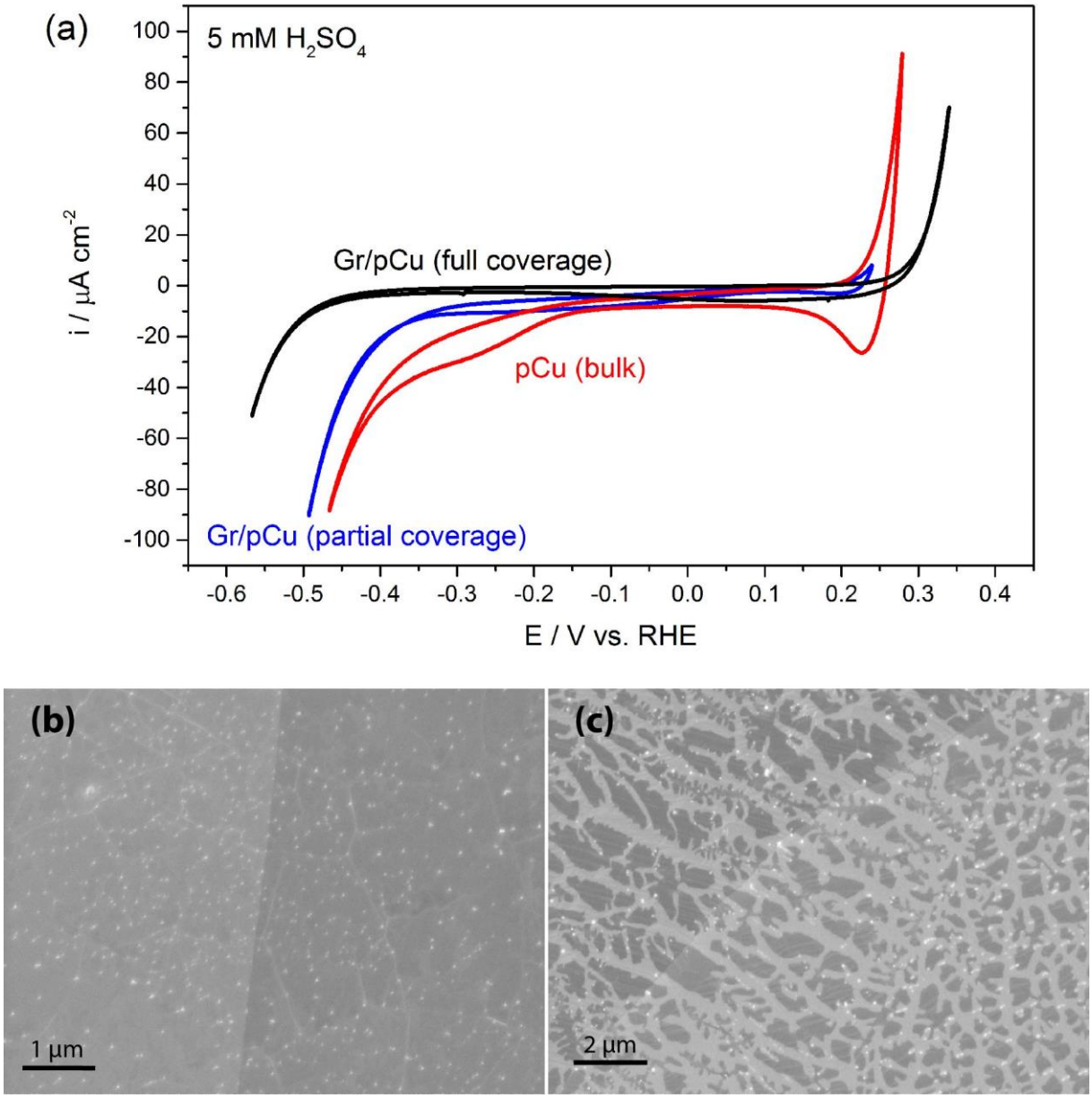

Figure 35. (a) Cyclic voltammograms of Gr/pCu with full coverage (black line) and partial coverage (blue line) in in 5 mM H_2SO_4. (Scan rate: 10 mV/s); SEM images of fully covered (b) and partially covered (c) samples.

To evaluate the long-term corrosion barrier characteristics, the as-grown Gr/pCu sample was kept in a 5 mM H_2SO_4 solution at room temperature for 16 hours. Figure 36a shows the CV of the as-prepared Gr/pCu (black line) and Gr/pCu sample after 16 hours (blue line). It is evident that after the aging period in H_2SO_4, the CV of Gr/pCu resembles that of bulk polycrystalline copper (red line). This indicates that 16 hours were enough for the solution to intercalate between Gr and pCu, and later decouple the Gr flakes from the surface and dissolve them into the solution. It is worth mentioning that during the aging, the

deaerated electrolyte was sealed in the cell but it was not degassed continuously, so traces of oxygen from the air could dissolve in the solution and accelerate the corrosion of the copper substrate. The complete absence of Gr on the Cu substrate was confirmed also by Raman spectra measured after the aging treatment of the Gr/pCu sample for 16 hours in 5 mM H_2SO_4, which doesn't show any typical peaks of Gr, (see Figure 36b).

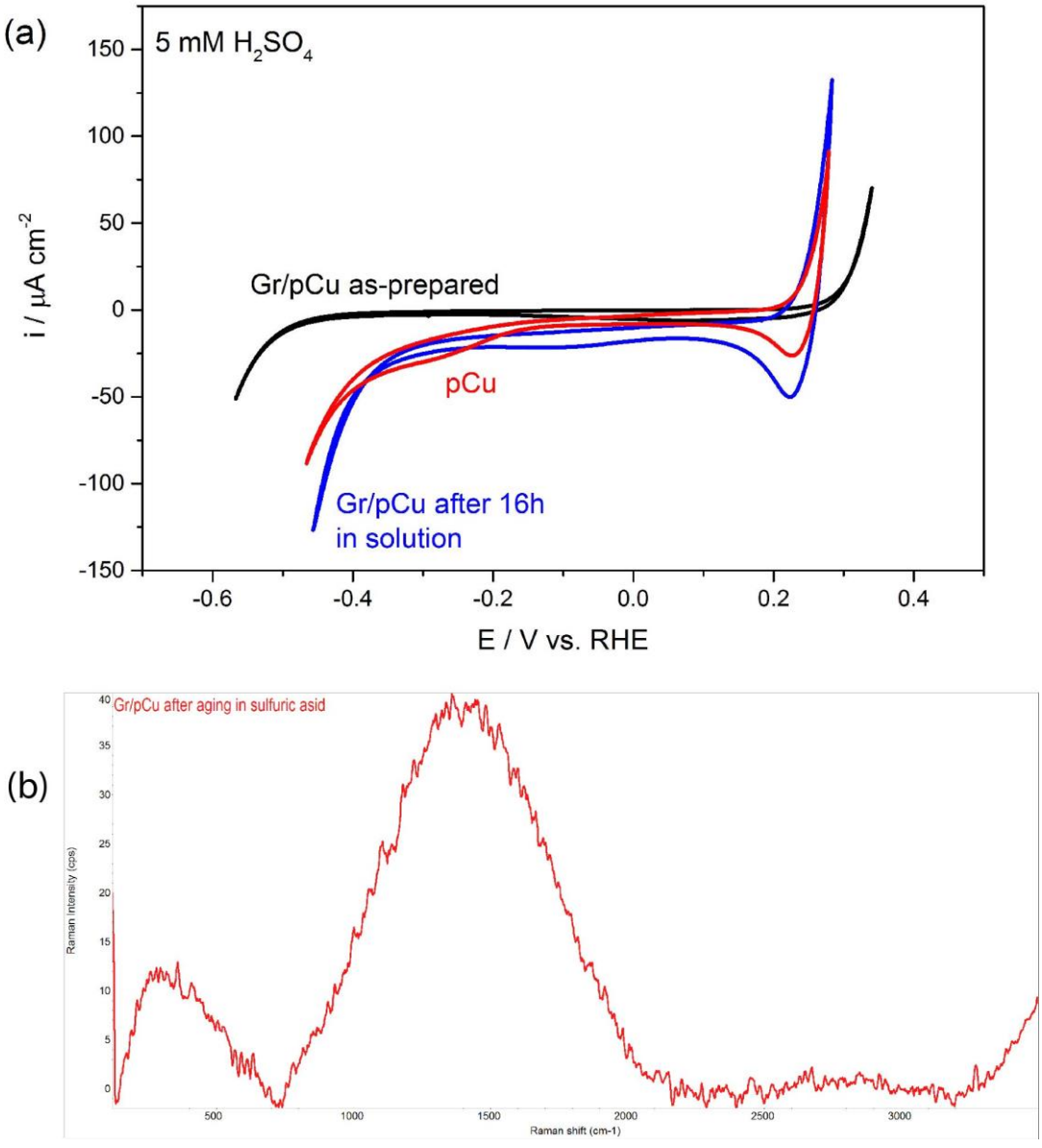

Figure 36. (a) Cyclic voltammograms of bulk pCu (red line); as-prepared Gr/pCu (black line) and Gr/pCu sample after 16 hours in 5 mM H_2SO_4. (Scan rate: 10 mV/s). (b) Raman spectrum of Gr/pCu sample after 16 hours in 5 mM H_2SO_4.

The corrosion behavior of Gr films on the Cu surface in aqueous solutions was characterized by determining the corrosion potential (E_{corr}) and the corrosion current (i_{corr}),

that were calculated from the Tafel plots analysis of cyclic voltammetry measurements. The anodic and cathodic polarization curves for the corrosion of bare pCu (red line) and Gr/pCu (black line) in different electrolytes are shown in Figure 37. All the measurements were corrected by IR ohmic drop, due to electrolyte resistance, to avoid nonlinear Tafel behavior at high currents.

The E_{corr} is the E_{oc} experimentally determined when other chemical reactions than metal oxidation/reduction are in act, such as oxygen reduction or H_2 evolution and therefore the potential shift from the $E_{M^+/M}$ equilibrium potential to a mixed potential (E_{corr}). When $E = E_{corr}$ the system dissolves at a rate given by the corrosion current i_{corr}. In general, E_{corr} of an electrode is a parameter that tells about the thermodynamic tendency of that metallic materials to be involved in corrosion reactions with the surrounding medium. Materials with more positive E_{corr} are more stable than those with more negative E_{corr}. Thus, a system with more negative E_{corr} has a higher tendency to participate in the corrosion reactions, whereas more positive E_{corr} is typically found in corrosion protected systems.

The cathodic curves in Figure 37 show the presence of two linear regions and a limiting current between them. For copper in deaerated acids, where HER is the only possible reaction, the linear region with slope 120 mV/dec is predicted [93]. Our measurements show that the upper linear region (low overvoltage) has Tafel slope in the range 150 ÷ 192 mV/dec which is higher than in deaerated solutions. The higher values can be explained by another cathodic reaction such as reduction of copper oxides from the surface. The cathodic Tafel slope values of the lower linear region are in the range 115 ÷ 136 mV/dec for both bulk Cu and Gr/pCu samples, which indicates chemisorption of the proton and its discharge to be the rate-limiting step. These values are in agreement with other workers, who obtained similar cathodic polarization curves for corrosion of copper in deaerated acid solutions [142].

The anodic Tafel slope values for Cu and samples covered with Gr are different. In case of uncovered samples the values for perchloric and sulfuric acids are around 31 ÷ 37 mV/dec and slightly higher for HCl solution 47 mV/dec which is in great agreement with literature [93]. Samples covered with Gr instead show higher value 85 mV/dec in all three acids which tells as about slight different mechanism of copper dissolution in presents of Gr layer on the surface.

The E_{corr} of Gr coated Cu was around 60 ÷ 100 mV more negative than bare Cu sample (Table 3). The E_{corr} shifts toward less noble values indicates that the Gr coating acts as a cathode in the galvanic couple [60,143]. Since E_{corr} measures the general tendency of a system to be corroded, the shift in E_{corr} toward more negative values indicates that the Gr coating should decrease the thermodynamic stability of the Cu substrate. This phenomena was initially unexpected, since the coating of a metal surface usually leads to the ennoblement of the open-circuit potentials (shift to positive value), and this was the general observation for copper electrode coated by polypyrrole or multilayer graphene [144–146]. However, these findings are fully in agreement with what reported by Kirkland et al. [147], which investigated polycrystalline copper coated by a single or few layers of Gr, where a shift of E_{oc} to less noble value was observed.

The i_{corr} is a measure of the corrosion rate can be determined by the extrapolation linear Tafel region of either the cathodic or anodic polarization curve [148]. Both pCu and Gr/pCu anodic branch shows a longer and better defined Tafel region since the anodic part of the potentiodynamic polarization plot is constant over a decade of current density. On the other hand, the cathodic polarization curves show some deviations from Tafel behavior, also because of the influence of HER. The anodic linear Tafel region is extrapolated back to the E_{corr} to give the net rate of the anodic reaction at the corrosion potential, i.e. the i_{corr} and the derived corrosion current density, j_{corr}. The corrosion rate, v_{corr}, was then calculated using j_{corr} values according to eq. (23):

$$V_{corr} = j_{corr}\, W / \rho\, F \qquad (23)$$

Where W is the equivalent weight, that is 31.7 g for Cu, ρ is the material density (8.94 g/cm^3 for Cu), F is the Faraday's constant, (96485 C/mol) and the sample area, A, is 0.125 cm^2. All corrosion rates were expressed as millimeters penetration per year (mm/yr).

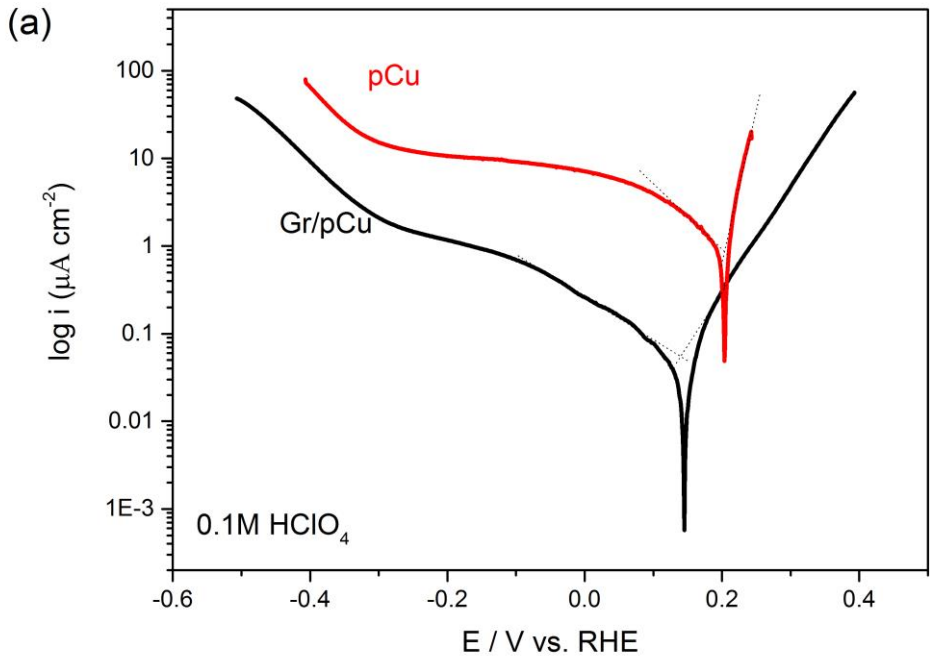

Figure 37a. Polarization curves on the positive going sweep on polycrystalline copper (red lines) and copper covered with graphene layer (black lines) in 0.1M $HClO_4$.

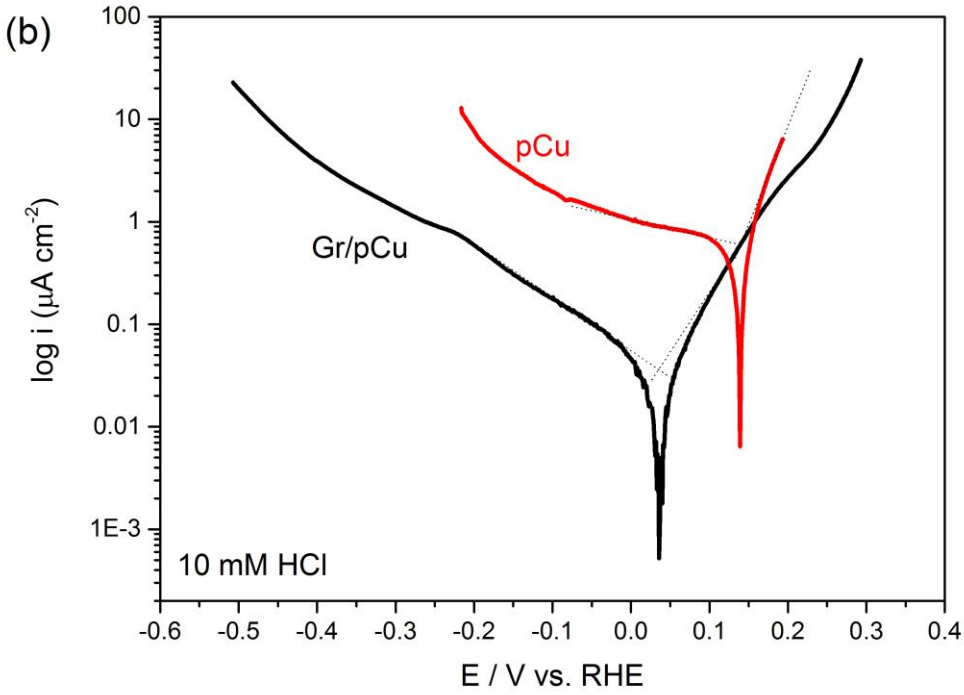

Figure 37b. Polarization curves on the positive going sweep on polycrystalline copper (red lines) and copper covered with graphene layer (black lines) in 10 mM HCl.

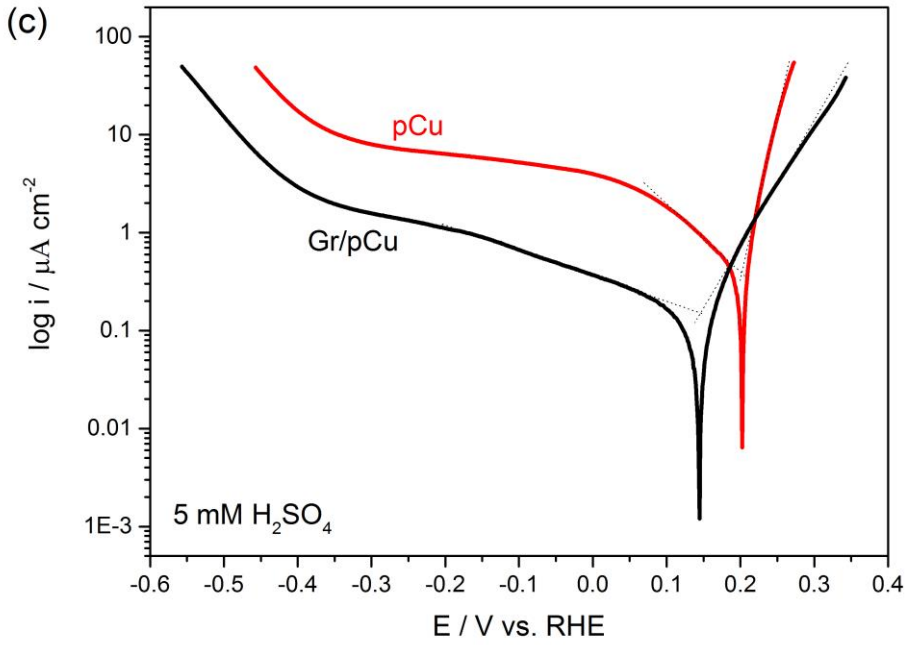

Figure 37c. Polarization curves on the positive going sweep on polycrystalline copper (red lines) and copper covered with graphene layer (black lines) in 5 mM H_2SO_4.

From the polarization curves in Figure 37 and data in Table 3, a slight difference in term of bulk pCu i_{corr} was observed between different acids. The corrosion rate in 0.1 M $HClO_4$ electrolyte was the highest (more than 2 time higher than in HCl solution and 3 times than in H_2SO_4), possibly due to the different pH of the electrolytes (cathodic effect) [93]. Slightly higher corrosion rate of pCu in 10 mM HCl electrolyte comparing with that in 5 mM H_2SO_4 (Table 3) is a result of different mechanisms of Cu dissolution in these acids, in fact, in oxygen free sulfuric acid, Cu dissolves to form Cu^{2+} ions [149] whereas in dilute hydrochloric acid copper creates soluble $CuCl_2^-$ complex with Cl^- ions [93].

Table 3. Corrosion rate of pCu and Gr/pCu samples in different acids.

Electrolyte	Sample	E_{corr}, V vs.RHE	i_{corr}, A/cm^2	v_{corr}, mm/yr
0.1 M $HClO_4$	Gr/pCu	+0.143	1.17×10^{-6}	0.014
	pCu	+0.202	9.04×10^{-6}	0.105
10 mM HCl	Gr/pCu	+0.037	1.09×10^{-6}	0.013
	pCu	+0.136	4.09×10^{-6}	0.047
5 mM H_2SO_4	Gr/pCu	+0.144	1.42×10^{-6}	0.016
	pCu	+0.2	2.49×10^{-6}	0.029

When bulk polycrystalline pCu was covered with Gr, the free corrosion currents observed at Gr/pCu in the $HClO_4$, HCl and H_2SO_4 were lower than at pCu, which in turn end up in lower corrosions rates, with a concomitant negative shift in the E_{corr} of approximately 100 mV. (Table 3). Therefore, the underlying copper has a higher tendency to corrode when protected by graphene, but the kinetic is lower than in bare copper.

Some works in the literature report that the faster oxidation of copper underlying Gr layer than on bare Cu electrode is due to the high electrical conductivity graphene. Zhou et al. suggest that in the presence of a Gr coating, the electrons generated in the copper oxidation reaction could be rapidly transported to the Cu_2O/graphene/air interface thus promoting O_2 reduction. In the present case, the graphene layer is in contact with an electrolyte solution where the O_2 concentration is by far lower. Furthermore, Gr is not a good catalyst for O_2 reduction, therefore, it may be concluded that even though E_{corr} is less noble than in uncovered copper, the inhibition of O_2 reduction results in the decrease of the anodic reaction rate as observed in the polarization curves for Gr coated Cu samples. Therefore, in this case the Gr is acting primarily as an inhibitor of the cathodic reaction, which is in contrast to the dominant mechanism acting upon other metals such as Ni surface where Gr slows the kinetics of Ni ionization [147]. However, once Gr is removed, the corrosion current of the pCu increases sharply and the intersection point of the Tafel plot shifts from the corrosion potential of the Gr/pCu film (black line) to that of the bare pCu (red line in Figure 37).

In order to achieve further information about the stability of Gr on Cu in acidic solution, *in situ* Raman spectroscopy (514 nm laser) experiments were performed. Raman spectra recorded after cycling Gr/pCu sample in 0.1 M $HClO_4$ in a suitable potential windows, show that the Gr layer remains attached to the Cu surface after the contact with ClO_4^- electrolyte and also after cycling the potential between the potential window comprised by HER and Cu dissolution (Figure 38a).

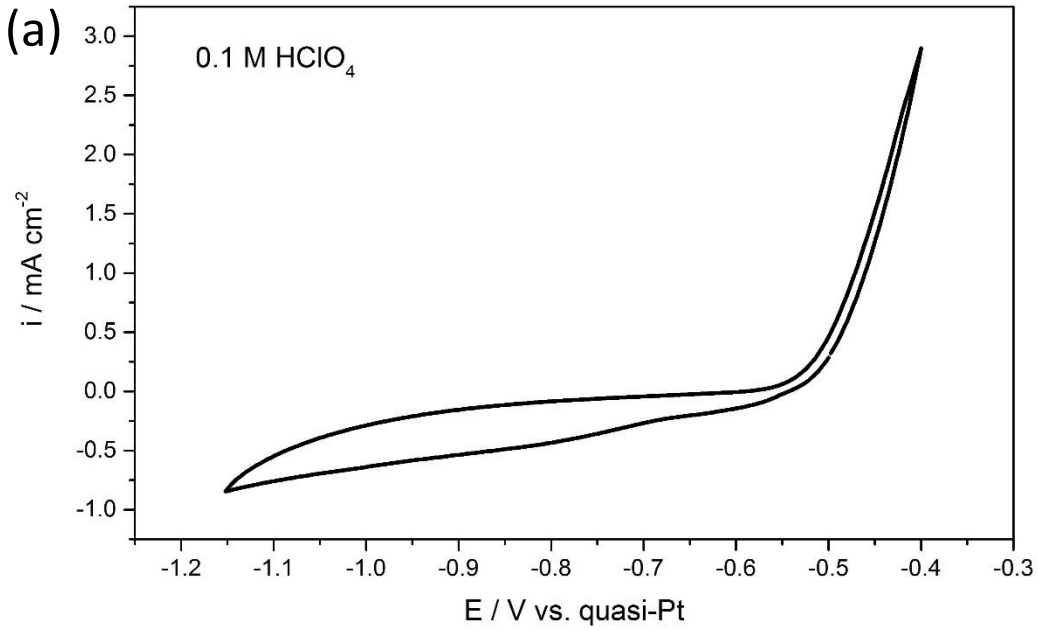

Figure 38a. CV on Gr/pCu in 0.1 M $HClO_4$ (scan rate: 20 mV/s).

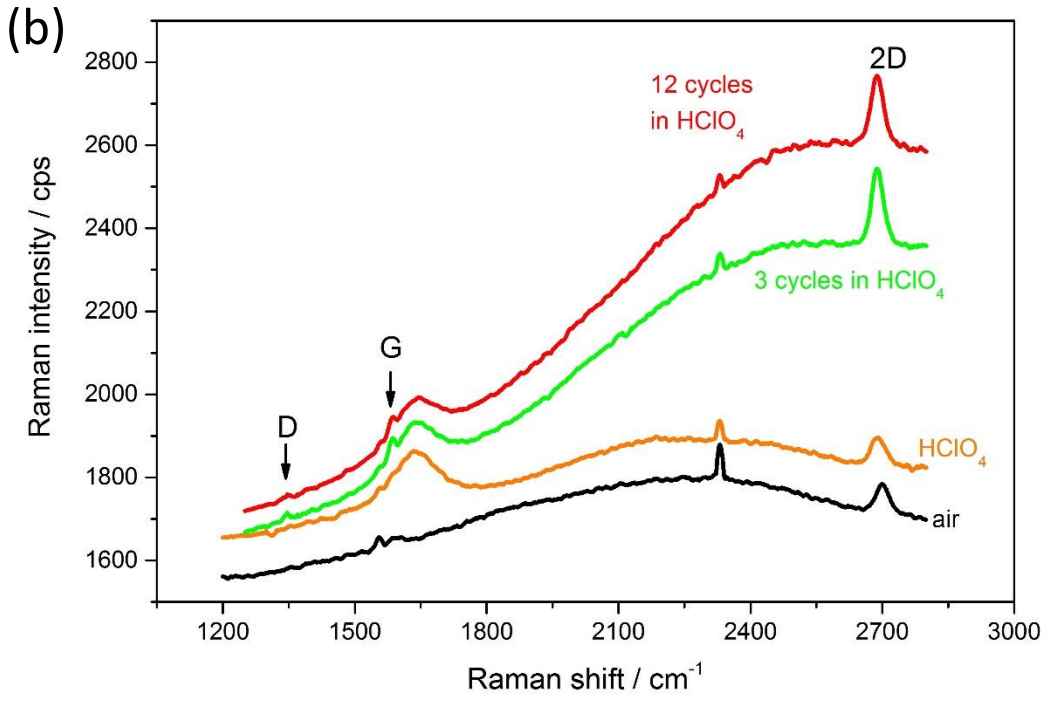

Figure 38b. *In situ* Raman spectra before and after CV.

After the contact with the electrolyte solution, the height of Gr bands remains almost the same like when Gr/pCu is exposed to air (orange line in Figure 38b). The G band at

$\sim$1590 cm^{-1} is covered by a broad peak (around 1639 cm^{-1}) due to the electrolyte and 2D band is red shifted. The D band at $\sim$1360 cm^{-1} is absent on both spectra, measured in air and in electrolyte respectively. After 3 CV cycles in $HClO_4$ (Figure 38a) the intensity of the 2D band increases and the D band appears on the Raman spectra (green line in Figure 38b). Changes in the Raman spectra after the cyclic voltammetry can be explained by the intercalation of the solution between Gr and Cu in the points of defects or grain boundaries, where reaction of copper dissolution takes place.

4.3. STM investigation of G on Cu in air

Scanning tunneling microscopy investigations were carried out on Gr layers deposited by chemical vapor deposition on both polycrystalline copper and Cu(111). The Gr/Cu samples, prepared by LPCVD, were transferred to the EC-STM system for the surface morphology investigation. The transfer involves the unavoidable exposure of the sample to ambient air, therefore, it is possible that the bare regions of Cu, where the Gr film exhibits local discontinuities are subjected to oxidation. Furthermore, formation of copper oxide during the CVD process under non-perfectly controlled UHV conditions, cannot be excluded. Copper oxides grown amid copper grain boundaries or on the bare copper surface have an amorphous disordered structure resulting in a very rough surface, that quite hard to scan with STM because of the high probability of tip crash. Conversely, the regions covered by the Gr layer maintains the flat morphology of the underlying crystalline Cu surface, and this allows to scan the surface with high sensitivity, obtaining highly resolved images of atomic steps.

Typical STM topographic images of as-deposited Gr on Cu(111) (Gr/Cu(111)) recorded in air are shown in Figure 39a. STM images were acquired at room temperature, and the use of different tunneling parameters shows in all cases very similar atomic features. The STM operated in the constant current mode; typical settings for STM data acquisition were tunneling current of about 1 ÷ 1.8 nA at a bias voltage from -500 to +500 mV. It is important to emphasize that most of the STM images presented in this work have been observed in more than three separate experiments. Large-scale image (726 nm × 726 nm) shows that the whole surface is covered by large Gr domains, resulting in atomically flat terraces (surface

areas of 300 ÷ 500 nm^2) that are suitable for the STM investigations (Figure 39a). The Gr domains mostly ends at Cu step-edges, but sometimes they can extend even over Cu step-edges [97]. Rasool et al. also showed that Gr grown on polycrystalline copper had continuity over Cu terraces and step-edges [150].

Figure 39b shows an exposed Cu(111) surface covered with amorphous copper oxide. An STM image of a Cu(111) surface partially coated with Gr is displayed in Figure 39c. The upper left part of the image is the uncovered Cu surface, whereas the lower right flat terraces are covered with Gr. The difference between Gr covered and uncovered region is evident, emphasizing the high roughness of amorphous copper oxide (Figure 39b and c).

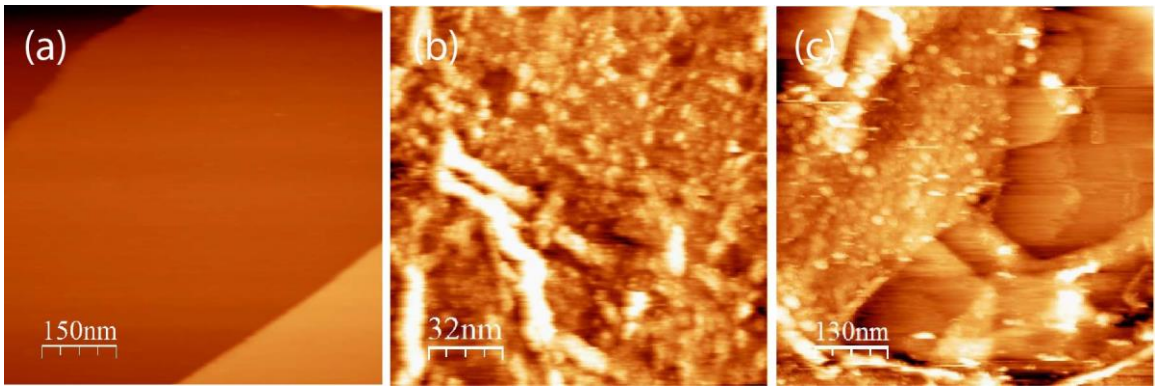

Figure 39. Topography STM images (a) Gr on Cu(111) (I_t = 1.8 nA, V_b = -82 mV); (b) uncovered parts of Cu(111) (I_t = 1 nA, V_b = -195 mV); (c) partially covered Cu(111) by Gr (I_t = 1 nA, V_b = -109 mV).

The STM images of Gr are characterized by a complex contrast which depends on the interference between the electronic states of carbon atoms with those from the metal substrate underneath. The STM images with high atomic resolution (Figure 40) clearly show the hexagonal Moiré pattern that is caused by interference effects between upper carbon lattices and (111) facets of Cu. In the present case the Moiré structure shows an in-plain periodicity around 2.0 ± 0.4 nm, and at the same time the primitive honeycomb lattice of Gr (the original image is somewhat distorted by a uniform thermal drift during scanning, so it was corrected). The slight elongation of the hexagonal lattice could be attributed to thermal and electro-mechanical drifts in the STM and to a possible slight mismatch in the calibration of the x and y translators.

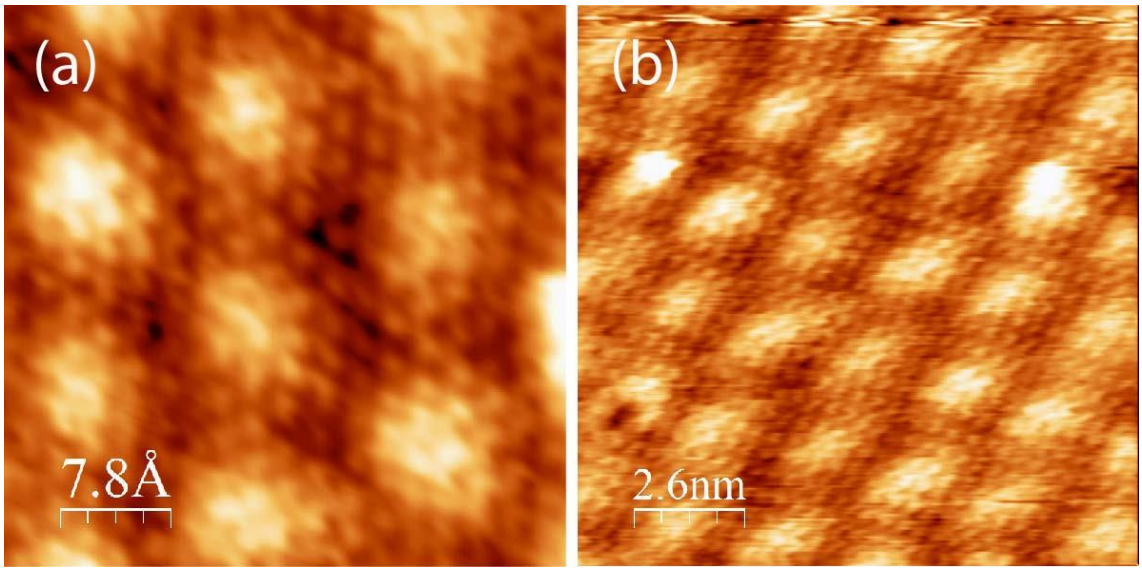

Figure 40. High-resolution STM images of the Gr on Cu(111) in air (I_t = 1.8 nA; V_b = +136 mV); a – corrected (drift and scanner) and b – original image, respectively.

The presence of the Moiré can be used as an indicator to determine the quality of the Gr layer. We find that the vast majority of the samples show one preferred orientation of the Gr domains. This results is also compatible with the previous LEED data (Figure 32), that shows a clear preference of the Gr layer to align with specific directions of the copper substrate. This result is also in agreement with previous ultrahigh vacuum surface STM studies reported by other groups for Gr grown on Cu in UHV [97,99,151]. Gao et al. reported two dominant domains showing two different Moiré patterns with 6.6 nm and 2.0 nm spacing, respectively, where the Gr lattice is rotated by 0° and 7° with respect to the Cu(111) substrate. The interatomic distance between two nearest neighbour *a* is around 2.9 Å which is similar to the Gr lattice (2.46 Å) [7]. Zhao et al. report that Gr grows primarily in registry with the underlying Cu(111) substrate lattice [151]. A schematic hard-sphere model to illustrate the formation of Moiré patterns on Cu(111) is given in Figure 41. Atomic resolution topography in air was the first step to identify Gr layer on the surface of Cu. The Gr, grown directly on copper surface by LPCVD is not completely defect-free at the nanoscale. Besides the observation of Gr on terraces, other obvious surface features that can be easily imaged are some dark lines that are several hundred nanometers long and ~1.7 Å thick of average (Figure 42). Such features are likely connected to grain boundaries of the Gr film.

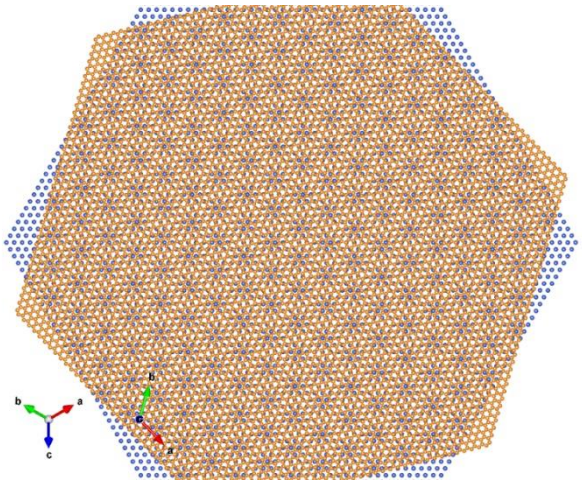

Figure 41. Schematic hard-sphere model of Moiré pattern of Gr on Cu(111). (blue balls are copper atoms; orange balls are carbon atoms).

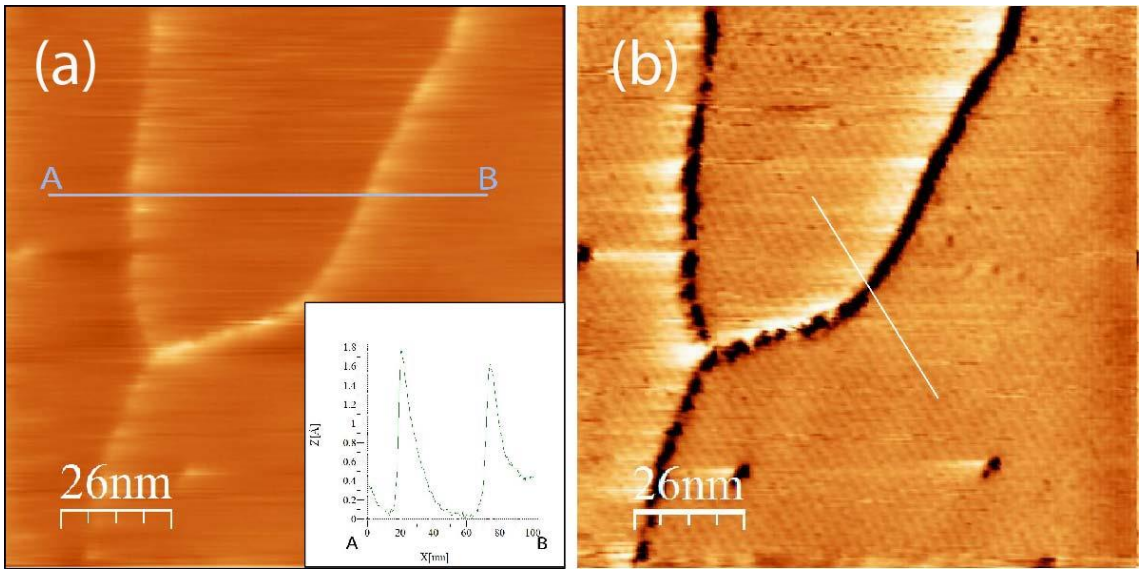

Figure 42. STM images of the grain boundaries of the Gr on Cu(111).

Topographic and current STM images of such morphological features are shown in Figure 42a and b, respectively. It seems that different Gr grains have the same orientation (white line on Figure 42b).

Figure 43 presents another typical white defects (corrugated bright protrusions) on Gr/Cu(111) surfaces with lateral dimensions of 10-15 nanometers. The nature of these defects is not completely clear. The possible reason for the formation of such features on the surface could be low H_2 gas flux and the time of annealing, that resulted in a high density of copper oxide residues, which remained on the surface during the growth of Gr. High

quality of Gr on Cu(111) with I_D/I_G ratio lower than 0.3 was obtained in wide range of temperatures from 830 to 900°C, after annealing the CU(111) sample in the CVD chamber at a H_2 pressure of 2-3 mbar (Figure 43a). High I_D/I_G ratio (> 0.4) was typically observed if the pressure of hydrogen was not higher than 1 mbar (temperature 850°C) as shown on Figure 43b, c. At very low H_2 pressure (0.1 mbar) surface resulted covered with defects and I_D/I_G ratio was higher than 1 (Figure 43d and Raman spectra on Figure 43e).

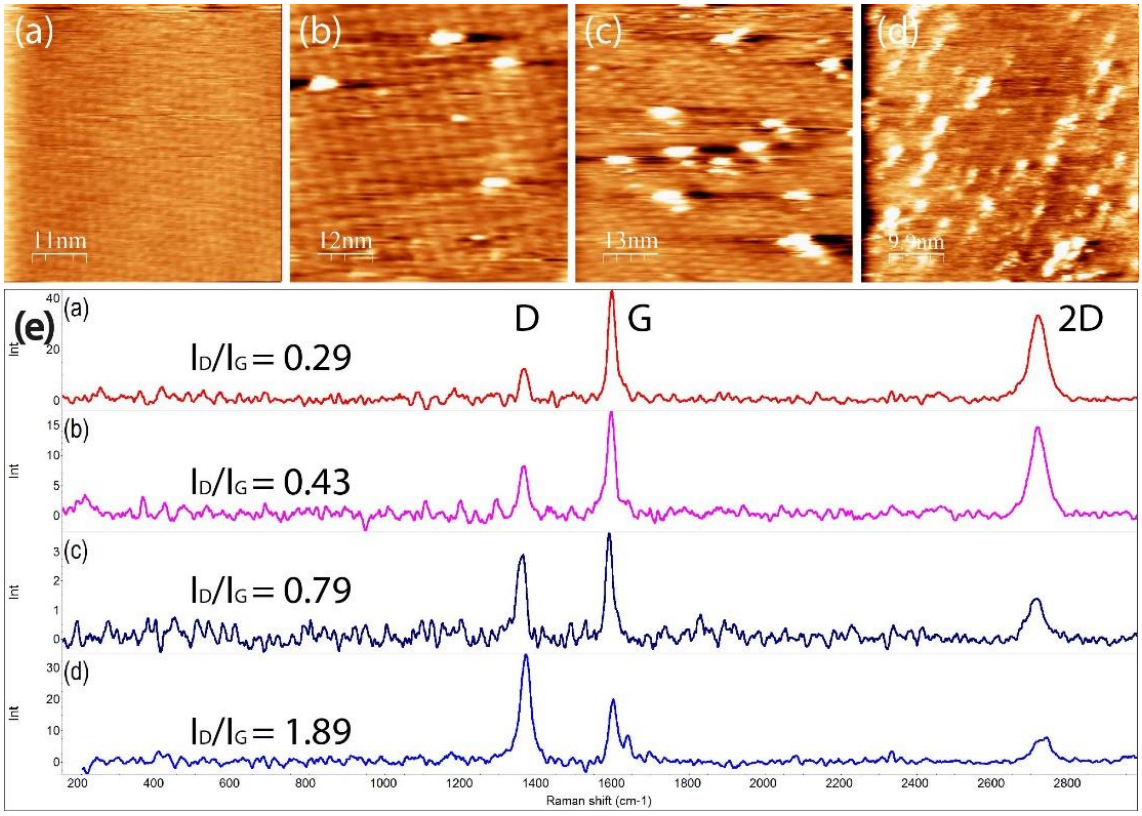

Figure 43. STM images of the defects on Gr/Cu(111) (523 nm, 5 mW, Cu background subtracted).

Topographic STM images of defective and clean Gr with good continuity of the film and low level of defects are shown in Figure 44a and b, respectively. The sample shown in Figure 44a presents high I_D/I_G ratio (0.55), whereas the one in Figure 44b has a low I_D/I_G ratio (0.2). The terraces of the sample with less defective Gr layer are much stable and the step-edges are sharp, conversely to the surface of the sample in Figure 44a where high number of edge defects are present. Figure 44b shows also the presence of wrinkles formed during the cooling down. The formation of wrinkles is due to the compressive stress of the Gr film arising from the different thermal coefficient of expansion between Gr and the underlying metal substrate [67]. An example of this type of defect can be observed on the Figure 44b.

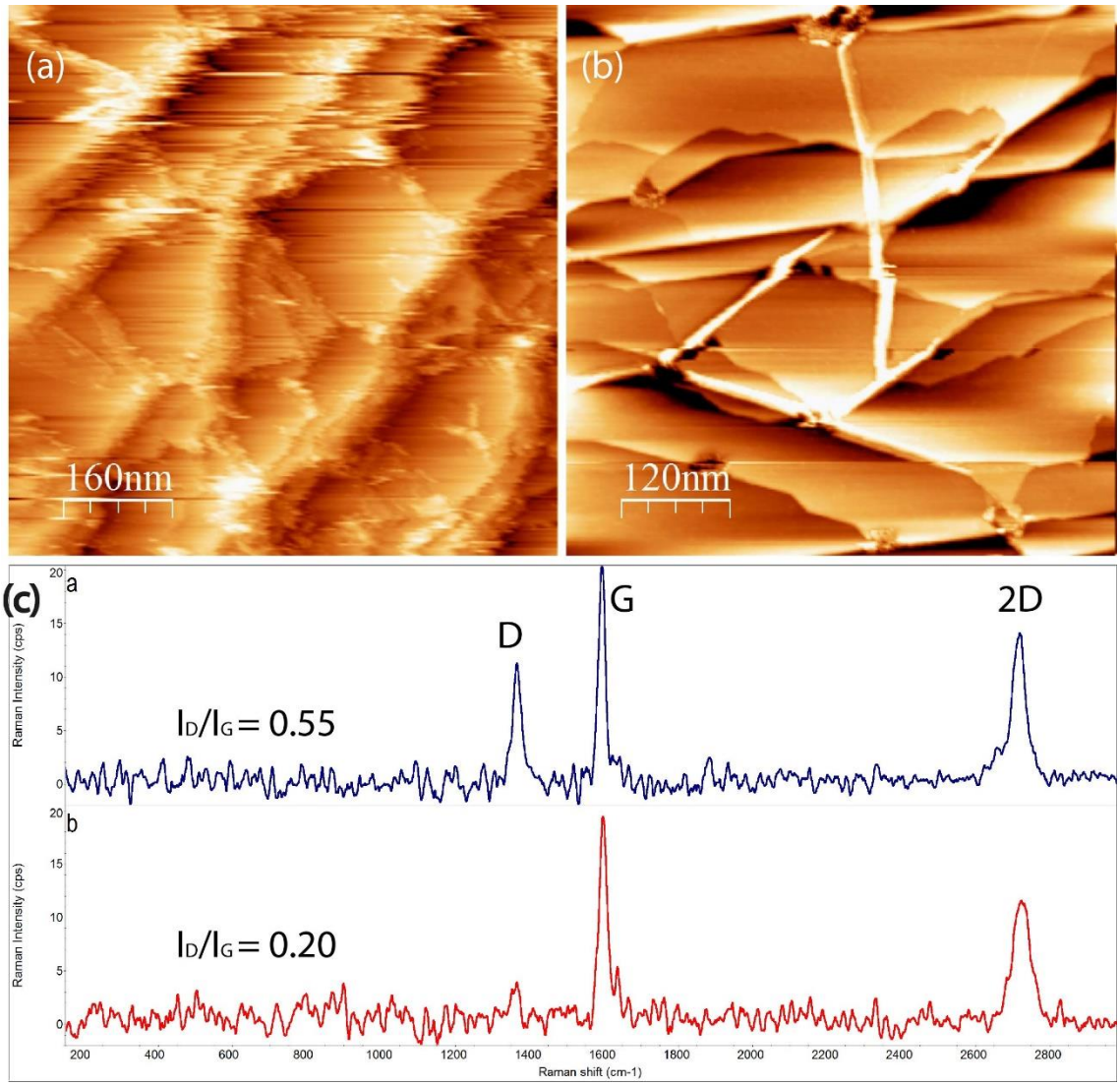

Figure 44. Topography STM images of Gr/Cu(111) in air with different I_D/I_G ratio: (a) 0.55; (b) 0.2.

Figure 45a demonstrates bright stripes passing through different copper terraces (marked with yellow arrow). From the magnified STM image in Figure 45b and the profile line in Figure 45c, it can be seen that this stripe has an average height of 1.6 nm and a width of 25 nm (marked by the white arrow in Figure 45b). These parameters are consistent with other studies of Gr wrinkles [67,152,153].

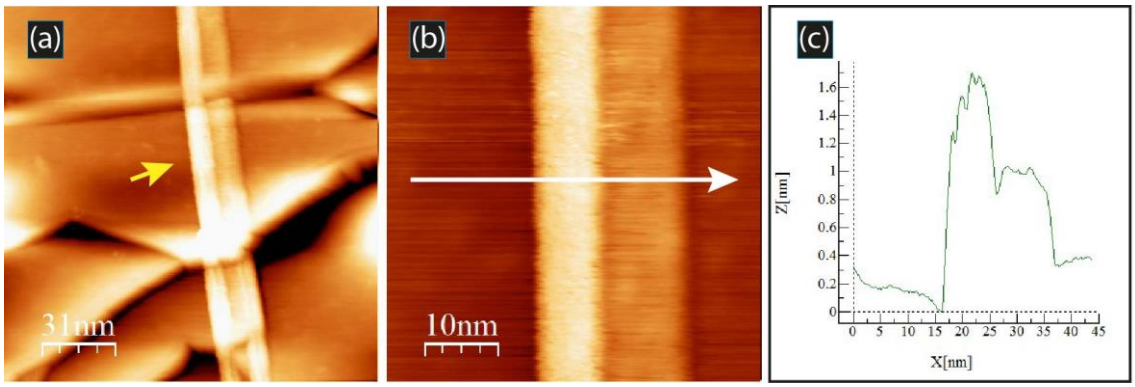

Figure 45. Topography (a) and high resolution (b) STM images of the Gr/Cu(111) in air (I_t = 1 nA; V_b = -302 mV); (c) profile line from the image (b) shown by white arrow.

4.4. STM investigation of graphene on copper in water

Figure 46b reports the STM Gr/Cu(111) image recorded on a sample covered with a drop of bi-distilled water. It is worth nothing that Moiré pattern with hexagonal lattice can be observed also in these conditions comparing to surface measured in air (Figure 46a). SEM image (Figure 46c) shows the partially covered surface of the copper sample with different grades of grey colour for the Gr domains and this is probably due to different thickness of Gr film. Raman spectra (Figure 46d) has no D band so this islands of Gr have very low amount of defects which is also proved by clean STM images in air and in water. After the contact of the surface with water, Raman spectrum shows much higher intensity of the characteristic graphitic peaks. This effect could be the result of copper oxidation under the Gr layer possibly due to the permeation of oxygen or water through the grain boundaries of Gr covering the Cu substrate [119]. In fact, low domain size (< 2 µm) of Gr and high density of grain boundaries allow water to intercalate between Gr and Cu while oxygen can diffuse under Gr film and create oxides with copper substrate. The resulting copper oxide can decrease the interaction between copper and carbon atoms [134], so the I_{2D}/I_G ratio increase from 0.64 to 1.5. The 2D peak was red shifted of 27 cm^{-1} from 2706 to 2679 cm^{-1}; the shift seems to be attributed to the compressive strain in Gr layer induced by the difference of thermal expansion coefficients of copper and Gr [119]. The D band increased so tah the I_D/I_G ratio increased from 0.12 of as-prepared Gr to 0.25, after the STM measurements in water.

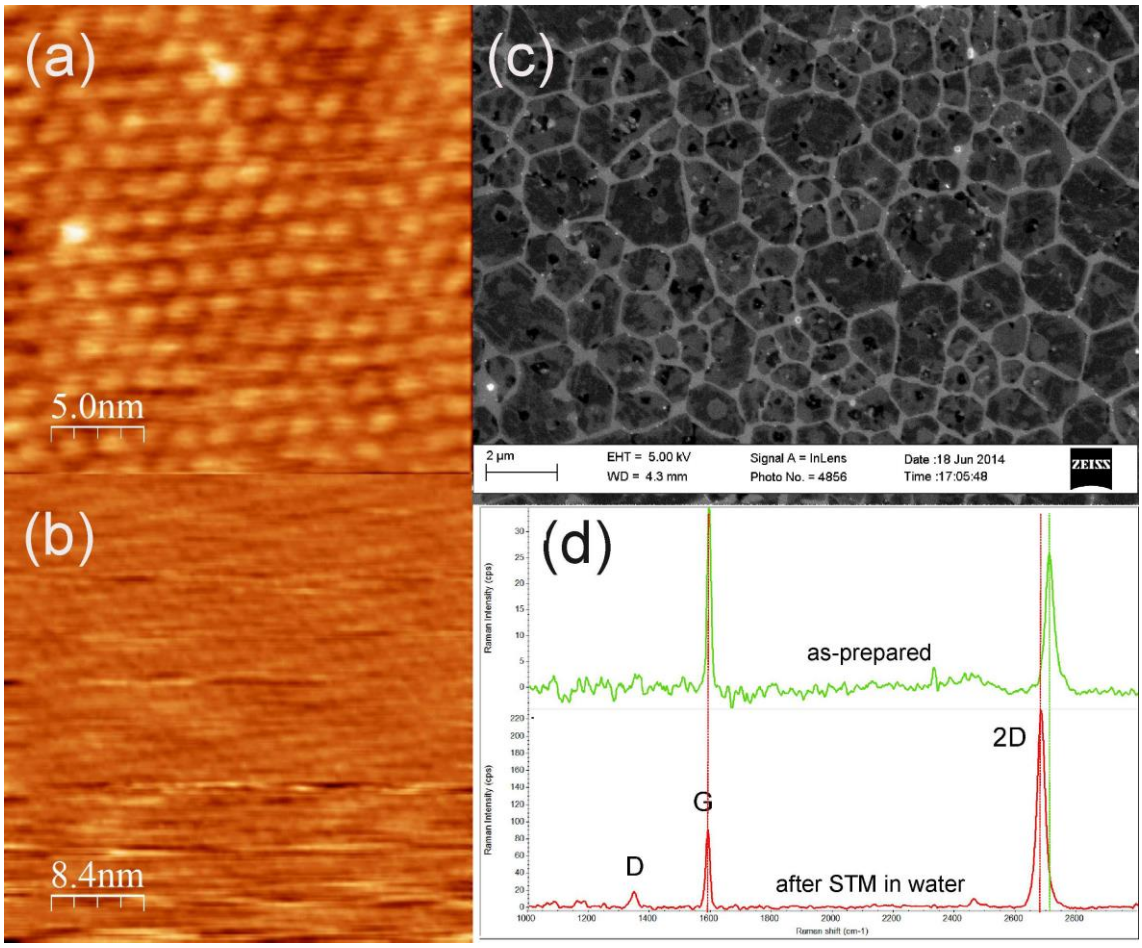

Figure 46. STM images of the Gr/Cu(111) a) in air (I_t = 1 nA, V_b = -138 mV); b) in water (I_t = 1nA, V_b = -189 mV; c) SEM image of the Gr/Cu(111); d) Raman spectra of as-prepared (green line) and after STM measurements in water (red line).

4.5. EC-STM measurements

For more detailed investigation of the electrochemical properties and processes that occur on the surface of Gr/Cu samples, CV combined with STM measurements in different aqueous electrolyte solutions were performed. The structure of Gr layers prepared by CVD on polycrystalline copper and single crystals in perchloric, hydrochloric, sulfuric acids and potassium hydroxide solutions have been investigated with EC-STM.

An internal calibration against the substrate lattice constant was not possible due to missing data of the free copper surface in the potential region where desorption processes occur. In fact, the transfer of the sample from CVD chamber and EC-STM apparatus involve the inevitable contact with air so that where the surface is not covered with Gr, copper oxide forms thus making impossible the acquisition Cu surface with atomic resolution.

Furthermore, it was not possible obtaining a Cu resolved structure even under electrochemical environment, where oxides could be removed by cycling the sample in the available potential window due to the increase of the surface roughness.

In acidic solutions (pH < 5), the dissolution of the anodic oxides is too fast to provide passivity and, consequently, the metal dissolves in the oxidation potential range and even at open-circuit potential. Imaging of as-prepared samples at open-circuit proved to be difficult due to the presence of oxide surface structures formed during the sample transfer from CVD chamber to EC-STM cell.

As was described in Chapter 2, all electrolytes were deaerated before the introduction in the electrochemical cell of EC-STM. But due to relatively low volume of the cell and respectively thin layer of the electrolyte above the sample some traces of oxygen of air could be dissolved during the process of STM measurements. Shown in the Figure 47 are series of CVs obtained for a Gr/Cu(111) film in a 5 mM H_2SO_4 recorded at room temperature at a scan rate of 10 mV/s in the range 0.4 ÷ -0.65 V vs. RHE. Cycling of the sample in cathodic region is removing the air-formed oxide film on the sample surface. Oxygen, presented in the fresh solution in the beginning of the experiments, if the top part of the STM set-up was opened, is reduced after couple of cycles.

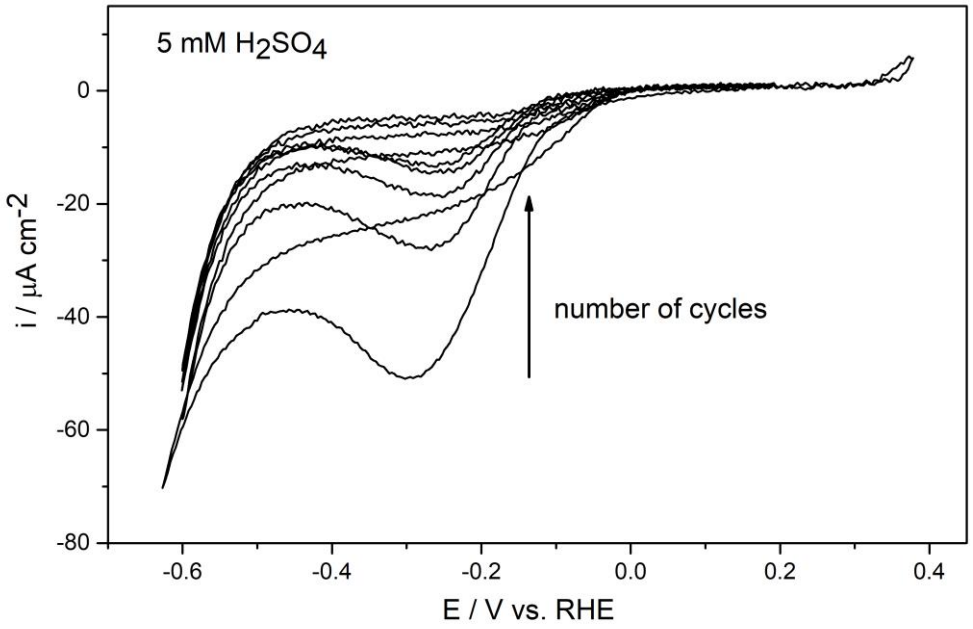

Figure 47. Cyclic volammograms of Gr/Cu(111) in 5 mM H_2SO_4 (scan rate: 10 mV/s).

4.5.1. $HClO_4$ electrolyte solution

In dilute perchloric acid solutions, the bulk oxides of copper are not stable according to the Pourbaix diagram [5]. Previous study of the clean Cu(111) surface, exposed to the $HClO_4$ acid electrolytes, reports CV with featureless double-layer region from -0.35 to 0.15 V vs. RHE. Anodic dissolution of the Cu(111) in 0.1 M $HClO_4$ starts at potentials more positive than 0.15 V, which is very close to the E_{oc} of the copper. Cathodic region is limited by HER at ca. -0.35 V [154,155]. The surface of the Cu(111) observed in this double-layer region was (1 x 1) structure without any adsorbed species. Th clean surface of Cu(111) in $HClO_4$ electrolyte without specific adsorption of ClO_4^- anions were also confirmed by Brisard et al. They showed that the oxygen reduction current on the Cu in $HClO_4$ is much higher than in H_2SO_4 solution, where surface is blocked by ordered sulfate adlayers [156].

In comparison, Friebel et al. reports the CV of Cu(111) in 0.1 M $HClO_4$ with pair of peaks at +0.25 and +0.15 V vs. RHE (O'/O), corresponding to the formation of a passivating oxygen-containing adlayer (Figure 48) [157]. They also observed a long-range hexagonal structure covering the entire Cu(111) surface which can be described by a (4 x 4) unit cell which is not rotated with respect to the unit cell of the bare Cu(111) substrate in the potential range between massive hydrogen evolution at -350 and -150 mV. Cu(111)-(1 x 1) were visible only in a small region from -0.15 to 0.05 V. The peak at -0.28 V vs. RHE in the Figure 48 marked as X was unclear to authors and wasn't described.

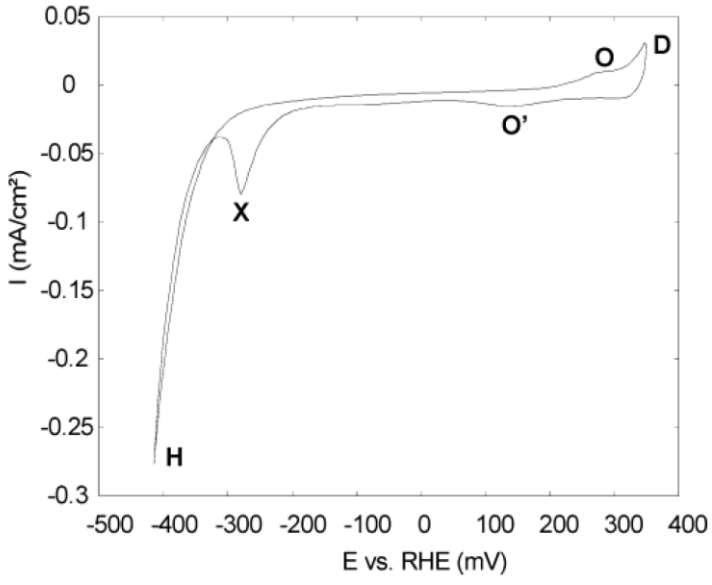

Figure 48. CV of Cu(111) in 0.1 M $HClO_4$ (scan rate: 10 mV/s) [157].

In this work first attempts of EC-STM measurements were carry out with Gr, deposited on polycrystalline copper as a support, in 10 mM $HClO_4$ solution. The cyclic voltammogram of a Gr/pCu electrode in aqueous 10 mM $HClO_4$ measured at a scan rate 10 mV/s in electrochemical cell of STM instrument is shown in Figure 49.

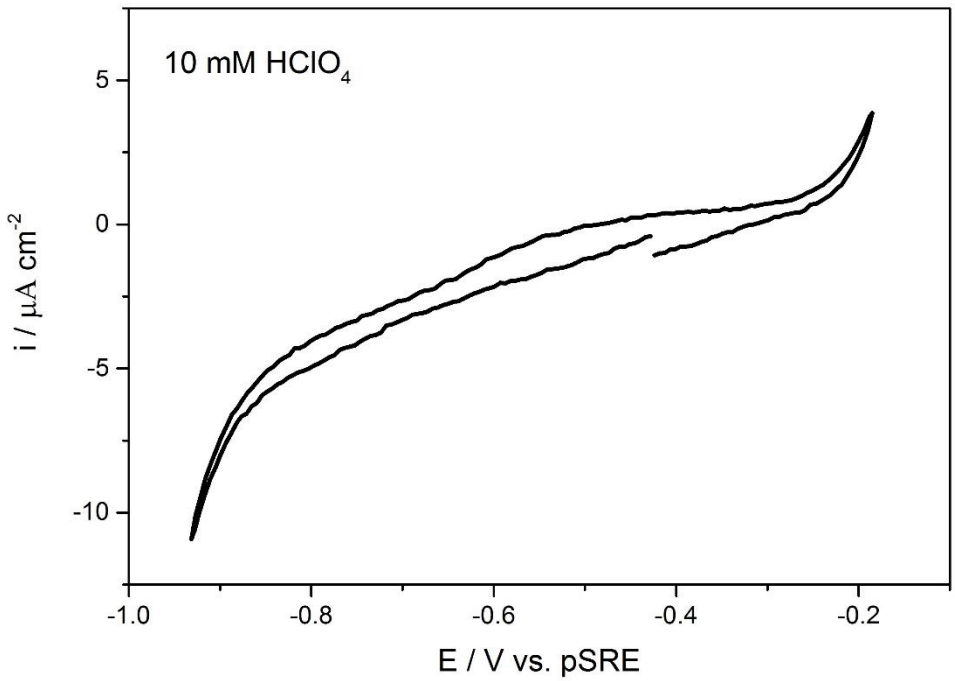

Figure 49. Cyclic voltammogram of Gr/pCu in 10 mM $HClO_4$ (scan rate 10 mV/s).

STM images of Gr/pCu in 10 mM $HClO_4$ solution in the potential range -0.3 ÷ -0.55 mV vs. pseudo-Ag/AgCl[1] (henceforth as pSRE) shows the existence of well-defined steps and large terraces with structures covering the entire surface which cannot be described due to polycrystallinity of the Cu substrate (Figure 50).

The comparison of the images obtained in air and in 10 mM $HClO_4$ at the applied potential of -0.55 V vs. pSRE shows very similar Moiré structures (Figure 50a and c). The inserts of power spectra in Figure 50a and c allows to measure the periodicity of the Moiré around 1.1 ± 0.1 nm for both cases. From the information about the behavior of Cu in $HClO_4$ described before we can conclude that the nature of the Moiré patterns, obtained in

[1] The reference electrode was not so stable and there is no precise value versus RHE but it still can be seen that the scanned potential was in a region more negative than Cu dissolution.

solution is the same as the one observed in air and different from the results of Cu(111) in $HClO_4$ electrolyte, where typically only Cu(111)-(1x1) structure is observed [154,155]. Due to polycrystallinity of the Cu substrate the structures were expected to be different in different points of the sample. But almost on all Cu surface the Moiré patterns were similar. This result could be explained by reconstruction of the topmost copper layers to the most energetically stable structure during the high temperature annealing in CVD process. According to Lu et al. polycrystalline copper reconstructs to Cu(100) structure [119]. The mismatch of the Gr layer with this reconstructed topmost layer of copper creates Moiré patterns on all surface of copper. Figure 50b shows high resolution STM image of Gr/pCu recorded in air, where honeycomb structure can be observed. Moiré patterns on different terraces could be observed in $HClO_4$ solution at -0.45 V vs. pSRE (Figure 50d).

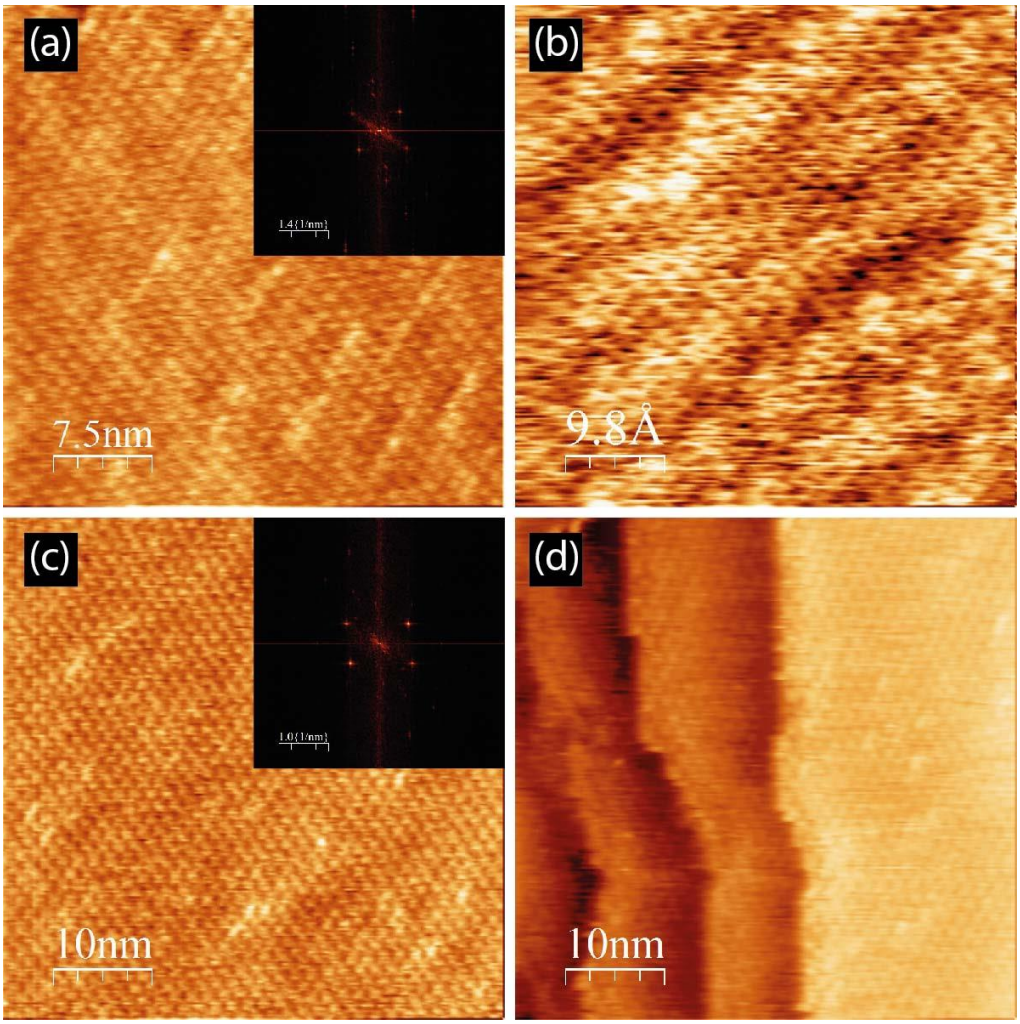

Figure 50. The STM image of Gr/pCu in air (a, b) (I_t =1.7 nA ; V_b = +144 mV) and 10 mM $HClO_4$ electrolyte (c, d) I_t =1.7 nA ; V_b = +144 mV, E_s = -0.55 V vs. pSRE in (c) and -0.45 V vs. pSRE for (d). Inserts in (a) and (c) are the power spectra obtained by using Fourier transforms of these images.

Figure 51a-c shows the STM images recorded on Gr/pCu in ClO_4^- electrolyte at -0.3 V vs. pSRE (E_s); that is a value very close to the onset of the copper dissolution. At the applied potential the local surface structure shows to change with time, and this is evident if we focused on the blue arrows showing the same spot of the surface on different images. Furthermore, change of the step-edge in the lower right part of the images can be clearly seen, even though Moiré pattern apparently doesn't change. This behavior was justified considering the dissolution of atomic step of copper under the Gr layer, as can be seen from the Insert in Figure 51b, where the measured height of the profile line is ~2.4 nm, similar to the atomic step of Cu(111) [151].

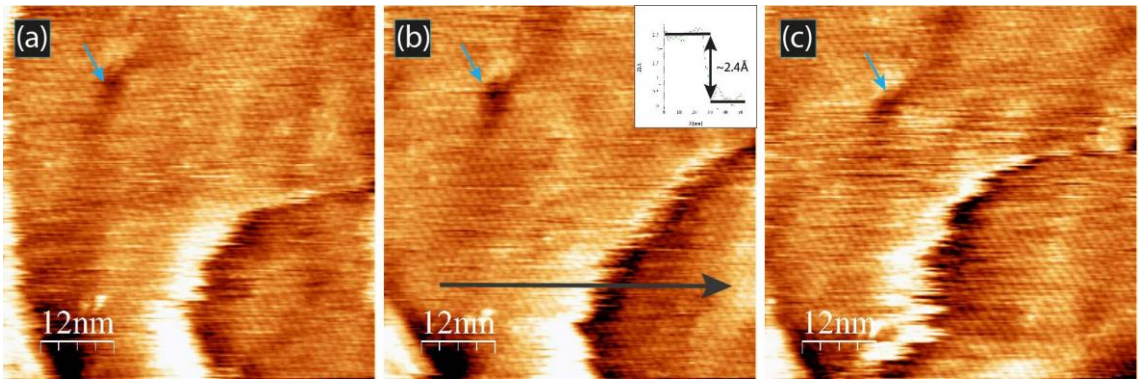

Figure 51. The STM image of Gr/pCu in 10 mM $HClO_4$ electrolyte at E_s = -0.3 V vs. pseudo-Ag/AgCl (I_t =1.7 nA; V_b = +144 mV) Insert in b is a profile of shown by the black arrow.

Similar experiments were extended on Gr deposited on Cu(111) single crystal; the CV of Gr/Cu(111) in 10 mM $HClO_4$ solution is shown in Figure 52. The CV does not show any particular peak, associable to anion adsorption/desorption and hydrogen/oxygen evolution, allowed an available potential window of almost 0.8 V.

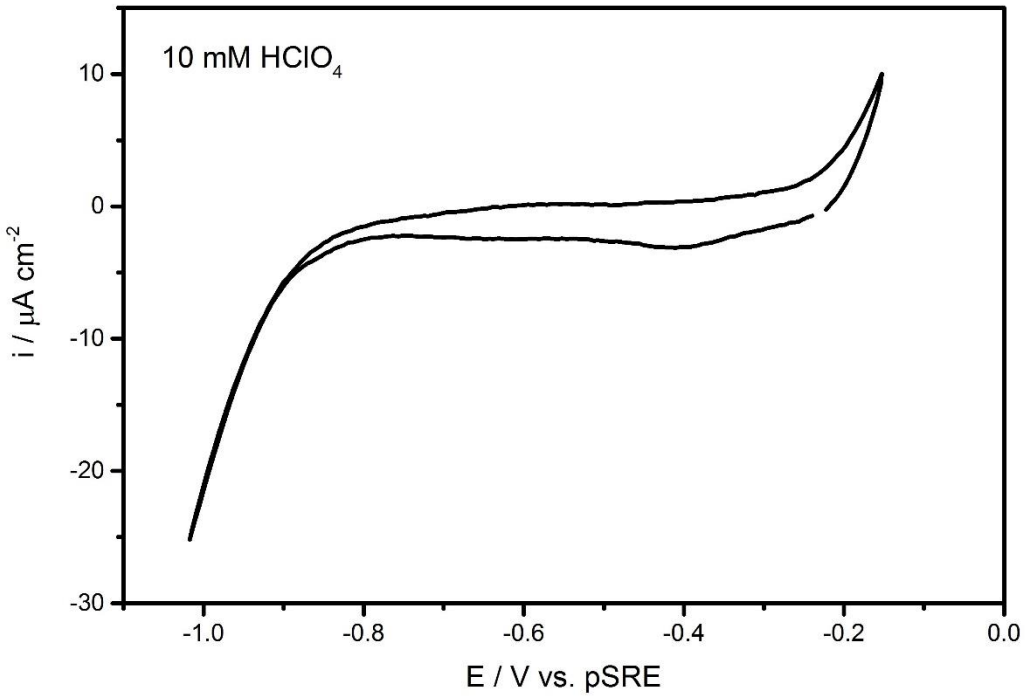

Figure 52. Cyclic voltammogram of Gr/Cu(111) in 10 mM $HClO_4$ (scan rate: 10 mV/s).

The STM images of Gr/Cu(111) surface taken in 10 mM $HClO_4$ electrolyte are shown in Figure 53. The evolution of the surface structure is indicative that corrosion processes are present at the applied potential -0.5 V vs. pSRE, conversely to what observed from the CV analysis where there should not be any corrosion processes at that potential (Figure 52). The dissolution of the copper starting from the step-edges (blue arrow) on Figure 53a-c is reported. Magnified STM image (Figure 53d) shows the presence of a Moiré pattern for Gr on Cu(111) with the step of 2 nm, which is the typical value obtained for all our results. This result can be explained by dissolution of the Cu step-edges under the Gr film due to intercalation of the solution through the defects of Gr layer.

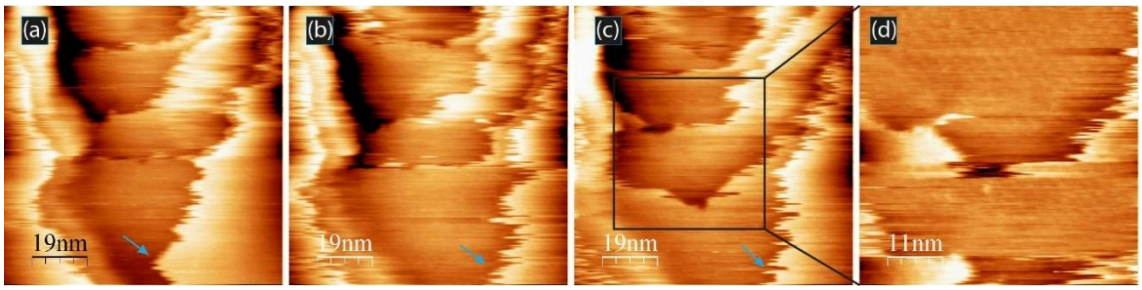

Figure 53. The STM image of Gr/Cu(111) in 10 mM $HClO_4$ electrolyte. (I_t =1.8 nA; V_b = +200 mV; E_s = -0.5 V vs. pSRE).

Another example taken at high resolution shows surface changes at -0.5 V vs. pSRE (Figure 54). The hole from the left top part of the image (blue arrow) is growing through dissolving the step-edges (Figure 54a-c). The measured profile line (Figure 54d) confirms the monoatomic terraces of the Cu. Notwithstanding the evidence of Cu dissolution, Moiré pattern resulting from the interaction of Gr with the underlying Cu(111) is still observed, attesting the persistence of Gr on the surface of the sample.

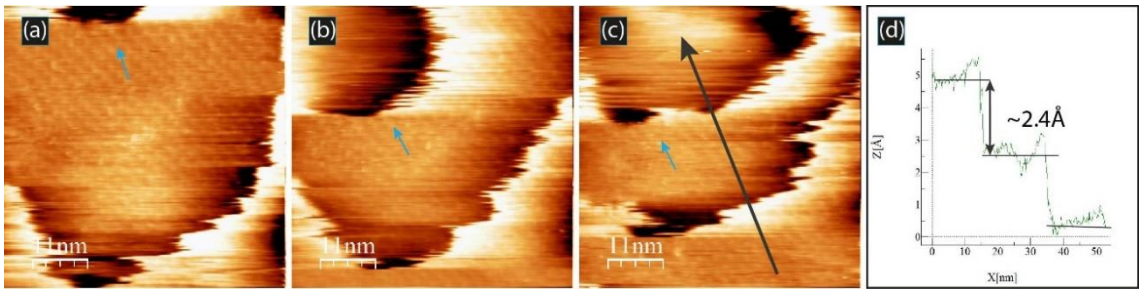

Figure 54. (a-c) High resolution STM image of Gr/Cu(111) in 10 mM $HClO_4$ electrolyte. (I_t =1.8 nA; V_b = +200 mV; E_s = -0.5 V vs. pSRE); (d) Profile line from image (c).

In order to avoid the error of the unstable pSRE reference electrode the system of the EC-STM was upgraded with an external saturated calomel reference electrode (SCE), connected to the electrochemical cell by Tygon tube, filled with the working electrolyte. This new set up assures a more reliable reference system but can introduce more background noise due to the antenna effects of the electrolyte tube, thus losing in image resolution. The as-prepared sample was immersed in 0.1 M $HClO_4$ at the open-circuit potential and the potential was swept negative at 10 mV/s to the hydrogen evolution region, then back into the Cu dissolution region, and then finally to about 0.15 V vs. RHE in the double-layer region, where there should be no Cu dissolution and no surface oxide formation. CV of Gr/Cu(111) in 0.1 M $HClO_4$ with normalized potential is presented in Figure 55. The black line shows the

first cycle of the as-prepared Gr and the red line is a CV after a couple of cycles. It was found that the onset for HER, which is more negative in samples covered with Gr, shifts to more positive potential after scanning the potential towards more positive values where high dissolution of Cu take place.

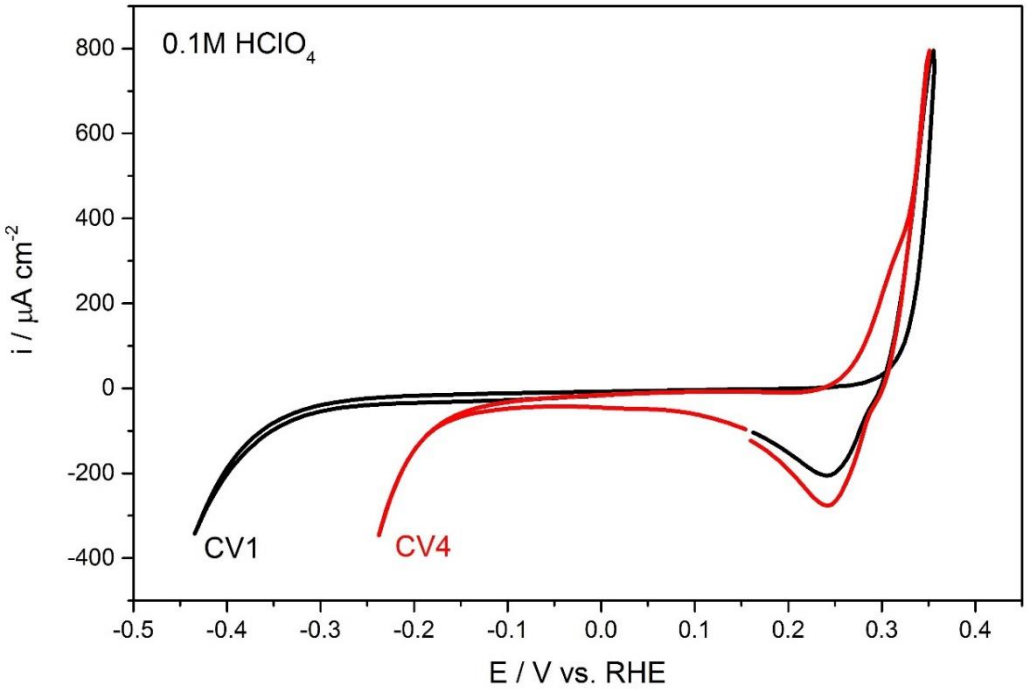

Figure 55. Cyclic voltammograms of Gr/Cu(111) in 0.1 M $HClO_4$ (scan rate: 10 mV/s).

Figure 56 shows *in situ* images of Gr/Cu(111) in 0.1 M $HClO_4$ at E_{oc} (a) and at -0.09 V vs. RHE (b). Islands are observed on the surface (blue arrow Figure 56b) which indicates the re-deposition of Cu after the dissolution at E_{oc} (left image).

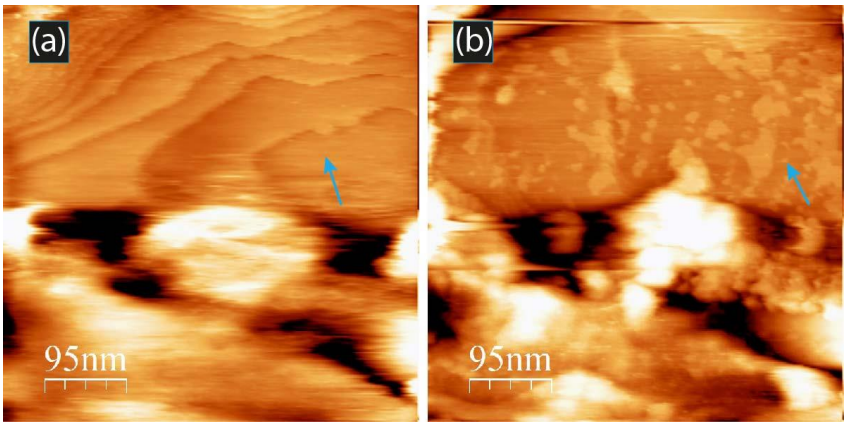

Figure 56. *In situ* STM of Gr/Cu(111) in 0.1 M $HClO_4$ (I_t =1 nA; V_b = 100 mV) (a) at E_{oc}; (b) at E_s = -0.09 V vs. RHE).

To study the anodic dissolution of copper under Gr, the potential was first swept in the cathodic direction to -0.3 V, at which large terraces around 150 nm were observed (Figure 57). Figure 57b is a magnified image of the central region of Figure 57a, where two step-edges of copper, covered by Gr are clearly visible. The morphology displayed in this image did not change as the potentials increased from -0.3 to 0.15 V vs. RHE.

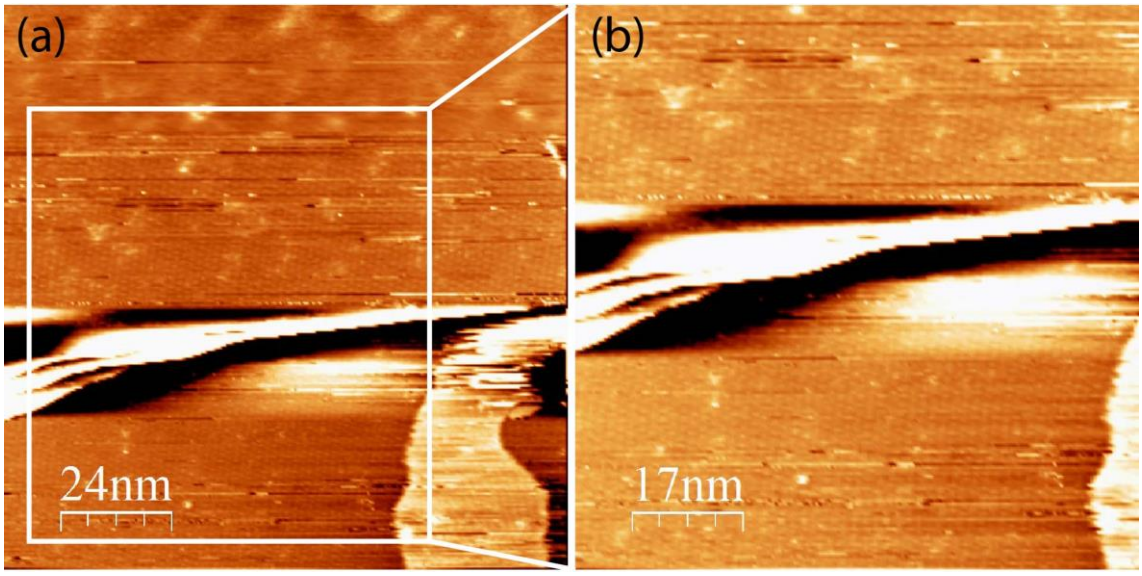

Figure 57. (a) STM images of Gr/Cu(111) in 0.1 M $HClO_4$ I_t = 1 nA; V_b = 105 mV; E_s = -0.3 V vs. RHE ; (b) magnified image of the center spot of (a) .

In 0.1 M $HClO_4$ solution at potential of double layer region (from 0.15 to -0.3 V vs. RHE), the measured STM images were stable over an extended period of time (Figure 58a). This indicates that the Gr/Cu(111) surface remains essentially unchanged on the scale of imaging investigated. In order to follow the real-time modification of the surface exposed to the electrolyte, Gr/Cu(111) electrode potential was changed during the STM image acquisition. The same place imaged starting from -0.1 V to 0.24 V is shown in Figure 58b and c. No changes are observed on the Gr/Cu(111) till the potential is swept to 0.24 V vs. RHE (Figure 58c). At 0.26 V the fast corrosion process was observed and the obtained images were of poor significance due to the high noise level.

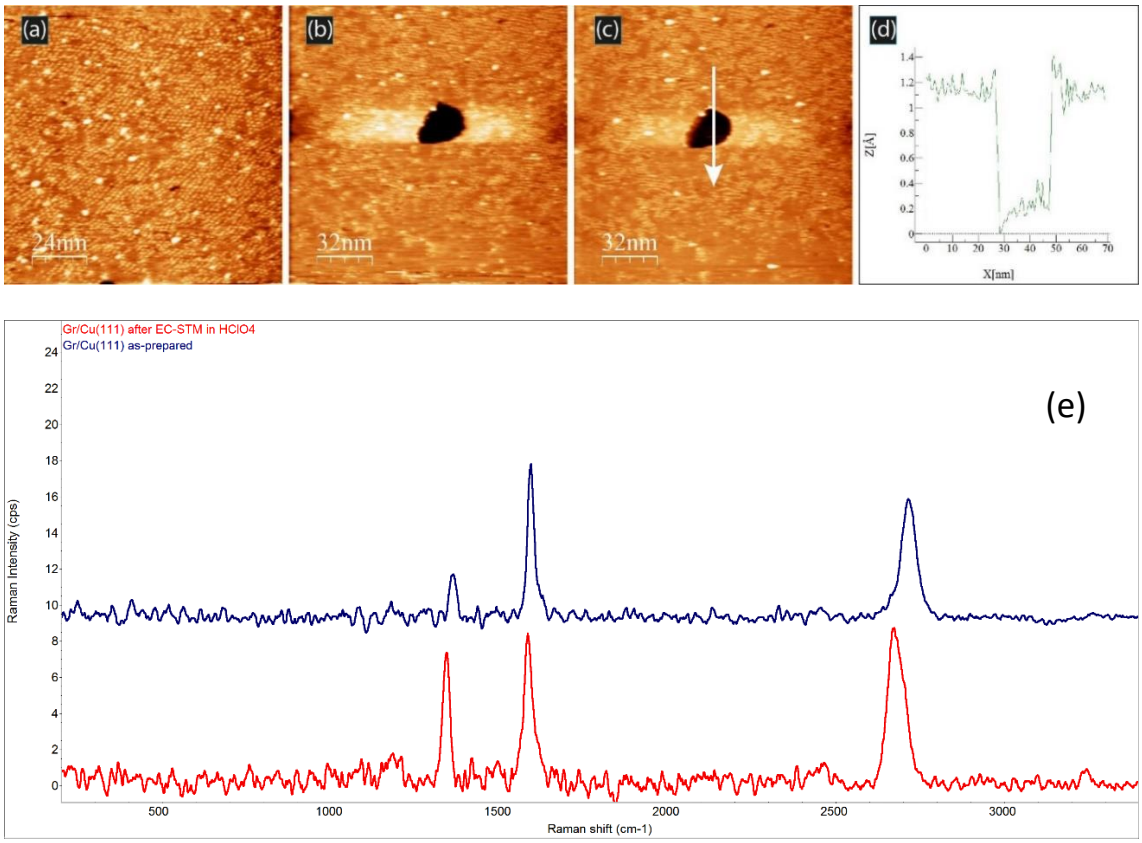

Figure 58. Topography STM image of Gr/Cu(111) in 0.1 M $HClO_4$ (I_t =1 nA; V_b = -265 mV) (a) E_s = -0.2 V; (b) E_s = -0.1 V; (c) E_s = 0.24 V vs. RHE. (d) Profile line from image (c); (e) Raman spectra as-prepared (blue line) and after the EC-STM measurements (red line).

The depth of a pit in Figure 58b and c could be easily measured from the STM height profile, as shown in Figure 58d. The averaged value is 1.2 Å**,** which is very close to the height of Gr layer on Cu (1.5 ± 0.2 Å) [151]**.** Therefore, this pit is a defect in the single layer of Gr. Raman spectra comparison before and after *in situ* STM measurements (blue and red lines in Figure 58e, respectively) shows similar behavior as in the case of the STM measurements of Gr/Cu(111) in water (Figure 46d). The intensity of the D band (1360 cm^{-1}) was higher after the contact with acidic electrolyte, which means that the number of defects in the Gr layer increased. Also, the shift of the 2D band from 2710 cm^{-1} to 2695 cm^{-1} is observed. In contrast, the increasing of the 2D peak is very small. This result can be explained by lower oxidation of the underlying Cu surface, covered by uniform continuous Gr layer with low number of defects.

Figure 59 shows series of STM images of the Gr/Cu(111) sample at a comparable resolution in 0.1 M $HClO_4$ collected as a function of potential over the same scanned area. At

a potential close to the onset of copper dissolution reaction (more positive than 0.2 V) a surface changes can be observed. At this potential, unstable images were recorded, probably due to the increase of Cu^{2+} concentration and to the strong influence of the faradaic current on the process of imaging (image at 0.192 V vs. RHE).

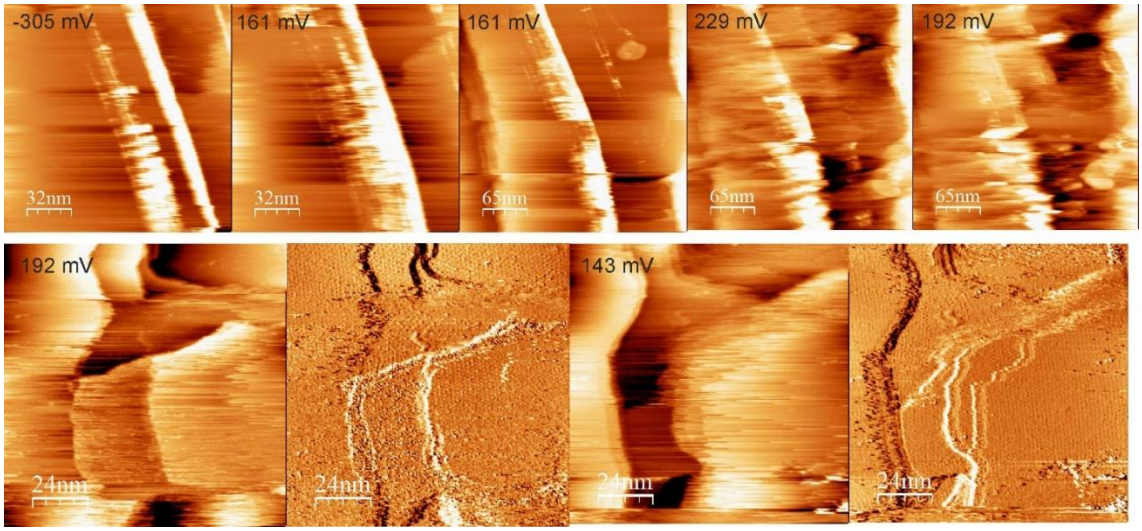

Figure 59. STM images at different potentials (I_t =1 nA; V_b = 130 mV).

The surface roughness increased by shifting the potential to values close to copper dissolution and back to the re-deposition. When the potential is reversed back into the double layer region, smoothening of the surface is observed (image at 0.143 V vs. RHE).

The power spectra on the left and right side of the STM image on Figure 60 shows two Moiré patterns with similar orientation and pitch on the different terraces of the Cu surface after the corrosion reaction. This is indicative that the intercalation of the electrolyte between the Gr layer and Cu surface was slow and the process of Cu dissolution occurred preferentially at the step-edges (Figure 60). Similar results were reported by Wlasny et al. after the XPS and AES analysis of corrosion processes on copper single- and poly-crystals coated with Gr [158]. They proposed the intercalation of the electrolyte as the most probable mechanism for the corrosion of Gr covered Cu.

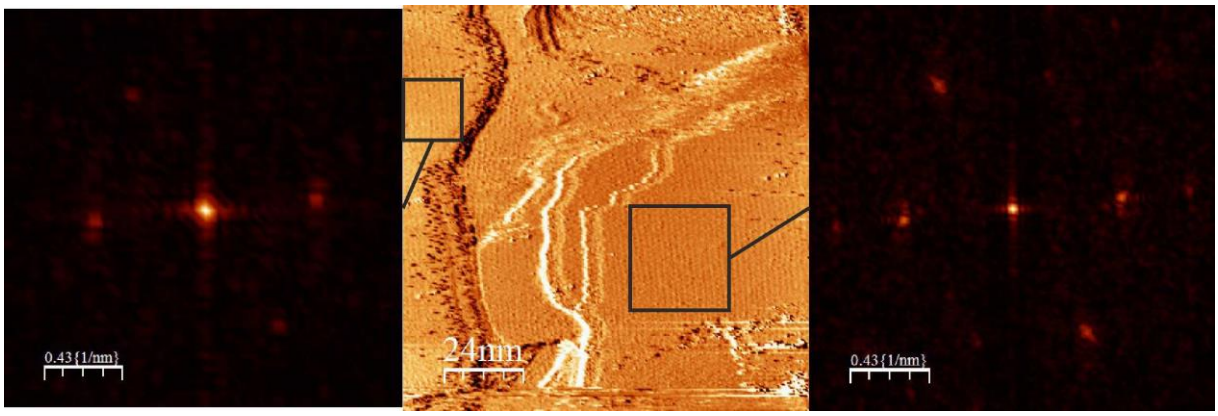

Figure 60. Current image of the STM with the Moiré patterns on different terraces. Insert is the power spectra obtained by using Fourier transforms of the image.

SEM images before and after *in situ* STM measurements are shown in Figure 61a and b, respectively. Figure 61a of the as-prepared Gr/Cu(111) sample shows good coverage of the Gr film on the surface of copper. Small holes around 50 ÷ 100 nm preferentially on the step-edges were observed after corrosion (Figure 61b).

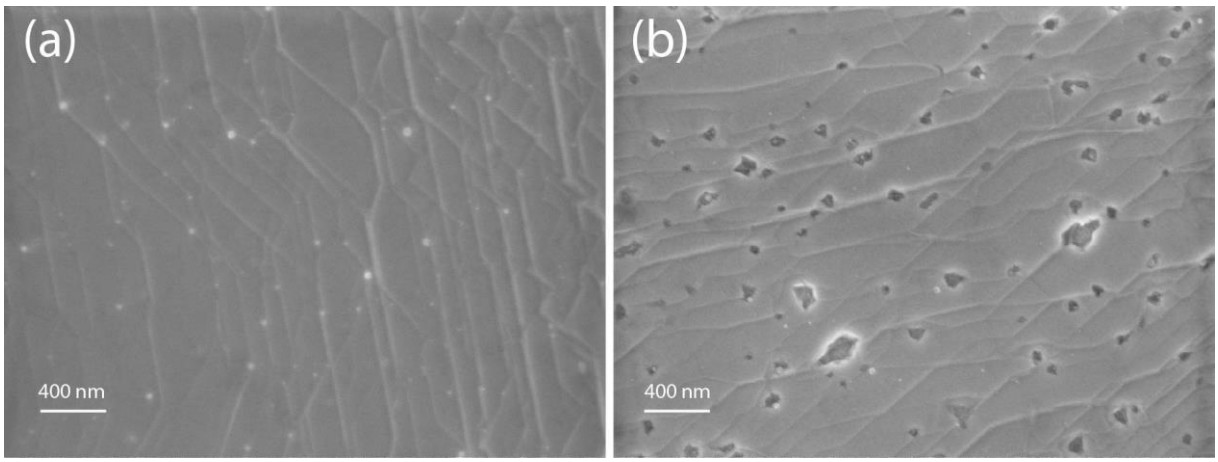

Figure 61. SEM images of Gr/Cu(111) before and after EC-STM in $HClO_4$ at corrosion potentials.

4.5.2. HCl electrolyte solution

Hydrochloric acid is one of the most corrosive non-oxidizing acids when in contact with copper and is successfully handled only in dilute concentrations [52]. In dilute hydrochloric acid at various Cl^- concentrations and pH values, in the absence of oxygen, the complex $CuCl_2^-$ principal dissolution product formed. The reaction may be written as outlined below:

$$Cu + Cl^- = CuCl_{ads} + e^- \qquad (24)$$

$$CuCl_{ads} + Cl^- = CuCl_2^- \qquad (25)$$

The reaction of Cu dissolution in 10 mM HCl occurs preferentially at step-edges [159]. Suggs and Bard reported that they never observed bare copper at a step-edge. They explained it by immediate adsorption of the Cl^- anions on Cu as soon as the $CuCl_2^-$ complex dissolves [160].

Chlorides, adsorbed on Cu(111) single crystal, form a well ordered (√3 x √3)R30° superstructure at positive potentials. The chloride adsorbate causes a restructuring of the surface topography, so that the terraces change their shape and steps run preferentially along a few directions which enclose slightly distorted angles of 120°. The adsorbate structure is ideally hexagonal and commensurate to the Cu(111) lattice at negative electrode potentials near the onset of the HER where the copper surface can be imaged with atomic resolution [161].

The acquisition of images on an as-prepared Gr/Cu(111) surface at E_{oc} in 10 mM HCl proved to be demanding due to the presence of surface oxides formed during the transfer of the sample from the CVD chamber to the electrochemical cell. Figure 62a and b shows SEM and Raman of this sample. As can be seen from the Figure 62a Cu(111) was partially covered and Gr had a high number of defects which was confirmed by the high D band around 1370 cm^{-1} (ratio of I_D/I_G is 1.16) of Raman spectrum (Figure 62b).

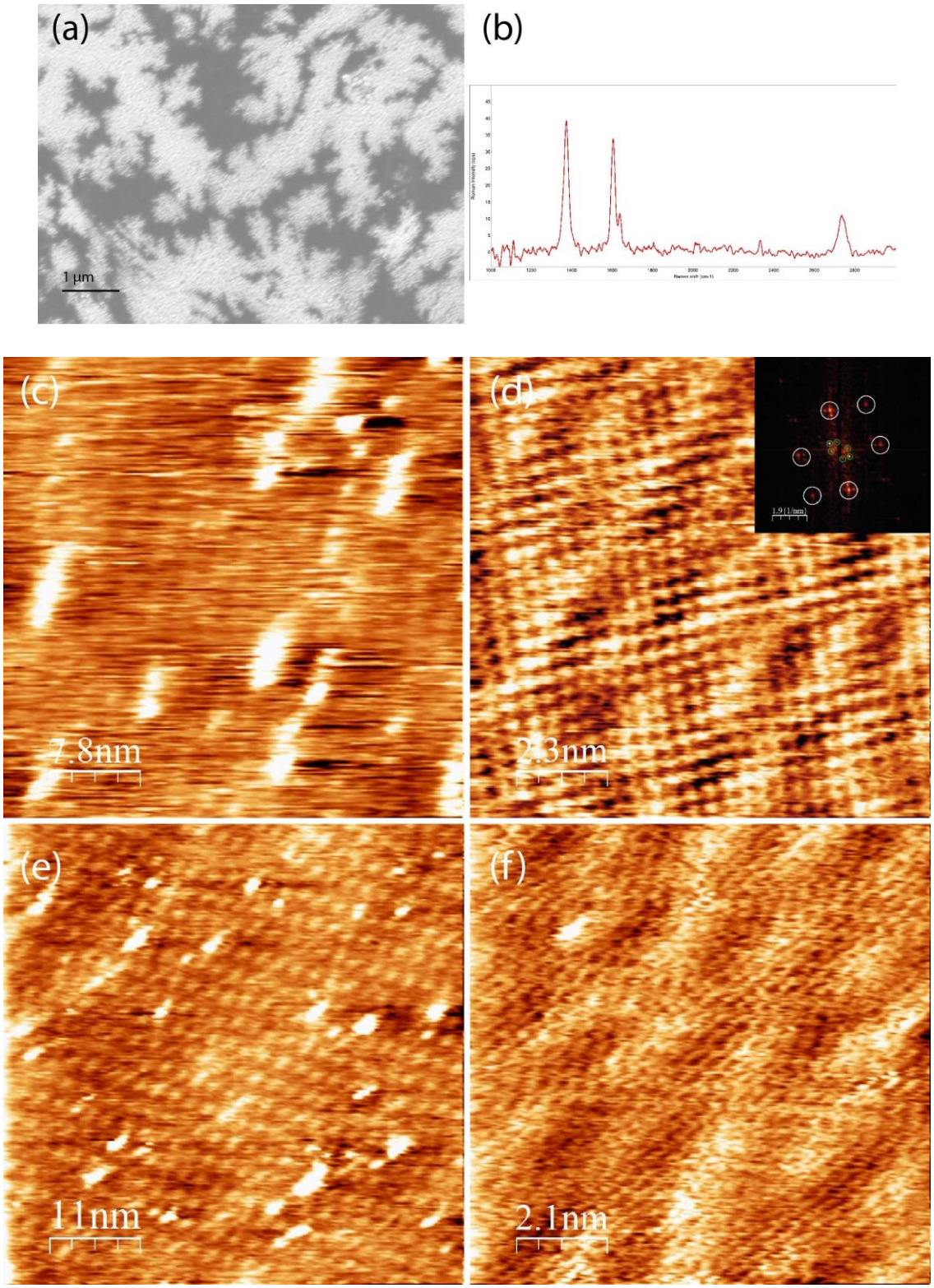

Figure 62. SEM image (a) and Raman spectrum (b) of the partially covered Gr/Cu(111) sample. Topography and high resolution STM images obtained on the surface of this sample in air (c, d) (I_t = 1 nA, V_b = -108 mV) and 10 mM HCl at E_{oc} (e, f) (I_t = 1 nA, V_b = -108 mV). Insert is the power spectra obtained by using Fourier transforms of the image (d).

The STM images recorded in air (Figure 62c) shows Gr with bright defects, similar to the STM images, previously reported in this thesis. High resolution image (Figure 62d) and the corresponding power spectra obtained by using fast Fourier transformation (FFT) (insert in Figure 62d) show stretched hexagonal structure with atomic distance around 4.5 Å (marked by the green color circles) and a Moiré pattern (the white circles) with around 1.6 nm periodicity hexagonal structure (stretched in one direction probably due to the scanner drift). Copper step is 2.56 Å and for Gr is 2.45 Å, so the high distance 4.5 Å could be indeed explained by drift of the scanner. The same parameters of the surface structure were still observed on images measured in 10 mM HCl at E_{oc} (Figure 62f). Topography STM images, obtained in solution (Figure 62e) showed white points indicative of defects, which were observed also during the STM scan in air.

In order to observe the corrosion process of Gr/Cu(111) sample at E_{oc} in 10 mM HCl the changes of the surface morphology were monitored as a function of time. Slow dissolution of the surface on the time scale of the STM imaging process were observed. The dissolution process is shown in Figure 63 (all images of this STM series show the same area, but at different time). In Figure 63a-h it can be observed that one atomic copper layer was slowly dissolved (blue arrows). White defects are blocking the corrosion process and remain unchanged during acquisition time lapse. This can confirm that white spots are not of copper oxide, which should dissolve in this experimental conditions. Figure 63j shows a magnified image of the zone where speed of corrosion slowed down. In Figure 63k, l it can be seen a second copper layer, which starts to dissolve (green circles mark same spot on images).

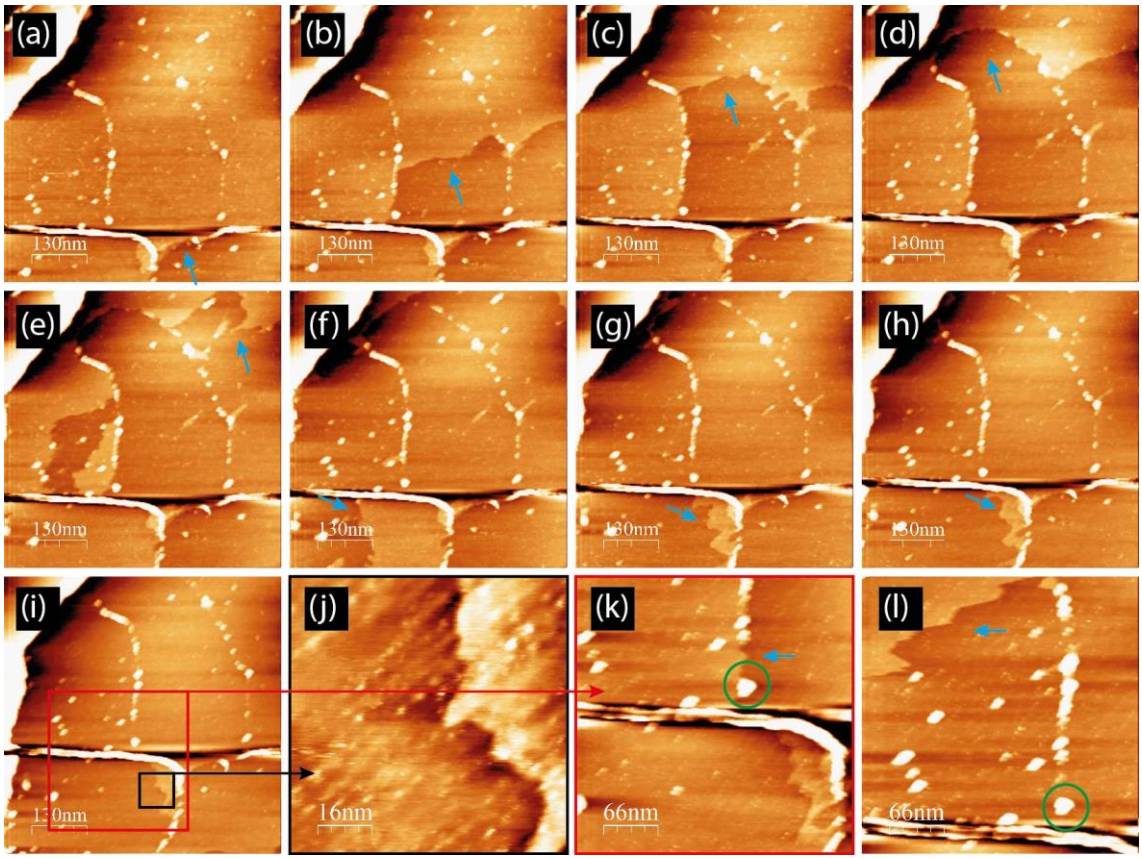

Figure 63. STM images of corrosion process of Gr/Cu(111) in 10mM HCl at E_{oc} (I_t = 1 nA, V_b = -108 mV).

Figure 64 shows a series of *in situ* STM images of Gr/Cu(111) surface recorded in 10 mM HCl at E_{oc}, where the initial stage in the dissolution of the monoatomic steps of copper crystal is observed. At this condition, Cu dissolution proceeds in different directions unequally. As it can be seen from Figure 64a-f only the surface from the upper part of the image shows strong dissolution while the bottom part remains almost unchanged.

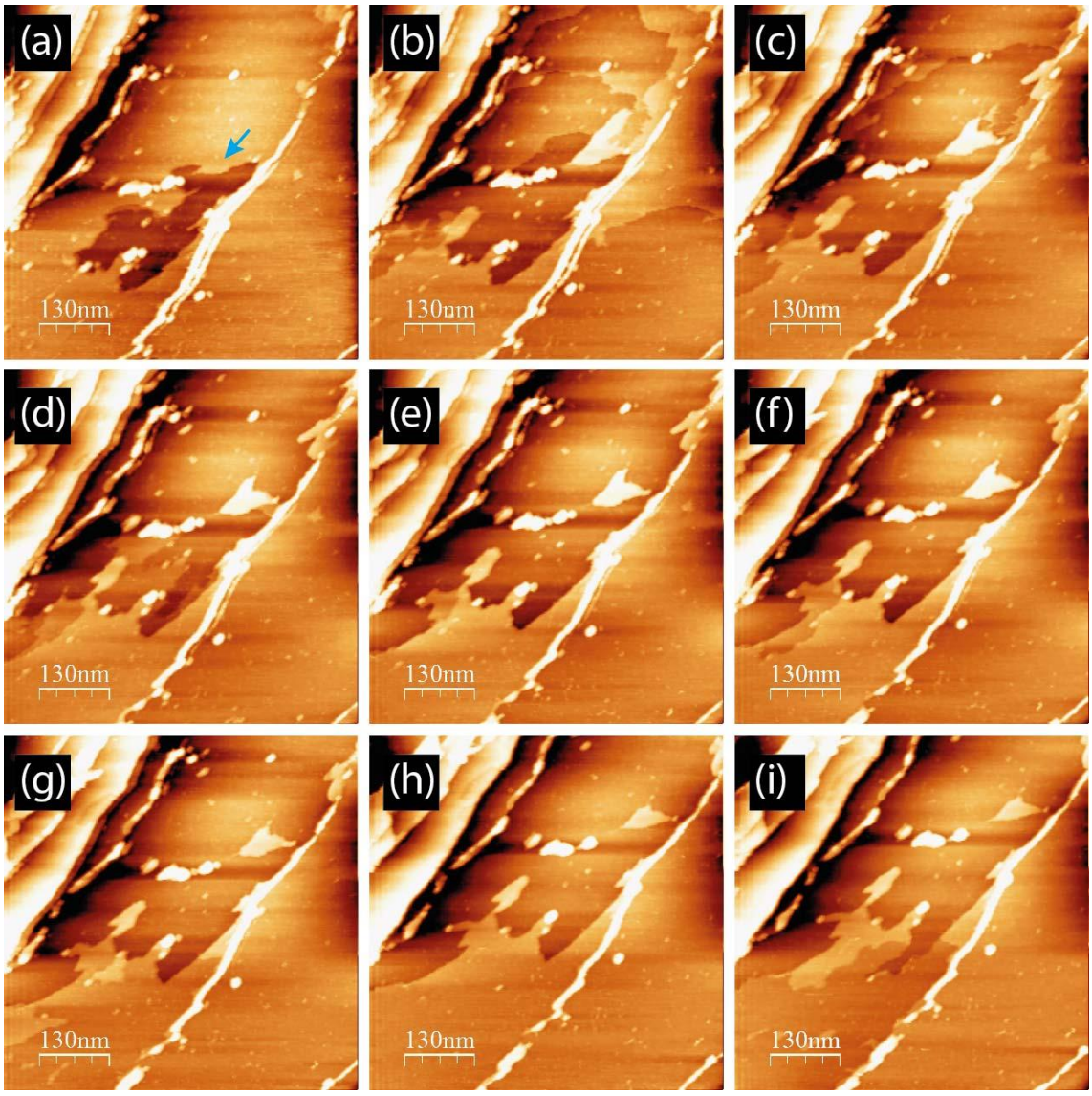

Figure 64. STM images of corrosion process of Gr/Cu(111) in 10 mM HCl at E_{oc} (I_t = 1 nA, V_b = -108 mV).

Figure 65 shows a dissolving step-edge (marked with blue arrows) with the Moiré pattern visible over the Cu terraces. In this example the Cu dissolution starts from some of steps and the process occurs almost only in one direction.

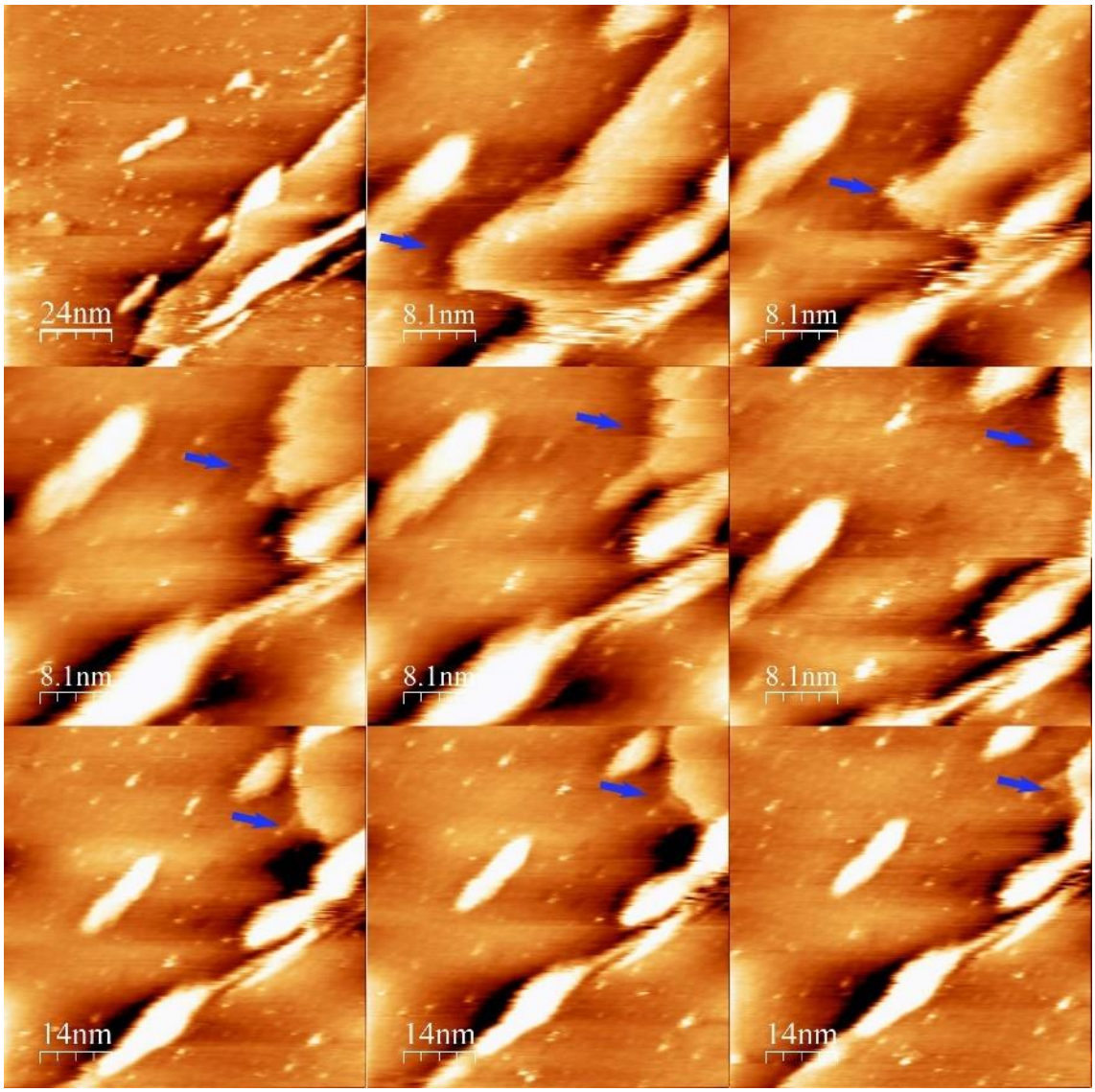

Figure 65. STM images of corrosion process of Gr/Cu(111) in 10mM HCl at E_{oc} (I_t = 1 nA, V_b = -108 mV).

Figure 66 shows STM scans of the same area with a time interval of about 90 sec. Regions of different contrast are visible, consisting of slightly etched regions of Gr/Cu(111) having different layer number.

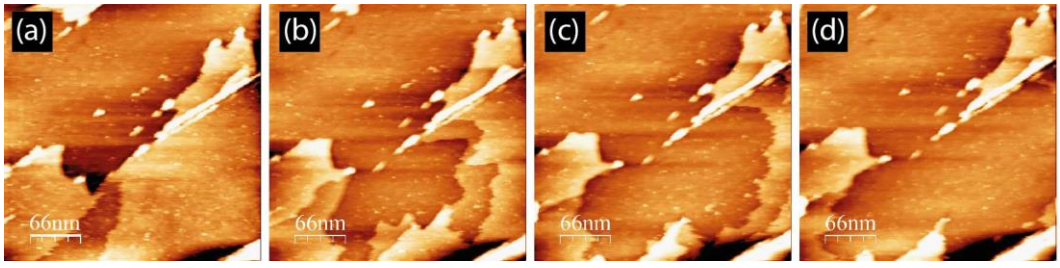

Figure 66. STM images of corrosion process of Gr/Cu(111) in 10mM HCl at E_{oc} (I_t = 1 nA, V_b = -108 mV).

As the potential of the Gr/Cu(111) surface was hold at E_{oc} in 10 mM HCl, slow corrosion of the Gr/Cu(111) sample was observed (Figure 67).

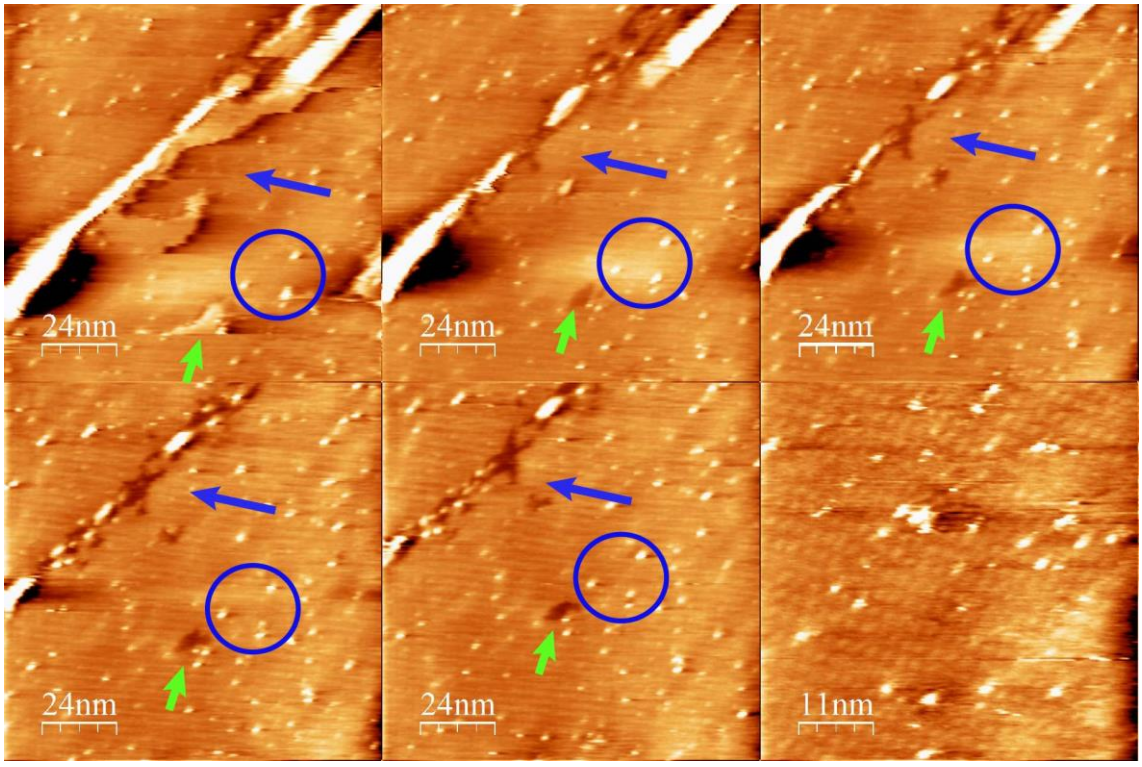

Figure 67. STM images of corrosion process of Gr/Cu(111) in 10mM HCl at E_{oc} (I_t = 1 nA, V_b = -108 mV).

The images in Figure 67 show the key terraces and features, which are marked with blue circle on the images, so that the dissolution process with time can be easily followed. An examination of the images in Figure 67 reveals that even though some thermal drift is present, the dissolution of Cu in Gr/Cu(111) occurs along edges. This is illustrated by the blue arrows. The defects in the Gr layer allowed oxygen molecules from air reaching the copper surface and create small amounts of copper oxides, but after dissolution the surface remains unchanged. Strong water intercalation and Cu dissolution under Gr in this case do not occur. Raman measurements showed that the peak of G band is as high as before the experiment so that the Gr layer is basically unchanged during the electrochemical investigation.

When the Gr/Cu(111) sample was visually examined by optical microscope under magnification after the *in situ* STM measurements, the surface was heavily pitted and oxidized (

Figure 68), but most of the surface was bright due to protection from corrosion/oxidation by Gr layer.

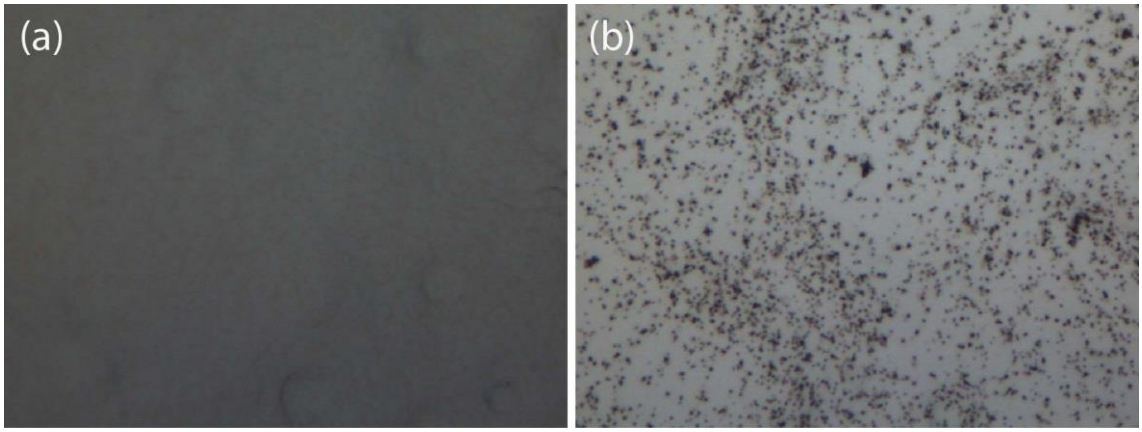

Figure 68. Optical microscope images of Gr/Cu(111) (105 x 140 µm): (a) as-grown Gr; (b) after EC-STM measurements in 10 mM HCl. (Different spots).

Figure 69 shows representative CV curves obtained on Gr/Cu(111) in 10 mM HCl at 10 mV/s. HER potential shifts drastically after the potential was scanned towards active anodic dissolution of Cu (red line comparing to black one in Figure 69). In order to avoid the corrosion process of the surface in the beginning of the STM measurements, the potential was set at potential value within the double-layer region (-0.3 V vs. RHE).

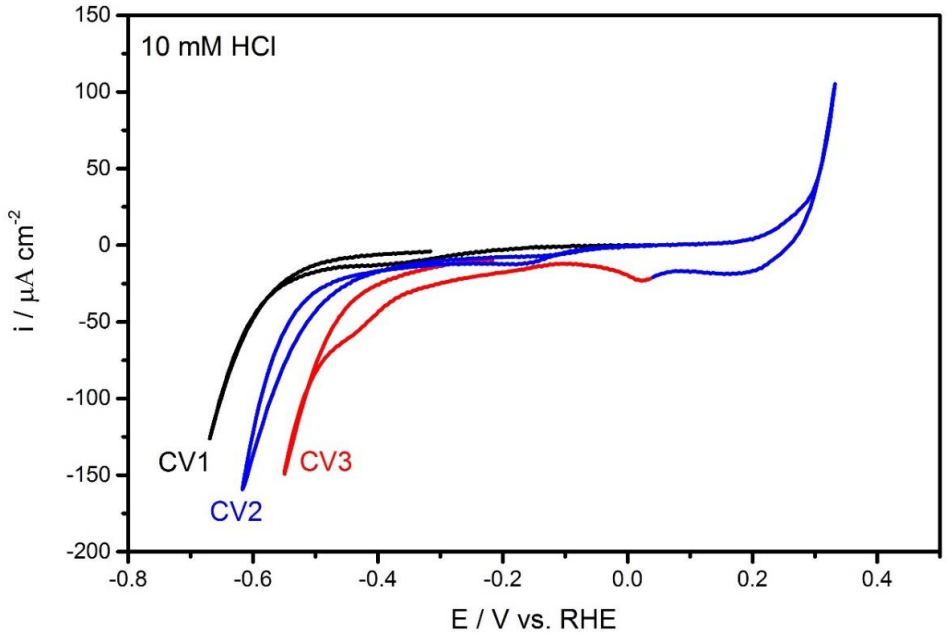

Figure 69. Cyclic voltammetry of the Gr/Cu(111) in 10 mM HCl. Scan rate: 10 mV/s.

Figure 70 shows the comparison of images obtained in the same region at potential of -0.3 V and at E_{oc}. At this potential the surface remains stable but it starts to change as soon as overvoltage is switched of and the sample remains at E_{oc}. The corrosion process at this conditions is fast and the image became very noisy. The copper dissolves via a step-flow mechanism without pitting. A cathodic step (sample potential, E_s = -0.3 V) reversed the process with the progressive recovering of smooth substrate terraces and the stability of the image increased. The Moiré patterns can be clearly observed in the image with the higher resolution (magnification image of the black square in the lower right image of Figure 70).

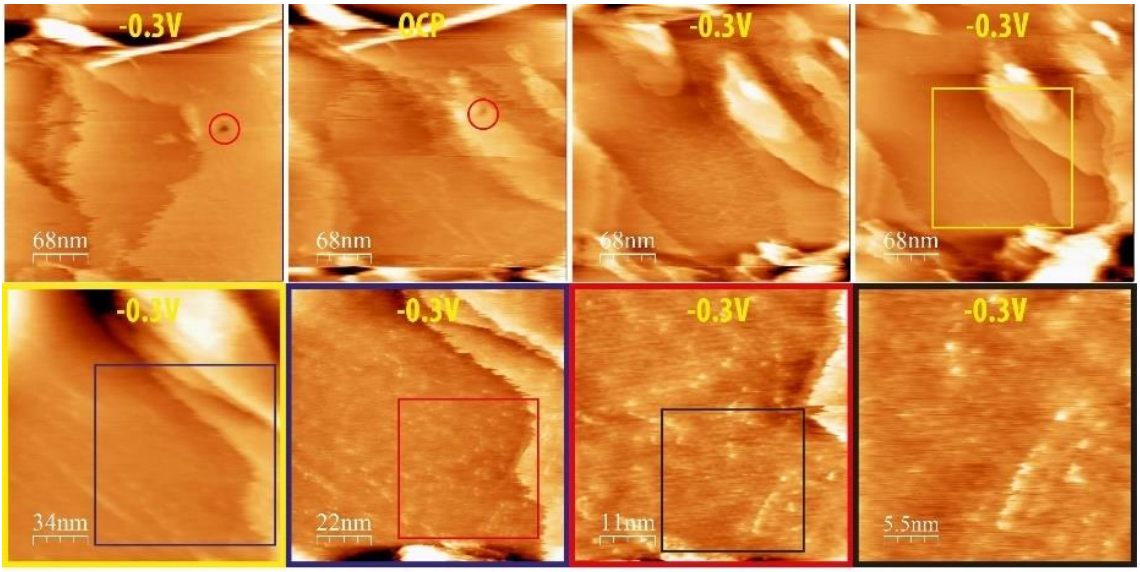

Figure 70. STM images of Gr/Cu(111) in 10 mM HCl (I_t = 1 nA; V_b = +195 mV).

Figure 71 shows the series of the *in situ* STM images obtained at slightly more anodic potentials than -0.3 V, where the slow changes of the surface can be detected. When the potential of the Gr/Cu(111) surface was swept slowly positive in 10 mM HCl (pH 2.1) to potentials 0.0 V vs. RHE, dissolution of Cu began. The potential was selected so that the rate of Cu dissolution was slow, and therefore successive STM images showed obvious, but not too drastic, differences. When the imaging showed signs of moderate dissolution, the potential was swept back in negative direction to -0.057 V. As can be seen from the images the reaction of the copper dissolution starts preferentially at the step-edges (blue and yellow arrows in Figure 71) and proceed preferentially in one direction.

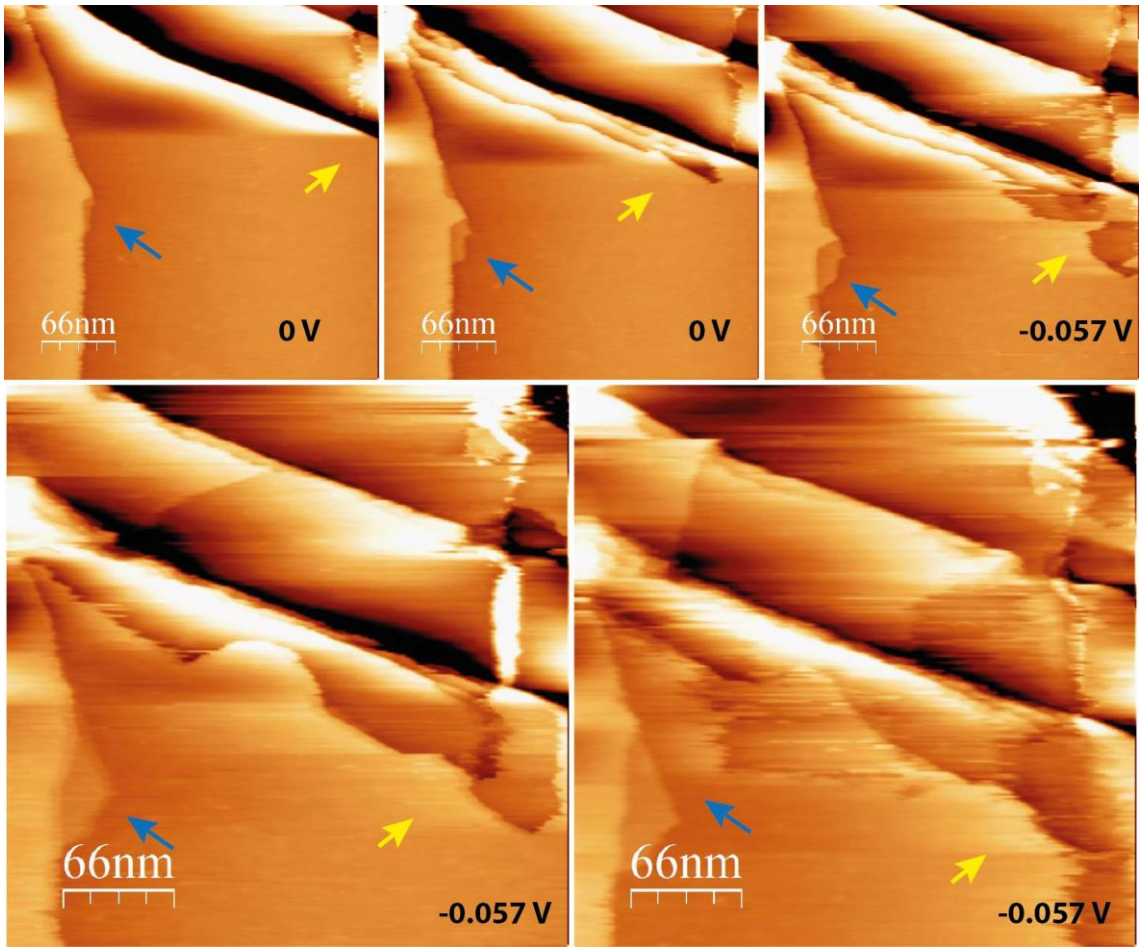

Figure 71. STM images of Gr/Cu(111) in 10 mM HCl (I_t = 1 nA; V_b = -84 mV).

When the surface is fully covered with Gr (Figure 72) the Cu(111) shows to be stable at potentials more positive than those showed before (0.043 V vs. RHE), where corrosion occurred.[2] The stabilization of Cu surface underneath Gr layer can be explained by the protection that Gr exerts from the contact with H^+ and Cl^- when even step-edges are inaccessible.

The difference in the potentials, at which structural changes of the Gr/Cu(111) surface are observed is a result of the very local information obtained by *in situ* STM. CV measurements in contrast give us the surface average information about the processes occurred.

[2] Large terraces with typical Moiré patterns can be observed on the current images of the surface in the lower row of Figure 72

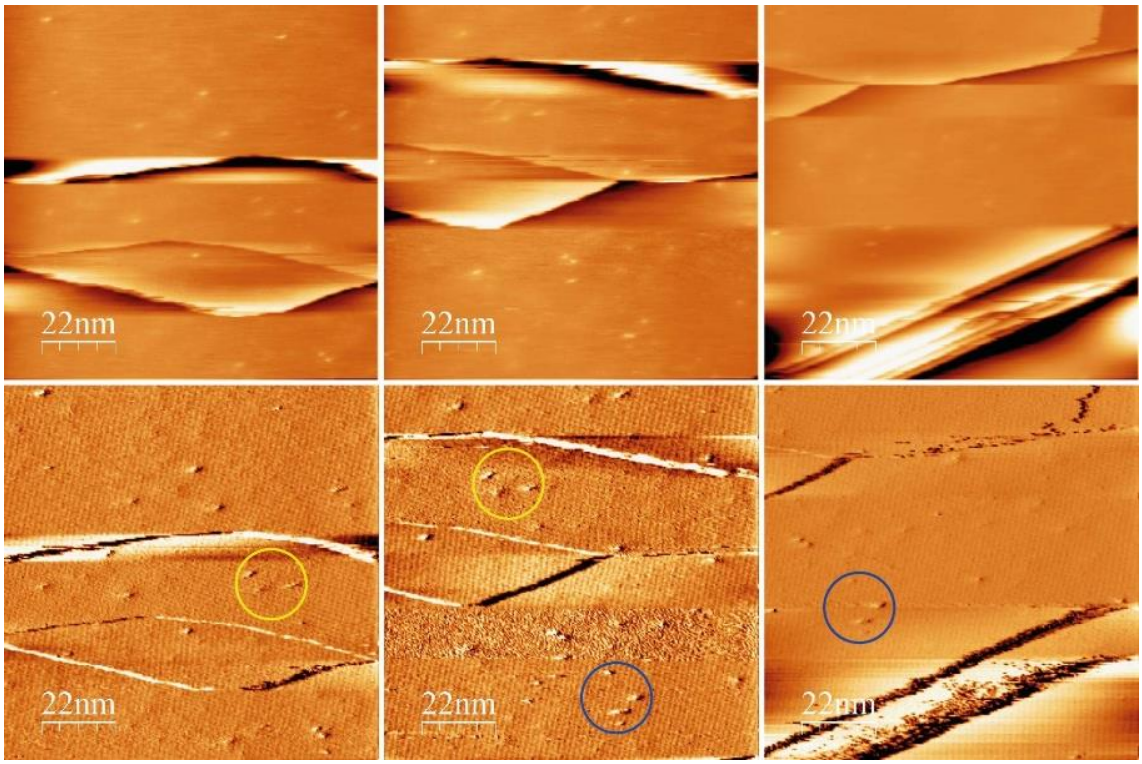

Figure 72. STM images of Gr/Cu(111) in 10 mM HCl (I_t = 1 nA; V_b = -99 mV; E_s = +0.043 V vs. RHE).

4.5.3. H_2SO_4 electrolyte solution

Copper dissolution process in O_2 free H_2SO_4 solution is a two-step process, where the second step is the rate limiting one [149]:

$$Cu = Cu^{+}_{ads} + e^{-} \qquad (26)$$

$$Cu^{+}_{ads} = Cu^{2+} + e^{-} \qquad (27)$$

In dilute sulfuric acid solutions the adsorption and desorption of sulfate anions on the Cu(111) surface strongly depend on the electrode potential. At potential below that for the dissolution of Cu the sulfate/bisulfate anions (designated hereafter simply as sulfate) adsorb on the surface. The typical representative CV of sulfate adsorption–desorption on Cu(111) in aqueous 5 mM H_2SO_4 electrolyte (pH = 2) is shown in Figure 73. The potential window accessible for the experiments in sulfuric acid was limited by two reactions, the oxidative Cu dissolution reaction at the anodic limit and the hydrogen evolution reaction at the cathodic limit. This current-potential curve is in a good agreement with the previously reported voltammograms obtained from clean, well-ordered Cu(111) surfaces in 5 mM H_2SO_4 [162].

Sweeping in the cathodic direction, the large peak around -0.28 V corresponds to sulfate desorption. The anodic peak around -0.075 V corresponds to sulfate adsorption. The surface morphology and molecular structure in the presence of sulfate ions was investigated and described in details in the doctoral thesis of Wilms [95].

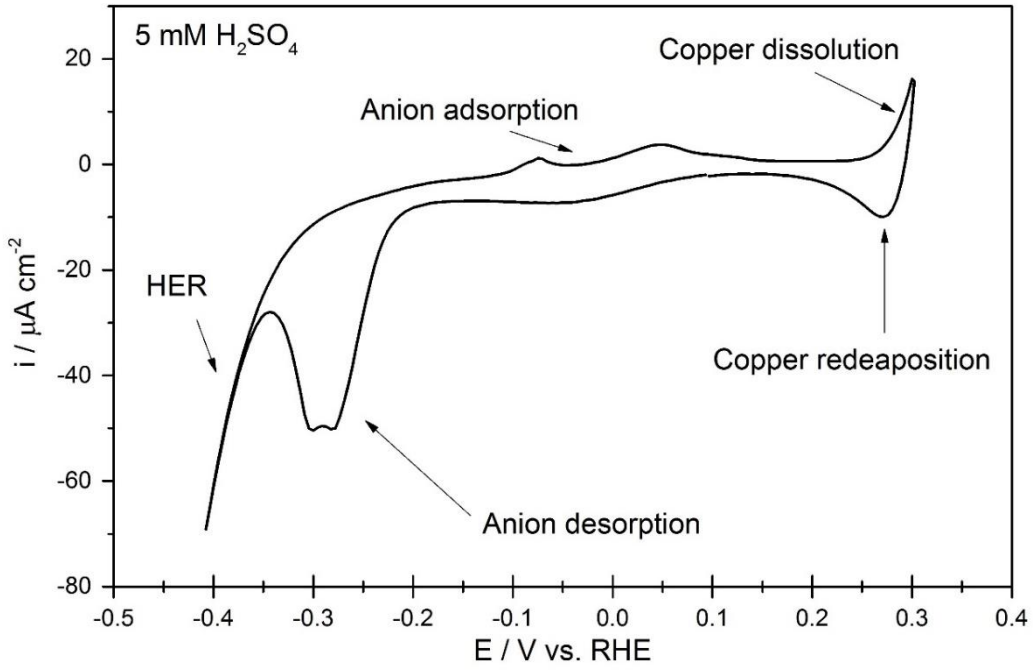

Figure 73. CV of Cu(111) in 5 mM H_2SO_4. Scan rate: 10 mV/s.

Figure 74 summarizes steady-state CV (sweep rate: 10 mV/s) obtained in the electrochemical cell of the EC-STM setup in 5 mM H_2SO_4 saturated with argon on bare Cu(111) (red line) and Gr/Cu(111) (black line). The results demonstrate the strong dependence of the reactivity on the nature of the electrode. Compared to the CV obtained on Cu(111) the entire shape of the CV changes when Gr films are present on the surface of the single crystal. The reasons for these differences are mainly related to the different reactivity of the Cu and Gr. The Gr/Cu(111) exhibits a wider potential window than clean Cu(111). While Cu^{2+} ions are formed in sulfuric acid, the presence of a Gr films on the Cu electrode leads to a surface passivation against dissolution. Note that the onset potential due to Cu dissolution is shifted toward more positive values when Gr is present (Figure 74). Equally, the onset of the HER is shifted to more negative potentials than on bare Cu(111). From CV measurements, adsorption and desorption peaks of sulfate in diluted sulfuric acid

on the Gr/Cu(111) are not observed. This observation indicates a weak interaction of the sulfate ad-species with Gr and the absence or poor sulfate intercalation between Gr and the Cu(111) support.

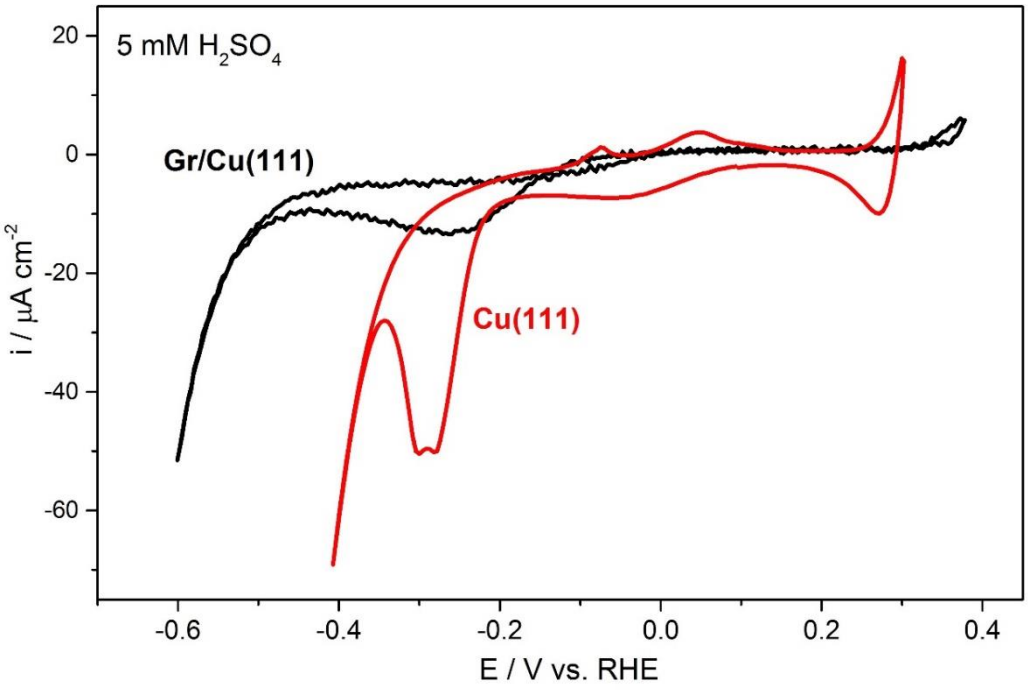

Figure 74. Cyclic voltammograms of Cu(111) (red line) and Gr/Cu(111) (black line) in 5 mM H_2SO_4 saturated with argon (Scan rate: 10 mV/s).

The typical STM image of Cu(111) surface taken in 5 mM H_2SO_4 electrolyte at -0.1 V, which is more negative than the potential of copper dissolution, shows the existence of atomically flat terraces (Figure 75a). The length of the terraces varies between 20 ÷ 50 nm and the height of steps is around 0.23 nm corresponding to monoatomic height of copper. In the high resolution STM image taken at -0.1 V (Figure 75b), the Moiré pattern with long range periodicity around 0.27 ± 0.2 nm and 0.37 ± 0.2 nm of the adsorbed sulfate anions is observed. This results is in excellent agreement with literature [162]. It is well known that adsorbed bisulfate anions results in surface reconstruction of Cu(111) single crystal electrode [163]. Wilms et al. was the first to observe a superstructure with a highly ordered $(\sqrt{3} \times \sqrt{7})SO_4^{2-}$ anions co-adsorbed with water molecules on a reconstructed topmost layer of Cu single crystal surface, in the double layer range, by *in situ* STM technique [163]. The reconstruction of the Cu topmost atomic layer has been verified by bias-dependent STM

images and this model was used to explain appearance of the long range modulation of the Moiré structure [164]. The expansion of the topmost Cu layer leads to a misfit with respect to the second Cu layer.

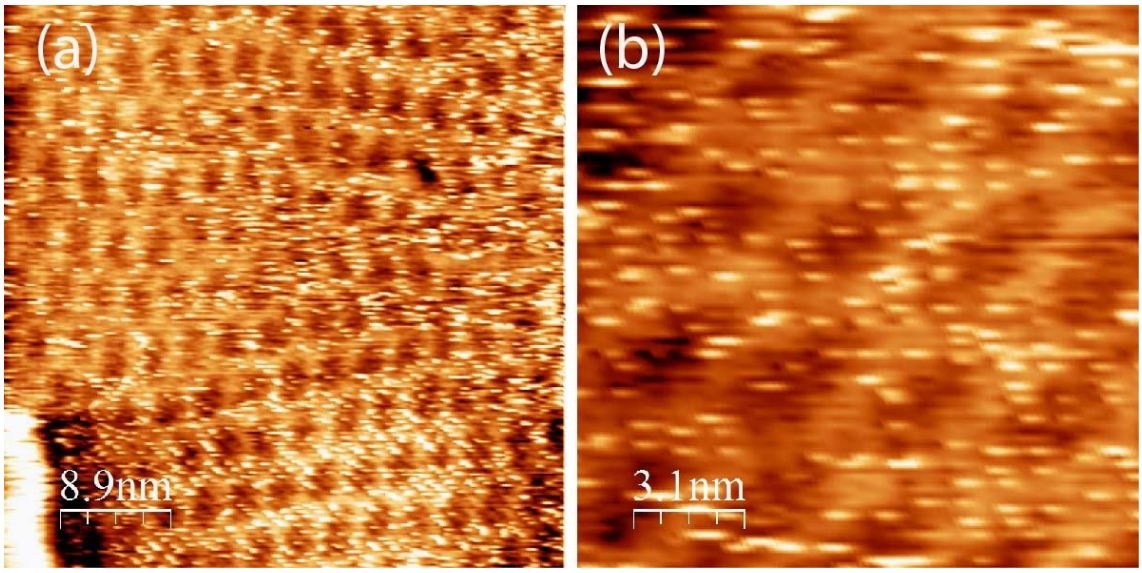

Figure 75. The STM images of Cu(111) in 5 mM H_2SO_4 electrolyte. (a)Topography; (b) atomic resolution (I_t = 1.8 nA, V_b = -43 mV, E_s = -0.1 V vs. RHE).

In case of Gr/Cu(111), the STM images in 5 mM H_2SO_4 shows the Moiré pattern (around 2 nm) similar to the images of the Gr/Cu(111) in air and other acids (Figure 76). Unlike the sulfate layer on Cu(111), a condensed layer of adsorbed sulfate has not been observed on Gr/Cu(111) by EC-STM (Figure 76). Since sulfate anions do not adsorb on Gr in sulfuric acid, the only superstructure present is the Moiré pattern of Gr on Cu,. A well-defined terrace structures were present on the surface with terrace widths of 10 ÷ 20 nm (Figure 77). Although similar images were easily obtained, the very large terraces were not always present.

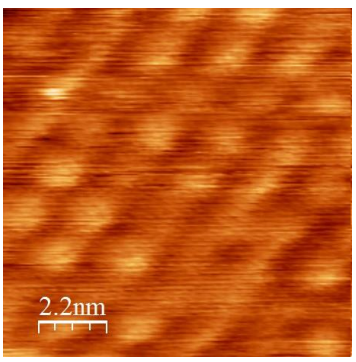

Figure 76. STM image of Gr/Cu(111) in 5 mM H_2SO_4 (I_t = 1.8 nA, V_b = +134 mV, E_s = 0.1 V vs. RHE).

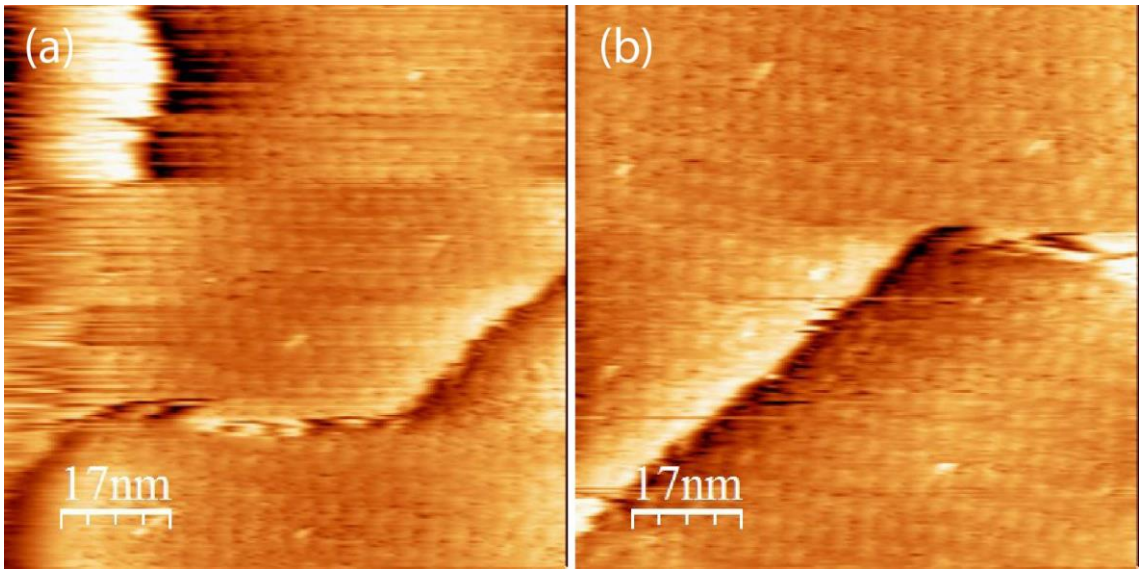

Figure 77. Continuity of Gr through the Cu step-edge (I_t = 1.8 nA, V_b = +35 mV, E_s = -0.2 V vs. RHE).

Conversely to model system, real crystal of Gr has defects in its structure, such us point defects, dislocations or even holes. Figure 78 shows STM images revealing the surface morphology defects, such as linear dislocation Figure 78a and pit defect Figure 78c of Gr layer on Cu(111). They are the weak points of the protective properties of Gr layer.

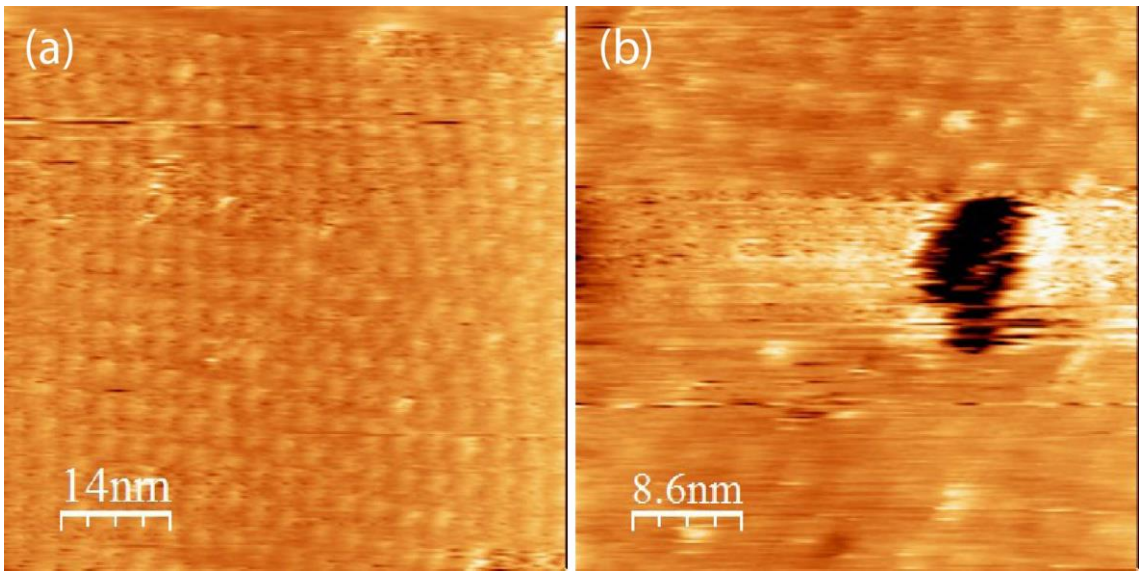

Figure 78. STM images of surface defects: (a) line dislocation in Moiré pattern; (b) hole in the Gr film (I_t = 1.8 nA, V_b = +35 mV, E_s = -0.2 V vs. RHE).

As can be seen from the images, obtained by optical microscope, before electrochemical measurements, the sample had bright, shiny copper appearance (Figure 79a). After the EC-STM measurements in 5 mM sulfuric acid sample still has bright zones of

the Cu protected by Gr, with grain size around couple of microns (Figure 79b). It also contains dark points and line features, where corrosion took place. Raman spectra in Figure 79c shows the shift of the 2D band and the increase of the D and 2D peaks intensities, these changes occur after the *in situ* STM measurements in the 5 mM H_2SO_4 solution. Furthermore, peaks around 415, 526 and 628 cm^{-1} (typical peaks of copper oxide [59]) appear due to the oxidation of the Cu. Since only grain boundaries or defects take part in the electrochemical reaction [135], this can be used in future study of electrochemically active metal NPs loaded on Gr supports.

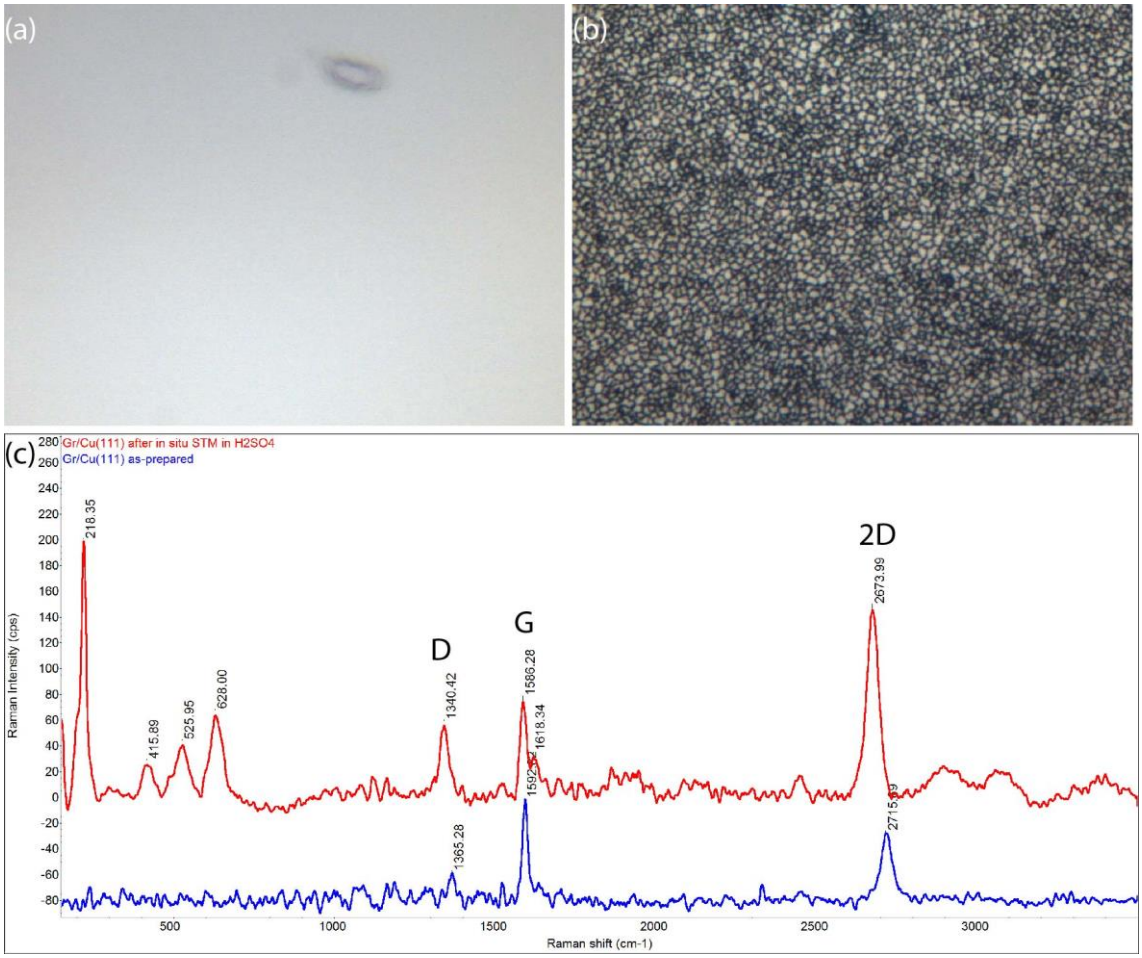

Figure 79. Optical microscope images of Gr/Cu(111) (105 x 140 µm, 50x LWD): (a) as-prepared; (b) after *in situ* STM in 5 mM H_2SO_4; (c) Raman spectra before and after EC-STM measurements.

4.5.4. KOH electrolyte solution

The electrochemical behavior of Cu in alkaline solutions is well known [36,39,44]. Figure 80 compares the CV behavior of Cu(111) and Gr/Cu(111) in Ar-saturated 0.1 M KOH solution

obtained in the electrochemical STM cell. The potential was cycled between the hydrogen and oxygen evolution regions. There are two anodic peaks (A1, A2) and two cathodic peaks (C1 and C2) (red line in Figure 80).

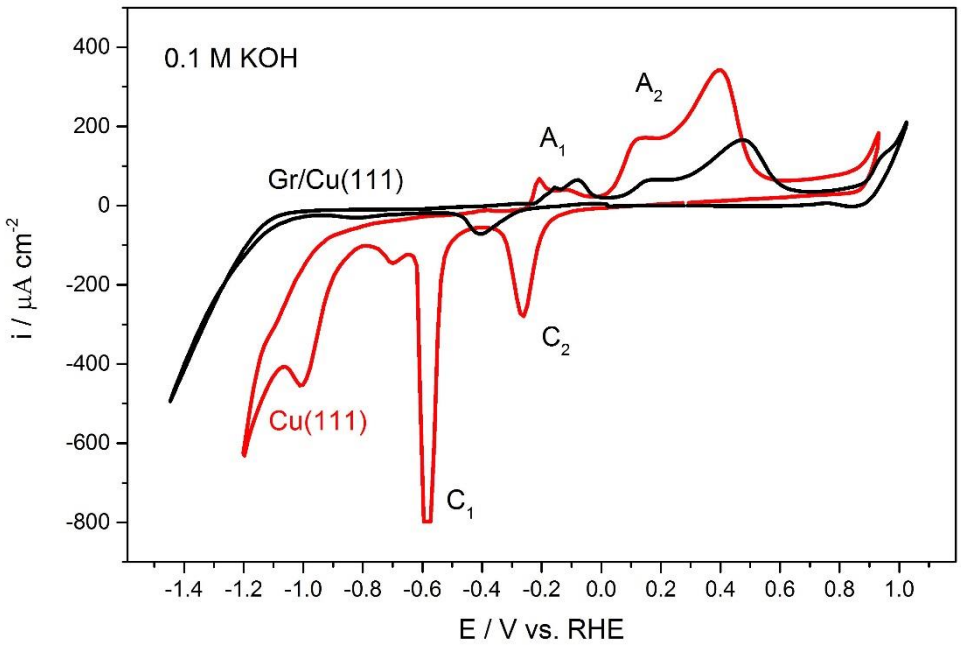

Figure 80. Cyclic voltammograms of Cu(111) and Gr/Cu(111) in 0.1 M KOH, scan rate: 10 mV/s.

The anodic peaks A_1 (-0.2 V) and A_2 (broad peak between 0.2 and 0.4 V) corresponds to the formation of Cu_2O and $Cu_2O/CuO,Cu(OH)_2$ duplex layers, respectively [32]. The related cathodic peaks C_2 (-0.25 V) and C_1 (around -0.6 V) correspond to the reduction of Cu(II) to Cu(I) and of Cu(I) to metallic Cu, respectively.

$$A_1/C_1: Cu \leftrightarrow Cu^+ + e^- \qquad (28)$$

$$A_2/C_2: Cu^+ \leftrightarrow Cu^{2+} + e^- \qquad (29)$$

A slight difference in electrochemical behavior on Gr/Cu(111) sample is observed. The anodic waves A_1 and A_2 are still present. The A_1 peak is shifted to more positive potential (-0.05 V vs. RHE), while A_2 peak is smaller, and also slightly shifted in negative direction (Figure 80 black line). The electrochemical behavior of Gr/Cu(111) can be explained by passivation of copper surface by Gr layer, where reaction of Cu oxidation and reduction reaction of copper oxides occur only through the defects and grain boundaries of the Gr layer. The

obtained results are similar to that reported by Ambrosi et al. [165]. The authors report that the Cu(111) covered with multilayer Gr layers showed very low redox peaks compared with bare Cu. They propose that the small redox signals indicate presence of some holes in Gr, so the total area of the copper electrode is smaller.

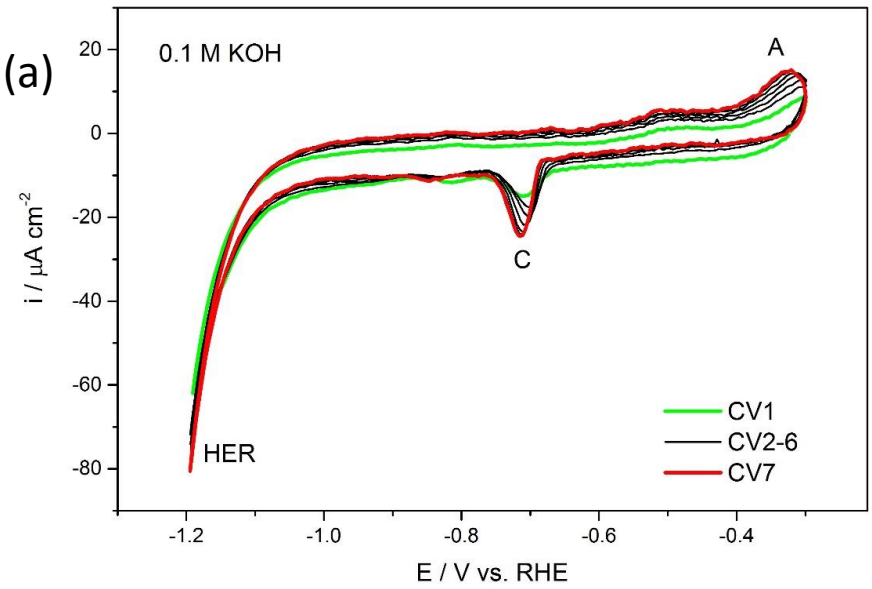

Figure 81a. Cyclic voltammograms of Gr/Cu(111) in 0.1 M KOH with the potential scanned between -0.3 and -1.2 V vs. RHE (scan rate: 10 mV/s).

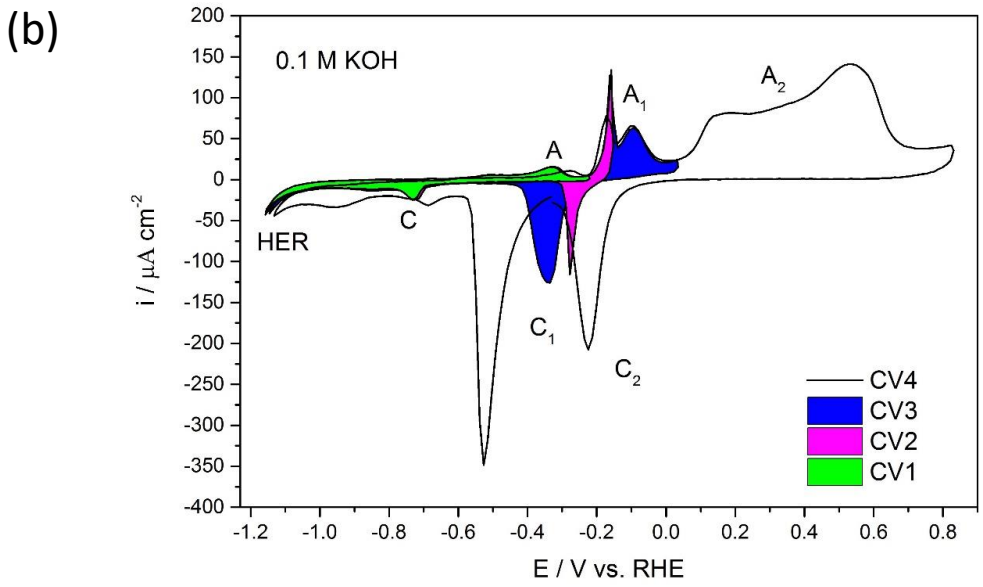

Figure 81b. Cyclic voltammograms of Gr/Cu(111) in 0.1 M KOH with the potential scanned between +0.8 and -1.2 V vs. RHE (scan rate: 10 mV/s).

Figure 81a shows a voltammogram that was obtained when the potential was cycled in a region more negative with respect to the oxidation region. A small anodic peak A with its maximum at around -0.33 V vs. RHE (for a scan rate of 10 mV/s) and a cathodic peak C with the same charge at -0.73 V vs. RHE were detected. These peaks could be explained by the adsorption-desorption processes on the surface. Similar peaks for the Cu(111) in the 0.1 M NaOH solution were observed by Maurice et al. [48]. The adsorbed species were assigned to OH groups. *In situ* STM measurements done by their group showed adsorbate free terraces at potentials more negative than C peak and the transition to rougher terraces after sweeping the potential to A peak in the anodic scan [48]. In our experiments these peaks are slightly lower and their presence can be due to the imperfection of the Gr layer so that uncovered copper surface was present at which the adsorption-desorption process can occur. Figure 81b shows step-by-step increase of the potential range in the anodic direction.

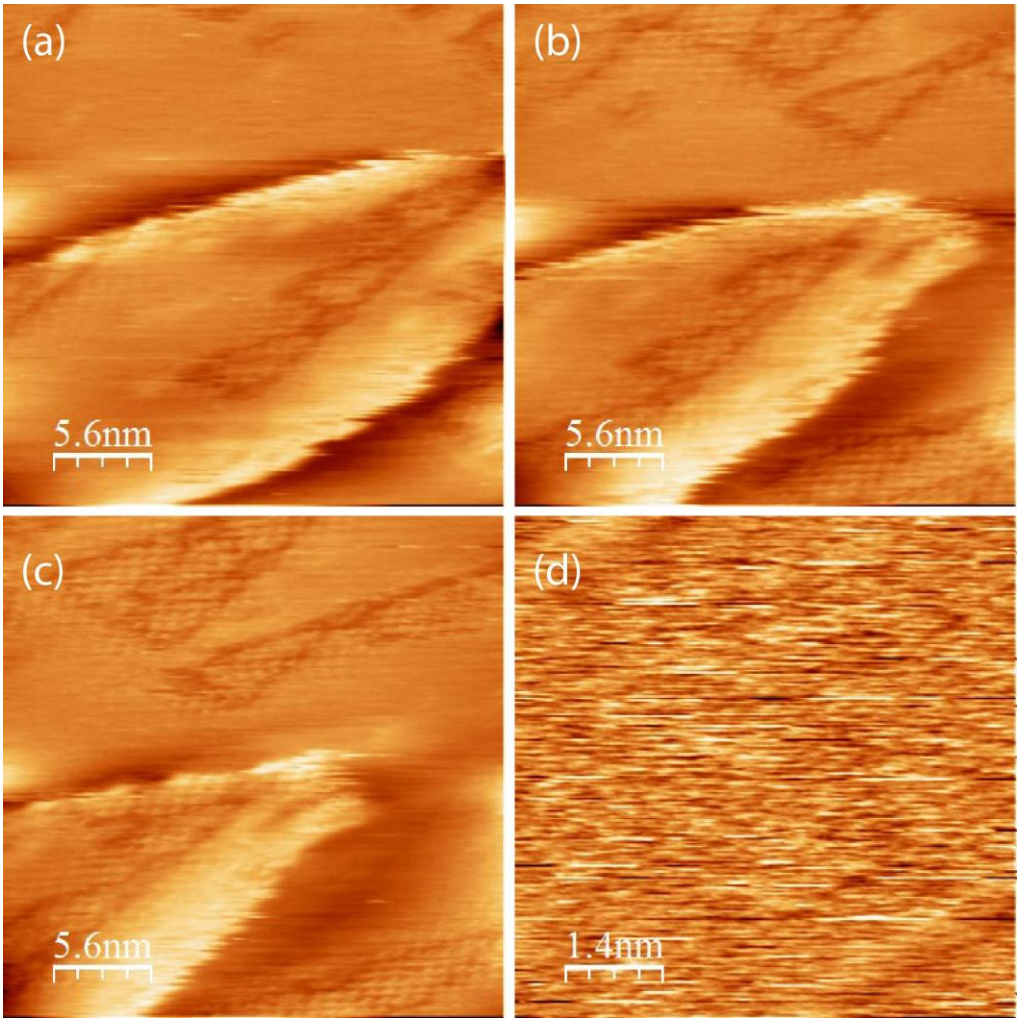

Figure 82. STM images of Gr/Cu(111) in 0.1 M KOH at -0.73 V vs. RHE (I_t = 1.8 nA, V_b = +111 mV).

Figure 82a reports the STM measurements of the Gr/Cu(111) surface, where the reduction of the Cu_2O is observed at potential of -0.73 V vs. RHE after the cycling in the oxidation-reduction region. CVs confirmed that potential step of STM measurements lay after the cathodic reduction peak. The reduction of the oxide is characterized by the formation of the organized islands that were cover by bright structures, which now cover the surface only partially. They form both on the plane and at step-edges and slowly evolve with time (Figure 82a-c). At higher magnification, an ordered hexagonal structure with lattice parameter range from 0.58 to 0.9 nm (due to small drift) are observed Figure 82c which is similar to the hexagonal lattice parameter of 0.6 ± 0.05 nm reported by Maurice et. al [48]. It means the surface, observed by STM, is probably bulk Cu(111) covered by hydroxide/hydroxyl groups. Raman measurements confirmed this assumption. Just small islands (Figure 83a and b) and black graphitic fibers (Figure 83c) showed the Raman signal of carbon. Gr film is broken up into scrolled sheets after the CV in 0.1M KOH.

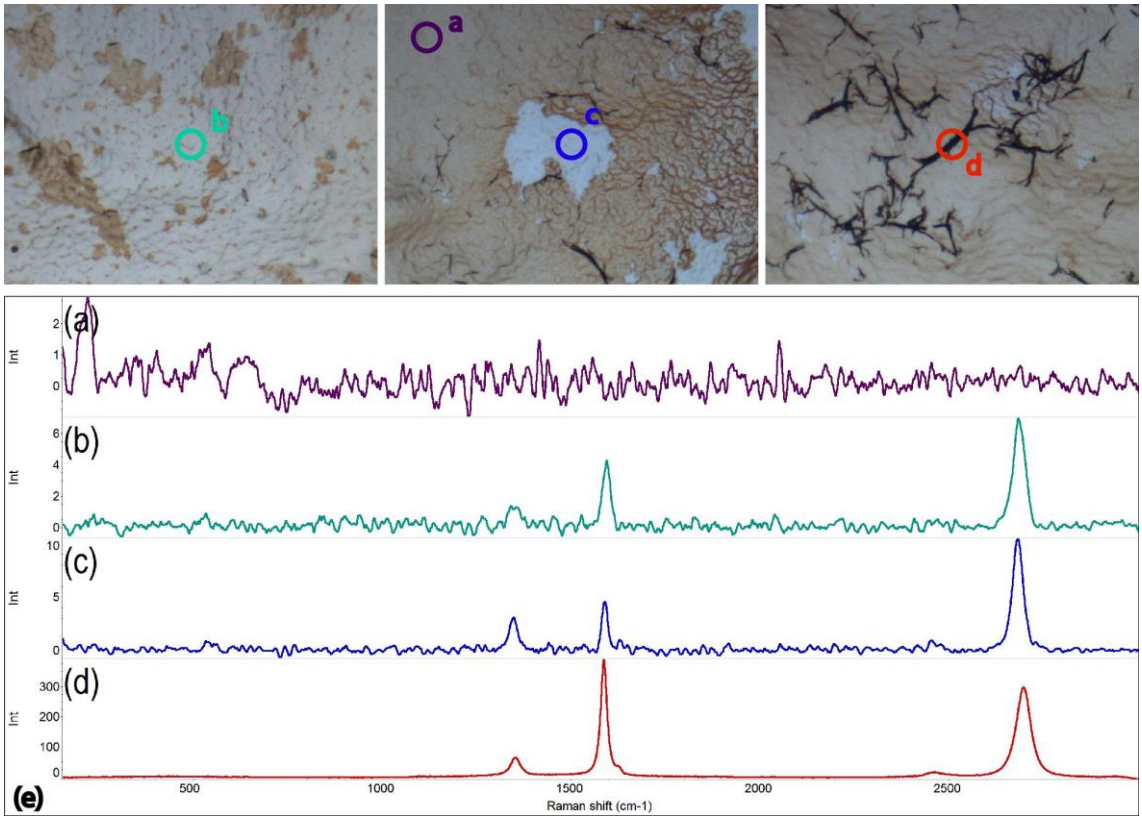

Figure 83. Raman spectra (e) of Gr/Cu(111) after EC-STM measurements in different spots (a-d) of optical microscope images (105 x 140 µm).

4.6. Conclusions

The experimental findings show that a surface Gr layers, grown on Cu, are sufficient to passivate the surface oxidation and corrosion for the short term period. The Moiré patterns, which can be used as support for deposition of metal NPs, were directly observed in different electrolytes using a combination of electrochemical and STM techniques. The step of Moiré is around 2 ± 0.4 nm, typical for the structure of Gr/Cu(111) observed in our different experiments in air and various solutions.

The microscopic structures of monolayer Gr, such as hexagonal carbon lattices, grain boundaries, and wrinkles, which cannot be fully recognized by other surface analysis methods, were observed.

Holes and other defects were created by an etching process (anodic dissolution), if the samples were not in the unreactive double layer region during electrochemical measurements. This behavior at high positive potentials is characteristic for the dissolution of the substrate which is a result of the poor corrosion protection properties of Gr at high anodic potential in acidic electrolytes. Still, the flat and well-ordered surface parts may be used for STM studies. Gr films are suitable to STM measurements since terraces width are big enough to perform proper structural studies.

5. Investigation of metal NPs deposited on Gr films

5.1. Introduction

In this part of the work, Gr/Cu surfaces were used as substrates for the deposition of metal NPs. Pd and Co NPs were used as prototypical catalytic nanoparticles that are active in the HER reaction. The Pd deposition was done by electrochemical deposition or by PVD. Co NPs were deposited by PVD technique. By means of EC-STM and other characterization techniques such as SEM and XPS, the structure and morphology of the resulting films have been investigated. Particular emphasis has been given to the comprehension of the changes induced on the NPs by electrochemical working conditions relevant for the HER.

5.2. Palladium

Up to date Pt-based catalysts remain the best solutions for the water splitting reactions [1]. However, due to the scarcity and high cost of Pt, the research of new catalysts that could replace Pt is gaining more and more momentum. Pd, being a more abundant and less expensive metal, is a potential substitute for Pt, especially when it is in the form of NPs. Actually, it was reported that small palladium nanoparticle supported on Au(111) exhibit higher electrocatalytic reactivity toward HER comparing to bulk metal [166].

At first attempt to deposit Pd NPs on Gr/pCu substrate was done by using the double-pulse deposition technique according to the procedure optimized by Stimming et al. [140]. We expected that Gr should act similarly to HOPG substrate [119, 120]. The deposition was accomplished in an unstirred aqueous solution of 0.6 mM $PdSO_4$ in 0.1 M H_2SO_4, which was purposely deaerated by purging with Ar. The first step was a nucleation pulse of t_n = 10 ms at a nucleation potential of E_n = 153 mV vs. RHE. After that a growth potential (E_g = 293 mV vs. RHE) at more positive value was applied for 100 sec. The Nernst potential calculated for 0.6 mM Pd^{2+} (the standard reduction potential of Pd^{2+} to Pd is 0.915 V vs. RHE) is 0.82 V v. RHE.

For detailed characterization of the morphology of the deposited films, high-resolution scanning electron microscopy (SEM) images were recorded (Figure 84). The whole surface

results to be covered by a thick corrugate Pd layer. It was found that Pd deposition occurs even without applying a cathodic potential. After the introduction of the Gr/pCu sample in a $PdSO_4$ solution the spontaneous reduction of Pd^{2+} on the surface of the sample results in the massive formation of Pd NPs (Figure 84b). SEM micrographs indicate that the whole Gr/pCu surface is covered by Pd NPs (Figure 84).

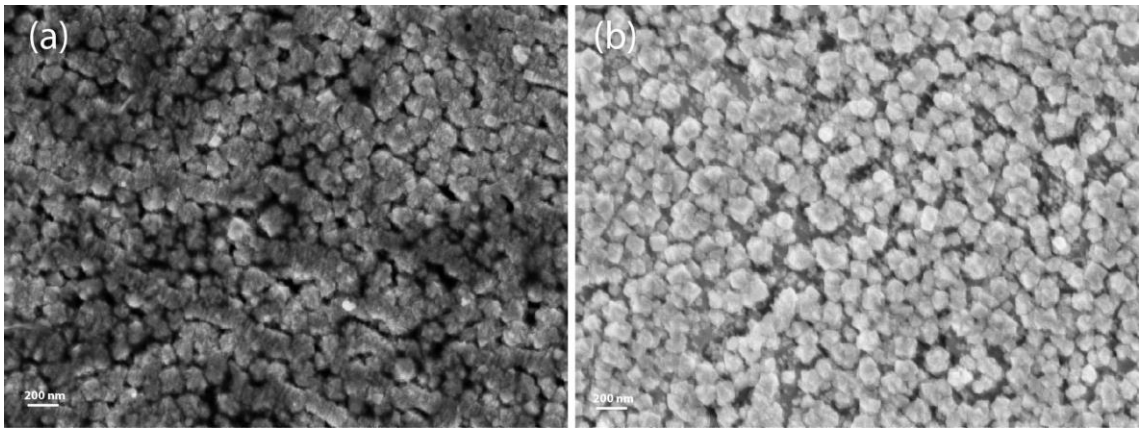

Figure 84. SEM images of Pd NPs deposited from aqueous solution of 0.6 mM $PdSO_4$ in 0.1 M H_2SO_4 (a) Double-pulse technique E_n = +153 mV vs. RHE, t_n 10 ms, E_g = +293 mV vs. RHE, t_g = 100 sec; (b) Electroless deposition at open-circuit potential t_g = 60 sec.

To find the paramenters for the peparation of NPs suitable for STM measurements we have studied the coverage of the NPs as a function of time and potential of the deposition. SEM images showed that micrometer-sized Gr grains presents a uniform distribution of Pd NPs, which are randomly scattered on the entire surface (Figure 85).

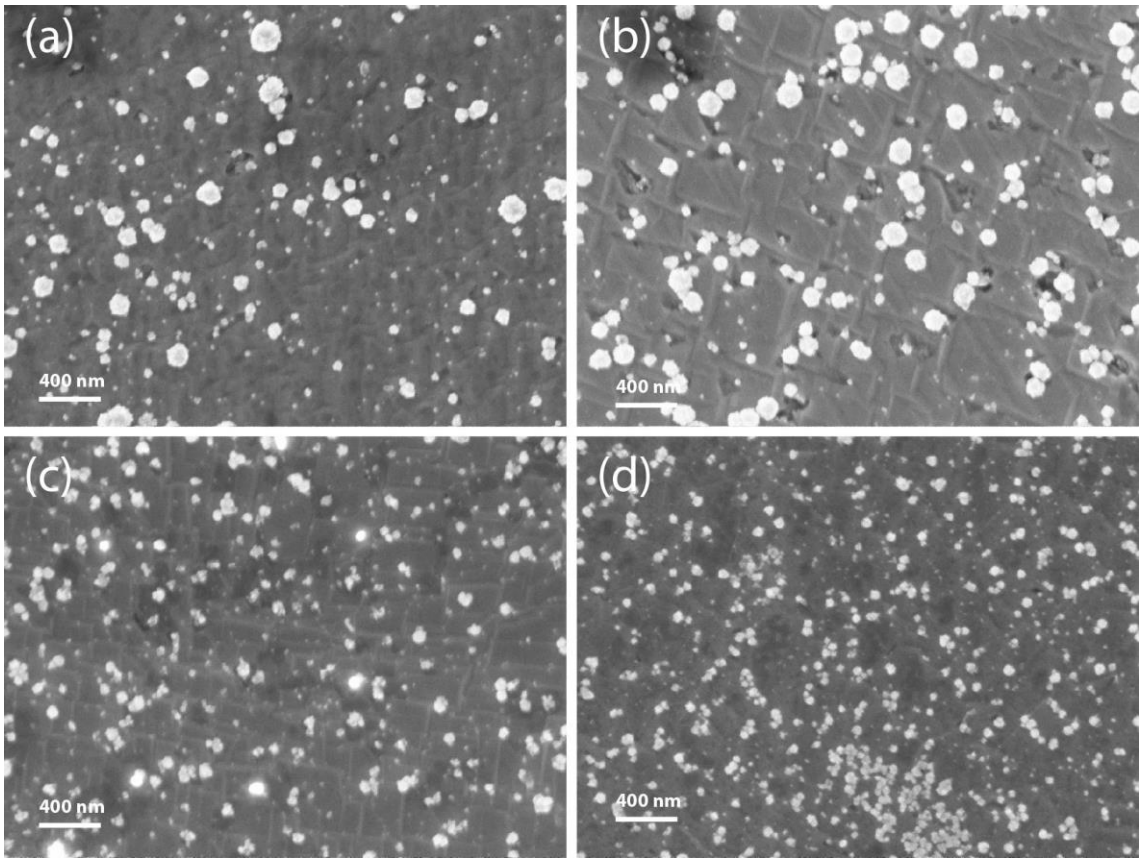

Figure 85. SEM images of Pd NPs deposited on Gr/pCu from aqueous solution of 0.6 mM $PdSO_4$ in 0.1 M H_2SO_4 at (a)-(c) E_g = +153 mV vs. RHE (Time of deposition: (a) 5 sec; (b) 15 sec; (c) 30 sec) and (d) E_g = +243 mV vs. RHE (Time of deposition: 5 sec).

Because of the spontaneous process of Pd electroless deposition the size of the NPs and the distribution cannot be controlled and the size of the Pd NPs results large for the STM measurements (Figure 85a-c). At more positive deposition potential (E_g = +293 mV vs. RHE, Figure 85d) the size of the deposited NPs was smaller due to slower the deposition rate. However, the idea of decreasing further the deposition rate by applying an even more positive potential was not doable due to the concomitant Cu support dissolution.

The spontaneous electroless deposition of Pd NPs by displacement was observed also on Gr/Cu(111) samples (Figure 86), providing results that are very similar compared to the polycrystalline Cu samples. Note that Pd NPs aggregate into big sizes of a few hundred nanometers, forming a random distribution on the Gr/Cu surface.

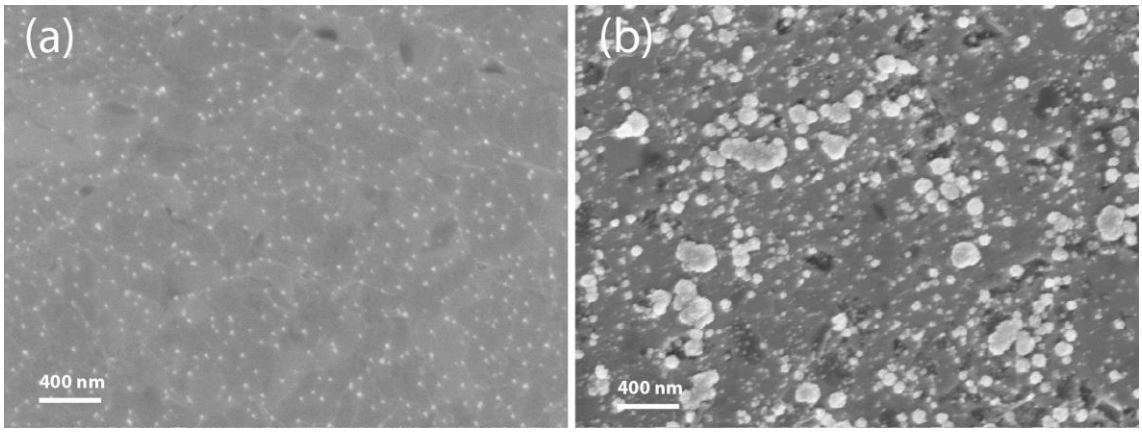

Figure 86. SEM images of free Gr/Cu(111) (a), and Pd NPs after 5 min in solution of 0.6 mM $PdSO_4$ in 0.1 M H_2SO_4 (b).

In order to verify that the particles observed by SEM correspond indeed to Pd NPs, we perform energy dispersive x-ray analysis (EDX). The EDX spectra of a cluster of NPs deposited on the Gr/Cu(111) substrate, shown in Figure 87, reveals that Pd related peaks at around 2.85 keV are present, as well as Cu and C peaks, as expected. The EDX analysis confirmed that this area contained only Cu, C and Pd. However, these outcomes do not indicate whether Pd NPs grow all over Gr layer or only over defects or grain boundaries. To obtain this information, *in situ* STM measurements were performed.

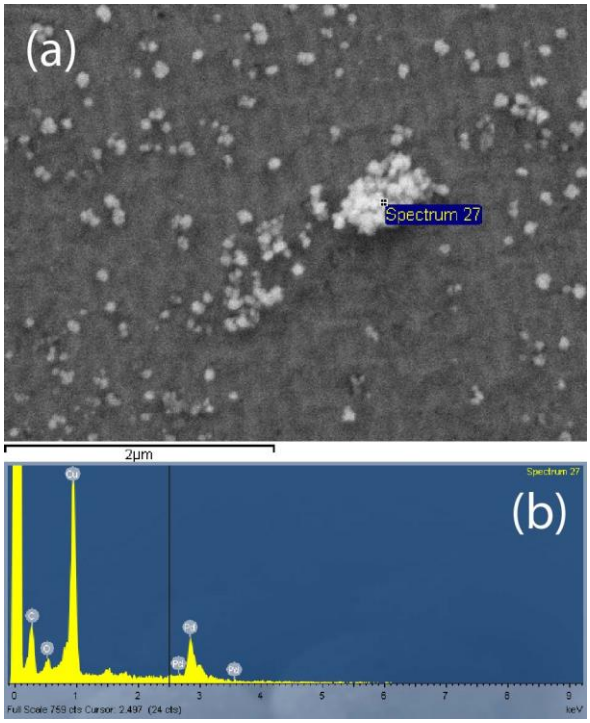

Figure 87. (a) SEM image of the Pd nanocluster; (b) EDX spectrum of the Pd nanocluster.

Investigation of Pd electrodeposition on Gr/Cu(111) by *in situ* STM on a nanometer scale was performed. In this experiments the drop of solution with 0.1 M H_2SO_4 + 0.6 mM $PdSO_4$ (volume of the drop is 10 µL) was added in the standard solution of 5 mM H_2SO_4 of the EC-STM cell (volume around 2.3 mL) after stable STM images in pure acid solution were obtained. The results of the *in situ* STM measurements in Figure 88 show that in case of bare Cu(111) even after one drop all the surface is covered by Pd NPs due to the electroless deposition described above (Figure 88a and b). In comparison to the bulk material the samples covered with Gr (Gr/Cu(111) in Figure 88c and d) remain clean and only Moiré patterns are observed. This results can be explained by inertness of the basal plane of the Gr on Cu(111). Step-edges, observed on STM images of Gr/Cu(111) samples also doesn't covered with Pd probably due to Gr layer, which in this particular example goes through all the step-edge and cover it from the reaction with Pd.

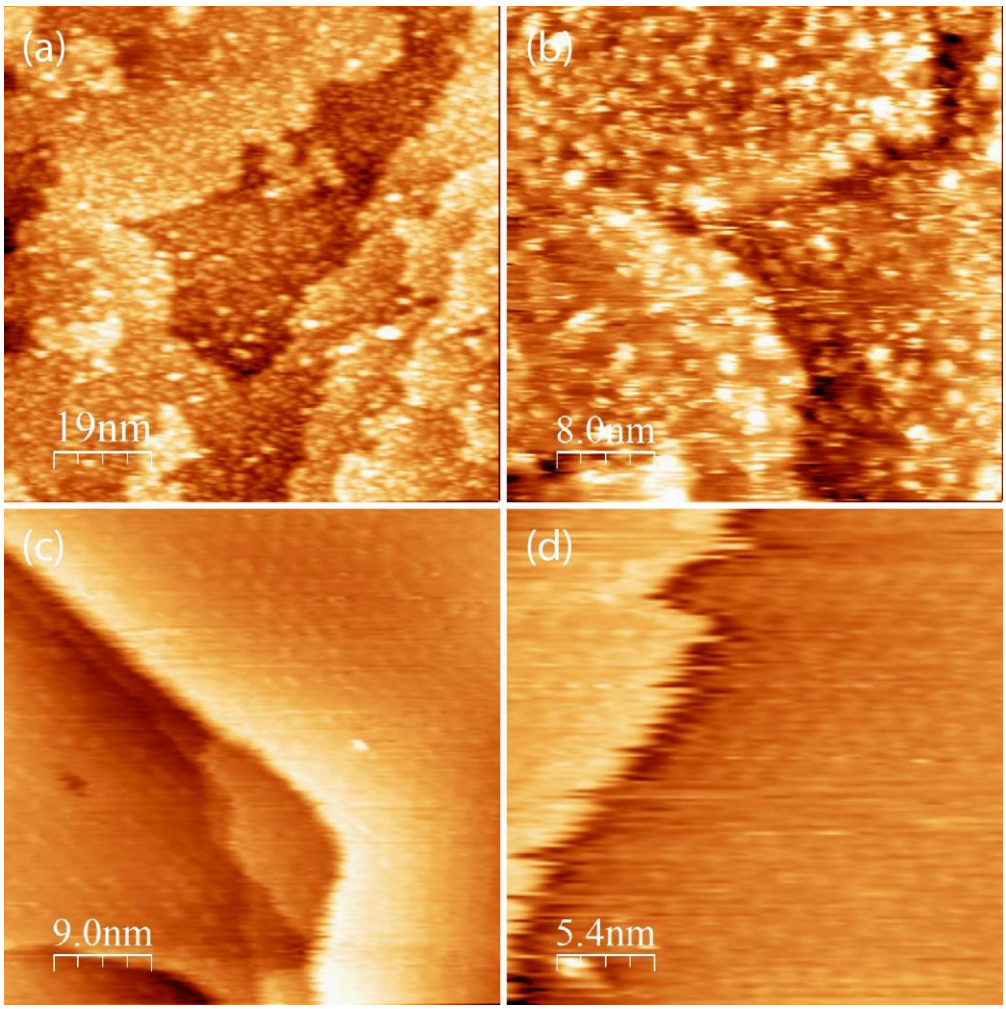

Figure 88. STM images of Cu(111) (a), (b) (I_t = 1 nA, V_b = -69 mV, E_s = -0.14 V) and Gr/Cu(111) (c), (d) (I_t = 1 nA, V_b = -66 mV, E_s = -0.09 V) in 0.1 M H_2SO_4 + 0.6 mM $PdSO_4$.

It appears, that in Gr/Cu(111), the Gr layer blocks the electroless deposition of Pd. Gr is an optimal electron collector, therefore it would help in sustaining the electron flow from copper anodic microdomains to Gr/Cu(111) cathodic microdomains. However, a possible explanation of such behavior is that Gr completely cover the copper surface avoiding the exposition of even small copper domains that would be sufficient for trigger the electroless deposition. In fact, thermodynamic oxidation potential of Gr is much more positive than copper, and therefore it cannot become effective without an applied overpotential.

In order to have more precise control of the Pd deposition process on the Gr/Cu sample surface, the PVD technique in UHV conditions was used. The deposition rate of Pd on the surface was estimated to be around 0.12 ML/min from Angle-resolved XPS (ARXPS) measurements. The deposition of Pd NPs on the surface was checked by XPS. All the XPS measurements were performed at room temperature, using non-monochromatized Al-Kα radiation (1486.6 eV) and pass energy of 50 eV and 20 eV for survey and high-resolution spectra, respectively.

Figure 89a and b present peaks located at 335.8 and 341.1, can be assigned to the binding energy of Pd $3d_{5/2}$ and Pd $3d_{3/2}$ respectively, demonstrating the presence of Pd [168].

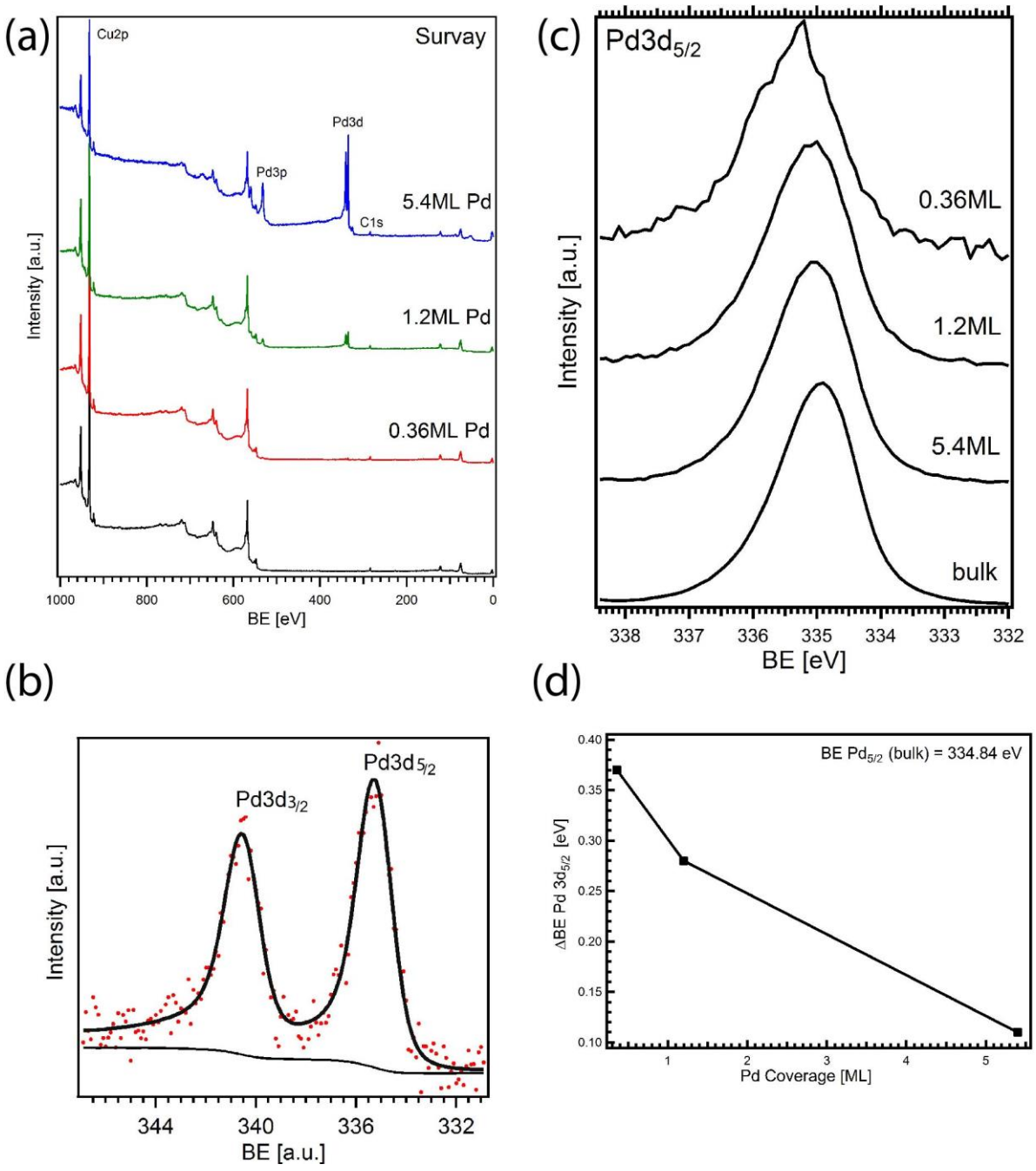

Figure 89. (a) Pd $3d_{5/2}$ XPS data of different Pd(x ML)/G/Cu(111) systems (x = 5.4, 1.2 and 0.36) and (b) ΔBE of the Pd $3d_{5/2}$ signal for the three studied systems, as a function of the Pd coverage.

Figure 89c reports the Pd 3d high resolution photoemission spectra of Pd $3d_{5/2}$, corresponding to different Pd coverage, i.e. Pd(x ML)/Gr/Cu(111) where x = 5.4, 1.2 and 0.36. Figure 89d summarizes the changes in Pd 3d binding energy (ΔBE with respect to the bulk Pd) at different Pd coverage. At low Pd coverage the BE of the Pd 3d peak is shifted towards higher BE and it progressively shifts to bulk like value increasing the coverage.

Similar results have been previously reported also in the case of Pd NPs deposited on HOPG substrate [169].

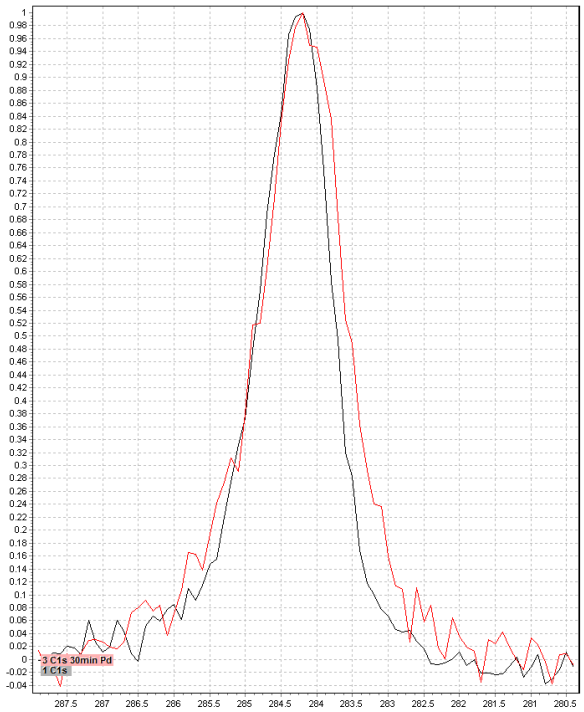

Figure 90. C 1s XPS spectra of Gr/Cu(111) (black line) and Pd/Gr/Cu(111) (red line).

Figure 90 shows the C 1s spectra for the Gr/Cu(111) surface and for the three different Pd (x ML)/Gr/Cu(111) samples (x = 5.4, 1.2 and 0.36). The analysis of these spectra indicates that there is no evident chemical interaction between Pd and Gr and the Pd deposition does not lead to the formation of metal carbides, which is in agreement with previous results reported in the literature [169].

SEM images show how Pd NPs cover the surface of Gr/Cu(111) (Figure 91). After deposition of more than 1 ML of Pd on the Gr/Cu(111) substrate SEM images show uniform coverage of all the surface Figure 91a and b. When only 0.36 ML of the Pd was deposited only islands of Pd with size around 200 nm were observed on the surface of Gr/Cu(111) (Figure 91c).

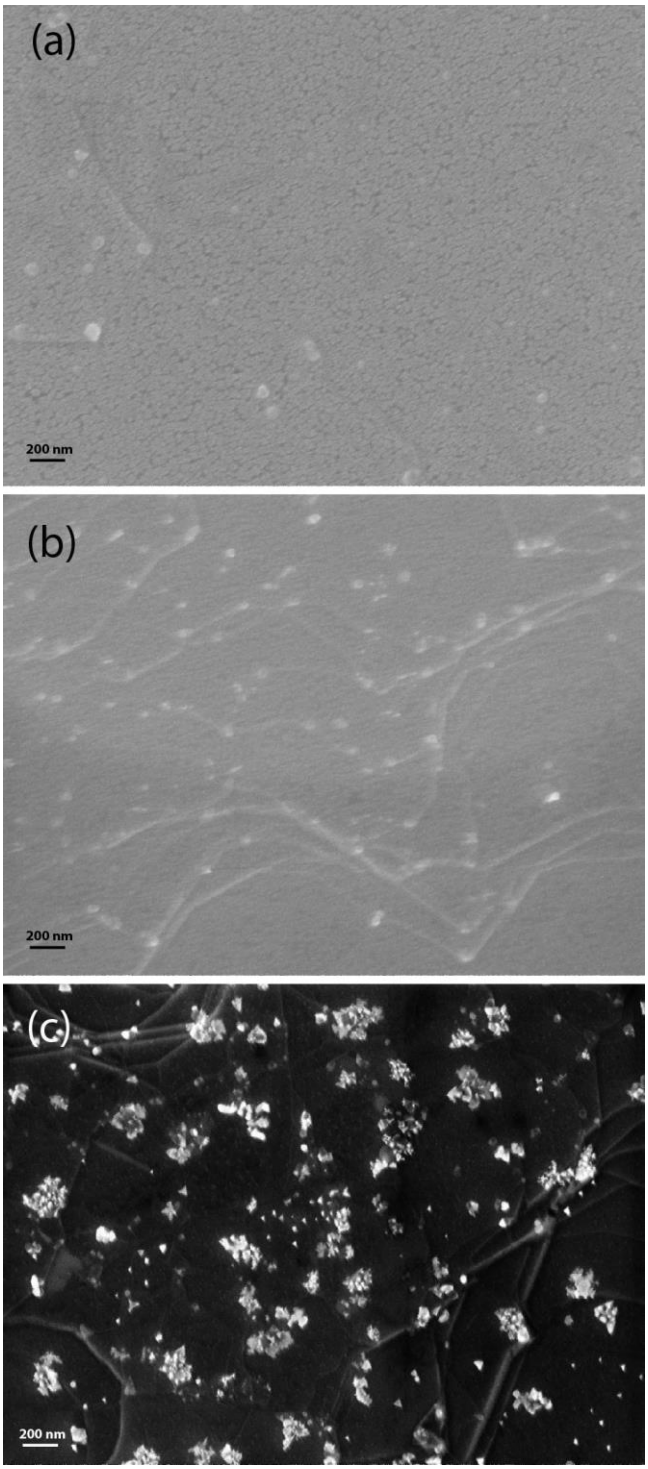

Figure 91. SEM images of PVD deposited Pd(x ML)/G/Cu(111): (a) 5.4 ML; (b) 1.2 ML; (c) 0.36 ML.

The electrocatalytic activity of Pd/Gr/Cu(111) has been examined towards HER. The results have been compared with Gr/Cu(111) substrate and bulk Cu in order to understand whether the presence of Gr allows a sufficient stable potential window to study the changes on Pd NPs by EC-STM.

The electrochemical properties of Gr/Cu(111) in solutions have already been investigated indicating that this support is by itself not active toward HER and shows passivation of copper surface (see Chapter 4). Cyclic voltammograms for Gr/Cu(111), and the Pd NPs deposited on the Gr/Cu(111) substrate with a different loading (0.36 ML, 1.2 ML, and 5.4 ML) are shown in Figure 92. Voltammograms were obtained in argon saturated 5 mM H_2SO_4 solution, whereas the potential was scanned toward positive direction and then to negative direction, at a scan rate of 10 mV/s. The effect of the Pd NPs on the properties of Pd free Gr/Cu(111) sample is reflected by the shift of HER onset potential towards more positive values. It is interesting to observe that CV of the Pd modified Gr/Cu(111) samples don't have the typical features of hydrogen adsorption-desorption or Pd oxide films as was observed on bulk Pd [170] or Pd deposited on HOPG [169].

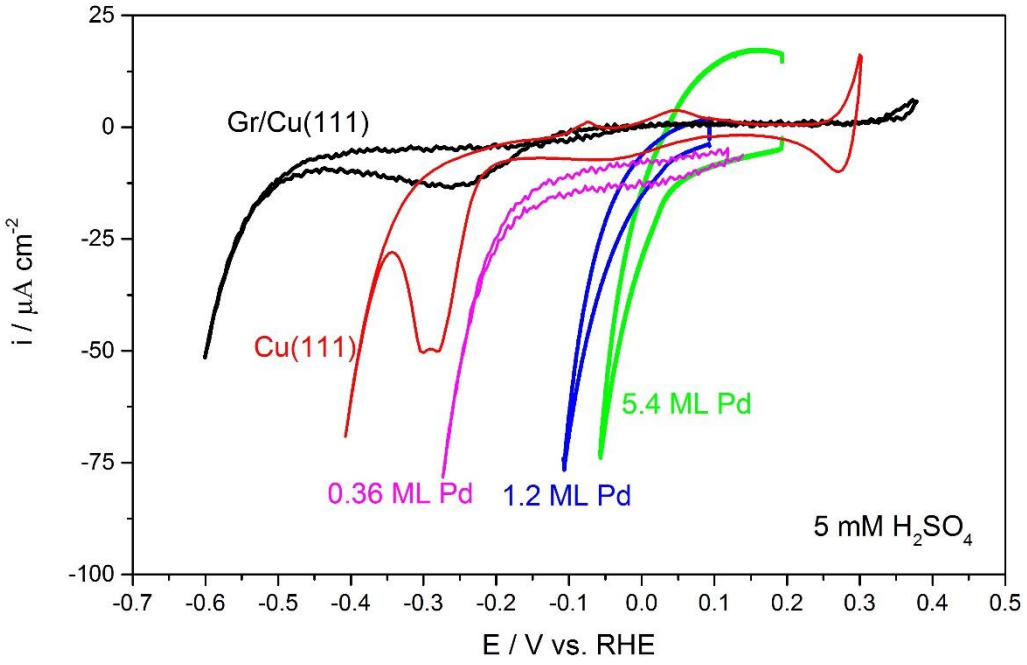

Figure 92. Voltammograms of the Gr/Cu(111) electrode (black line), Cu(111) (red line) and the Pd NPs deposited on the Gr/Cu(111) substrate with the thickness of 0.36 ML (magenta line), 1.2 ML (blue line) and 5.4 ML (green line) in argon saturated 5 mM H_2SO_4 solution (scan rate: 10 mV/s).

The HER at the Pd NPs on the Gr/Cu(111) substrate shows an onset potential at more positive value than Gr/Cu(111) and naked Cu(111) surfaces, even if only a 0.36 ML of Pd was deposited. At the Pd(5.4 ML)/Gr/Cu(111) surface (Figure 92, green line), the onset potential is at ca. 0.05 V vs. RHE, which is more positive by more than +0.25 V than the onset potential

of both Cu(111) substrate and Pd(0.36 ML)/Gr/Cu(111). Similarly H_2 evolution at Pd(1.2 ML)/Gr/Cu(111) surface (Figure 92, blue line), started at ca. 0 V vs. RHE. Strangely, the Pd(0.36 ML)/Gr/Cu(111) surface showed a lower electrocatalytic activity for HER than the Pd(1.2 ML)/Gr/Cu(111) so that further investigation are needed to better clarify this behavior. However, it appears that the catalytic activity depends on the number of monolayers deposited over the Gr/Cu(111) surface, and it is reasonable to assert that the difference in HER current density of Pd-based electrodes is possibly associated to a different electrochemical active surface area.

The onset potential at Pd/Gr/Cu(111) electrodes were close to those reported at Pt electrode which is known to be one of the most effective electrocatalyst for HER [1]. HER activity for Pd(5.4 ML)/Gr/Cu(111) was very similar to those observed at polycrystalline Pd [171] and Pd single crystal surfaces [170], and were different from those observed at copper substrates. Thus, the electrochemical activity for HER was very much increased by the deposition of Pd of less than monolayer on the Gr/Cu(111) substrate. The stability of the Pd NPs on the surface of Gr was checked by SEM after the electrochemical measurements in 0.1 M H_2SO_4. Figure 93a shows the SEM image for the as-prepared Pd(5.4 ML)/Gr/Cu(111) sample obtained by PVD at 1.1 kV, emission current 10 mA and filament current 2.5 A after 45 min of deposition. Figure 93b report the SEM image after electrochemical investigation, where the potential was scanned only in the cathodic direction investing HER region. Figure 93c shows the SEM image after the acquisition of CV in O_2 satured solution and investigating also the anodic part of the available potential window (insert of Figure 93c).

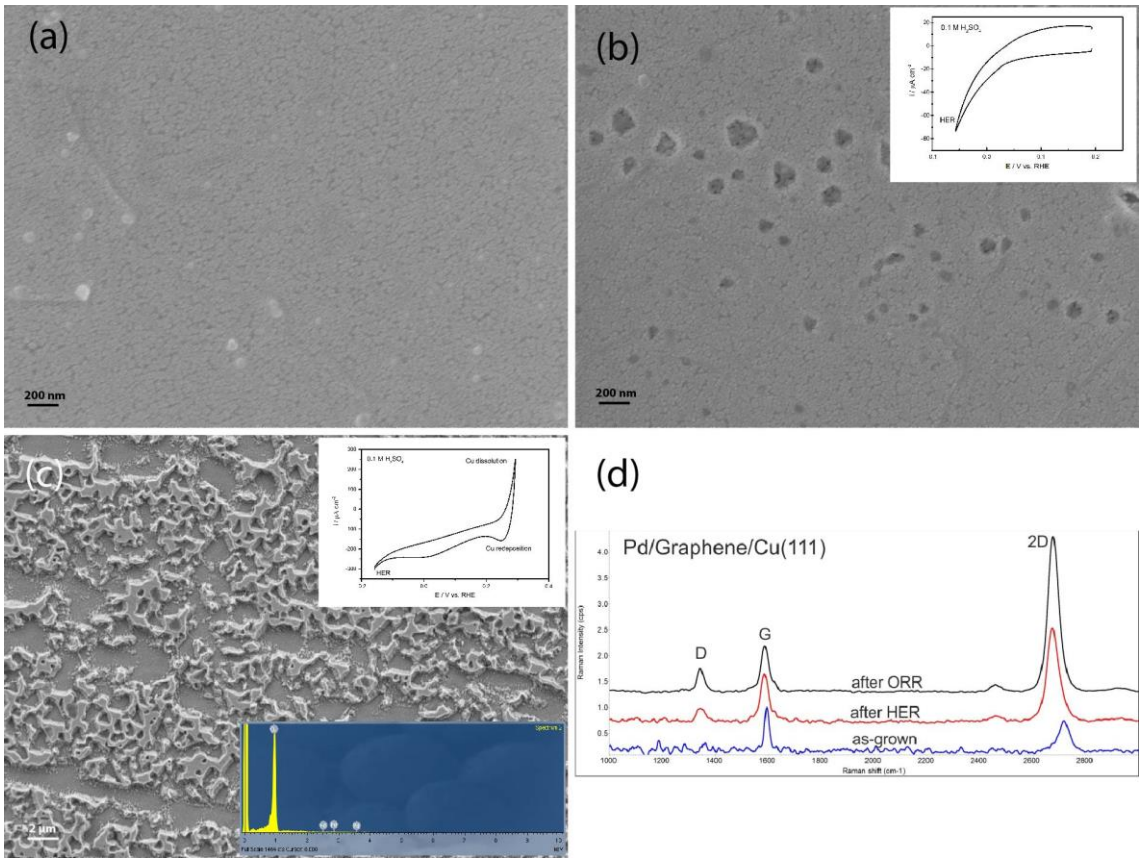

Figure 93. SEM images: (a as-prepared Pd(5.4 ML)/Gr/Cu(111); (b) Pd(5.4 ML)/Gr/Cu(111) after HER cycles (insert: CV of Pd(5.4 ML)/Gr/Cu(111) in 0.1 M H_2SO_4, scan rate: 10 mV/s); (c) after ORR (insert top right: full range CV, insert bottom right: EDX spectrum; (d) Raman spectra after each step.

The comparison of the SEM images of the surface of as-prepared sample with SEM images, obtained after each step, shows that after HER the surface remains almost the same as just prepared and only some small changes (grey hollows in Figure 93d) could be observed. The explanation of this spots could be the effect of the H_2 gas bobbles growth on the surface during the high negative potential. Figure 93c present SEM after the full range CV scan. Surface became very rough due to copper dissolution, however, EDX and Raman spectra (Figure 93d) proved that Pd and Gr are still present on the surface even after the measurements involving Cu dissolution.

5.3. Cobalt

In the last part of the work we finally examined the behavior in electrolyte solutions of Co NPs. Co as non-noble metal attracts a lot of scientific and technological interests for the development of the low cost but effective catalyst for HER. According to theoretical

calculation Co has a low energy barrier for H adsorption [172]. Many Co-based materials have been designed to catalyze the HER especially in combination with graphene which increase the stability of catalysts [2,3,173].

Co was deposited by PVD on the surface of Gr/Cu(111) to obtain Co/Gr/Cu(111). Islands of Co were formed by evaporating (up to 8.5 min) in ultrahigh vacuum conditions the equivalent coverage of 3 ML of Co on the Gr/Cu(111) surface at 60 °C ($P \leq 10^{-9}$ mbar). Figure 94 shows STM image of the Gr/Cu(111) surface after 3ML Co deposition.

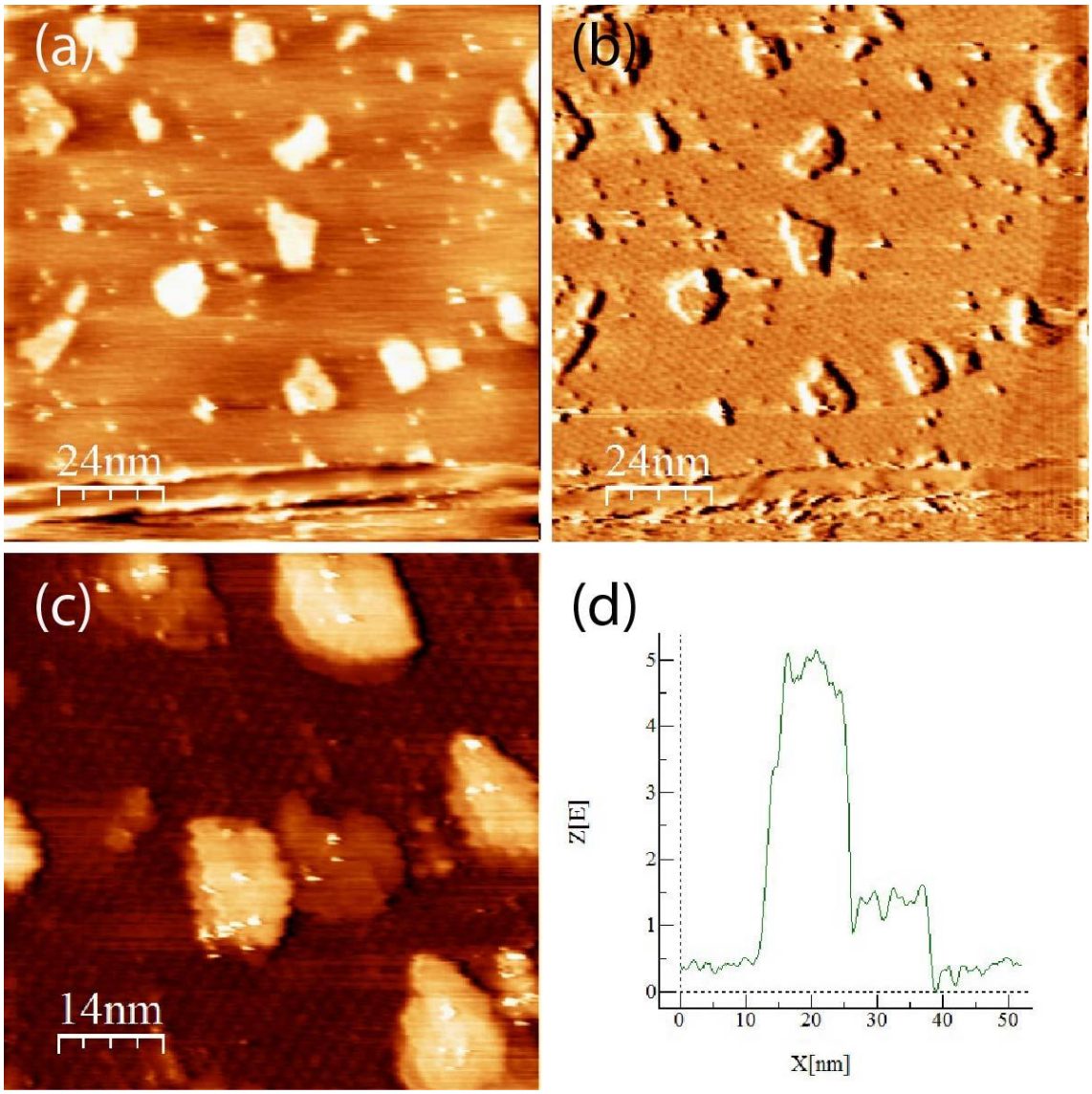

Figure 94. Topography (a) and high resolution (c) STM images in air of the Gr/Cu(111) surface after 3 ML of Co deposition by PVD (I_t = 1.8 nA, V_b = -50 mV); (b) current image of the a. (d) Profile line in the middle of the image c.

Contrast of Figure 94c is adjusted so that fine structures on both Gr/Cu(111) substrate and Co islands can be clearly observed. Topographic images of the as deposited film show the presence of Co well separated three dimensional islands growing following a typical Volmer-Weber morphology Liao et al. report similar results of 3D growth of Co clusters on Gr/Ru(0001) surfaces [174]. The average size of the Co islands is around 15 nm, and the height is from 1.5 to 4.6 nm for 1 to 3 layers respectively (Figure 94d). Our electrochemical experiments showed that Co NPs, as a non-noble metal, are not stable on the surface in acidic solutions and were completely dissolved after the contact with solution.

In order to protect Co NPs from dissolution, it was exploited the ability of Co to intercalate under the Gr layer as a consequence of a thermal treatment [175]. For this reason, a sample with 3ML Co on Gr/pCu was heated at 400°C for 15 minutes. Figure 95a is the XPS data of Gr/pCu sample (black line) and 3 ML Co NPs deposited by PVD (red line), whereas the green line belongs to the sample of Co intercalated under Gr. Furthermore, blue line on Figure 95a shows the intercalated Co sample after the polarization measurements in 0.1 M $HClO_4$. XPS data indicate that after intercalation the Co 2p is still present and the ratio of the C 1s to Co 2p is increased from 0.062 (red line) to 0.115 (green line).

After the intercalation in UHV conditions, the sample was transferred to electrochemical cell through the transfer system in order to avoid the contact of the sample with ambient atmosphere and oxidation of the reactive Co NPs. The polarization measurement of Gr/Co/pCu sample in 0.1 M $HClO_4$ is shown in Figure 95c. The onset potential of HER measured by linear sweep voltammetry is around -0.38 V vs. RHE. This potential is similar to one, measured on Gr layers without NPs and lower than HER onset potential of bulk copper, which means that the Co NPs do not influence the reactivity of the Gr/pCu sample after intercalation. This result doesn’t support the literature reports of extremely low overvoltage of HER on Co, covered with Gr [2,3], probably due to very low amount of Co metal (3 ML), used in our experiments.

XPS analysis of the sample after electrochemical measurements (blue line in Figure 95a) shows increasing of the C 1s peak due to contamination from the solution and appearance of the peak of oxygen (O 1s peak marked by arrow in Figure 95a). High

resolution XPS spectra of Co 2p before and after electrochemical measurements are presented in Figure 95b. The main peak of Co 2p at 778.2 eV after the measurements in 0.1 M $HClO_4$ has lower intensity (blue line) than before (green line) but still shows typical metallic state of the Co without oxide component, which shifts the main Co $2p_{3/2}$ peak to 780.4 eV [176]. This data proves that Gr layer prevents the oxidation of intercalated Co.

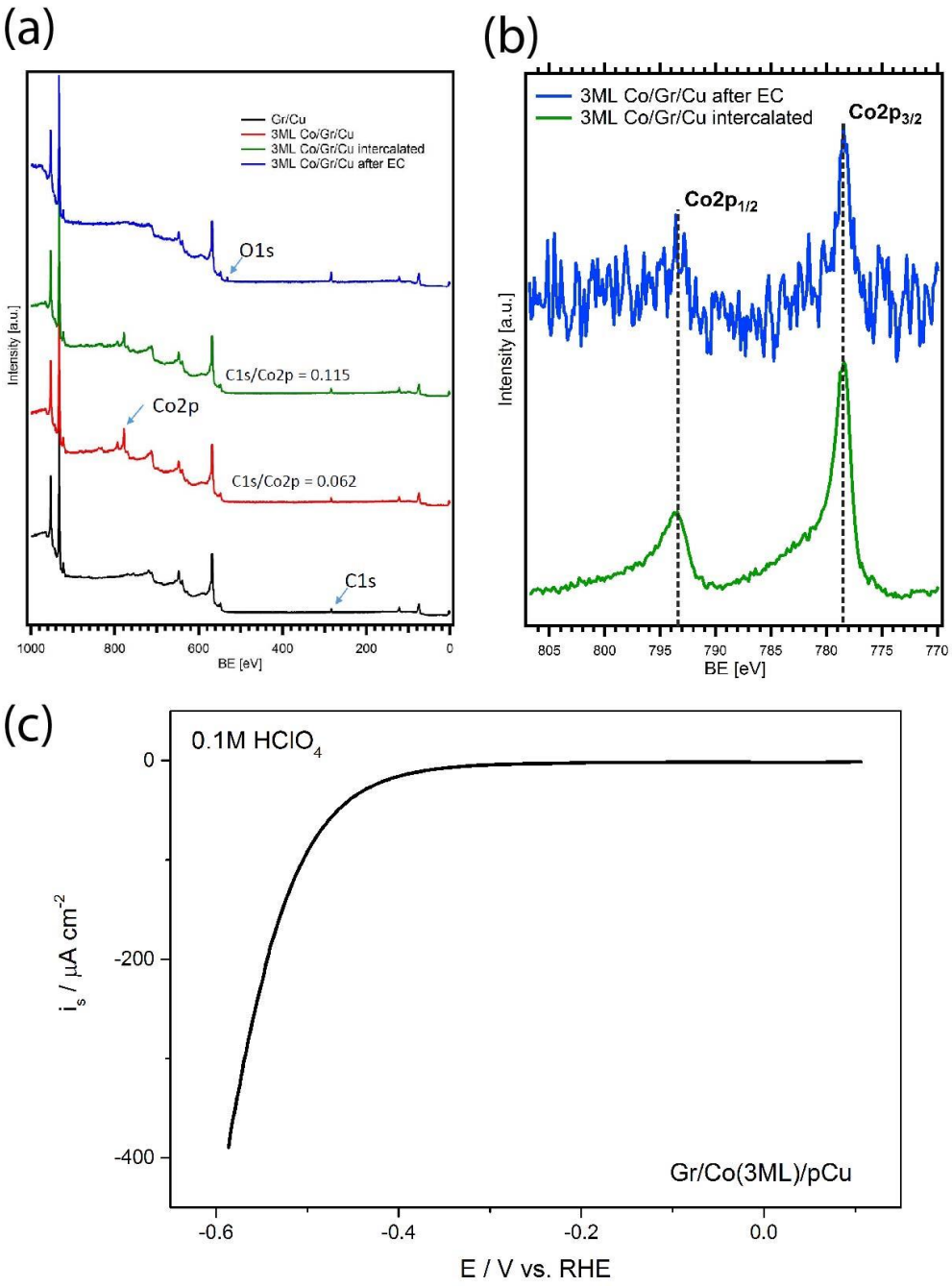

Figure 95. (a) XPS spectra of Gr/pCu sample (black line), 3 ML Co/Gr/pCu (red line), Gr/Co/pCu (green line). Gr/Co/pCu after the polarization measurements (blue line); (b) High resolution XPS spectra of Co 2p ; (c) linear sweep voltammogram of Gr/Co/Cu(111) in 0.1 M $HClO_4$ (scan rate: 5 mV/s).

The experiment of the intercalation of 3ML Co was extended to the Gr/Cu(111), which gave the possibility to study the structure of the surface by EC-STM. The same increasing of the C 1s/Co 2p ratio from 0.07 to 0.188, for Gr/Co/Cu(111) sample, was observed (Figure 96a). High resolution XPS spectra of C 1s doesn't show changes in the carbon peak between the intercalated and non-intercalated sample (Figure 96b). Consequently, the increase of the C 1s/ Co 2p ratio is due to lower intensity of Co NPs, covered by Gr.

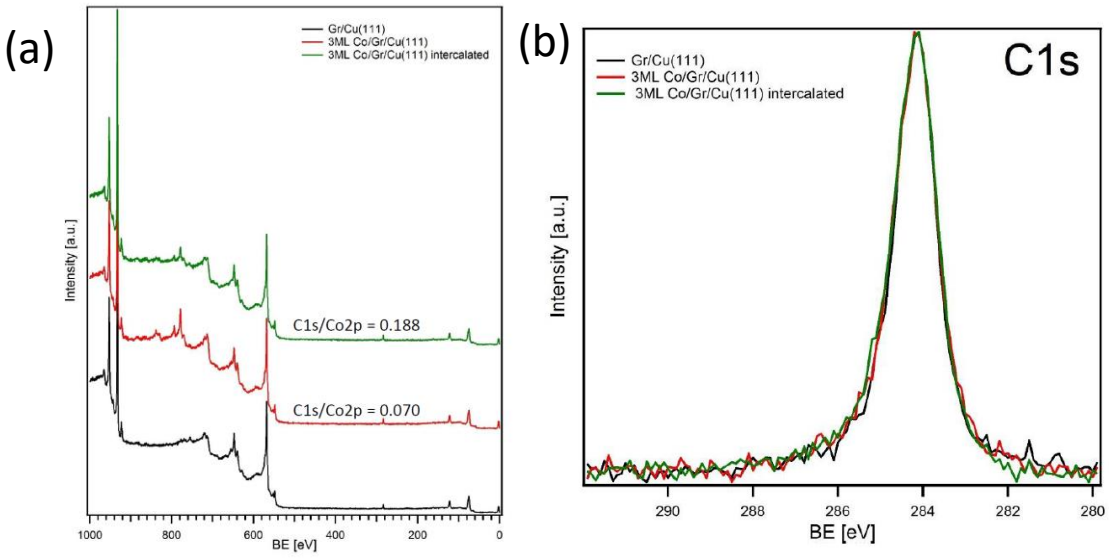

Figure 96. (a) XPS spectra of Gr/pCu sample (black line) with 3 ML Co NPs deposited by PVD (red line), which than were intercalated under Gr (green line).

Figure 97 presents the STM image of Gr/Cu(111) with 3 ML Co intercalated at 400 °C under the Gr. Co islands on the surface of the Gr/Co/Cu(111) sample, similar to those Co/Gr/Cu(111) (Figure 94a-c), weren't observed. Only small defects (bright points) on the surface, typical for Gr layer, which were discussed previous, can be seen. Moiré pattern with step 1.6 ± 0.1 nm, similar for all our experiments was observed. Our results are in agreement with earlier reports [175]. Decker et al. studied intercalation of Co NPs under Gr layer on Ir (111). They explain the similar periodicity and orientation of Gr Moiré patterns before and after intercalation of the Co by pseudomorphic character of the Co layer with substrate.

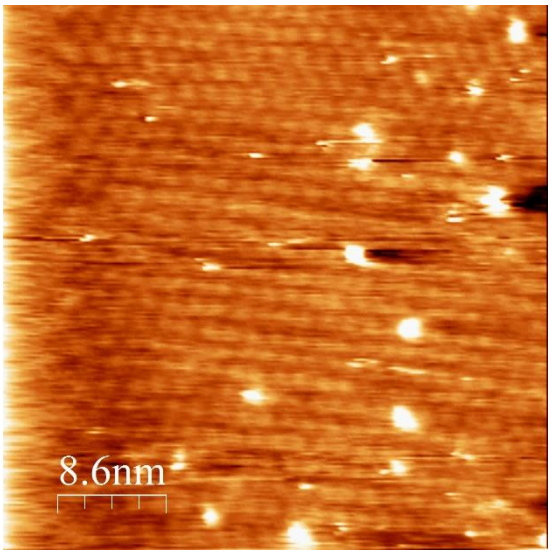

Figure 97. High resolution STM image of 3ML Co intercalated in Gr/Cu(111) sample in air (I_t = 1.8 nA, V_b = +10 mV)

HER on the sample with higher amount of Co (10 ML) intercalated in Gr/Cu(111) sample was studied by CV (Figure 98). The higher Co loading was supposed to increase the influence of the Co NPs on the electrochemical behavior. CV shows how onset of HER potential shifts to more positive values in the presence of Co NPs, but it is still less active than the bulk Cu(111). Typical peaks of desorption (around -0.3 V) and adsorption (> -0.1 V), observed on the bulk Cu(111) are absent on the samples on Gr/Cu(111) and Gr/Co/Cu(111) samples.

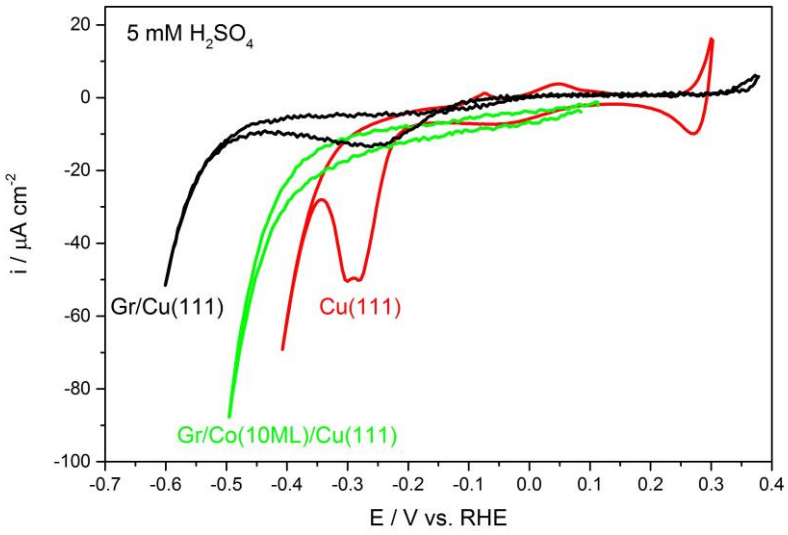

Figure 98. CV of 10 ML Co intercalated in Gr/Cu(111) (green line) compared with Gr/Cu(111) sample (black line) and bulk Cu(111) (red line) in 5 mM H_2SO_4. Scan rate: 10 mV/s.

The investigation of the Co/Gr/Cu(111) was extended in alkaline electrolyte (0.1 M KOH), where Co NPs should be stable [177]. Figure 99 shows the STM results, obtained for Co(5 ML)/Gr/Cu(111) in air (a) and in 0.1 M KOH (b). At -0.71 V Co islands (bright areas) with height of 1 atomic layer (0.25 nm) were observed (Figure 99c). They were stable in these conditions.

Cyclic voltammogram of Co/Gr/Cu(111) sample in 0.1 M KOH is shown in Figure 99d. Two anodic peaks at 0 V and 0.2 V vs. RHE and the corresponding cathodic counterparts at approx. -0.2 V and -0.4 V vs. RHE are present and are appointed to Cu oxidation step, which was already described in a previous chapter of this thesis in. The peak at around 0.8 V vs. RHE was not observed in CV of bulk Cu(111) or Gr/Cu(111). According to Burke and Murphy [178], Co in 1 M NaOH has two peaks at 0.4 V and ca. 0.95 V which were attributed to oxidation of Co to CoO and subsequent oxidation of CoO to Co_3O_4, respectively. In our case, the peak at 0.4 V was not observed and it can be explained by the fact that during the transfer of our sample from the preparation chamber to EC-STM, the Co NPs already oxidized to CoO, so only the second peak of cobalt-cobaltic oxide formation is present (peak around 0.85 V vs. RHE). The stability of these particles on the Gr/Cu(111) surface in 0.1 M KOH was also confirmed by SEM analysis. Figure 100 shows the SEM images of as-prepared Gr/Cu(111) sample before Co deposition (a), sample covered by 5 ML Co film (b), and surface of Co/Gr/Cu(111) sample after the *in situ* STM measurements in 0.1 M KOH solution (c). SEM image in Figure 100b presents uniform coverage of the 5 ML Co film. After the measurements in 0.1 M KOH electrolyte SEM shows that Co NPs remain on the surface (Figure 100c).

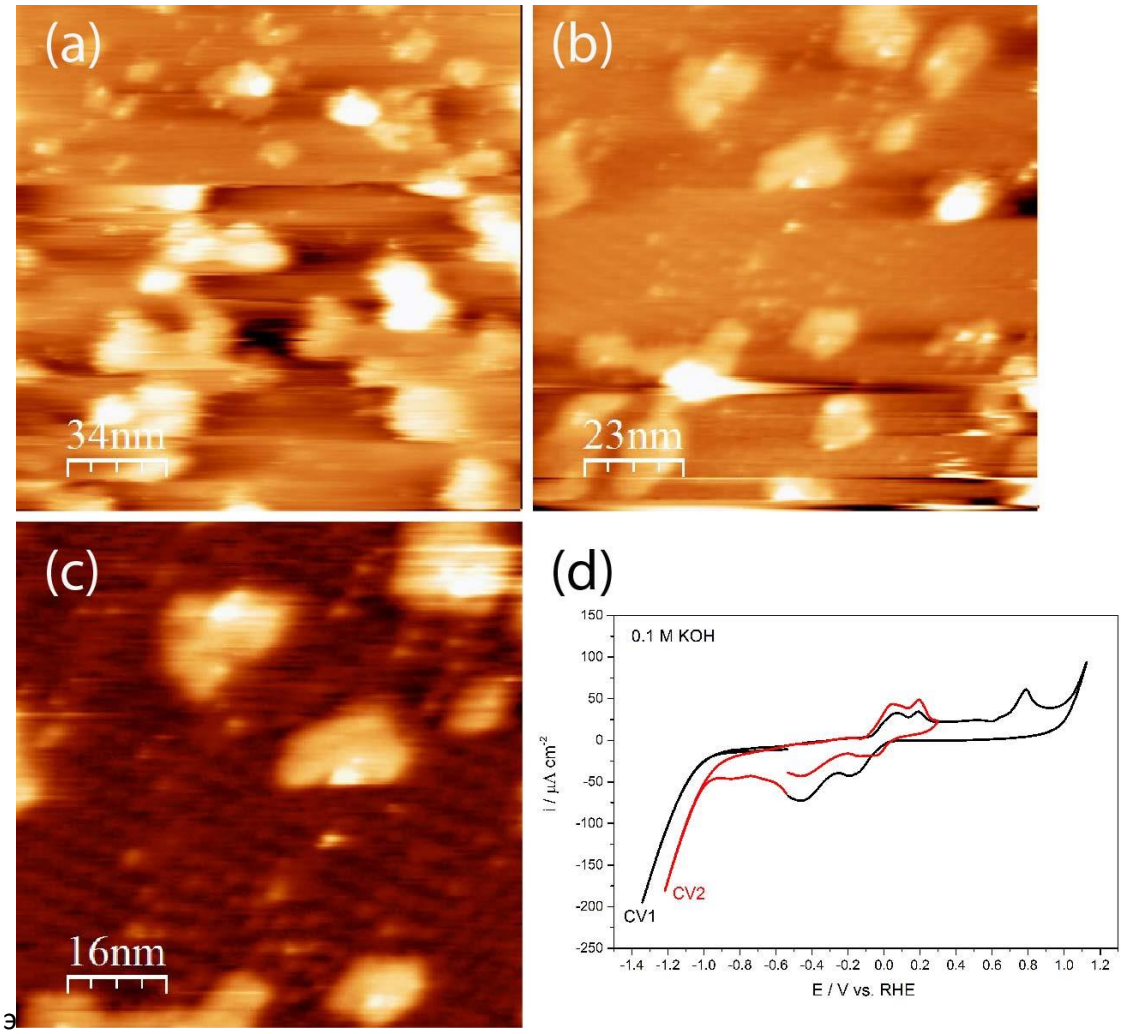

Figure 99. STM images of Co(5 ML)/Gr/Cu(111) (a) in air (I_t = 1.8 nA, V_b = +10 mV); (b) in 0.1 M KOH (I_t = 1.8 nA, V_b = +492 mV; E_s = -0.71 V); (c) Close-up of the center of the image b; (d) CV of Co(5 ML)/Gr/Cu(111) in 0.1 M KOH (scan rate: 10 mV/s).

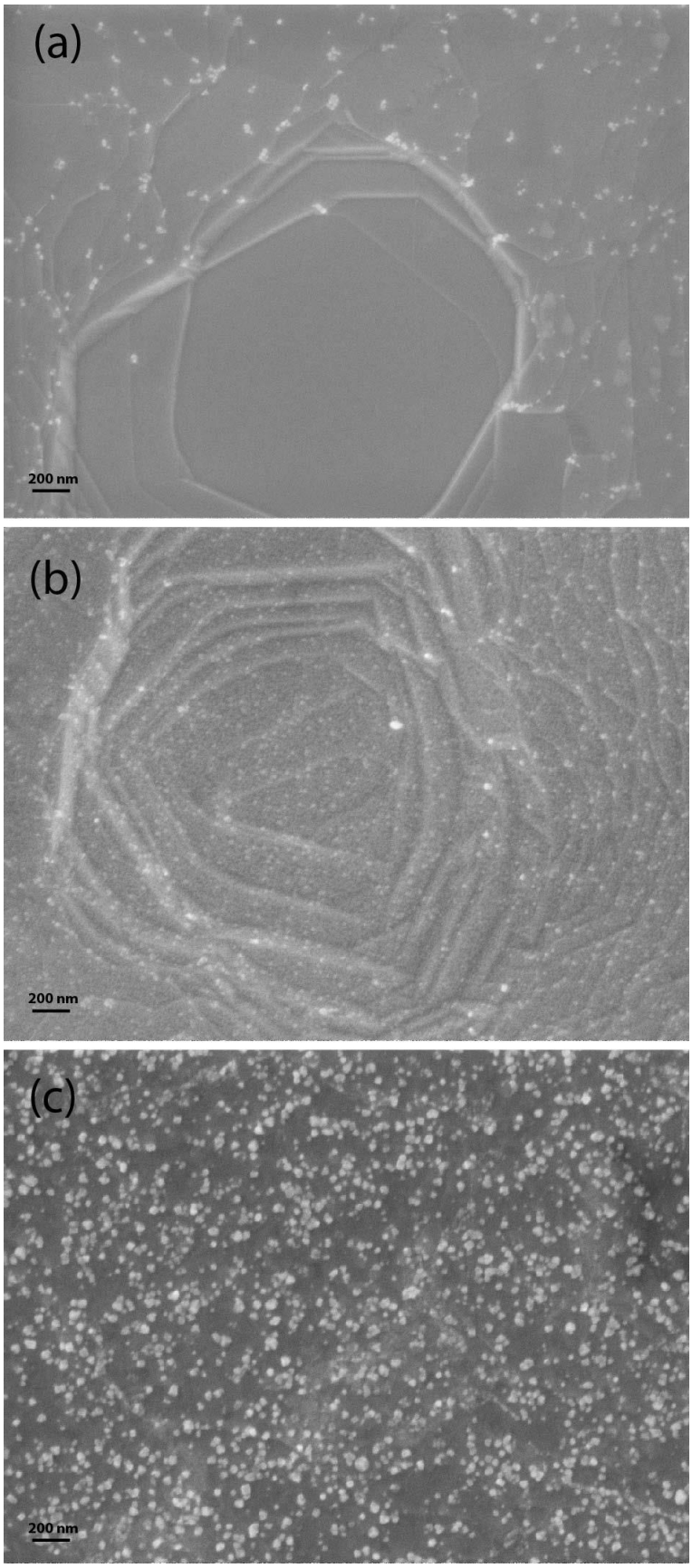

Figure 100. SEM images of Gr/Cu(111) as-prepared (a); with 5 ML Co (b) and after *in situ* STM in 0.1 M KOH (c).

The Raman spectra reported in Figure 101 shows how the quality of Gr on Cu surface changes after the deposition and intercalation of Co NPs, and after the *in situ* STM measurements of Co/Gr/Cu(111) system in 0.1 M KOH electrolyte solution.

The cobalt deposition on the surface of Gr/Cu(111) increases the number of defects as demonstrated by the I_D/I_G ratio, which increased from 0.25 to 0.66, moreover the 2D peak became less intense (i.e. I_{2D}/I_G ratio decreased from 0.72 to 0.53). In addition, after Co deposition 2D band of Gr were slightly broader (magenta line in Figure 101) due to increasing of disorder [179]. An even stronger effect can be observed when Co is intercalated under the Gr layer (I_D/I_G ratio is 0.86 and I_{2D}/I_G is 0.5). It is not surprising due to the fact that for the process of intercalation cobalt brakes C-C bond in Gr layer and forms defects. Ideally, these C atoms should recombine after the intercalation of Co under Gr, but some of them remain unbonded and this increases the D band of Raman spectrum (orange line in Figure 101).

After the *in situ* STM measurements of the Co/Gr/Cu(111) sample in 0.1 M KOH, the Raman spectrum was quite different (red line on Figure 101): all the three peaks were much more intense, the D band increased drastically (I_D/I_G = 2.5) and the peak D' at 1625 cm^{-1}, activated by an intravalley scattering process which also requires defects, appeared. The 2D peak also increased and became higher then G band (I_{2D}/I_G = 1.2). All this changes, observed also in previous experiments, can be explained by intercalation of the solution under the Gr, decoupling it from the surface of Cu [119].

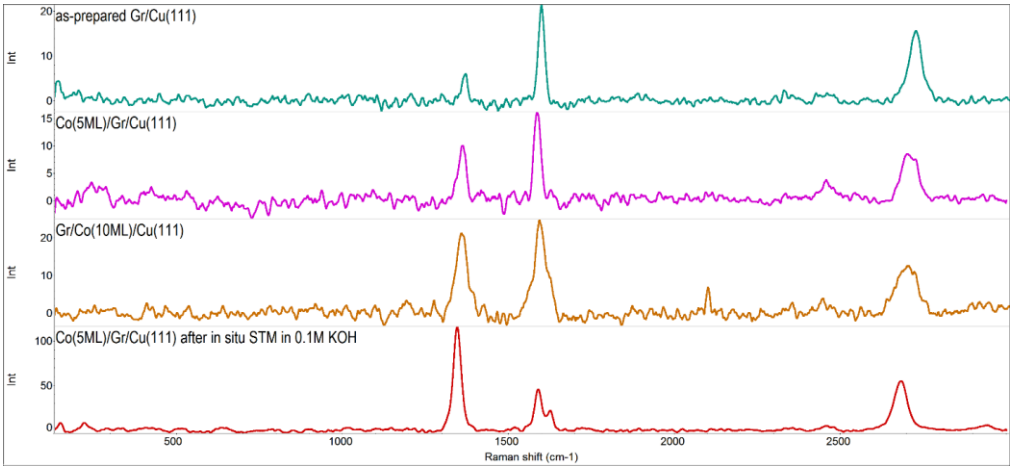

Figure 101. Raman spectra of as-prepared Gr/Cu(111) (green line); Gr/Cu(111) sample after PVD deposition of 5ML Co (magenta line); Gr/Cu(111) sample after intercalation of 10ML Co (orange line); 5ML Co/Gr/Cu(111) sample after *in situ* STM in 0.1M KOH (red line).

5.4. Conclusions

For better understanding of the catalytic efficiency of the metal NPs, a correlation of the surface structure and coverage with the reactivity of HER on the NPs surface was investigated by both structural analysis technique such as STM and electrochemical methods.

Two different type of metals: noble Pd and non-noble Co were used to study their catalytic activity toward HER.

The electrochemical deposition of Pd metal NPs was made directly on Gr/Cu(111) samples from $PdSO_4$ solutions in H_2SO_4 acid. Due to the spontaneous process of Pd deposition on the Gr/Cu surface by metal displacement reaction, the precise control of the amount of the deposited Pd was difficult.

More suitable method of PVD was used to obtain required quantity of metal NPs.

Cyclic voltammetry was used in order to study the influence of Pd metal coverage of the samples on the HER. The activity of palladium toward HER was found to increase with increasing the amount of Pd NPs on the surface. The HER on active Pd NPs at potentials, close to Cu dissolution complicated the *in situ* STM study of these samples.

Co NPs also were deposited by PVD process in UHV. The experiments show very low stability of Co NPs in acidic solutions. Annealing of the Co/Gr/Cu(111) leads to intercalation of Co atoms between the Gr layer and the Cu substrate. This phenomenon was used to protect Co from dissolution in acids by Gr layer. The activity of intercalated Gr/Co/Cu(111) toward HER was measured by CV, but the structural STM study didn't give useful information due to very low amount of loaded metal and very complicated interface system liquid/Gr/Co/Cu(111).

To avoid fast dissolution of Co NPs *in situ* measurements in 0.1 M KOH were performed. This system allowed to observe stable Co islands on the surface of Gr/Cu(111) samples.

6. Summary

Immediately after its discovery, graphene (Gr) became one of the most promising materials for a variety of technological applications. In the last years, a great deal of studies have been focusing on the understanding of its fundamental physicochemical properties, reaching outstanding results. On the other hand, the comprehension of the functional properties of Gr and its interaction with other system is still a field in its infancy, which is still based on a high level of empiricism. This lack of knowledge can be possibly filled by the preparation of "model composite systems" and the exploitation of in situ technique that allows the study of functional systems directly during their use. In this work Gr of high quality with low number of defects and grain boundaries was grown on Cu substrates by Low Pressure Chemical Vapour Deposition (LPCVD) in order to obtain highly reproducible supports for metal NPs. The resulting nanocomposites were used as model catalysts for fundamental studies. CVD was chosen as Gr growth technique since it is a fast method with high yield, which allows to obtain layers with highly controlled morphology and defectivity. Cu was selected as substrate for Gr growth due to the low solubility of C in Cu [70] and "self-limiting" character of the deposition [67]. The deposition of Gr films was performed in our home-built cold-wall reactor: Hydrogen gas was used for the annealing of the Cu sample before growth in order to remove the native copper oxide layer from the surface and ethylene was used as carbon precursor. This newly build CVD reactor could be used for deposition of Gr on different metal substrates. By a systematic investigation of the growth parameter, it has been possible to identify the optimal recipe for the growth of a fully covering defect Gr layer, which consisted of 10 min of growth time, 1 mbar of C_2H_4 pressure, at 850°C.

Raman spectroscopy as fast, nondestructive characterization technique, was used to confirm the formation of Gr, due to its characteristic vibrational fingerprint, which can be used to characterized the main structural properties of Gr layers. The coverage and morphology of Gr on Cu age were analyzed by SEM. Additional characterization by XPS and LEED were used to support the results. STM was used to analyze the topography of the graphene/copper surface and confirm the uniformity of the Gr layer. It has been found that

on Cu(111) single crystals, Gr forms a long-range hexagonal Moiré superstructures with a 2 ± 0.4 nm periodicity.

One of the aims of this research work was to further investigate Gr as a protective coating for Cu in electrochemical environment. The behavior of fully and partially covering Gr films was studied.

The combination of STM with electrochemical cell allowed to perform *in situ* measurements. The advantage of the investigation of graphene/copper system by EC-STM is that the morphology of the surface of Gr films under potential control can be observed and monitored as a function of time. Our study of the surface morphology changes during the potential variation of the samples in the electrolytes suggest that Gr layers protects Cu against the oxidation/dissolution in case of low number of grain boundaries and defects.

In the second part of the thesis, it was studied the morphology, structure and stability in electrochemical conditions of metals NPs supported on Gr/Cu. Pd and Co NPs deposited either by electrochemical deposition of PVD were used as archetypal noble and non-noble metal catalysts for the HER. Unfortunately, a limited stability of the NPs was observed especially for the Co NPs, so it was attempted to stabilize the metal by intercalation: i.e. forming a layer of Gr on top of the NPs, since it has been demonstrated to protect the metal nanoparticles and in some case to promote the chemical activity by the interfacial hybridization between metal and carbon states. However, in the present case no promotion effect was observed, but only a substantial loss of activity.

Bibliography

[1] I.E.L. Stephens, I. Chorkendorff, Minimizing the Use of Platinum in Hydrogen-Evolving Electrodes, Angew. Chemie Int. Ed. 50 (2011) 1476–1477.

[2] W. Zhou, J. Zhou, Y. Zhou, J. Lu, K. Zhou, L. Yang, Z. Tang, L. Li, S. Chen, N-doped carbon-wrapped cobalt nanoparticles on N-doped graphene nanosheets for high-efficiency hydrogen production, Chem. Mater. 27 (2015) 2026–2032.

[3] H. Zhang, Z. Ma, J. Duan, H. Liu, G. Liu, T. Wang, K. Chang, M. Li, L. Shi, X. Meng, K. Wu, J. Ye, Active Sites Implanted Carbon Cages in Core–Shell Architecture: Highly Active and Durable Electrocatalyst for Hydrogen Evolution Reaction, ACS Nano. 10 (2016) 684–694.

[4] A.T. N'Diaye, S. Bleikamp, P.J. Feibelman, T. Michely, Two-Dimensional Ir Cluster Lattice on a Graphene Moiré on Ir(111), Phys. Rev. Lett. 97 (2006) 215501.

[5] Z. Zhou, F. Gao, D.W. Goodman, Deposition of metal clusters on single-layer graphene/Ru(0001): Factors that govern cluster growth, Surf. Sci. 604 (2010) L31–L38.

[6] A.K. Geim, K.S. Novoselov, The rise of graphene, Nat. Mater. 6 (2007) 183–191.

[7] P.R. Wallace, The Band Theory of Graphite, Phys. Rev. 71 (1947) 622–634.

[8] A.H.C. Neto, F. Guinea, N.M.R. Peres, K.S. Novoselov, A.K. Geim, The electronic properties of graphene, Rev. Mod. Phys. 81 (2007) 109–162.

[9] K.S. Novoselov, A.K. Geim, S. V Morozov, D. Jiang, Y. Zhang, S. V Dubonos, I. V Grigorieva, A.A. Firsov, Electric Field Effect in Atomically Thin Carbon Films, Science. 306 (2004) 666–669.

[10] H.P. Boehm, R. Setton, E. Stumpp, Nomenclature and terminology of graphite intercalation compounds (IUPAC Recommendations 1994), Pure Appl. Chem. 66 (1994) 1893–1901.

[11] R.R. Nair, P. Blake, A.N. Grigorenko, K.S. Novoselov, T.J. Booth, T. Stauber, N.M.R.

Peres, A.K. Geim, Fine Structure Constant Defines Visual Transparency of Graphene, Science. 320 (2008) 1308–1308.

[12] D.C. Elias, R.R. Nair, T.M.G. Mohiuddin, S. V Morozov, P. Blake, M.P. Halsall, A.C. Ferrari, D.W. Boukhvalov, M.I. Katsnelson, A.K. Geim, K.S. Novoselov, Control of Graphene's Properties by Reversible Hydrogenation: Evidence for Graphane, Science. 323 (2009) 610–613.

[13] C. Lee, X. Wei, J.W. Kysar, J. Hone, Measurement of the Elastic Properties and Intrinsic Strength of Monolayer Graphene, Science. 321 (2008) 385–388.

[14] G.-H. Lee, R.C. Cooper, S.J. An, S. Lee, A. van der Zande, N. Petrone, A.G. Hammerberg, C. Lee, B. Crawford, W. Oliver, J.W. Kysar, J. Hone, High-Strength Chemical-Vapor-Deposited Graphene and Grain Boundaries, Science. 340 (2013) 1073–1076.

[15] A.A. Balandin, S. Ghosh, W. Bao, I. Calizo, D. Teweldebrhan, F. Miao, C.N. Lau, Superior Thermal Conductivity of Single-Layer Graphene, Nano Lett. 8 (2008) 902–907.

[16] K.I. Bolotin, K.J. Sikes, Z. Jiang, M. Klima, G. Fudenberg, J. Hone, P. Kim, H.L. Stormer, Ultrahigh electron mobility in suspended graphene, Solid State Commun. 146 (2008) 351–355.

[17] K.S. Novoselov, A.K. Geim, S. V Morozov, D. Jiang, M.I. Katsnelson, I. V Grigorieva, S. V Dubonos, A.A. Firsov, Two-dimensional gas of massless Dirac fermions in graphene, Nature. 438 (2005) 197–200.

[18] K.S. Kim, Y. Zhao, H. Jang, S.Y. Lee, J.M. Kim, K.S. Kim, J.-H. Ahn, P. Kim, J.-Y. Choi, B.H. Hong, Large-scale pattern growth of graphene films for stretchable transparent electrodes, Nature. 457 (2009) 706–710.

[19] S. Bae, H. Kim, Y. Lee, X. Xu, J.-S. Park, Y. Zheng, J. Balakrishnan, T. Lei, H. Ri Kim, Y. Il Song, Y.-J. Kim, K.S. Kim, B. Özyilmaz, J.-H. Ahn, B.H. Hong, S. Iijima, Roll-to-roll production of 30-inch graphene films for transparent electrodes, Nat. Nanotechnol. 5 (2010) 574–578.

[20] F. Bonaccorso, L. Colombo, G. Yu, M.D. Stoller, V. Tozzini, A.C. Ferrari, R.S. Ruoff, V. Pellegrini, Graphene, related two-dimensional crystals, and hybrid systems for energy

conversion and storage, Science. 347 (2015) 1246501–1246501.

[21] J.-U. Park, S. Nam, M.-S. Lee, C.M. Lieber, Synthesis of monolithic graphene–graphite integrated electronics, Nat. Mater. 11 (2011) 120–125.

[22] M.P. Levendorf, C.S. Ruiz-Vargas, S. Garg, J. Park, Transfer-Free Batch Fabrication of Single Layer Graphene Transistors, Nano Lett. 9 (2009) 4479–4483.

[23] F. Schwierz, Graphene transistors, Nat. Nanotechnol. 5 (2010) 487–496.

[24] M.D. Stoller, S. Park, Y. Zhu, J. An, R.S. Ruoff, Graphene-Based Ultracapacitors, (2008) 6–10.

[25] S. Stankovich, D.A. Dikin, G.H.B. Dommett, K.M. Kohlhaas, E.J. Zimney, E.A. Stach, R.D. Piner, S.T. Nguyen, R.S. Ruoff, Graphene-based composite materials, Nature. 442 (2006) 282–286.

[26] H. Chang, L. Tang, Y. Wang, J. Jiang, J. Li, Graphene Fluorescence Resonance Energy Transfer Aptasensor for the Thrombin Detection, Anal. Chem. 82 (2010) 2341–2346.

[27] K. Oura, V.G. Lifshits, A. Saranin, A. V. Zotov, M. Katayama, Surface Science. An Introduction., Springer, 2003.

[28] J.D. Wood, S.W. Schmucker, A.S. Lyons, E. Pop, J.W. Lyding, Effects of Polycrystalline Cu Substrate on Graphene Growth by Chemical Vapor Deposition, (2011) 4547–4554.

[29] G.H. Han, F. Güneş, J.J. Bae, E.S. Kim, S.J. Chae, H.-J. Shin, J.-Y. Choi, D. Pribat, Y.H. Lee, Influence of Copper Morphology in Forming Nucleation Seeds for Graphene Growth, Nano Lett. 11 (2011) 4144–4148.

[30] I. Platzman, R. Brener, H. Haick, R. Tannenbaum, Oxidation of Polycrystalline Copper Thin Films at Ambient Conditions, J. Phys. Chem. C. 112 (2008) 1101–1108.

[31] B. Beverskog, Revised Pourbaix Diagrams for Copper at 5-150 °C, Ski Rep. (1995).

[32] H.-H. Strehblow, B. Titze, The investigation of the passive behaviour of copper in weakly acid and alkaline solutions and the examination of the passive film by esca and ISS, Electrochim. Acta. 25 (1980) 839–850.

[33] U. Sander, H.-H. Strehblow, J.K. Dohrmann, I n Situ Photoacoustic Spectroscopy of Thin Oxide Layers on Metal Electrodes. Copper in Alkaline Solution, J. Phys. Chem. 85 (1981) 447–450.

[34] H.-H. Strehblow, H.-D. Speckmann, Corrosion and layer formation of passive copper in alkaline solutions, Werkstoffe Und Korrosion. 35 (1984) 512–519.

[35] M.R.G. De Chialvo, S.L. Marchiano, A.J. Arvía, The mechanism of oxidation of copper in alkaline solutions, J. Appl. Electrochem. 14 (1984) 165–175.

[36] J.C. Hamilton, J.C. Farmer, R.J. Anderson, In Situ Raman Spectroscopy of Anodic Films Formed on Copper and Silver in Sodium Hydroxide Solution, J. Electrochem. Soc. 133 (1986) 739–745.

[37] M. Lohrengel, J. Schultze, H. Speckmann, H.-H. Strehblow, Growth, corrosion and oxide films investigated by pulse techniques, Electrochim. Acta. 32 (1987) 733–742.

[38] J. Gomez Becerra, R.C. Salvarezza, A.J. Arvia, The influence of slow Cu(OH)2 phase formation on the electrochemical behaviour of copper in alkaline solutions, Electrochim. Acta. 33 (1988) 613–621.

[39] W. Kautek, XPS Studies of Anodic Surface Films on Copper Electrodes, J. Electrochem. Soc. 137 (1990) 2672.

[40] S.T. Mayer, R.H. Muller, An In Situ Raman Spectroscopy Study of the Anodic Oxidation of Copper in Alkaline Media, J. Electrochem. Soc. 139 (1992) 426–434.

[41] B. Millet, C. Fiaud, C. Hinnen, E.M.M. Sutter, A correlation between electrochemical behaviour, composition and semiconducting properties of naturally grown oxide films on copper, Corros. Sci. 37 (1995) 1903–1918.

[42] Y. Feng, K.-S. Siow, W.-K. Teo, K.-L. Tan, A.-K. Hsieh, Corrosion Mechanisms and Products of Copper in Aqueous Solutions at Various pH Values, CORROSION. 53 (1997) 389–398.

[43] H.Y.H. Chan, C.G. Takoudis, M.J. Weaver, Oxide Film Formation and Oxygen Adsorption on Copper in Aqueous Media As Probed by Surface-Enhanced Raman Spectroscopy, J. Phys. Chem. B. 103 (1999) 357–365.

[44] C.A. Melendres, G.A. Bowmaker, J.M. Leger, B. Beden, In-situ synchrotron far infrared spectroscopy of surface films on a copper electrode in aqueous solutions, J. Electroanal. Chem. 449 (1998) 215–218.

[45] J. Kunze, V. Maurice, L.H. Klein, H.-H. Strehblow, P. Marcus, In situ STM study of the duplex passive films formed on Cu(111) and Cu(001) in 0.1 M NaOH, Corros. Sci. 46 (2004) 245–264.

[46] H.-H. Strehblow, V. Maurice, P. Marcus, Initial and later stages of anodic oxide formation on Cu, chemical aspects, structure and electronic properties, Electrochim. Acta. 46 (2001) 3755–3766.

[47] J. Kunze, V. Maurice, L.H. Klein, H.-H. Strehblow, P. Marcus, In Situ Scanning Tunneling Microscopy Study of the Anodic Oxidation of Cu(111) in 0.1 M NaOH, J. Phys. Chem. B. 105 (2001) 4263–4269.

[48] V. Maurice, H.-H. Strehblow, P. Marcus, In situ STM study of the initial stages of oxidation of Cu(111) in aqueous solution, Surf. Sci. 458 (2000) 185–194.

[49] V. Maurice, H.-H. Strehblow, P. Marcus, In Situ Scanning Tunneling Microscope Study of the Passivation of Cu(111), J. Electrochem. Soc. 146 (1999) 524–530.

[50] A. Cohen, Corrosion: Materials, Vol. 13B, ASM International, 2005.

[51] R.W. Revie, H.H. Uhlig, Corrosion and Corrosion Control: An introduction to corrosion science and engineering, 2008.

[52] J.R. Davis, Copper and Copper Alloys, ASM Specialty Handbook, 2001.

[53] F.L. Laque, H.R. Copson, eds., Corrosion resistance of Metals and Alloys, Reinhold Publishing Corporation, 1963.

[54] G. Giovannetti, P.A. Khomyakov, G. Brocks, V.M. Karpan, J. Van Den Brink, P.J. Kelly, Doping graphene with metal contacts, Phys. Rev. Lett. 101 (2008) 4–7.

[55] M.C. Schabel, J.L. Martins, Energetics of interplanar binding in graphite, Phys. Rev. B. 46 (1992) 7185–7188.

[56] J.S. Bunch, S.S. Verbridge, J.S. Alden, A.M. van der Zande, J.M. Parpia, H.G. Craighead,

P.L. McEuen, Impermeable Atomic Membranes from Graphene Sheets, Nano Lett. 8 (2008) 2458–2462.

[57] S. Chen, L. Brown, M.P. Levendorf, W. Cai, S.Y. Ju, J. Edgeworth, X. Li, C.W. Magnuson, A. Velamakanni, R.D. Piner, J. Kang, J. Park, R.S. Ruoff, Oxidation resistance of graphene-coated Cu and Cu/Ni alloy, ACS Nano. 5 (2011) 1321–1327.

[58] D.A.C. Brownson, L.J. Munro, D.K. Kampouris, C.E. Banks, Electrochemistry of graphene: not such a beneficial electrode material?, RSC Adv. 1 (2011) 978–988.

[59] F. Zhou, Z. Li, G.J. Shenoy, L. Li, H. Liu, Enhanced Room-Temperature Corrosion of Copper in the Presence of Graphene, ACS Nano. 7 (2013) 6939–6947.

[60] M. Schriver, W. Regan, W.J. Gannett, A.M. Zaniewski, M.F. Crommie, A. Zettl, Graphene as a long-term metal oxidation barrier: Worse than nothing, ACS Nano. 7 (2013) 5763–5768.

[61] P.R. Kidambi, B.C. Bayer, R. Blume, Z.J. Wang, C. Baehtz, R.S. Weatherup, M.G. Willinger, R. Schloegl, S. Hofmann, Observing graphene grow: Catalyst-graphene interactions during scalable graphene growth on polycrystalline copper, Nano Lett. 13 (2013) 4769–4778.

[62] W. Norimatsu, M. Kusunoki, Epitaxial graphene on SiC{0001}: advances and perspectives, Phys.Chem.Chem.Phys. (2014) 3501–3511.

[63] G.M. Rutter, J.N. Crain, N.P. Guisinger, T. Li, P.N. First, J.A. Stroscio, Scattering and Interference in Epitaxial Graphene, Science. 317 (2007) 219–222.

[64] J. Kim, H. Park, J.B. Hannon, S.W. Bedell, K. Fogel, D.K. Sadana, C. Dimitrakopoulos, Layer-Resolved Graphene Transfer via Engineered Strain Layers, Science (80-.). 342 (2013) 833–836.

[65] M.J. Allen, V.C. Tung, R.B. Kaner, Honeycomb carbon: A review of graphene, Chem. Rev. 110 (2010) 132–145.

[66] W.S. Hummers, R.E. Offeman, Preparation of Graphitic Oxide, J. Am. Chem. Soc. 80 (1958) 1339–1339.

[67] X. Li, W. Cai, J. An, S. Kim, J. Nah, D. Yang, R. Piner, A. Velamakanni, I. Jung, E. Tutuc, S.K. Banerjee, L. Colombo, R.S. Ruoff, Large-area synthesis of high-quality and uniform graphene films on copper foils, Science. 324 (2009) 1312–1314.

[68] C. Mattevi, H. Kim, M. Chhowalla, A review of chemical vapour deposition of graphene on copper, J. Mater. Chem. 21 (2011) 3324–3334.

[69] X. Li, W. Cai, L. Colombo, R. Ruoff, Evolution of graphene growth on Ni and Cu by carbon isotope labeling, Nano Lett. 12 (2009) 1–15.

[70] G.A. López, E.J. Mittemeijer, The solubility of C in solid Cu, Scr. Mater. 51 (2004) 1–5.

[71] H. Kim, C. Mattevi, M.R. Calvo, J.C. Oberg, L. Artiglia, S. Agnoli, C.F. Hirjibehedin, M. Chhowalla, E. Saiz, Activation energy paths for graphene nucleation and growth on Cu, ACS Nano. 6 (2012) 3614–3623.

[72] X. Li, C.W. Magnuson, A. Venugopal, J. An, J.W. Suk, B. Han, M. Borysiak, W. Cai, A. Velamakanni, Y. Zhu, L. Fu, E.M. Vogel, E. Voelkl, L. Colombo, R.S. Ruoff, Graphene films with large domain size by a two-step chemical vapor deposition process, Nano Lett. 10 (2010) 4328–4334.

[73] S. Bhaviripudi, X. Jia, M.S. Dresselhaus, J. Kong, Role of kinetic factors in chemical vapor deposition synthesis of uniform large area graphene using copper catalyst, Nano Lett. 10 (2010) 4128–4133.

[74] R.M. Jacobberger, M.S. Arnold, Graphene Growth Dynamics on Epitaxial Copper Thin Films, Chem. Mater. 25 (2013) 871–877.

[75] C. Hwang, K. Yoo, S.J. Kim, E.K. Seo, H. Yu, L.P. Bir, Initial Stage of Graphene Growth on a Cu Substrate, (2011) 22369–22374.

[76] K. Celebi, M.T. Cole, J.W. Choi, F. Wyczisk, P. Legagneux, N. Rupesinghe, J. Robertson, K.B.K. Teo, H.G. Park, Evolutionary kinetics of graphene formation on copper, Nano Lett. 13 (2013) 967–974.

[77] W. Wu, L.A. Jauregui, Z. Su, Z. Liu, J. Bao, Y.P. Chen, Q. Yu, Growth of single crystal graphene arrays by locally controlling nucleation on polycrystalline Cu using chemical vapor deposition, Adv. Mater. 23 (2011) 4898–4903.

[78] Q. Yu, L.A. Jauregui, W. Wu, R. Colby, J. Tian, Z. Su, H. Cao, Z. Liu, D. Pandey, D. Wei, T.F. Chung, P. Peng, N.P. Guisinger, E. a Stach, J. Bao, S.-S. Pei, Y.P. Chen, Control and characterization of individual grains and grain boundaries in graphene grown by chemical vapour deposition., Nat. Mater. 10 (2011) 443–449. doi:10.1038/nmat3010.

[79] H. Chen, W. Zhu, Z. Zhang, Contrasting Behavior of Carbon Nucleation in the Initial Stages of Graphene Epitaxial Growth on Stepped Metal Surfaces, 186101 (2010) 1–4.

[80] J.A. Venables, G.D.T. Spiller, M. Hanbucken, Nucleation and growth of thin films, 399 (1984).

[81] C. Ratsch, J. a. Venables, Nucleation theory and the early stages of thin film growth, J. Vac. Sci. Technol. A Vacuum, Surfaces, Film. 21 (2003) S96.

[82] D.J. Gardiner, Practical Raman spectroscopy, Springer-Verlag, 1989.

[83] M.S. Dresselhaus, A. Jorio, R. Saito, Characterizing Graphene, Graphite, and Carbon Nanotubes by Raman Spectroscopy, Annu. Rev. Condens. Matter Phys. 1 (2010) 89–108.

[84] R.J. Nemanich, S.A. Solin, First- and second-order Raman scattering from finite-size crystals of graphite, Phys. Rev. B. 20 (1979) 392–401.

[85] G.A. Somorjai, Introduction to Surface Chemistry and Catalysis, (1994) 667.

[86] P.J. Gellings, H.J.M. Bouwmeester, The CRC Handbook of Solid State Electrochemistry, CRC Press, Inc., 1997.

[87] D. Pletcher, F.C. Walsh, Industrial Electrochemistry, 1993.

[88] V.S. Bagotsky, Fundamentals of electrochemistry, Second Edi, John Wiley & Sons, Inc, 2006.

[89] G. Jerkiewicz, From electrochemistry to molecular-level the solid-liquid electrochemical interface - An overview, in: Solid-Liquid Electrochem. Interfaces, American Chemical Society, Washington, DC, 1997: pp. 1–12.

[90] D.C. Grahame, The electrical double layer and the theory of electrocapillarity., Chem. Rev. (1947) 441–501.

[91] J.E.B. Randles, A cathode ray polarograph. part II. The current-voltage curves., Trans. Faraday Soc. 44 (1948) 327–338.

[92] A. Sevcik, Oscillographic polarography with periodical triangular voltage, Collect. Czechoslov. Chem. Commun. 13 (1948) 349–377.

[93] J.O. Bockris, B.E. Conway, E. Yeager, R.E. White, Comprehensive Treatise of Electrochemistry. Electrochemical Materials Science., 1981.

[94] M. Stern, A.L. Geary, Electrochemical Polarization, J. Electrochem. Soc. 104 (1957) 559.

[95] M. Wilms, Potentiodynamische Rastertunnelmikroskopie an Fest / Flüssig-Grenzflächen : Apparative Entwicklung und Untersuchungen zur Sulfat-Adsorption auf Cu (111), PhD Thesis (1999).

[96] G. Binnig, H. Rohrer, C. Gerber, E. Weibel, Surface studies by scanning tunneling microscopy, Phys. Rev. Lett. 49 (1982) 57–61.

[97] L. Gao, J.R. Guest, N.P. Guisinger, Epitaxial graphene on Cu(111), Nano Lett. 10 (2010) 3512–3516.

[98] H.I. Rasool, E.B. Song, M. Mecklenburg, B.C. Regan, K.L. Wang, B.H. Weiller, J.K. Gimzewski, Atomic-Scale Characterization of Graphene Grown on Copper (100) Single Crystals, J. Am. Chem. Soc. 133 (2011) 12536–12543.

[99] T. Niu, M. Zhou, J. Zhang, Y. Feng, W. Chen, Growth Intermediates for CVD Graphene on Cu(111): Carbon Clusters and Defective Graphene, J. Am. Chem. Soc. 135 (2013) 8409–8414.

[100] R. Sonnenfeld, P.K. Hansma, Atomic-resolution microscopy in water., Science. 232 (1986) 211–213.

[101] K. Itaya, In situ scanning tunneling microscopy in electrolyte solutions, Prog. Surf. Sci. 58 (1998) 121–247.

[102] J. Tersoff, D.R. Hamann, Theory and application for the scanning tunneling microscope, Phys. Rev. Lett. 50 (1983) 1998.

[103] J. Tersoff, D.R. Hamann, Theory of the scanning tunneling microscope, Phys. Rev. B. 31 (1985) 805–813.

[104] J. Bardeen, Tunneling from a many-particle point of view, Phys. Rev. Lett. 6 (1961) 57–59.

[105] M. Wilms, M. Kruft, G. Bermes, K. Wandelt, A new and sophisticated electrochemical scanning tunneling microscope design for the investigation of potentiodynamic processes, Rev. Sci. Instrum. 70 (1999) 3641–3650.

[106] K. Besocke, An easily operable scanning tunneling microscope, Surf. Sci. 181 (1987) 145–153.

[107] M. Wilms, M. Schmidt, G. Bermes, K. Wandelt, New and versatile ultrahigh vacuum scanning tunneling microscope for film growth experiments, Rev. Sci. Instrum. 69 (1998) 2696–2703.

[108] M. Wilms, Diplomarbeit, Universitat Bonn, 1994.

[109] I. Horcas, R. Fernández, J.M. Gómez-Rodríguez, J. Colchero, J. Gómez-Herrero, A.M. Baro, WSXM: A software for scanning probe microscopy and a tool for nanotechnology, Rev. Sci. Instrum. 78 (2007) 1–8.

[110] W. Polewska, R.J. Behm, O.M. Magnussen, In-situ video-STM studies of Cu electrodeposition on Cu(100) in HCl solution, Electrochim. Acta. 48 (2003) 2915–2921.

[111] M.R. Vogt, F.A. Möller, C.M. Schilz, O.M. Magnussen, R.J. Behm, Adsorbate-induced step faceting of Cu(100) electrodes in HCl, Surf. Sci. 367 (1996).

[112] J. Ustarroz, X. Ke, A. Hubin, S. Bals, H. Terryn, New insights into the early stages of nanoparticle electrodeposition, J. Phys. Chem. C. 116 (2012) 2322–2329.

[113] Y. Hasegawa, J.F. Jia, K. Inoue, A. Sakai, T. Sakurai, Elemental contrast of local work function studied by scanning tunneling microscopy, 386 (1997) 328–334.

[114] T. Brülle, U. Stimming, Platinum nanostructured HOPG - Preparation, characterization and reactivity, J. Electroanal. Chem. 636 (2009) 10–17.

[115] D.R. Stulland, C.G. Sinke, Thermodynamic properties of elements, 18th ed., ACS, 1956.

[116] Y.H. Lee, J.H. Lee, Scalable growth of free-standing graphene wafers with copper(Cu) catalyst on SiO2/Si substrate: Thermal conductivity of the wafers, Appl. Phys. Lett. 96 (2010) 2–4.

[117] Y. Zhang, Z. Li, P. Kim, L. Zhang, C. Zhou, Anisotropic hydrogen etching of chemical vapor deposited graphene, ACS Nano. 6 (2012) 126–132.

[118] J.W.M. Frenken, J.F. van der Veen, Observation of Surface Melting, Phys. Rev. Lett. 54 (1985) 134–137.

[119] A.-Y. Lu, S.-Y. Wei, C.-Y. Wu, Y. Hernandez, T.-Y. Chen, T.-H. Liu, C.-W. Pao, F.-R. Chen, L.-J. Li, Z.-Y. Juang, Decoupling of CVD graphene by controlled oxidation of recrystallized Cu, RSC Adv. 2 (2012) 3008–3013.

[120] A.C. Ferrari, J.C. Meyer, V. Scardaci, C. Casiraghi, M. Lazzeri, F. Mauri, S. Piscanec, D. Jiang, K.S. Novoselov, S. Roth, A.K. Geim, Raman spectrum of graphene and graphene layers, Phys. Rev. Lett. 97 (2006) 1–4.

[121] C. Casiraghi, Raman intensity of graphene, Phys. Status Solidi Basic Res. 248 (2011) 2593–2597.

[122] D.M. Basko, Boundary problems for Dirac electrons and edge-assisted Raman scattering in graphene, Phys. Rev. B - Condens. Matter Mater. Phys. 79 (2009).

[123] I. Calizo, W. Bao, F. Miao, C.N. Lau, A.A. Balandin, The effect of substrates on the Raman spectrum of graphene: Graphene- on-sapphire and graphene-on-glass, Appl. Phys. Lett. 91 (2007) 2–4.

[124] Y.Y. Wang, Z.H. Ni, T. Yu, Z.X. Shen, H.M. Wang, Y.H. Wu, W. Chen, A.T.S. Wee, Raman studies of monolayer graphene: The substrate effect, J. Phys. Chem. C. 112 (2008) 10637–10640.

[125] S.D. Costa, A. Righi, C. Fantini, Y. Hao, C. Magnuson, L. Colombo, R.S. Ruoff, M.A. Pimenta, Resonant Raman spectroscopy of graphene grown on copper substrates, Solid State Commun. 152 (2012) 1317–1320.

[126] X. Li, C.W. Magnuson, A. Venugopal, R.M. Tromp, J.B. Hannon, E.M. Vogel, L. Colombo, R.S. Ruoff, Large-Area Graphene Single Crystals Grown by Low-Pressure

Chemical Vapor Deposition of Methane on Copper, J. Am. Chem. Soc. 133 (2011) 2816–2819.

[127] K. Celebi, M.T. Cole, K.B.K. Teo, H.G. Park, Observations of Early Stage Graphene Growth on Copper, Electrochem. Solid-State Lett. 15 (2012) K1.

[128] W.T.S. Ramos, T.H.R. Cunha, I.D. Barcelos, D.R. Miquita, G.A. Ferrari, S. de Oliveira, L.M. Seara, E.G.S. Neto, A.S. Ferlauto, R.G. Lacerda, The role of hydrogen partial pressure on the annealing of copper substrates for graphene CVD synthesis, Mater. Res. Express. 3 (2016) 45602.

[129] J.M. Wofford, S. Nie, K.F. McCarty, N.C. Bartelt, O.D. Dubon, Graphene islands on Cu foils: The interplay between shape, orientation, and defects, Nano Lett. 10 (2010) 4890–4896.

[130] W. Ge, B. Lu, W. Li, J. Lu, Z. Ye, Synthesis of graphene together with undesired CuxO nanodots on copper foils by low-pressure chemical vapor deposition, Vacuum. 97 (2013) 9–14.

[131] I. Vlassiouk, M. Regmi, P. Fulvio, S. Dai, P. Datskos, G. Eres, S. Smirnov, Role of hydrogen in chemical vapor deposition growth of large single-crystal graphene, ACS Nano. 5 (2011) 6069–6076.

[132] C. Mattevi, G. Eda, S. Agnoli, S. Miller, K.A. Mkhoyan, O. Celik, D. Mastrogiovanni, G. Granozzi, E. Carfunkel, M. Chhowalla, Evolution of electrical, chemical, and structural properties of transparent and conducting chemically derived craphene thin films, Adv. Funct. Mater. 19 (2009) 2577–2583.

[133] D. Tahir, S. Tougaard, Electronic and optical properties of Cu, CuO and Cu 2 O studied by electron spectroscopy, J. Phys. Condens. Matter. 24 (2012) 175002.

[134] S. Gottardi, K. Müller, L. Bignardi, J.C. Moreno-López, T.A. Pham, O. Ivashenko, M. Yablonskikh, A. Barinov, J. Björk, P. Rudolf, M. Stöhr, Comparing Graphene Growth on Cu(111) versus Oxidized Cu(111), Nano Lett. 15 (2015) 917–922.

[135] Y.P. Hsieh, M. Hofmann, K.W. Chang, J.G. Jhu, Y.Y. Li, K.Y. Chen, C.C. Yang, W.S. Chang, L.C. Chen, Complete corrosion inhibition through graphene defect passivation, ACS

Nano. 8 (2014) 443–448.

[136] S. Syed, Atmospheric corrosion of materials, Emirates J. Eng. Res. 11 (2006) 1–24.

[137] R.L. McCreery, Advanced Carbon Electrode Materials for Molecular Electrochemistry, Chem. Rev. 108 (2008) 2646–2687.

[138] X.-W. Liu, J.-J. Mao, P.-D. Liu, X.-W. Wei, Fabrication of metal-graphene hybrid materials by electroless deposition, Carbon N. Y. 49 (2011) 477–483.

[139] D. Prasai, J.C. Tuberquia, R.R. Harl, G.K. Jennings, K.I. Bolotin, Graphene: Corrosion-Inhibiting Coating, ACS Nano. 6 (2012) 1102–1108.

[140] W. Ju, M. Favaro, C. Durante, L. Perini, S. Agnoli, O. Schneider, U. Stimming, G. Granozzi, Pd Nanoparticles deposited on nitrogen-doped HOPG: New Insights into the Pd-catalyzed Oxygen Reduction Reaction, Electrochim. Acta. 141 (2014) 89–101.

[141] M. Favaro, L. Perini, S. Agnoli, C. Durante, G. Granozzi, A. Gennaro, Electrochemical behavior of N and Ar implanted highly oriented pyrolytic graphite substrates and activity toward oxygen reduction reaction, Electrochim. Acta. 88 (2013) 477–487.

[142] C.P. Kim, K. Nobe, Polarization of Copper in Acidic and Alkaline Solutions, Corrosion. 27 (1971) 382–385.

[143] R.K. Singh Raman, P. Chakraborty Banerjee, D.E. Lobo, H. Gullapalli, M. Sumandasa, A. Kumar, L. Choudhary, R. Tkacz, P.M. Ajayan, M. Majumder, Protecting copper from electrochemical degradation by graphene coating, Carbon N. Y. 50 (2012) 4040–4045.

[144] A.M. Fenelon, C.B. Breslin, The electrochemical synthesis of polypyrrole at a copper electrode : corrosion protection properties, 47 (2002) 4467–4476.

[145] V. Mišković-Stanković, I. Jevremović, I. Jung, K. Rhee, Electrochemical study of corrosion behavior of graphene coatings on copper and aluminum in a chloride solution, Carbon N. Y. 75 (2014) 335–344.

[146] B.P. Singh, B.K. Jena, S. Bhattacharjee, L. Besra, Surface & Coatings Technology Development of oxidation and corrosion resistance hydrophobic graphene oxide-polymer composite coating on copper, Surf. Coat. Technol. 232 (2013) 475–481.

[147] N.T. Kirkland, T. Schiller, N. Medhekar, N. Birbilis, Exploring graphene as a corrosion protection barrier, Corros. Sci. 56 (2012) 1–4.

[148] E. McCafferty, Validation of corrosion rates measured by the Tafel extrapolation method, Corros. Sci. 47 (2005) 3202–3215.

[149] E. Mattsson, J.O. Bockris, Galvanostatic studies of the kinetics of deposition and dissolution in the copper + copper sulphate system, Trans. Faraday Soc. 55 (1959) 1586.

[150] H.I. Rasool, E.B. Song, M.J. Allen, J.K. Wassei, R.B. Kaner, K.L. Wang, B.H. Weiller, J.K. Gimzewski, Continuity of Graphene on Polycrystalline Copper, Nano Lett. 11 (2011) 251–256.

[151] L. Zhao, K.T. Rim, H. Zhou, R. He, T.F. Heinz, A. Pinczuk, G.W. Flynn, A.N. Pasupathy, Influence of copper crystal surface on the CVD growth of large area monolayer graphene, Solid State Commun. 151 (2011) 509–513.

[152] Y. Zhang, T. Gao, Y. Gao, S. Xie, Q. Ji, K. Yan, H. Peng, Z. Liu, Defect-like structures of graphene on copper foils for strain relief investigated by high-resolution scanning tunneling microscopy, ACS Nano. 5 (2011) 4014–4022.

[153] W.J. Zhu, T. Low, V. Perebeinos, a a Bol, Y. Zhu, H.G. Yan, J. Tersoff, P. Avouris, Structure and Electronic Transport in Graphene Wrinkles, Nano Lett. 12 (2012) 3431–3436.

[154] L.J. Wan, K. Itaya, In Situ Scanning Tunneling Microscopy of Benzene, Naphthalene, and Anthracene Adsorbed on Cu(111) in Solution, Langmuir. 13 (1997) 7173–7179.

[155] J. Inukai, Y. Osawa, K. Itaya, Adlayer Structures of Chlorine, Bromine, and Iodine on Cu(111) Electrode in Solution: In-Situ STM and ex-Situ LEED Studies, J. Phys. Chem. B. 102 (1998) 10034–10040.

[156] G. Brisard, N. Bertrand, P.N. Ross, N.M. Marković, Oxygen reduction and hydrogen evolution-oxidation reactions on Cu(hkl) surfaces, J. Electroanal. Chem. 480 (2000) 219–224.

[157] D. Friebel, T. Mangen, B. Obliers, C. Schlaup, P. Broekmann, K. Wandelt, On the

existence of ordered organic adlayers at the Cu(111)/electrolyte interface, Langmuir. 20 (2004) 2803–2806.

[158] I. Wlasny, P. Dabrowski, M. Rogala, I. Pasternak, W. Strupinski, J.M. Baranowski, Z. Klusek, Impact of electrolyte intercalation on the corrosion of graphene-coated copper, Corros. Sci. 92 (2015) 69–75.

[159] D.W. Suggs, A.J. Bard, Scanning Tunneling Microscopic Study with Atomic Resolution of the Dissolution of Cu(111) Electrodes in Aqueous Chloride Media, J. Am. Chem. Sociaity. 116 (1994) 10725–10733.

[160] D.W. Suggs, A.J. Bard, Scanning Tunneling Microscopic Study with Atomic Resolution of the Dissolution of Cu(100) in Aqueous Chloride Solutions, J. Phys. Chem. 99 (1995) 8349–8355.

[161] P. Broekmann, M. Wilms, M. Kruft, C. Stuhlmann, K. Wandelt, In-situ STM investigation of specific anion adsorption on Cu(111), J. Electroanal. Chem. 467 (1998) 307–324.

[162] M. Wilms, P. Broekmann, M. Kruft, Z. Park, C. Stuhlmann, K. Wandelt, STM investigation of specific anion adsorption on Cu(111) in sulfuric acid electrolyte, Surf. Sci. 402–404 (1998) 83–86.

[163] M. Wilms, P. Broekmann, C. Stuhlmann, K. Wandelt, In-situ STM investigation of adsorbate structures on Cu(111) in sulfuric acid electrolyte, Surf. Sci. 416 (1998) 121–140.

[164] P. Broekmann, M. Wilms, A. Spaenig, K. Wandelt, Morphological aspects of sulfate-induced reconstruction of Cu(111) in sulfuric acid solution: in situ STM study, Prog. Surf. Sci. 67 (2001) 59–77.

[165] A. Ambrosi, A. Bonanni, Z. Sofer, M. Pumera, Large-scale quantification of CVD graphene surface coverage, Nanoscale. 5 (2013) 2379.

[166] J. Meier, J. Schiøtz, P. Liu, J.K. Nørskov, U. Stimming, Nano-scale effects in electrochemistry, Chem. Phys. Lett. 390 (2004) 440–444.

[167] W. Ju, T. Brülle, M. Favaro, L. Perini, C. Durante, O. Schneider, U. Stimming, Palladium

Nanoparticles Supported on Highly Oriented Pyrolytic Graphite: Preparation, Reactivity and Stability, ChemElectroChem. 2 (2015) 547–558.

[168] M. Simões, S. Baranton, C. Coutanceau, Enhancement of catalytic properties for glycerol electrooxidation on Pt and Pd nanoparticles induced by Bi surface modification, Appl. Catal. B Environ. 110 (2011) 40–49.

[169] M. Favaro, S. Agnoli, L. Perini, C. Durante, A. Gennaro, G. Granozzi, Palladium nanoparticles supported on nitrogen-doped HOPG: a surface science and electrochemical study., Phys. Chem. Chem. Phys. 15 (2013) 2923–2931.

[170] M. Hara, U. Linke, T. Wandlowski, Preparation and electrochemical characterization of palladium single crystal electrodes in 0.1 M H2SO4 and HClO4. Part I. Low-index phases, Electrochim. Acta. 52 (2007) 5733–5748.

[171] L.D. Burke, An Examination of the Electrochemical Behavior of Palladium in Base, J. Electrochem. Soc. 140 (1993) 1292.

[172] C. Lin, C. Chen, J. Wang, Mechanistic Studies of Water - Gas-Shift Reaction on Transition Metals, (2011) 18582–18588.

[173] Z. Wei, Y. Chen, J. Wang, D. Su, M. Tang, S. Mao, Y. Wang, Cobalt Encapsulated in N-Doped Graphene Layers: An Efficient and Stable Catalyst for Hydrogenation of Quinoline Compounds, ACS Catal. (2016) 5816–5822.

[174] Q. Liao, H.J. Zhang, K. Wu, H.Y. Li, S.N. Bao, P. He, Nucleation and growth of monodispersed cobalt nanoclusters on graphene moiré on Ru(0001), Nanotechnology. 22 (2011) 125303.

[175] R. Decker, J. Brede, N. Atodiresei, V. Caciuc, S. Blügel, R. Wiesendanger, Atomic-scale magnetism of cobalt-intercalated graphene, Phys. Rev. B. 87 (2013) 41403.

[176] W. Luo, S. Zafeiratos, Tuning Morphology and Redox Properties of Cobalt Particles Supported on Oxides by an in between Graphene Layer, J. Phys. Chem. C. 120 (2016) 14130–14139.

[177] H. Gomez Meier, J.R. Vilche, A.J. Arvia, The electrochemical behaviour of cobalt in alkaline solutions Part I. The potentiodynamic response in the potential region of the

Co/CoO couple, J. Electroanal. Chem. 134 (1982) 251–272.

[178] L.D. Burke, M.M. Murphy, The Electrocatalytic Behavior of Cobalt (and Iron) Electrodes at Low Potential in Base, J. Electrochem. Soc. 138 (1991) 88.

[179] A.C. Ferrari, Raman spectroscopy of graphene and graphite: Disorder, electron-phonon coupling, doping and nonadiabatic effects, Solid State Commun. 143 (2007) 47–57.

Appendix A. Papers and conferences

Papers

M. Zanatta, L. Calvillo, J. Zheng, G. A. Rizzi, C. Durante, G. Giallongo, **D. Chirkov**, L. Colazzo, C. Marega, A. Gennaro, G. Granozzi. Cu_2O/TiO_2 heterostructures on a DVD as easy&cheap photoelectrochemical sensors. Thin Solid Films, 603 (2016) 193-201.

Conferences

D. Chirkov, C. Durante, T. Kosmala, S. Agnoli, A. Gennaro. EC-STM characterization of graphene supported metal nanoparticles. Giornate dell'Elettrochimica Italiana (GEI2016), 11-14 September 2016, Gargnano, Italy.

D. Chirkov, C. Durante, T. Kosmala, S. Agnoli, A. Gennaro. Graphene supported metal nanoparticles studied by EC-TM. 11th International Symposium on Electrochemical Micro and Nanosystem Technologies (EMNT2016), 17-19 August 2016, Brussels, Belgium.

D. Chirkov, C. Durante, T. Kosmala, S. Agnoli, A. Gennaro. EC-STM characterization of CVD grown graphene and Nitrogen Doped graphene. Giornate dell'Elettrochimica Italiana (GEI2015), 20-24 September 2015, Bertinoro, Italy.